A multi-technical mineralogical, petrological and geochemical approach to the origin of ore mineralizations in the mafic - ultramafic rocks of the Ivrea-Verbano Zone, Piedmont, Northern Italy

Dissertation

BSc. Ing. Peter Kollegger, MSc.

Montanuniversität Leoben
Department of Applied Geosciences and Geophysics
Chair or Resource Mineralogy

Supervisor

Ao.Univ.-Prof. Dr.phil. Oskar A. R. Thalhammer

August 2013

Affidavit

I declare in lieu of oath, that I wrote this thesis and performed the associated research myself, using only the literature cited in this volume.

Peter Kollegger

“Dadurch, daß man einen Bericht Report nennt, wird er nicht besser.”

Helmut Qualtinger

Österreichischer Schauspieler, Schriftsteller, Kabarettist und Rezitator
* 8. Oktober 1928 - † 29. September 1986

Abstract

This thesis is divided into four major parts, according to the main aims of this study. The topic of this thesis was the evaluation of mineralogical, petrological and geochemical characteristics of twelve Fe-Ni-Cu-PGM ore deposits, hosted by the Ivrea-VerbanoZone (IVZ), Northern Italy. The IVZ is interpreted as upended section through lower continental crust and the upper mantle region, which comprises the ore hosting lithologies of the Main Gabbro (Sella Bassa deposit), the Cyclic Units (Gula, Guaifola and Isola deposits), the Ultramafic Pipes (Bec d' Ovaga, Valmaggia, Castello di Gavala, Piancone la Frera and Fei di Doccio deposits) and the La Balma - Monte Capio ultramafic sill (Penninetto, Campello Monti and Alpe Laghetto deposits).

The sulfur isotopic study was conducted on representative samples of each of the twelve sulfide deposits. The isotopic analyses were carried out on pyrrhotite and pentlandite minerals. Isotopic data on each of the stable S isotopes (^{32}S, ^{33}S, ^{34}S and ^{36}S) was gained using a Secondary Ion Mass Spectrometry (SIMS), whereupon the mass dependent ($\delta^{34}S_{VCDT}$) and mass independent fractionation factors ($\Delta^{33}S$ and $\Delta^{36}S$) were calculated. On the one hand, the mass independent fractionation factors were used to interpret the silica and sulfide magma evolution of the investigated mantle lithologies, together with their according sulfide deposits. On the other hand, the mass dependent fractionation factors were interpreted to identify the internal and/or external origin of the sulfur forming the sulfide minerals of pyrrhotite and pentlandite. The results revealed a common magma origin of the deposits hosted by the Main Gabbro and the Cyclic Units, a related but evolved magma origin for the deposits of the Ultramafic Pipes, and an independent magma source for the deposits hosted by the La Balma - Monte Capio ultramafic sill. The evaluation of the mass dependent fractionation factors showed contamination by external sulfur for each of the deposits of the Cyclic Units, as well as for the Fei di Doccio pipe deposit and the Penninetto deposit. All these interpretations are confirmed by the direct correlation with the geological context of the single deposits.

U-Pb age data on zircons of the Fei di Doccio Ultramafic Pipe was gained using a Sensitive High Resolution Ion Micro Probe (SHRIMP II). A total of 23 analyses have been performed on two larger zircons (up to 170µm) and five smaller grains (around 30µm). The zircon grains show an intimate intergrowth with base metal sulfides and hydromagmatic phases. The age of 277±6 Ma was interpreted as the true crystallization age of the pipe, whereas the ages in the range between 277 and 251 Ma are interpreted as rejuvenated ages due to disturbance of the isotope equilibrium by fluids. Thermal rejuvenation was neglected by temperature calculations. This interpretation is in accordance with field observations and the dating of the regional scale magmatic event in the IVZ.

The halogen composition (F, Cl, OH) as well as the trace element contents (REE, U, Th, Y) of 154 apatite minerals of each of the Ultramafic Pipes at Bec d' Ovaga, Castello di Gavala, Piancone la Frera, Valmaggia and Fei di Doccio were analyzed using a Jeol JXA 8200 Superprobe. A generally juvenile mantle character is proposed for both, the melts and the fluids involved in the formation of the apatites. It is clearly evident that the fluids affecting the Ultramafic Pipes are not related to the metasomatic fluids of the Finero Complex. An influence by the metasediments of the adjacent Kinzigite Formation can be neglected. Complex de-mixing processes of fluids and vapors have to

be taken in consideration. The apatites of the Bec d' Ovaga pipe preserved the magmatic signature best, the Valmaggia, the Fei di Doccio and the Piancone la Frera apatites were intermediately affected by coexisting fluids. The strongest chlorine enrichment, with accompanying REE accumulation, is shown by the Castello di Gavala pipe.

A new analytical-statistical technique for the compositional analyses of mineral phases by RAMAN spectroscopy was invented. This new technique was applied to apatites hosted by the Ultramafic Pipes of Bec d' Ovaga, Castello di Gavala and Valmaggia. The results show a maximum use of the advantages of RAMAN spectroscopy, e.g. in-situ analysis, and analysis of very small mineral grains, and a very high level of precision, particularly if compared to standard electron-microscope analyses. This innovative technique is considered immanently important for further investigations because it opens a wide range for a non-destructive and easy-to-use chemical analysis of minerals and materials which possess a relationship between their chemical compositions and their Raman-active vibration modes.

Zusammenfassung

Diese Dissertation ist, entsprechend der Haupt-Untersuchungsziele, in vier Teile unterteilt. Das übergeordnete Ziel dieser Dissertation ist die Untersuchung und Evaluierung von mineralogischen, petrologischen und geochemischen Charakteristika von zwölf Fe-Ni-Cu-PGM Erz-Lagerstätten innerhalb der Ivrea-Verbano Zone (IVZ); Nord-Italien. Die IVZ wird als exhumierte und aufgekippte Sektion durch die Einheiten der unteren Kruste und des oberen Mantles interpretiert. Die lithologischen Einheiten, welche die Erz-Lagerstätten führen, werden wie folgt unterteilt: Main Gabbro (Sella Bassa Lagerstätte), Cyclic Units (Gula, Guaifola und Isola Lagerstätten), Ultramafic Pipes (Bec d' Ovaga, Valmaggia, Castello di Gavala, Piancone la Frera und Fei di Doccio Lagerstätten) und La Balma - Monte Capio ultramafic sill (Penninetto, Campello Monti and Alpe Laghetto Lagerstätten).

Die Untersuchung der Schwefel Isotopen wurde an repräsentativem Probenmaterial, welches jeder der zwölf untersuchten Erz-Lagerstätten entnommen wurde, durchgeführt. Die Analysen wurden jeweils an Pyrrhotit und Pentlandit Mineralen vollzogen. Auf Basis der Messung aller stabiler Isotopen des Schwefels (^{32}S, ^{33}S, ^{34}S und ^{36}S) mittels Secondary Ion Mass Spectrometry (SIMS) wurden die massenabhängigen ($\delta^{34}S_{VCDT}$) und massenunabhängigen (Δ^{33}S and Δ^{36}S) Fraktionierungsfaktoren ermittelt. Die massenunabhängigen Fraktionierungsfaktoren wurden zur gemeinsamen Interpretation der Silikat und Sulfid Magma Entwicklung, der erzführenden Einheiten sowie der Sulfid Erz-Lagerstätten herangezogen. Mit Hilfe der massenabhängigen Fraktionierungsfaktoren wurde die externe und/oder interne Herkunft des Schwefels innerhalb der Erzminerale der einzelnen Lagerstätten evaluiert. Auf Basis dieser Analysen können folgende Annahmen getroffen werden: Die Lagerstätten des Main Gabbro und der Cyclic Units besitzen eine gemeinsame Magmaherkunft. Eine ähnliche, jedoch differenzierte Magmaherkunft kann für die Ultramafic Pipes angenommen werden, wohingegen den Lagerstätten innerhalb des La Balma - Monte Capio ultramafic sill eine unabhängige Magmenquelle zu unterstellen ist. Mit Hilfe der massenabhängigen Fraktionierungsfaktoren konnte die Kontamination durch externen Schwefel für folgende Erz-Lagerstätten nachgewiesen werden: Gula, Guaifola und Isola (Cyclic Units), Fei di Doccio (Ultramafic Pipe), Penninetto (La Balma - Monte Capio ultramafic sill). Alle Annahmen, welche auf Basis der Schwefelisotopie getroffen wurden, korrelieren mit den lithologischen Interpretationen der einzelnen Lagerstätten sowie mit den regionalen geologischen Annahmen innerhalb der IVZ.

Die U-Pb Altersdatierung von Zirkonen der Fei di Doccio Ultramafic Pipe wurde an einer Sensitive High Resolution Ion Micro Probe (SHRIMP II) durchgeführt. Insgesamt wurden 23 Einzelanalysen von zwei größeren (bis zu 170µm) und fünf kleineren Zirkonen (ca. 30µm) aufgenommen. Jeder dieser Zirkone weist eine innige Verwachsung sowohl mit den Sulfid Vererzungen als auch mit hydro-magmatischen Phasen auf. Das tatsächliche Kristallisationsalter der Zirkone der Fei di Doccio Ultramafic Pipe wurde mit 277±6 Ma bestimmt. Die verjüngten Alterswerte (277 bis 251 Ma) wurden höchstwahrscheinlich durch die Interaktion mit Fluiden hervorgerufen, welche zu einer Störung der Isotopengleichgewichte geführt haben. Auf Basis von Temperaturkalkulationen kann eine Verjüngung durch thermale Interferenzen ausgeschlossen werden. Diese Interpretationen stimmen weitestgehend mit Feld-Beobachtungen sowie mit der regionalen Altersbestimmung des magmatischen Events der IVZ überein.

Die Anionen-Zusammensetzung (F, Cl, OH) sowie die Spurenelement und REE Gehalte von insgesamt 154 Apatit Einzelmineralen der fünf Ultramafic Pipes (Bec d' Ovaga, Castello di Gavala, Piancone la Frera, Valmaggia und Fei di Doccio) wurden mittels einer Jeol JXA 8200 Superprobe analysiert. Ein generell juveniler Mantel-Charakter kann sowohl für die Fluide als auch für die Magmen, welche in die Entstehung der Apatite involviert waren, angenommen werden. Die Fluide besitzen keinen Zusammenhang mit den metasomatischen Fluiden des Finero Complex. Ein Einfluss der angrenzenden Kinzigite Formation kann ausgeschlossen werden. Komplexe Entmischungsprozesse der Fluide müssen in Betracht gezogen werden. Die Apatite der Bec d' Ovaga pipe zeigen die geringsten Veränderungen der magmatischen Signaturen. Die Apatite von Valmaggia, Fei di Doccio und Piancone la Frera zeigen eine intermediäre Beeinflussung durch koexistierende Fluide. Die stärksten Interaktionen mit Fluiden, welche zu Anreicherungen von Cl und REE geführt haben, können für die Apatite von Castello di Gavala angenommen werden.

Eine neue analytisch-statistische Methode zur Analysen von chemischen Mineral- Zusammensetzung mittels RAMAN Spektroskopie wurde im Zuge dieser Dissertation konzipiert. Die Entwicklung dieser neuen Technik basiert auf der Analytik von Apatiten der Ultramafic Pipes von Bec d' Ovaga, Castello di Gavala und Valmaggia. Diese Methode kombiniert alle Vorteile der RAMAN Spektroskopie (z.B. in-situ Analytik, die Analyse sehr kleiner Minerale) mit einer sehr hohen Präzision der statistischen Auswertung. Dies wird besonders im Vergleich mit Standard elektronenmikroskopischen Analysen deutlich. Diese innovative Methode ist von großer Bedeutung, da sie eine zerstörungsfreie und einfach durchzuführende chemische Analyse von Mineralien und Materialien ermöglicht, wobei als Voraussetzung eine Interaktion zwischen der chemischen Zusammensetzung und den Raman-aktiven Schwingungsmoden zu bestehen hat.

Acknowledgement

Allen Personen, die mir während der letzten Jahre unterstützt haben, möchte ich an dieser Stelle ein „Herzliches Dankeschön!“ aussprechen.

Größten Dank schulde ich Ao.Univ.-Prof. Dr.phil. Oskar A. R. Thalhammer für seine Unterstützung während der letzten Jahre. Es waren seine stets offene Tür, und seine unerschöpflichen Antworten auf viele Fragen sowie seine Unterstützung bei der Planung und Organisation, die maßgeblichen Anteil am Gelingen dieser Arbeit hatten.

Besonders hervorheben möchte ich die Unterstützung von Dr. Federica Zaccarini und Prof Dr. Giorgio Garuti. Durch die Bereitstellung von Probenmaterial und Daten, die in diese Arbeit einbezogen worden sind, durch die logistische Unterstützung der Geländeund Auslandsaufenthalte, sowie durch die Vermittlung ihres jahrzehntelangen Erfahrungsschatzes im Bereich der Ivrea-Verbano Zone, ist diese Arbeit erst möglich geworden.

Besonderer Dank gilt meinen Freunden und Bürokollegen Dipl.-Geol. Elisabeth Henjes-Kunst und MSc. Gerald Doppler, die stets eine fachliche Unterstützung waren und die Büroarbeit zu einem angenehmen Unterfangen gemacht haben. Nochmals hervorheben möchte ich die langjährige Freundschaft mit MSc. Gerald Doppler welcher mir auch privat stets eine Stüze war und ist.

Herrn Dr.mont. Dipl. Ing. Thomas Unterweissacher sei hier besonders gedankt welche mich in die Untiefen der Software Latex eingeführt hat.

Sämtliche Mitarbeiter des Lehrstuhl für Rohstoffmineralogie mit Univ.-Prof. Dr.phil. Johann Raith an der Spitze haben sehr viel zum Gelingen dieser Arbeit beigetragen.

Hervorheben möchte ich die stets exzellente Unterstützung bei organisatorischen Angelegenheiten von Frau Judith Bergthaler sowie die hervorragende technisch - wissenschaftliche Unterstützung durch Herrn Helmut Mühlhans. Für die hervorragende wissenschaftliche und persönliche Unterstützung möchte ich weiters Ao.Univ.-Prof. Dr. Ronald J. Bakker und MSc. Dr.mont. Amir Morteza Azim Zadeh sehr herzlich danken.

Besonders hervorheben möchte ich das exzellente Arbeitsklima am Lehrstuhl für Rohstoffmineralogie weshalb mir all seine Mitarbeiter ans Herz gewachsen sind!

Der allergrößte Dank gilt natürlich meiner Frau Mag^{a} Johanna Kollegger die mich seit nunmehr neun Jahren erträgt und mich zu jedem Zeitpunkt voll unterstützt hat.

The University Centre of Applied Geosciences Styria (UZAG) is greatly acknowledged for funding this PhD project. My sincere thanks are directed to the Institute of Applied Geosciences and Geophysics (University of Leoben), the Institute of Earth Sciences (University of Graz) and the Institute of Applied Geosciences (Graz University of Technology)

The Centre for Exploration Targeting (CET) at The University of Western Australia is gratefully acknowledged for partly funding analytical work and facilitating the interchange of Peter Kollegger and Marco L. Fiorentini between Australia and Austria. Special thanks go to Assoc. Professor Dr. Marco L. Fiorentini for facilitating the isotope analyses in WA and his valuable scientific support during the entire project. This contribution is a product of collaboration between UZAG, the CET and the Australian Research Council (ARC) Centre of Excellence for Core to Crust Fluid Systems (CCFS). Finally, I would like to thank the staff at MinSep Laboratories (Denmark, Western Australia) for help during the mounting and polishing of the samples.

Contents

Introduction

The Ivrea-Verbano Zone (IVZ) provides one of the world´s most classical and most spectacular cross-sections through rocks of intermediate to deep continental crust. This together with excellent access and sufficient outcrops is the reason that the IVZ has been the subject of numerous petrological, geochemical, structural, and petrophysical studies during the past seven decades. Several ore deposits occurring in the mafic and ultramafic rocks of the IVZ have been documented. However, these ore deposits have been poorly investigated. The available scientific data is fragmentary, limited and a comprehensive investigation on the basis of modern analytical techniques is lacking. In particular the genetic relationship between the different deposits distributed over the IVZ is an unsolved question still, and the timing of ore formation is still vague. Furthermore, the possibly significant role of volatiles in the course of ore fomation, as well as the subsequent influence of metamorphic and metasomatic processes still remain a matter of discussion.

Therefore, this thesis aims in general at a comprehensive and multidisciplinary study on the different types of ore deposits occurring in the mafic and ultramafic rocks of the Ivrea-Verbano Zone (IVZ). Emphasis was placed on mineralogical, petrological and geochemical aspects in order to find relationships between the different deposits to find common and/or disjunctive features to define the environmental conditions and the geodynamic setting in which the deposits were formed. Further emphasis was directed to a detailed investigation of the metallogenetic aspects of the ore mineralisations in order to establish the physico-chemical conditions (i.e. fluid-melt-solid relationships) prevailing during the ore formation, as well as for the interaction between the host rocks and the ore mineralizations.

Finally this thesis provides a comprehensive S-isotopic study of the ore minerals, and U-Th-Pb-isotopic data for age determinations of the ore deposits.

These investigations provide a general, as well as detailed view on the different mineralizations and facilitate a differentiation between the main ore hosting lithologies of the IVZ.

To achieve these goals the highly sophisticated and state of the art analytical techniques were employed , apart of standard mineralogical and petrological methods i.e. transmitted and reflected light microscopy and the use of a comprehensive literature dataset as cited in the references chapter.

Sulfur isotope data (i.e.^{32}S, ^{33}S, ^{34}S and ^{36}S) were obtained by a secondary ion mass spectrometer (SIMS) CAMECA IMS 1280 ion probe, a member of the latest generation of double focusing, magnetic-sector SIMS instruments at the Centre for Microscopy, Characterisation and Analysis, University of Western Australia, Perth.

U-Th-Pb-isotope data for the calculation of the zircon age values was collected via a Sensitive High Resolution Ion Micro Probe (SHRIMP II) at the Department of Imaging and Applied Physics at the John De Laeter Center for Isotope Research, Curtin University, Perth (Western Australia), was applied.

Electron-microprobe (EMP) analyses of the different mineral phases were accomplished using a Jeol JXA 8200 Superprobe at the "Eugen F. Stumpfl Laboratory" at the Department of Applied Geosciences and Geophysics, University of Leoben (Austria).

The analyses of apatite were conducted a using a LABRAM (ISA Jobin Yvon) Raman

spectrometer at the Department of Applied Geosciences and Geophysics, University of Leoben (Austria).

Statistical data analyses accomplished in this thesis were carried out using the software package R version 2.12.2 (2011-02-25) was used (R Development Core Team, 2011).

The study of this thesis has been devided into four major parts, in accordance with four major targets and concordant with the analytical techniques applied. Significant portions of these four chapters are already published, or are either in review at international journals, or existent as manuscripts ready for submission.

General Geology

The Ivrea-Verbano Zone (IVZ) is interpreted as an upended section through lower continental crust and the upper mantle region. (Rutter et al., 2007; Diehl et al., 2009; Schmid et al., 2004; Quick et al., 2003).

The IVZ is bounded to the east by a 2-3 km wide shear zone, the Cossato-Mergozzo-Brissago Line (CMB Line), which contains syn-mylonitic intrusions (Fig. 1). This tectonic lineament forms the contact between the IVZ and the Strona-Ceneri Zone (Mulch et al., 2002).

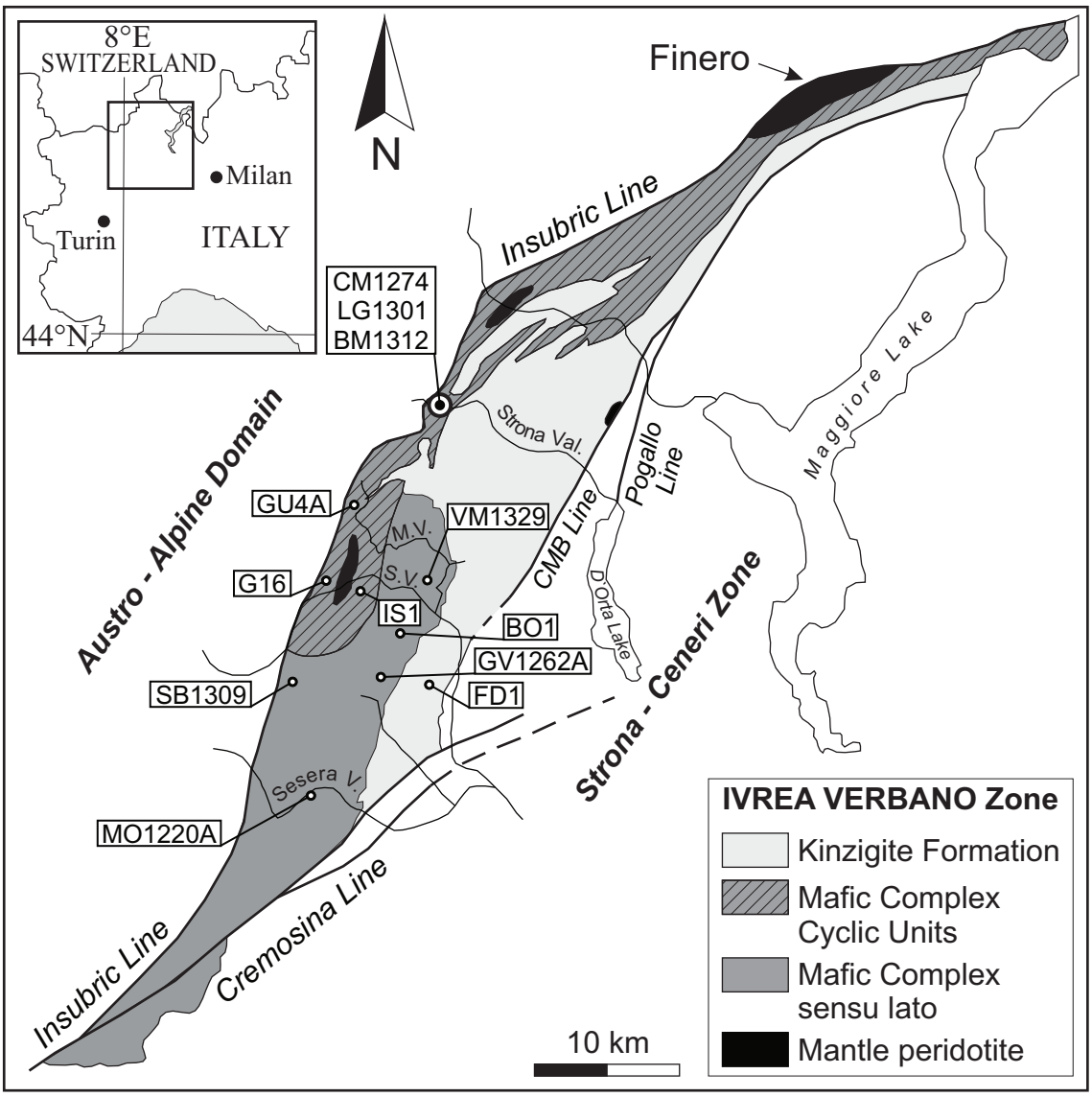

Figure 1: Geological sketch map of the Ivrea-Verbano Zone showing the main lithotectonic divisions and the locations of the sulfide deposits. Deposits: BM: Penninetto, BO: Bec d'Ovaga, CM: Campello Monti , FD: Fei di Doccio, G: Guaifola, GU: Gula, GV: Castello di Gavala, IS: Isola, LG: Alpe Laghetto, MO: Piancone la Frera, SB: Sella Bassa, VM: Valmaggia.

The western boundary is represented by a subvertical strike-slip system, which corresponds to the Insubric Line (Schreiber et al., 2010) and contains mylonites and schists (Quick et al., 1995). The IVZ has a maximum thickness of about 20 km and is tilted to a subvertical position forming an asymmetrical anticline-structure. The present exposure and orientation are mainly the consequences of tilting by about 90 degrees and uplift during Alpine collision (Peressini et al., 2007).

To interpret the ore genesis, the litho-tectonic position of the sulfide mineralizations within the upper mantle, the lower crust as well as the transitional zone between these two units is of special importance. The lower crustal rocks are represented by the Kinzigite Formation, a sequence of high-grade ortho- and parametamorphic rocks (Quick et al., 1995). The Kinzigite Formation is made up by high-grade ortho- and parametamorphic rocks, mainly biotite-sillimanite gneisses, amphibolites, marbles, with minor quartzites and graphite-rich schists and represents the stratigraphically-upper part of the IVZ (Bea and Montero, 1997). Rivalenti et al. (1981) and Quick et al. (1995) concluded that the gabbroic magmas of the Basic Complex intruded the paragneiss of the Kinzigite Formation at intermediate to deep continental crustal levels and Peressini et al. (2007) interpreted this as an underplating event. During this process, the Kinzigite Formation, structurally located above the Mafic Complex, was metamorphosed to granulite facies conditions (Bea and Montero, 1997). The main lithologies of the Basic Complex are gabbros, pyroxenites and amphibole-gabbros, as well as fractionated peridotites and anorthosites and additionally gabbros grading upwards into diorites (Garuti et al., 1986; Quick and Sinigoi, 1992).

The transition between the lower crust and the upper mantle region consists of a layered series of peridotites, pyroxenites, and gabbros with intercalated granulitic metasediments (i.e. Cyclic Units, a part of the Basic Complex according to Ferrario et al. (1982); Garuti et al. (1986)). The second part of the Basic Complex is made up by homogeneous amphibole gabbro, the Main Gabbro, which grades upward into diorites (Garuti et al., 1986). A schematic transect through the crust - mantle transition zone, prior to tilting und uplifting during Alpine collision, is illustrated in Figure 2. Five Ultramafic Pipes intrude the Mafic Complex (i.e. Valmaggia, Castello di Gavala, Bec d' Ovaga and Piancone la Frera) and the Kinzigite Formation (Fei di Doccio), as shown in Figure 11. The pipes mainly consist of peridotites, pyroxenites and gabbros with an alkaline signature and an unusually elevated abundance of incompatible elements, reflected in the minor but ubiquitous occurrence of minerals such as apatite, zircon and baddeleyite (Zaccarini et al., 2004). Stockwork and disseminated Fe-Ni-Cu-Platinum Group Element (PGE) sulfide mineralization (Garuti et al., 1986, 1990; Fiorentini et al., 2002) is associated with all the known pipe occurrences in the IVZ. Mantle peridotite massifs occcur at the localities of Balmuccia, Baldissero and Finero which represent uplifted sub-continental upper mantle rocks (Quick et al., 1995). The Finero complex, shows a strong metasomatic overprint resulting in the occurrence of amphibole, phlogopite, apatite and carbonate (Garuti et al., 1995).

The magmatic sulfide association includes pyrrhotite, pentlandite and chalcopyrite, with minor pyrite, cubanite and mackinawite. Molybdenite, sphalerite, cobaltite, gersdorffite and graphite occur as accessory phases (Garuti et al., 2001). Four different groups of ore deposits including two subgroups can be distinguished, on the basis of their geological

location:

1) The deposit within the Main Gabbro at Sella Bassa (SB): The sulfides are hosted by layers of amphibole-olivine-pyroxenite between amphibole-gabbro layers (Thornber et al., 1993) close to the base of the outcropping Main Gabbro. (near the border to the Insubric Lineamant). There is no tectonic relationship with meta-sedimentary rocks of the Kinzigite Formation obvious (Cumming et al., 1987; Garuti et al., 1990).

2.) Deposits of the Cyclic Units: The Cyclic Units comprise cumulate peridotites, pyroxenites, gabbros, and anorthosites which are interlayered and separated by meta-sedimentary rocks of the Kinzigite Formation (Ferrario et al., 1982). There are contradicting interpretations whether the magmas of the Cyclic Units are related with those of the Main Gabbro or if they have a discrete origin (Fiorentini et al. (2002) and references therein). The sulfide deposits mainly occur concordant within pyroxenite fractionation layers in the vicinity and direct contact with intercalated meta-sediments (Garuti and Rinaldi, 1986a; Cumming et al., 1987; Thornber et al., 1993). Sulfide deposits are present at Isola (IS), Guaifola (G) and Gula (GU).

3.) Deposits hosted by the ultramafic sill of La Balma-Monte Capio: The La Balma-Monte Capio ultramafic sill (approximately 5 km by 400 m) is concordantly emplaced

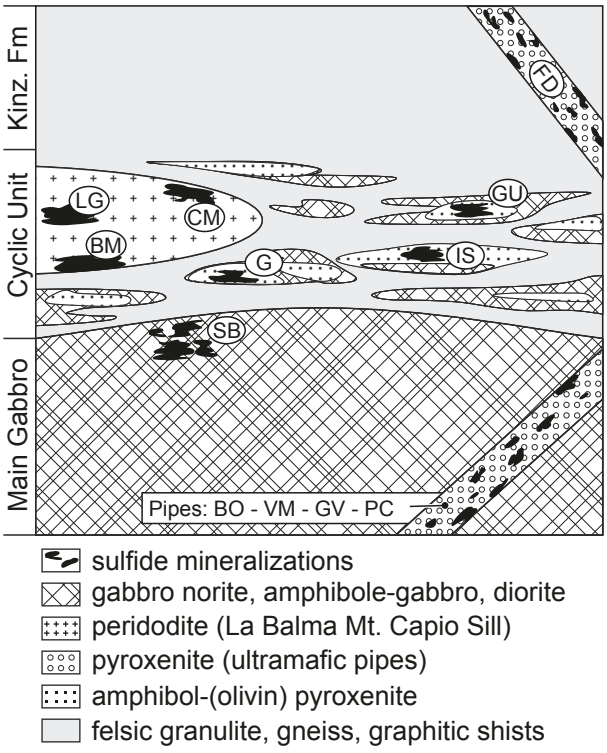

Figure 2: Schematic transect through the crust - mantle transition zone, prior to tilting und uplifting during Alpine collision. The deposits can be grouped according to their host lithologies: 1) La Balma - Monte Capio intrusion deposits: Penninetto (BM), Alpe Laghetto (LG) and Campello Monti (CM) - 2a) Ultramafic Pipes in the Main Gabbro: Bec d'Ovaga (BO), Castello di Gavala (GV), Piancone la Frera (MO) and Valmaggia (VM) - 2b) Ultramafic Pipe in the Kinzigite Formation: Fei di Doccio (FD) - 3) Main Gabbro deposit: Sella Bassa (SB) - 4) Cyclic Units deposits: Guaifola (G), Gula (GU) and Isola (IS) - Not to scale!

within the Kinzigitie Formation and consists of layered peridotite, with minor pyroxenite and amphibole-rich gabbro (Ferrario et al., 1983). The sulfide deposits occur in two distinct locations within the La Balma-Monte Capio ultramafic sill (Garuti, 1993). One deposit occurs at the basal contact of the sill with the meta-sediments of the Kinzigite Formation at Penninetto (BM) (Garuti, 1993).

The other two deposits are located well inside the ultramafic sequence far away from the meta-sediments, one at the transition of the peridotite and pyroxenite units at Alpe Laghetto (LG) (Ferrario et al., 1983) and the other within pyroxenites at Campello Monti (CM).

4) Deposits within Ultramafic Pipes: These pipes mainly consist of peridotites, pyroxenites and gabbros with an alkaline signature and an unusually elevated abundance of incompatible elements (Fiorentini et al., 2002), reflected in the minor but ubiquitous occurrence of minerals such as apatite, zircon and baddeleyite. They are discordantly emplaced within the Main Gabbro (a), as well as within the Kinzigite Formation (b).

4.a) The pipes within the Main Gabbro occur in the valley of Valsesia at the localities Valmaggia (VM), Bec d'Ovaga (BO) and Castello di Gavala (GV) as well as in the valley Valsessera, at the locality of Piancone la Frera (MO) (Garuti et al., 2001).

4.b) The ultramafic pipe of Fei di Doccio (FD) intrudes metapelites and marbles of the Kinzigite Formation (Garuti et al., 2001).

The general characteristics of the sulfide ores were examined in detail by Garuti et al. (1986), Garuti et al. (1990) and Garuti (1993). The base metal sulfide assemblages comprise pyrrhotite, pentlandite, chalcopyrite and minor cubanite, mackinawite, troilite and pyrite (Garuti et al., 1986). Primary and secondary ores with nearly identical metalogenic compositions were distinguished. The primary ore was presumably formed by demixing of an immiscible melt, forming a monosulfide solid solutions (Mss with a pyrrhotite composition) and subsequent exsolution of pentlandite and chalcopyrite. In a later step the primary ores were remobilized and re-deposited, due to fluid activity, forming the secondary ores (Garuti et al., 1986). The interpretations by Garuti et al. (1986) agree well with the general characteristics of Mss in magmatic systems (Naldrett, 2004).

1. SIMS In-situ ^{32}S, ^{33}S, ^{34}S and ^{36}S isotope analyses of 12 Fe-Ni-Cu PGE sulfide mineralizations of the Ivrea-Verbano Zone, Northern Italy

1.1. Abstract of this section

The integrated SIMS in-situ analysis of each stable sulfur isotope (^{32}S, ^{33}S, ^{34}S and ^{36}S) within sulfide minerals provides a powerful tool for the interpretation of the silicate-sulfide magma origin, the magma evolution, magmatic processes as well as possible external sulfur contaminations. Within the magmatic Fe-Ni-Cu-PGM paragenesis the major ore mineral pyrrhotite provides highly reliable S isotope values which are representative for the whole mineralization. The pentlandite analyses act as references. The evaluated mass dependent as well as mass independent fractionation factors facilitate together with a comprehensive analysis of the mineral chemistries a clear differentiation between the twelve investigated ore deposits.

The analysis accomplished on the Sella Bassa ores reveal a pure mantle origin of the magmas. Due to genetic interpretations of the mass dependent fractionation factors contamination by external sulfur is unlikely. A similar magma origin is proposed for the Cyclic Units which host the deposits of Guaifola, Gula, and Isola. Among the twelve investigated deposits the Cyclic Units deposits show the comparatively strongest contamination and hence S input from the meta-sediments of the Kinzigite Formation. For the magmas of the Ultramafic Pipes a mantle origin can be assumed, however the mass independent fractionation factors indicate some alteration of the mantle signatures. As these alterations are absent in the magmas of the Main Gabbro and the Cyclic Units no direct relationship with the magmas of Ultramafic Pipes is indicated. Within those pipes intruding the Main Gabbro, the Valmaggia, Bec d'Ovaga, Castello di Gavala and Piancone la Frera pipes, contamination is unlikely, whereas the single pipe intruding the metasediments of the Kinzigite Formation, the Fei di Doccio pipe, is clearly influenced by the incorporation of external sulfur from the host. Additionally the controversial discussion about the nature of the Piancone la Frera pipe can be definitely solved. Due to the highly similar signatures in both, the isotopic signatures and the mineral chemistries, a common origin with the remaining four pipes can be proposed.

The La Balma - Monte Capio ultramafic sill, hosting the deposits of Campello Monti , Alpe Laghetto and Penninetto, is presumably formed by an independent magma without a direct relationship to the remaining ore hosting formations. This is shown by the slight but distinct shifts in $\Delta^{33}S$ and $\Delta^{36}S$, which indicate mass independent fractionation during the genesis of the sill. The deposits of Campello Monti and Alpe Laghetto were presumably not influenced by the country rocks, whereas a relatively strong contamination and S input can be assumed for the Penninetto deposit.

All these interpretations and assumptions are in direct correlation with the geological context of the deposits which is assumed for the magmatic formation of the IVZ.

1.2. Introduction

The purpose of this study was to achieve a full sulfur isotope dataset (^{32}S, ^{33}S,^{34}S and ^{36}S) upon which a comprehensive interpretation of the ore formation of the deposits studied, is possible. The twelve investigated sulfide deposits belong to the group of magmatic Fe-Ni-Cu-PGM deposits (Naldrett, 2004; Arndt et al., 2005). They exhibit distinct differences in their metalogenetic characteristics, such as S fugacities, metal contents and especially S isotopic signatures. The isotopic analyses were carried out on the main ore forming mineral pyrrhotite and the major Ni carrier pentlandite. Together with the data set gained in this study, previous studies on $\delta^{34}S$ (accomplished on bulk sulfide by Heilmann and Lensch (1977); Garuti et al. (1986); Garuti (1993); Garuti et al. (2001)) were re-evaluated. The metalogenetic characteristics of the single minerals were investigated by electron microprobe analysis (EMPA), prior to the secondary ion mass spectrometry (SIMS). Thereupon a one to one comparison between the mineral chemistry and the isotopic composition was facilitated.

As the twelve deposits investigated belong to four separate lithological formations, a distinction between the main isotope-signature influencing factors was possible. These factors are mainly magmatic differentiation processes (mass-dependent and mass-independent fractionation) as well as sulfur incorporation from the country rocks.

To interpret the sulfur isotopic signatures, the litho-tectonic position of the sulfide mineralizations within the upper mantle, the lower crust as well as the transitional zone between these two lithologies is of special importance. The detailed delineation of the four different deposit groups including two subgroups can be found in the General Geology chapter.

1) Deposit within the Main Gabbro at Sella Bassa (SB).

2) Deposits of the Cyclic Units at Isola (IS), Guaifola (G) and Gula (GU).

3) Deposits hosted by the ultramafic sill of La Balma-Monte Capio at Alpe Laghetto (LG), Campello Monti (CM) and Penninetto (BM).

4) Deposits within Ultramafic Pipes. 4.a) The pipes within the Main Gabbro at Valmaggia (VM), Bec d'Ovaga (BO), Castello di Gavala (GV) and Piancone la Frera (MO) 4.b) The ultramafic pipe of Fei di Doccio (FD) which intrudes metapelites and marbles of the Kinzigite Formation.

On the basis of the obtained S-isotope results clear relationships between the lithological positions of the sulfide deposits, their hosting igneous rocks and their S-isotopic signatures could be established, together with detailed mineralogical and chemical investigations of the sulfide minerals. Distinct differences between the magmas of the ore hosting lithologies, the ultramafic intrusion of La Balma - Monte Capio (3 deposits), the Ultramafic Pipes (5 deposits), the Main Gabbro (1 deposit) and the Cyclic Units (3 deposits), became obvious and were interpreted in context with the general magmatic processes and the ore formation within the IVZ.

1.3. Material and Methods

The sample material taken for this isotope investigation derived from the numerous (more that 200), well documented samples investigated by Garuti et al. (1984) and Garuti et al. (1986). On the basis of detailed microscopical investigations and electron-microprobe

work carried out in this study, highly representative samples of each of the 12 investigated base-metal-sulfide deposits were selected for SIMS analyses. The composition of the sulfide paragenesis was analyzed by a Jeol JXA 8200 Superprobe at the "Eugen F. Stumpfl Laboratory", at the Department of Applied Geosciences and Geophysics, University of Leoben (Austria) using a Jeol JXA 8200 Superprobe. For each sulfide phase (pyrrhotite, pentlandite and if occurring chalcopyrite and pyrite) at least 10 analyses were conducted to reinforce the statistical background. Based on these statistics, representative paragenesis of pyrrhotite and pentlandite were localized and precisely cut out of their original positions within the foregoing 40x40 mm polished sections. To facilitate the SIMS analyses, the obtained fractions were mounted together with the corresponding standards. The standard set comprises in-house standards for pendlandite and pyrrhotite, provided by the Centre for Microscopy, Characterisation and Analysis, University of Western Australia, Perth. The SIMS analyses comprised each of the stable sulfur isotopes (^{32}S, ^{33}S,^{34}S and ^{36}S). Following the analyses the values were normalized to the corresponding standard, the Vienna Canyon Diablo Troilite (VCDT). The following mass dependent fraction factors were calculated: $\delta^{34}S_{VCDT}$ ($\delta^{34}S_{VCDT} = (^{34}S/^{32}S)_{sample} / (^{34}S/^{32}S)_{VCDT}$), $\delta^{33}S_{VCDT}$ ($\delta^{33}S_{VCDT} = (^{33}S/^{32}S)_{sample} / (^{33}S/^{32}S)_{VCDT}$) and $\delta^{36}S_{VCDT}$ ($\delta^{36}S_{VCDT} = (^{36}S/^{32}S)_{sample} / (^{36}S/^{32}S)_{VCDT}$)

The following mass independent fraction factors were calculated:
$\Delta^{33}S$ ($\Delta^{33}S = (^{33}S/^{32}S)_{sample} / (^{33}S/^{32}S)_{VCDT}$ - $[(^{34}S/^{32}S)_{sample} / (^{34}S/^{32}S)_{VCDT})]^{0.515}$) and
$\Delta^{36}S$ ($\Delta^{36}S = (^{36}S/^{32}S)_{sample} / (^{36}S/^{32}S)_{VCDT}$ - $[(^{34}S/^{32}S)_{sample} / (^{34}S/^{32}S)_{VCDT})]^{1.9}$).

1.4. Results

The complete dataset of the EMP as well as the SIMS analyses are summarized in Appendices A and B.

1.4.1. Compositional characteristics (EMP analyses)

The S and Fe concentrations in pyrrhotite and the Co concentrations in pentlandite, as the main compositional characteristics when focusing on sulfur isotopes analyzed by SIMS, are illustrated in appendix B. The single distributional analyses of appendix B show the the quality of the calculated element - mean values. Apart from the partially low sample numbers, each of the dirtibutional ranges can be described as largely normally distributed, wherefore the arithmetic mean values, which are illustrated in Figures 3, 9 and 10, can taken as significant values. Sulfur rich pyrrhotite assemblages are carried by samples of Campello Monti (CM), Sella Bassa (SB) and Piancone la Frera (MO); the latter two are additionally characterized by the occurrence of pyrite. All other sulfide deposits exhibit intermediate to low S ratios. The deposits within the Cyclic Units (i.e. Guaifola (G), Gula (GU) and Isola (IS)) feature more or less similar S ratios. At Guaifola (G) low S ratios are additionally mirrored by flame like troilite exsolutions within the pyrrhotite. The pipe hosted deposits can be divided in three different groups. The Valmaggia (VM) sulfide assemblage is dominated by troilite (S ratio = 0.5) with only minor pyrrhotite only. The second group (i.e. Fei di Doccio (FD), Castello di Gavala (GV) and Bec d' Ovaga (BO)) is characterized by pyrrothites with intermediate S ratios, whereas Piancone la Frera (MO) shows sulfur rich pyrrhotites. The La Balma - Monte Capio intrusion deposits

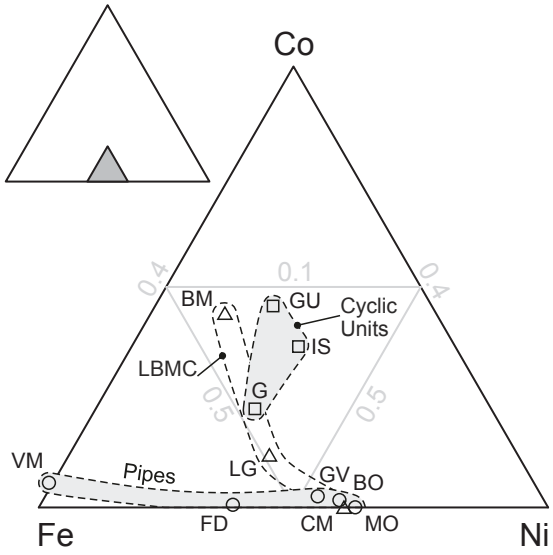

Figure 3: Ternary plot of mean Fe, Ni and Co in pentlanites; in atomic proportions. The data is enveloped according to the deposit hosting lithologies: LBMC: La Balma - Monte Capio intrusion, Pipes: Ultramafic Pipes, and Cyclic Units.

at Peninnetto (BM) and Alpe Laghetto (LG) exhibit relatively low pyrrhotite S ratios, whereas the pyrrhotites of Campello Monti (CM) are sulfur rich. The Peninnetto sulfide paragenesis exhibits subordinate troilite.

Two different groups can be distinguished on the basis of the Co contents in pentlandite: a) High Co-pentlandites are characteristic for the deposits of the Cyclic Units (i.e. Guaifola (G), Gula (GU) and Isola (IS)) and additionally for the pentlandites of the Penninetto (BM) deposit. b) The second group is characterized by Co contents < 1 at.% (Appendix A). Based on the Fe-Ni-Co compositions in pentlandites (Fig. 3) the deposits can be divided in: 1.) Ni rich assemblages of Castello di Gavala (GV), Bec d' Ovaga (BO), Campello Monti (CM) and Piancone la Frera (MO), 2.) Ni-Co rich assemblages of Alpe Laghetto (LG), Penninetto (BM), Guaifola (G), Gula (GU) and Isola (IS) and 3.) Fe rich assemblages of Fei di Doccio (FD) and Valmaggia (VM).

1.4.2. SIMS analyses

The entire data set of the SIMS measurements are summarized in Appendix A.

1.4.2.1. Precision of the $\delta^{34}S_{VCDT}$ data and deviation between pyrrhotite and pentlandite analyses

The single pyrrhotite and pentlandite $\delta^{34}S_{VCDT}$ results in comparison with relevant literature data for bulk massive sulfides (Heilmann and Lensch, 1977; Garuti et al., 1986; Garuti, 1993; Garuti et al., 2001) are illustrated in Figure 4.

The pyrrhotite analyses are generally fraught with significantly lower standard deviations compared those of the pentlandites. The two mineral species also vary in their divergences between the single analyses of one and the same sample. The pyrrhotites exhibit consistently low divergences (i.e. around 0.5 ‰) between the highest and the

lowest measured $\delta^{34}S_{VCDT}$ ratio. A single exception is represented by the Penninetto (BM) deposits with a deviation of 1.15 ‰. On the contrary, the pentlandite analyses differ significantly within the single samples, revealing at least 0.22 ‰ between the highest and the lowest mean value ($\delta^{34}S_{VCDT}$). The mean average pentlandite $\delta^{34}S_{VCDT}$ values lie regularly about 0.5 ‰ to 1 ‰ below those of the pyrrhotites, apart from the pentlandites of the Guaifola (G) which show a strong positive shift between 1 ‰ and 5 ‰. The analyses of the Castello di Gavala (GV) and Gula (GU) deposits exhibit variable $\delta^{34}S_{VCDT}$ deviations between -1 ‰ and -4 ‰. The Piancone la Frera (MO) and Alpe Laghetto (LG) analyses exhibit negative as well as positive deviations. The bulk massif sulfide $\delta^{34}S_{VCDT}$ literature data (Heilmann and Lensch, 1977; Garuti et al., 1986; Garuti, 1993; Garuti et al., 2001) largely coincide with the analyzed pyrrhotite values (Fig. 4) of this study, except those from Alpe Laghetto (LG) and Gula (GU).

1.4.2.2. Average $\delta^{34}S_{VCDT}$ and $\delta^{36}S_{VCDT}$ values of pyrrhotites The range between the highest and the lowest measured mean $\delta^{34}S_{VCDT}$ values are illustrated in Figure 5. Due to the intimate intergrowth of pyrrhotite and troilite in the sample of Valmaggia (VM) no reliable pyrrhotite SIMS analysis could be carried out, therefore literature data (Garuti et al. (1986) and Garuti et al. (2001)) were used for comparison.

The deposits of Alpe Laghetto (LG) and Campello Monti (CM) hosted by the La Balma - Monte Capio intrusion exhibit the comparatively lowest $\delta^{34}S_{VCDT}$ shifts. Only the pyrrothites of the Pennineto (BM) deposit, located at the basal contact of the La Balma - Monte Capio intrusion with the Kinzigite Formation, show distinct negative shifts between -1.76 ‰ and -2.91 ‰ $\delta^{34}S_{VCDT}$.

Two different characteristics become evident in the deposit hosted by the Ultramafic Pipes. Pipes which intrude the Main Gabbro (Fig. 1 and Fig. 2; i.e. Valmaggia (VM), Bec d'Ovaga (BO), Castello di Gavala (GV) and Piancone la Frera (MO)) exhibit comparatively low $\delta^{34}S_{VCDT}$ pyrrhotite values, whereas pyrrhotites of the single pipe intruding the Kinzigite Formation (i.e. Fei di Doccio pipe (FD)), show elevated $\delta^{34}S_{VCDT}$ values.

The single deposit hosted by the Mafic Complex (i.e. Sella Bassa (SB)) exhibits a mean $\delta^{34}S_{VCDT}$ value of 1.87 ‰. This is the highest $\delta^{34}S_{VCDT}$ pyrrhotite value, apart from the deposits hosted by Cyclic Units. These pyrrhotites show comparatively high positive shifts between 1.03 ‰ at Guaifola (G), 2.00 ‰ in Gula (GU) and 2.82 ‰ in Isola (IS), respectively.

The $\delta^{36}S_{VCDT}$ values follow the trend of the $\delta^{34}S_{VCDT}$ data but the $\delta^{36}S_{VCDT}$ values are shifting approximately twice as strong (Fig. 6). Again the pyrrhotites of Alpe Laghetto (LG) exhibit the lowest shifts around zero and the deposits of the Cyclic Units (Gula (GU) and Isola (IS)) as well as the Sella Bassa (SB) and the Penninentto (BM) deposits show the comparatively strongest shifts.

1.4.2.3. $\Delta^{33}S$ values and $\Delta^{36}S$ values For this comparison the $\delta^{34}S_{VCDT}$ values of pyrrhotites and the $\Delta^{33}S$ values of both pyrrhotites and pentlandites were matched and illustrated in Figure 7. The obvious signatures in Figure 7 largely follow the geological location of the deposits. The Sella Bassa (SB) deposit, the single deposit within the Main Gabbro, exhibits the lowest measured $\Delta^{33}S$ values. The deposits hosted by the Ultramafic Pipes as well as by the Cyclic Units form a more or less coherent block with intermediate

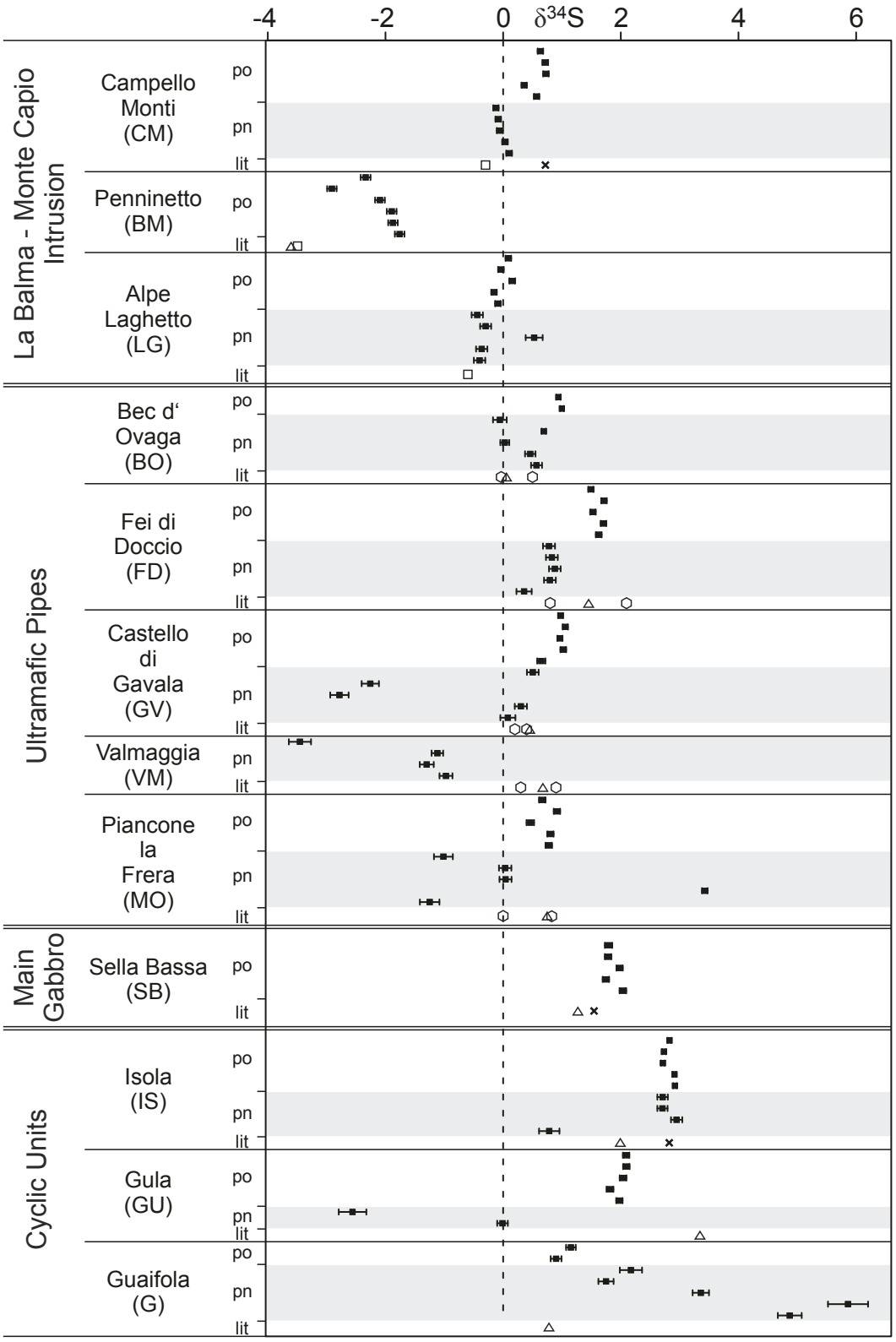

Figure 4: Single analyses of $\delta^{34}S_{VCDT}$ with corresponding $\pm 1\sigma$ standard deviation. The dposits are grouped according to the hosting lithologies: La Balma - Monte Capio intrusion, Ultramafic Pipes, Main Gabbro and Cyclic Units. The data is divided into: pyrrhotite (po), pentlandite (pn, grey shaded) and literature data (lit). Literature data: Crosses Heilmann and Lensch (1977), triangles Garuti et al. (1986), boxes Garuti (1993), diamonds Garuti et al. (2001).

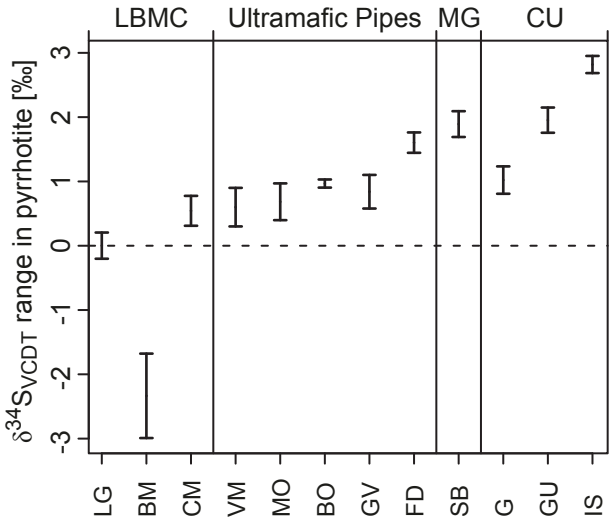

Figure 5: $\delta^{34}S_{VCDT}$ values in pyrrhotites. The bars indicate the range between the highest and lowest analysis. The deposits are subdivided according to their hosting lithologies: La Balma - Monte Capio intrusion (LBMC), Ultramafic Pipes, Main Gabbro (MG) and Cyclic Units (CU). Within the groups the values are sorted due to their mean zero point deviation. Deposits: BM: Penninetto, BO: Bec d'Ovaga, CM: Campello Monti , FD: Fei di Doccio, G: Guaifola, GU: Gula, GV: Castello di Gavala, IS: Isola, LG: Alpe Laghetto, MO: Piancone la Frera, SB: Sella Bassa, VM: Valmaggia.

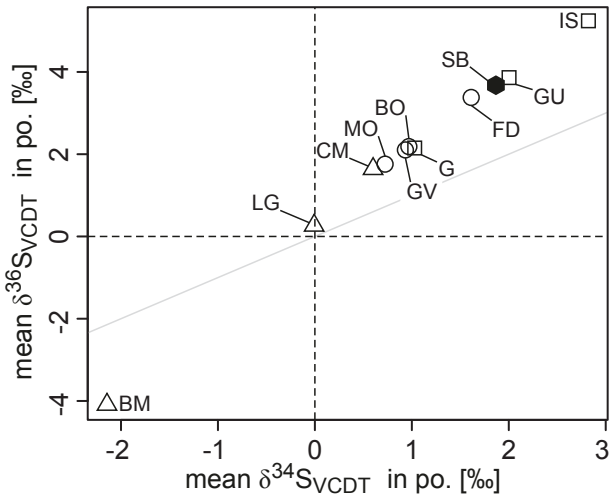

Figure 6: Mean $\delta^{36}S_{VCDT}$ versus $\delta^{34}S_{VCDT}$ values in pyrrhotite. The grey line indicates a one-to-one $\delta^{36}S_{VCDT}$ / $\delta^{34}S_{VCDT}$ ratio. Deposits: BM: Penninetto, BO: Bec d'Ovaga, CM: Campello Monti , FD: Fei di Doccio, G: Guaifola, GU: Gula, GV: Castello di Gavala, IS: Isola, LG: Alpe Laghetto, MO: Piancone la Frera, SB: Sella Bassa, VM: Valmaggia.

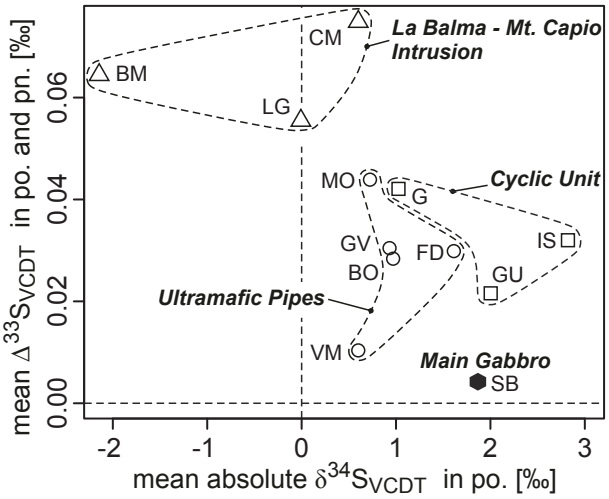

Figure 7: Mean $\delta^{34}S_{VCDT}$ values pyrrhotites versus mean $\Delta^{33}S$ values of pentlandites and pyrrhotites. The data points plot into distinct fields according to the deposit hosting lithologies. Zero values are indicated by straight dashed lines. The Valmaggia (VM) $\delta^{34}S_{VCDT}$ data point is a mean value of one analysis of Garuti et al. (1986) and two analyses of Garuti et al. (2001). Deposits: BM: Penninetto, BO: Bec d'Ovaga, CM: Campello Monti , FD: Fei di Doccio, G: Guaifola, GU: Gula, GV: Castello di Gavala, IS: Isola, LG: Alpe Laghetto, MO: Piancone la Frera, SB: Sella Bassa, VM: Valmaggia.

$\Delta^{33}S$ values (0.01 ‰ - 0.045 ‰) and intermediate to strongly positive $\delta^{34}S_{VCDT}$ shifts. A separate group is represented by the La Balma - Monte Capio deposits which exhibit $\Delta^{33}S$ values above 0.055 ‰ but, apart from the Penninetto (BM) pyrrhotites, low $\delta^{34}S_{VCDT}$ shifts.

The mean $\Delta^{33}S$ vs. mean $\Delta^{36}S$ diagram (Fig. 8) shows a significant distinction between the ore hosting lithologies. A clearly separated group is displayed by the deposits of the Ultramafic Pipes which plot into a narrow window with intermediate $\Delta^{33}S$ and $\Delta^{36}S$ shifts. The deposits of the Cyclic Units (i.e. Guaifola (G), Gula (GU) and Isola (IS)) as well as those of the Main Gabbro (i.e. Sella Bassa (SB)) exhibit both low $\Delta^{36}S$ and $\Delta^{33}S$ shifts. However the relatively high $\Delta^{33}S$ shifts of the Isola (IS) deposit represents an exception.

The deposits of the La Balma - Monte Capio intrusion (i.e. Alpe Laghetto (LG), Campello Monti (CM) and Penninetto (BM)) form an independent group with high $\Delta^{33}S$ shifts and variable $\Delta^{36}S$ shifts.

1.4.2.4. Pyrrhotite $\delta^{34}S_{VCDT}$ values versus Co in pendlandite

The comparison between the mean absolute $\delta^{34}S_{VCDT}$ values in pyrrhotite and the Co content in pendlandite is illustrated in Figure 9. A general positive trend between the Co contents and increasing (positive or negative) $\delta^{34}S_{VCDT}$ shifts becomes obvious. However, the Alpe Laghetto (LG) deposit sulfides do not follow this trend. The deposits hosted by the Cyclic Units as well as the Penninetto (BM) deposit, which is in contact with the Kinzigite Formation at the base of La Balma - Monte Capio intrusion, exhibit high Co pentlandites accompanied by pyrrhotites with comparatively high $\delta^{34}S_{VCDT}$ shifts. The pipe deposits as well as the Campello Monti (CM) deposit host low Co pentlandites and exhibit intermediate

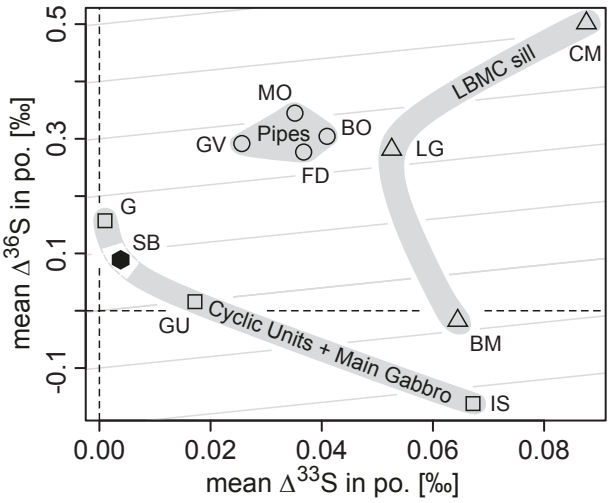

Figure 8: Mean $\Delta^{33}S$ versus mean $\Delta^{36}S$. The grey lines indicate one-to-one $\Delta^{33}S$ / $\Delta^{36}S$ ratios. LBMC sill: La Balma - Monte Capio sill. Deposits: BM: Penninetto, BO: Bec d'Ovaga, CM: Campello Monti , FD: Fei di Doccio, G: Guaifola, GU: Gula, GV: Castello di Gavala, IS: Isola, LG: Alpe Laghetto, MO: Piancone la Frera, SB: Sella Bassa, VM: Valmaggia.

pyrrhotite $\delta^{34}S_{VCDT}$ shifts. The Sella Bassa (SB) sample lacks any analyzable pentlandite.

1.4.2.5. $\delta^{34}S_{VCDT}$ values versus S/(Fe+S) ratios in pyrrhotite

The relation between the $\delta^{34}S_{VCDT}$ values and the S/(Fe+S) ratios in pyrrhotites is illustrated in Figure 10. A general trend between decreasing S contents and increasing $\delta^{34}S_{VCDT}$ values in pyrrhotites becomes evident. Especially the pipe hosted deposits follow this trend well. The Piancone la Frera (MO) deposit hosting high S pyrrhotites exhibits comparatively low $\delta^{34}S_{VCDT}$ shifts, on the contrary the S poor pyrrhotites of the Fei di Doccio (FD) show increased $\delta^{34}S_{VCDT}$ shifts. The deposits of the Cyclic Units are consistently made up by low S pyrrhotites with comparatively high $\delta^{34}S_{VCDT}$ shifts. Two deposits of the La Balma - Monte Capio intrusion (i.e. Campello Monti (CM) and Penninetto (BM)), follow this trend similarly. However, Sella Bassa (SB) and Alpe Laghetto (LG) pyrrhotites represent exceptions (Fig. 10). High S activities at Sella Bassa (SB), as well as those at Piancone la Frera (MO), are underlined by the occurrence of pyrite.

1.5. Discussion

1.5.1. Sulfur source and contamination

A summary of the processes taking place during the development of Ni-Cu-(PGE) deposits in mafic and ultramafic rocks was given by Arndt et al. (2005). Sulfur saturation and sufficient metal contents in the magma are the most important aspects for the formation of economic sulfide deposit. In a closed system without external S addition, sulfur saturation can be reached by progressed fractional crystallization leading to an immiscible sulfide liquid segregation. As a result disseminated interstitial sulfides would form, characterized by typical $\delta^{34}S$ mantle signatures.

Sulfur isotope signatures deviating from mantle values may be caused by internal as

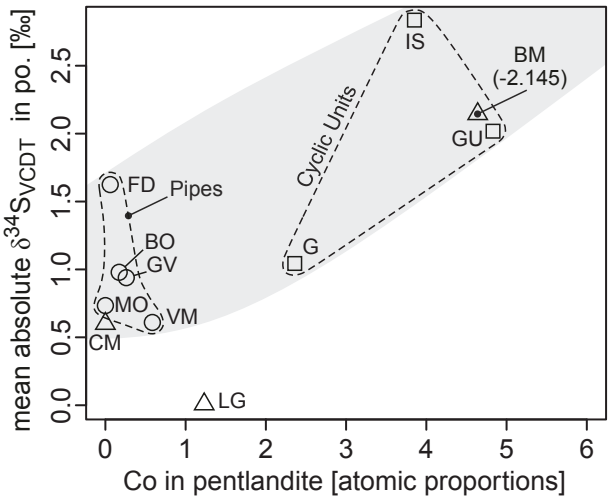

Figure 9: Mean absolute pyrrhotite $\delta^{34}S_{VCDT}$ values versus mean Co contents in pendlandite. The Peninetto (BM) $\delta^{34}S_{VCDT}$ values were taken as absolute values for presentation purposes (absolute deviation from zero). The gray shading indicates the general correlation between the two values (The Alpe Laghetto (LG) data is excluded due to an anomalous signature). The Valmaggia (VM) $\delta^{34}S_{VCDT}$ data point is a mean value of one analysis of Garuti et al. (1986) and two analyses of Garuti et al. (2001). Deposits: BM: Penninetto, BO: Bec d'Ovaga, CM: Campello Monti , FD: Fei di Doccio, G: Guaifola, GU: Gula, GV: Castello di Gavala, IS: Isola, LG: Alpe Laghetto, MO: Piancone la Frera, SB: Sella Bassa, VM: Valmaggia.

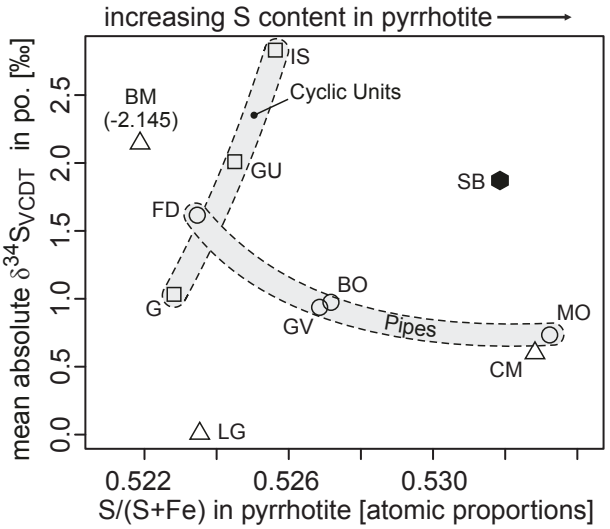

Figure 10: Mean absolute $\delta^{34}S_{VCDT}$ values versus mean sulfur stoichiometry in pyrrhotite. Deposits hosted by the Ultramafic Pipes as well as the Cyclic Units are enveloped. The Peninetto (BM) $\delta^{34}S_{VCDT}$ values were taken as absolute values for presentation purposes (absolute deviation from zero). Deposits: BM: Penninetto, BO: Bec d'Ovaga, CM: Campello Monti , FD: Fei di Doccio, G: Guaifola, GU: Gula, GV: Castello di Gavala, IS: Isola, LG: Alpe Laghetto, MO: Piancone la Frera, SB: Sella Bassa, VM: Valmaggia.

well as external magmatic processes. Degassing (i.e. formation of SO_2 and H_2S rich fluids) and/or separation of S-bearing liquids and/or solids represent possible internal processes (Marini et al., 2011). External processes are assimilation of country rock (Naldrett, 2004) and/or the interaction of the magma with oxidizing volatile-rich fluids carrying dissolved S species, as described by (Alard et al. (2011) and Giuliani et al. (2012)).

In general, the $\delta^{34}S_{VCDT}$ values of the IVZ deposits lie close to zero with a maximum shift of about 4 ‰ (Fig. 4). Therefore, the upper mantle can be considered as the main sulfur source for the ore formation. However, it has to be verified for each single deposit which of the internal or external processes are responsible for the observed deviations of the $\delta^{34}S_{VCDT}$ values.

The only considerable external sulfur source is provided by the Kinzigite Formation. Schnetger (1994) reported $\delta^{34}S_{VCDT}$ between -23 ‰ and +13 ‰ for Kinzigites in the Strona valley and sulfur contents up to 3200 ppm. This shows the high general potential of the Kinzigite Formation to act as an external sulfur distributor, particularly for those deposits which are in close proximity.

However, total or partial melting of solid material of the country rock and assimilation can be excluded for the IVZ deposits, because no indications, such as changes in the composition of the ultramafic host rocks, and/or significant contact metamorphism can be identified (cf. Lesher et al. (2001)). Therefore it can be interpreted that the discussed fluid related processes are responsible for the observed contaminations.

An example for solely internal processes which shifted the $\delta^{34}S_{VCDT}$ values is provided by the Sella Bassa (SB) deposit. This can stated, because the deposit is hosted by the Mafic Complex without any contact to the Kinzigite Formation and the mantle origin of the magma is verified by the low $\Delta^{33}S$ and $\Delta^{36}S$ values, as discussed in the following chapter. Therefore the relatively high $\delta^{34}S_{VCDT}$ values are presumably caused by internal magmatic processes as described by Marini et al. (2011).

In contrast to this, the mineral assemblages of the Cylic Unit deposits are dominated by low sulfur pyrrhotites which reflect a low S content in the original magma (Fig. 10). Therefore it is suggested, that S saturation was influenced by the addition of external sulfur from the Kinzigite Formation, as also described by Garuti et al. (1986). This suggestion is reinforced by comparatively high Co contents in pentlandites (Fig. 3 and Fig. 9), as the Co contents of original mantle magmas are considered to be low (McDonough and Sun, 1995). Consequently the shifted $\delta^{34}S_{VCDT}$ values of the three deposits (i.e. Gula, Guaifola and Isola) can be interpreted to be strongly influenced by variable S input from the adjacent Kinzigite Formation.

The $\delta^{34}S_{VCDT}$ isotopic composition of the pyrrhotites directly mirrors the lithological subdivision of the Ultramafic Pipes. The pipes emplaced in the Main Gabbro (i.e. Valmaggia (VM), Bec d'Ovaga (BO), Castello di Gavala (GV) and Piancone la Frera (MO)) exhibit low $\delta^{34}S_{VCDT}$ shifts, whereas the Fei di Doccio (FD) pipe which intrudes the Kinzigite Formation shows an elevated shift. Within the group of the Main Gabbro pipes external contamination can be excluded because they are presumably too far away from the external S source, i.e. the Kinzigite Formation. Consequently the slight $\delta^{34}S_{VCDT}$ shifts are most likely caused by internal magmatic and/or fluid related processes. This assumption is reinforced by the systematic relationship between the S ratio and the $\delta^{34}S_{VCDT}$ values in pyrrhotite as shown in Figure 10. The S rich pyrrhotites of the Piancone la

Frera (MO) deposit, indicate high S contents in the magma, assuming early S saturation, whereupon initial $\delta^{34}S_{VCDT}$ values (close to zero) were preserved. The deposits of Bec d' Ovaga (BO) and Castello di Gavala (GV) exhibit S poorer assemblages indicating S saturation at later magmatic stages. As a consequence the ore minerals where stronger influenced by the internal magmatic processes, yielding more elevated $\delta^{34}S_{VCDT}$ shifts. In contrast, the $\delta^{34}S_{VCDT}$ values of the Fei di Doccio (FD) pipe, intruding the Kinzigite Formation, clearly show some influence of external contamination by the host. This contamination, although limited, as indicated by low Co pentlandites, becomes obvious when comparing the $\delta^{34}S_{VCDT}$ values of the Main Gabbro pipes and those of the Fei di Doccio (FD) pipe (Fig. 5)

The $\delta^{34}S_{VCDT}$ values of the La Balma - Monte Capio ultramafic sill deposits again mirror their geological position. The deposit of Penninetto (BM), at the basal contact of the sill with the Kinzigite Formation, shows a relatively strong contamination yielding negative $\delta^{34}S_{VCDT}$ values, concordant with high Co contents in pentlandite and S poor pyrrhotite. In particular S poor pyrrhotite indicates the necessity of an addition of external S from the Kinzigite Formation to reach S saturation. The remaining two deposits in the central part of the sill, without any lithological contact to the Kinzigite Formation, exhibit zero $\delta^{34}S_{VCDT}$ values at Alpe Laghetto (LG) and low shifts at Campello Monti (CM). These values indicate a purely magmatic ore formation without external input. This pure magmatic origin is best shown by the Campello Monti deposit with low $\delta^{34}S_{VCDT}$, high S pyrrhotites and zero Co pentlandites. The elevated Co contents in pentlandites of the Alpe Laghetto (LG) deposit, might be explained by varying partitioning between a sulfide liquid and a coexisting mafic silicate melt (R-factor Naldrett et al. (1967); Naldrett (2004)).

Carbon and oxygen isotope data (Baker, 1988, 1990) as well as lead isotopic study (Cumming et al., 1987) strongly support these conclusions. The external contamination was characterized by variable fluid interaction strongly depending on the proximity between the Kinzigite Formation and the single ore deposits.

1.5.2. Magma origin

Shifts in $\Delta^{33}S$ and $\Delta^{36}S$ are attributed to mass independent fractionation and can be used for an interpretation of the sulfur origin in magmas (Farquhar and Wing, 2003; Farquhar et al., 2010; Fiorentini et al., 2012). Within samples older than 2.45 Ga Farquhar and Wing (2003) determined shifts between +12 ‰ and -3 ‰, whereas in younger samples strong shifts were absent. They related these signatures to mass independent fractionation in the low oxygen archean atmosphere.

The shifts in $\Delta^{33}S$ and $\Delta^{36}S$ of the samples are low and there is no geological indication for archean sediments involved in the IVZ lithologies. Nevertheless, the observed variations are systematic and significant and can be used for an interpretation of the magma derivation of the Cyclic Units, the La Balma - Monte Capio intrusion, the Ultramafic Pipes and the Main Gabbro, which has been interpreted in various ways (Ferrario et al., 1982; Pin and Sills, 1986; Voshage et al., 1990; Sinigoi et al., 1994; Garuti et al., 2001). The main question emerging within this context was whether the lithologies did derive from a common magma source, or not.

There are three distinct $\Delta^{33}S$ characteristics observable in Figure 7. Unmodified mantle

$\Delta^{33}S$ values are only shown by the Sella Bassa (SB) deposit. The deposits of the Cyclic Units were situated on top of the Main Gabbro during the assumed underplating event (Fig. 2). They show significant similarities to the mass-independent $\Delta^{36}S$ signatures of the Sella Bassa (SB) deposits within the Main Gabbro (Fig. 8). The deposits of Gula (GU) and Guaifola (G) exhibit low $\Delta^{33}S$ as well as $\Delta^{36}S$ values, similar to those of the Sella Bassa (SB) deposit. The Isola (IS) deposit follows the low $\Delta^{36}S$ values and only shows slightly elevated $\Delta^{33}S$ values. This indicates that the Cyclic Units and the Main Gabbro possess a closely related or a common magmatic source. The intercalation of the Cyclic Units with the Kinzigite Formation did not did not evoke mass independent fractionation wherefore the $\Delta^{33}S$ and $\Delta^{36}S$ signatures remained unchanged.

Each of the mean pyrrhotite $\Delta^{33}S$ and $\Delta^{36}S$ values of the Ultramafic Pipe deposits (i.e. Valmaggia (VM), Bec d'Ovaga (BO), Castello di Gavala (GV) and Piancone la Frera (MO)) and Fei di Doccio (FD)) plot into a narrow field in Figure 8. This clearly indicates a common magma source for each of the Ultramafic Pipes which experienced mass-independent fractionation yielding intermediate shifts in $\Delta^{36}S$ and $\Delta^{33}S$. As this narrow field is distinct from those of the Cyclic Units, the La Balma - Monte Capio intrusion and the Main Gabbro (Fig. 8) a distinct magma source can be assumed. Based on these interpretations also the Piancone la Frera (MO) pyroxenite intrusion is suggested to be part of the Ultramafic Pipes which was a long term matter of discussion (Garuti et al. (1986, 1990); Thornber et al. (1993); Garuti et al. (2001)).

The La Balma - Monte Capio deposits show the strongest shifts in $\Delta^{33}S$ values and apart from the Penninetto (BM) deposit also elevated $\Delta^{36}S$ shifts become obvious (Fig. 7). Therefore a distinct genesis of the La Balma - Monte Capio sill can be assumed which experienced the strongest observed mass-independent fractionation processes.

The $\Delta^{33}S$ and $\Delta^{36}S$ data clearly mirror the geological context of the main ore hosting litholigies of the Main Gabbro, the Cyclic Units, the La Balma - Monte Capio intrusion as well as the Ultramafic Pipes. However, the single processes leading to magma separation and mass-independent fractionation have to be identified in the future.

1.6. Conclusion

Based on the results of this study two main characteristics of the ore formation, the magma origin and the sulfur source, can be clearly verified. The magma origin can be interpreted with the aid of the mass independent fractionation factors of $\Delta^{33}S$ and $\Delta^{36}S$. At least three different kinds of magmas can be distinguished. The sulfur source can be specified using the $\delta^{34}S_{VCDT}$ values which delineate mass dependent fractionation. These values describe a possible contamination of the mainly magmatic ore hosting lithologies by the metasedimentary country rock (i.e. the Kinzigite Formation). Together with the comprehensive sulfide mineral analyses, a detailed interpretation and differentiation of the twelve single deposits is possible. Furthermore it becomes evident that mass dependent and mass independent fractionation occurred totally independent from each other.

The isotopic results showed that the pyrrhotite analyses, largely following the trends of previous bulk ore isotopic data, provide the preferential measure for these genetic interpretations. The data gained on pentlandite, which is fraught with higher errors, can be taken as a reference. However, the pentlandite signatures are not as systematic as the

pyrrhotite data. The higher fluctuation within the pendlandite isotopic compositions presumably developed during the exsolution of pentlandite from mono-sulfide-solid-solution (mss) with approximate pyrrhotite composition.

Based on the mass independent fractionation factors of $\Delta^{33}S$ and $\Delta^{36}S$ the magma of the Main Gabbro (hosting the Sella Bassa deposit) can be characterized as largely uninfluenced mantle magma. The Cyclic Units, genetically overlying the Main Gabbro, feature similar properties. Consequently, both the Main Gabbro and the Cyclic Units most likely derived from one closely related or common magma pulse. This similarity furthermore shows, that the mass independent fractionation factors were not influenced by the intercalation of the Cyclic Units with the genetically overlying metasediments of the Kinzigite Formation. The Cyclic Units host the deposits of Gula, Guaifola and Isola.

The Ultramafic Pipes of Valmaggia, Bec d'Ovaga, Castello di Gavala, Piancone la Frera as well as Fei di Doccio are presumably formed by the second, distinct group of magmas. The isotopic values show proximate mantle signatures ($\Delta^{33}S$ and $\Delta^{36}S$ values), however, they form a separate group which experienced some slight mass independent fractionation during the magma evolution. The similarities between the single pipe intruding the Kinzigite Formation (Fei di Doccio pipe) and the pipes intruding the Main Gabbro (Valmaggia, Bec d'Ovaga, Castello di Gavala and Piancone la Frera pipes) underline the assumption that late-stage magmatic processes did not change the mass independent signatures. This means that the mass independent fractionation factors ($\Delta^{33}S$ and $\Delta^{36}S$ values) are not affected by processes like intrusion or intercalation, crystallization and fluid interactions. Furthermore, it becomes very obvious that the pyroxenite intrusion of Piancone la Frera belongs to the group of Ultramafic Pipes, which was a matter of discussion in the past.

The La Balma - Monte Capio ultramafic was presumably formed by the third, distinct magma pulse. The isotopic values of $\Delta^{33}S$ and $\Delta^{36}S$ show that these magmas experienced exceptional mass independent fractionation within the IVZ. As the values show only slight, but significant, deviations from standard mantle signatures, a general mantle origin can be proposed. However, a direct relation with the magmas forming the Main Gabbro is unlikely, the reason why these magmas can be interpreted to be formed by a separate autonomous magma pulse.

The gained $\delta^{34}S_{VCDT}$ values together with the S ratios of pyrrhotite and the Co content of pendlandite are excellent indicators for the sulfur source during the ore formation. It is clearly shown that the single ores experienced variable contamination by external sulfur which correlates directly with the proximity of the ore hosting lithologies to the surrounding country rocks of the Kinzigite Formation.

No S-contamination is considered for the Ultramafic Pipes, which intrude the Main Gabbro. The slight shifts in the $\delta^{34}S_{VCDT}$ values are most likely caused by internal magmatic processes. The single pipe intruding the metasediments of the Kinzigite Formation, the Fei di Doccio pipe, shows some slight contamination by the host. It can be assumed that at least the differences between the mean values of the Main Gabbro pipes and the values of the Fei di Doccio pipe are caused by incorporation of external sulfur from the metasediments of the Kinzigite Formation.

The strongest S contamination is consistently shown by the ore deposits of the Cyclic Units at Guaifola, Gula and Isola. This assumtion is based on the comparatively high shifts in $\delta^{34}S_{VCDT}$ of the analyzed pyrrhotites as well as by the relatively high Co contents

of the pentlandites. This is in agreement with the close proximity of the ore deposits to the metasedimentary country rocks of the Kinzigite Formation.

Within the group of deposits hosted by the La Balma - Monte Capio ultramafic sill (Campello Monti, Alpe Laghetto and Penninetto) only the deposit of Penninetto is apparently influenced by contamination. The direct contact of the ores with the Kinzigite Formation metasediments presumably caused an S input and induced the negative shifts in $\delta^{34}S_{VCDT}$. The remaining two deposits (i.e. Campello Monti and Alpe Laghetto) experienced no contamination as they are located relatively far from the Kinzigite Formation.

The relatively high $\delta^{34}S_{VCDT}$ shifts of the Sella Bassa pentlandites are presumably caused by internal magmatic processes, but not by contamination by external sulfur. A reinforcement of this assumption is given by the low S contents in the ores. This assumes sulfur saturation at a relatively late magmatic stage, at a time, where internal magmatic processes like degassing and/or separation of S-bearing liquids and/or solids already occurred.

2. In-situ U-Pb measurement of magmatic zircons from the Ultramafic Pipe of Fei di Doccio, Ivrea-Verbano Zone, Italy - Juvenescence driven by fluid activity

2.1. Abstract of this section

This study addresses the widely debated and poorly understood chronological relationship between the emplacement of a series of alkaline Ultramafic Pipes, hosting base metal sulfide mineralization and the underplating event that affected the Ivrea-Verbano Zone of Northern Italy in the Late Carboniferous. The new in-situ SHRIMP ages are from zircons from the Fei di Doccio pipe that intruded the Kinzigite Formation, a crustal sequence of high-grade ortho- and parametamorphic rocks. In contrast to previous studies that relied on conventional zircon recovery through heavy liquid methods, the zircons were precisely cut out of their original positions from polished thin sections and mounted together with corresponding standards for in-situ analysis. This extraction technique provided invaluable information on the textural setting of the zircons, which proved essential in the interpretation of the ages. The zircon grains show an intimate intergrowth with base metal sulfides and hydromagmatic phases. A total of 23 analyses have been performed on two larger zircons (up to 170µm) and five smaller grains (around 30µm). In spite of textural homogeneity, the U-Pb isotopic results show significant variation in analysis spots from both within the same crystal and among different grains, leading to an age range between 251 and 277 Ma. The zircons analysed display a strong variation in Th and U contents both within the same crystal and among different grains. The age of 277±6 Ma deriving from spots displaying Th/U ratios of ~1 is interpreted as the true crystallization age of the pipe. Conversely, the age data derived from spots showing relatively low Th/U ratios are interpreted as rejuvenated ages due to disturbance from fluids. As the new crystallization age of the pipe is ca. 10 Ma younger than previous estimates, it can be suggested the emplacement of the pipe was not synchronous with the regional underplating event at ca. 288 Ma, but slightly younger. This interpretation is in accordance with the field data: it indicates that all the known pipes in the Ivrea-Verbano Zone consistently have sharp intrusive contacts with the Main Gabbro and the overlying granulitized Kinzigite Formation. These age data also confirm earlier hypotheses suggesting that the intrusion of alkaline ultramafic magmas into the deep crust of the Ivrea-Verbano Zone is genetically associated with widespread mantle metasomatism in the lithospheric mantle during the late Carboniferous.

Graphical Abstract

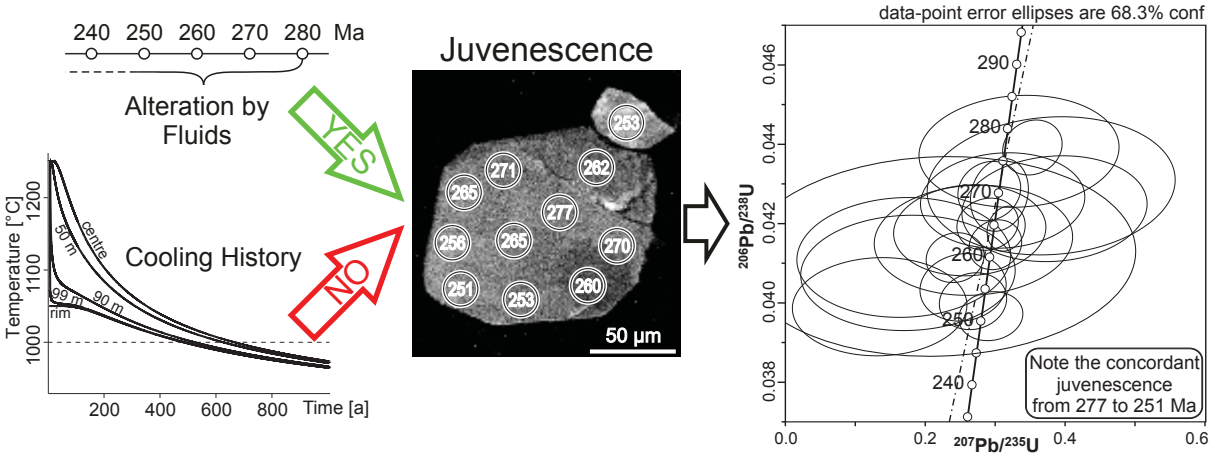

2.2. Introduction

The age and the evolution of the Ivrea-Verbano Zone, which is interpreted as an exhumed segment of the lower continental crust and subcontinental lithospheric mantle (Mehnert, 1975; Garuti et al., 1980; Peressini et al., 2007), is still a matter of discussion. The geological details are delineated in the General Geology chapter. Of particular interest is the poorly understood relationship between the Late Carboniferous underplating event (Peressini et al., 2007), which most likely triggered the emplacement of voluminous mafic magmas at the base of the continental crust and the widespread formation of base metal sulfide deposits (Garuti et al., 1986). Five pipe-like ultramafic bodies occur within the Main Gabbro at the localities of Valmaggia, Bec D'Ovaga, Castello di Gavala, Piancone la Frera, and within the Kinzigite Formation at Fei di Doccio (Garuti et al. (2001); Figure 11). These pipes display a strong alkaline nature and contain abundant volatile-bearing mineral phases, which reflect an intense fluid activity during their formation. Furthermore they host widespread Fe-Ni-Cu-Platinum Group Element (PGE) sulfide mineralization (Garuti et al., 2001; Fiorentini et al., 2002). The emplacement of these pipes at the upper mantle-lower crust transition is poorly understood. However, it appears that their formation is related to the large magmatic underplating event that Peressini et al. (2007) hypothesized, which was accompanied by localized mantle metasomatism (Fiorentini et al., 2002).

This study focused on the Fei di Doccio pipe, which is emplaced in the Kinzigite Formation, a sequence of lower crustal rocks. A genetic relationship between emplacement of the Ultramafic Pipes and the underplating event is based upon geochronological evidence. Previous age data suggest that the main underplating event occurred at around 288 Ma (Pin and Sills, 1986; Peressini et al., 2007). Similarly, Garuti et al. (2001) obtained emplacement ages of 288±3 Ma and 287±3 Ma for the Bec d'Ovaga and Fei di Doccio pipes, respectively. However, these ages were derived from conventional heavy liquid zircon concentrates. Therefore, these data may not be representative of the true crystallization age of the pipes because a xenocrystic origin of the analyzed zircons cannot be excluded. Furthermore, the synchronicity between the underplating event and the emplacement of the alkaline pipes could be questioned on the basis of field relationships. In fact, the pipes consistently display intrusive relationships with the Main Gabbro and Kinzigite Formation, suggesting that the crystallization age of the pipes should be younger than the underplating event. The novel approach which was applied in this study consisted in the identification of zircon grains in polished thin sections and assessing their magmatic origin on the basis of their habit and textural relations with the host rock. Then the U-Pb isotopic composition was measured in-situ. In the Fei di Doccio pipe where this study focussed, the intimate intergrowth of the zircons with the base-metal-sulfide minerals (Fig. 12) allows the precise determination of the age of the crystallization of the pipe as well as of the formation of the sulfide mineralization. The isotopic data generated in this study strengthens the hypothesis of i) the strong spatial and chronological link between the large-scale metasomatism associated with the underplating event, ii) the emplacement of the pipes and the formation of widespread Fe-Ni-Cu-PGE sulphide mineralization in the IVZ. In particular, this study sheds light on the role of mantle-derived fluids in the petrological evolution of magmatic systems emplaced in the lower crust.

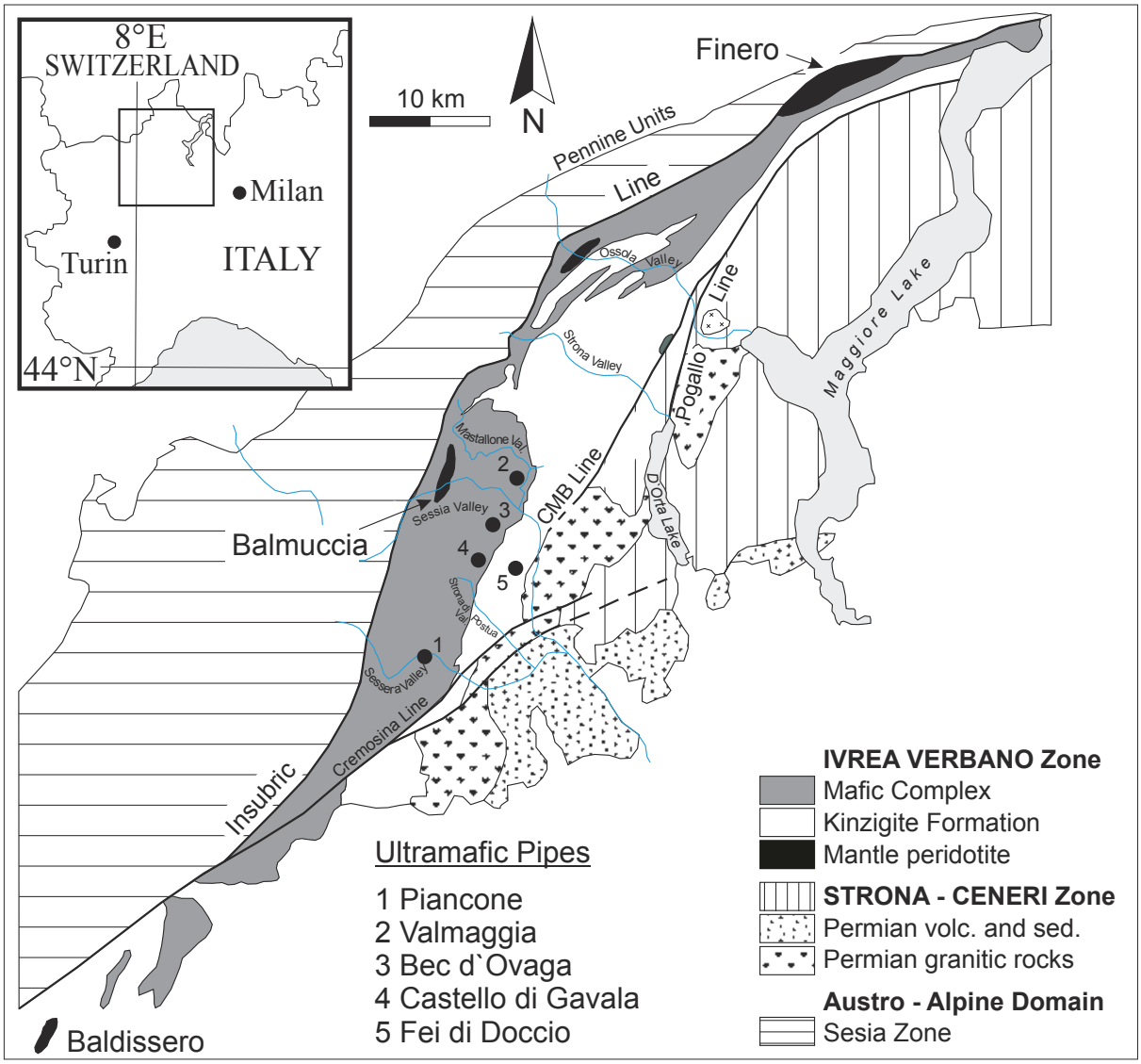

Figure 11: Geological sketch map of the Ivrea-Verbano Zone showing the main lithotectonic divisions and the locations of the Ultramafic Pipes (CMB line: Cossato-Mergozzo-Brissago line).

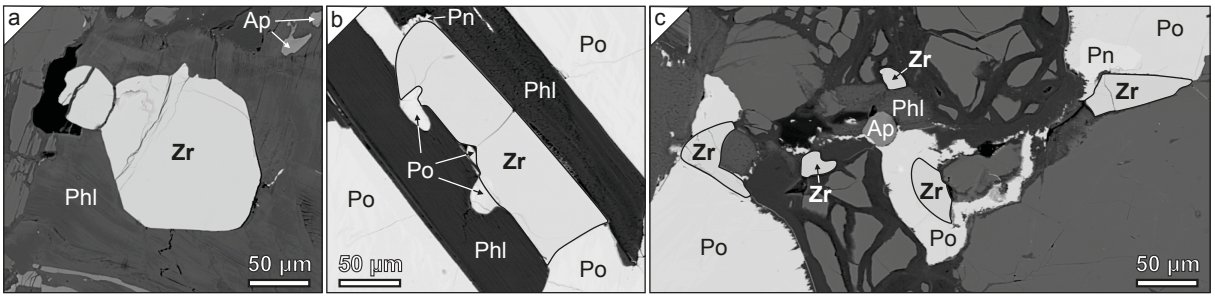

Figure 12: Back Scatter Electron images of: a) Zircon A, b) Zircon B and c) Zircon-Set C (5 minerals). Note the intimate intergrowth of the zircons with base metal sulfides and hydromagmatic phases (Zr= Zircon; Po=Pyrrothite; Pn=Pentlandite; Phl=Phlogopite, Ap=Apatite).

2.3. Material and methods

2.3.1. Zircon selection and imaging

Three to five polished sections from each pipe (i.e. at Valmaggia, Castello di Gavala, Bec d´Ovaga, Piancone la Frera and Fei di Doccio) were examined. Apart from microscopy, electron microprobe back-scattered-electron (BSE) and cathodoluminescence (CL) imaging was used to identify and quantify the amount of zircons in the different samples. Only within one polished section of the Fei di Doccio pipe (sample FD4) a sufficient, but rather limited, amount of zircons with adequate size (>20 µm) for SHRIMP II measurement could be localized. Sample FD4 was taken approximately 1m next to the contact of the Fei di Doccio ultramafic pipe with the surrounding host rock of the Kinzigite Formation. The same sample material is also described in Garuti et al. (2001), where information on its whole-rock geochemistry is provided. The major mineralogical constituents of sample FD4 are amphibole, olivine, clinopyroxene and phlogopite with minor spinel, apatite and carbonates. The ore mineralization consists of pyrrhotite, pentlandite and chalcopyrite with additional oxides, primarily ilmenite. In sample FD4 the adequately selected seven individual zircon grains are named in this study as follows: “Zircon A”, “Zircon B”, “Zircon-Set C” (a set of 5 minerals), as shown in Figure 12. The identification of zircons on the polished sections was accomplished using a Jeol JXA 8200 Superprobe at the “Eugen F. Stumpfl Laboratory” at the Department of Applied Geosciences and Geophysics, University of Leoben (Austria).

2.3.2. SHRIMP II analysis

In contrast to previous data that relied on conventional zircon recovery through heavy liquid methods, the zircons were precisely cut out of their original positions from the polished thin section of sample FD4 and mounted together with the corresponding BR266 zircon standards for in-situ analysis. This extraction technique provided invaluable information on the textural setting of the zircons, which proved essential in the interpretation of the ages. The delicate mounting and the final polishing processes were carried out at Minsep Laboratories, Western Australia. The preparation for the SHRIMP II analysis was accomplished according to the procedure described by Wingate and Kirkland (2011): cleaning in ethanol, petroleum ether, detergent (radioactive contamination cleaner) and distilled and deionized water, drying at 60°C, gold-coating to a thickness of about 40 nm, to ensure an edge-to-edge resistance of max. 25 Ω. The SHRIMP II measurement was carried out at the John De Laeter Center for Isotope Research, Curtin University, Perth (Western Australia). The operating conditions for U, Th, and Pb isotopic measurement were based on the manual of Wingate and Kirkland (2011). The primary beam was set to 20 µm diameter at 10 keV. The net primary ion current was 1.3 nA and the secondary ions were accelerated to 10 keV. The isotopes were cycled six times through the mass stations in the following sequence: 196 (species [90Zr216O]+, count time 2 s), 204 (204Pb+, 10 s), 204.1 (background, 10 s), 206 (206Pb+, 10-s), 207 (207Pb+, 40 s), 208 (208Pb+, 10 s), 238 (238U+, 5 s), 248 ([232Th16O]+, 5 s), and 254 ([238U16O]++, 2 s). Prior to analysis the measurement spot was cleaned by the primary ion beam for about 3 minutes. The data reduction was accomplished using the software packages SQUID 2.50 and Isoplot 3.71, following the protocol outlined by Wingate and Kirkland (2011). The sample

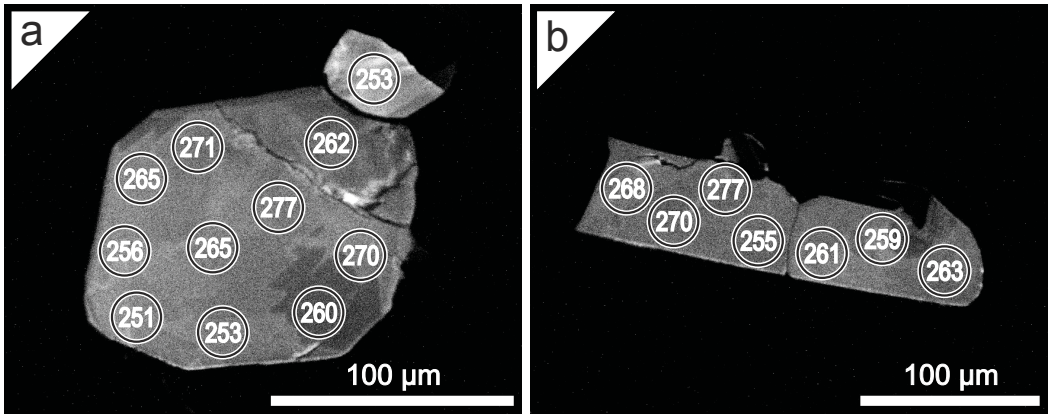

Figure 13: CL-images; SHRIMP II analysis points (spotsize is ~20 µm) on Zircon A and Zircon B. Numbers denote the mean $^{206}Pb/^{238}U$ Ages in Ma. For further isotopic data and standard deviations see Table 1. Note the CL-active halo above the 277 Ma analysis point, which surrounds a pyrrhotite grain (Fig. 12b).

analyses were standardized to the zircon standard "BR266" with 909 ppm 238U and a 206Pb/238U age of 559.0 Ma (Stern, 2001) and corrected for common lead (204Pb+).

2.4. Results

2.4.1. Textural analysis

The investigated zircons show an intimate intergrowth with base metal sulfide minerals (Fig. 12a, 12b and 12c), mainly pyrrhotite and pentlandite. The non sulfide paragenesis is dominated by hydromagmatic phases, predominantly phlogopite, apatite and amphibole. In general, the investigated zircons do not exhibit any strong zonation detectable using back-scattered-electron (BSE) or cathodoluminescence (CL) imaging (Figures 12 and 13). Therefore, the zircons appear to be largely homogeneous, with no distinct stages of growth or different generations. Zircon A exhibits an euhedral shape (Fig. 12a); however, the core zone of this zircon is influenced by a five to ten µm wide multiple crack system, crosscutting approximately one third of the mineral. In the upper right corner of Figure 12a, another small zircon with a stronger CL intensity occurs. It is separated from the larger mineral by a non CL active crack filling. The CL image of the larger mineral does not show any distinct zonation despite the less active area in the bottom right corner, as shown in Figure 13. The lath-shaped Zircon B is intimately intergrown with surrounding pyrrhotite, pentlandite and phlogopite (Fig. 12b). This textural relationship is particularly evident on the left side of Figure 12b, whereas Figure 13 shows CL active haloes around the pyrrhotite grains surrounding Zircon B. Additionally, some pentlandite grains occur at the upper right corner of the zircon (Fig. 12b). Also the smaller zircons (Zircon-Set C) do not possess any visible zonation as shown in Figure 12c, where the strong intergrowth between the zircon grains and the sulfide mineralization is recognizable. In the center of Figure 12c, a paragenesis of zircon, pyrrhotite and apatite is visible. Because of their relatively large size, Zircon A and Zircon B allow multiple measurement spots with SHRIMP II.

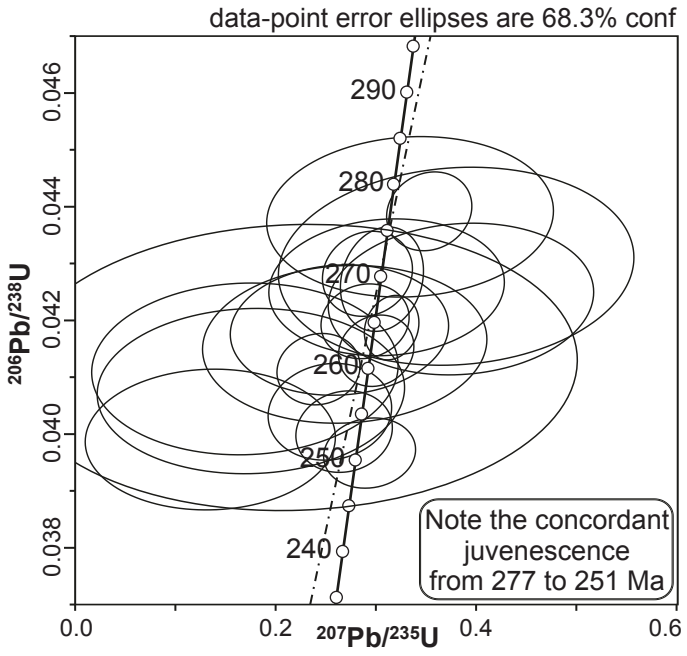

Figure 14: Concordia plot of the SHRIMP II U-Th-Pb isotopic analyses obtained on zircon A.

2.4.2. Age data distribution

Within the eight standard analyses on standard BR266, the 1 σ external spot-to-spot error of the Pb/U isotopic ratios was 0.52 %, which indicates the high quality of the measurement set. The results of the analyses are presented in Table 1 and selected concordia plots are shown in Figure 14. Multiple measurement spots were placed on Zircon A and Zircon B (i.e. eleven and seven times, respectively), whereas the smaller minerals (Zircon-Set C) were analyzed once. Isotopic compositions vary strongly among different zircon groups as well as between the single analyses within the larger Zircon A and Zircon B, as shown in Table 1 and Figure 13. Within the age distribution of Zircon A, a pattern can be recognized. Comparable young age values can be found in the two broken parts in the upper-right corner of the mineral. These areas are influenced by several cracks within the mineral, as shown in Figure 12a. The value of 252 Ma is one of the youngest ages of the whole measurement set. In general, the age values become younger from the core to the margin of the single zircons, with the youngest age (251 Ma) at the rim in the bottom left corner of Zircon A (Fig. 13). Within the less CL-active area of Zircon A, illustrated by the darker zone at the bottom-right side of the mineral (Fig. 13), elevated Th and U concentrations were measured (Analysis Zircon-A.3 in Table 1). The lowest U and Th concentrations were detected on the small zircon with a higher CL intensity in the upper right corner of Figure 13a (analysis Zircon-A.10 in Table 1). No distinct age distribution (core / rim) is visible within the lath shaped Zircon B (Fig. 13), although single values vary between 255 and 277 Ma. The single analyses of zircons in Zircon-Set C show similar age ranges between 260 and 271 Ma. Generally, the variation of individual mineral ages and that between the zircon groups (A-B-C) is almost identical, ranging between 251 and 277 Ma.

Table 1: SHRIMP U-Th-Pb isotopic analyses of zircons from the Fei di Doccio ultramafic pipe

Spot	U (ppm)	Th (ppm)	Th/U	$^{206}Pb/^{238}U$	$\pm1\sigma$	$^{207}Pb/^{235}U$	$\pm1\sigma$	$^{206}Pb/^{238}U$ Age [Ma]	$\pm1\sigma$
Zircon-A.1	112	67	0.61	0.0404	0.0006	0.2545	0.0406	255.5	3.4
Zircon-A.2	136	66	0.5	0.0401	0.0005	0.2689	0.0318	253.3	2.9
Zircon-A.3	215	202	0.97	0.0412	0.0004	0.2435	0.0275	260.1	2.6
Zircon-A.4	193	108	0.58	0.0397	0.0004	0.2939	0.0304	251.0	2.5
Zircon-A.5	137	101	0.76	0.0429	0.0005	0.2923	0.0296	270.6	3.0
Zircon-A.6	151	97	0.66	0.0420	0.0004	0.2896	0.0290	265.3	2.7
Zircon-A.7	158	110	0.72	0.0419	0.0004	0.3161	0.0180	264.5	2.3
Zircon-A.8	130	79	0.63	0.0439	0.0005	0.3537	0.0281	277.2	2.8
Zircon-A.9	169	127	0.78	0.0428	0.0006	0.3062	0.0274	269.9	3.7
Zircon-A.10	90	57	0.65	0.0400	0.0008	0.1362	0.0822	253.0	5.0
Zircon-A.11	142	85	0.62	0.0415	0.0004	0.3007	0.0248	262.1	2.5
Zircon-B.1	110	98	0.92	0.0425	0.0009	0.3859	0.0874	268.4	5.3
Zircon-B.2	84	63	0.78	0.0404	0.0011	0.1027	0.1236	255.2	6.9
Zircon-B.3	115	111	1	0.0440	0.0009	0.3355	0.0945	277.3	5.7
Zircon-B.4	98	79	0.83	0.0414	0.0010	0.1708	0.1007	261.2	6.0
Zircon-B.5	75	51	0.71	0.0417	0.0016	0.2231	0.1857	263.1	10.1
Zircon-B.6	104	88	0.88	0.0409	0.0009	0.1768	0.1009	258.7	5.8
Zircon-B.7	113	85	0.78	0.0427	0.0008	0.3118	0.0778	269.6	4.8
Zircon-C.1	86	63	0.75	0.0430	0.0011	0.3809	0.1169	271.6	7.0
Zircon-C.2	97	75	0.8	0.0419	0.0007	0.2643	0.0719	264.7	4.6
Zircon-C.3	104	86	0.85	0.0417	0.0009	0.27	0.0938	263.4	5.6
Zircon-C.4	109	89	0.84	0.0412	0.0012	0.122	0.1393	260.4	7.7
Zircon-C.5	98	86	0.91	0.0426	0.0019	0.0321	0.2199	269.0	11.6

All isotopic data is corrected for common lead (^{204}Pb) as described by Wingate and Kirkland 2011. $\pm1\sigma$ denotes the standard deviation of the foregoing data column

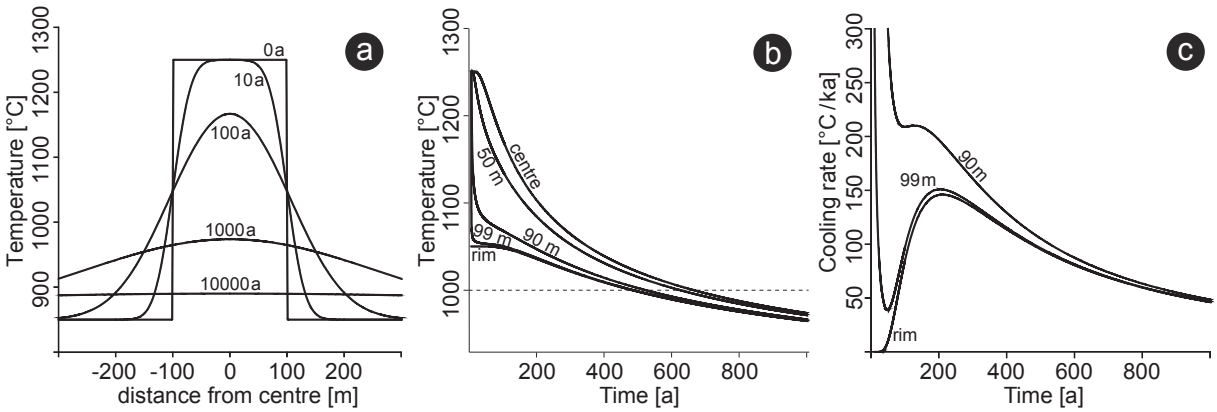

Figure 15: Cooling of the Fei di Doccio pipe according to the model by Stüwe (2007). a.) Isothermic lines across the intrusion with time elapsed from t=0. b.) and c.) Temperature - time and cooling rate - time diagram, respectively. The single lines indicate lateral sections from the center of the pipe at 0 m to the rim at 100 m.

2.4.3. Temperature calculation during cooling of the Fei di Doccio pipe

The cooling of the Fei di Doccio ultramafic body was calculated following the "one-dimensional intrusions model" postulated by Stüwe (2007). The initial conditions as well as the coordinate system were chosen similarly to this model. The coordinate system has its origin in the center of the pipe. The initial conditions are: T0 = Ti within the intrusion and T0 = Tb at the border between the intrusion and its surrounding host rock. (T0: onset temperatures of calculation, Ti: intrusion temperature, Tb: boundary temperature of the host rock). The boundary conditions were changed for these calculations, in order to reflect the IVZ scenario. The intrusion temperature Ti was set to 1250 °C for an ultramafic intrusion (in accordance to the assumptions of Henk et al. (1997); Phipps Morgan (2001) and Robinson et al. (2001)). The host rock temperature Tb was chosen at 850 °C in comparison to the magmatic underplating temperature model postulated by Henk et al. (1997). The thermal diffusivity $\varkappa$ was specified by Stüwe (2007) with a value of 10-6 m^2s^{-1}. Analogue values were obtained by Katsura (1995) (7-8x10^{-7} m^2s^{-1}) for the thermal diffusivity in the upper mantle and by Zindler and Hart (1986) (6x10^{-7} m^2s^{-1}) for not further specified mantle rocks. The one dimensional extent "l" of the Fei die Doccio intrusion, which corresponds to the diameter of the pipe, was estimated to be about 200m, on the basis of field observations. The results of this calculation are illustrated in Figure 15a,b,c. Figure 15b shows the temperature - time relationship for selected lateral sections from the core at z = 0 m to the rim at z = 100 m. As described, Sample FD4 was taken approximately 1 m next to the contact of the pipe to the host rock which corresponds to the z-coordinate position of 99m (in a distance of 99 m from the center of the 200m wide pipe). This position is cooled initially extremely fast, reaches the 1000°C isotherm after 600a and the 900°C isotherm after approximately 6000a (Fig. 15b). This fast cooling is also demonstrated by the cooling rates at the onset of the model calculation, which are shown in Figure 15c. From infinite rates at t = 0, values between 50 and 150 °Cka^{-1} are reached within the first 1000a.

2.5. Discussion

Age data from in-situ U-Pb measurement of zircons from the Fei di Doccio pipe yield a range between 251 Ma and 277 Ma. The spread of the obtained ages, both within a single zircon as well as among different grains, is somehow surprising, particularly when considering the observed internal homogeneity of the zircon crystals. This age variability needs to be explained. It is hypothesize that Pb loss is responsible for the observed juvenescence during the emplacement of the Fei di Doccio pipe. In this context the relative significance of three processes that may have operated and caused juvenescence are discussed: 1) temperature related juvenescence, 2) juvenescence triggered by metamictization, and 3) fluid related juvenescence.

2.5.1. Temperature related juvenescence

The Fei di Doccio pipe is a relatively small intrusion (i.e. with an assumed diameter below 200m). The temperature difference between the intrusion and the host rock is comparatively low (i.e. presumably 400°C) and the thermal equilibration is almost reached after 10000a, as illustrated in Figure 15a. The calculated cooling rate well above 50 °Cka-1 is extremely high. To reach a concordant timespan as observed in the samples investigated (~ 25 Ma, based on the obtained U-Pb age data set in the range of 251 - 277 Ma), much lower cooling rates would be necessary because the blocking temperature for Pb loss in zircon is determined between 900 and 1100°C (Cherniak et al., 1991; Williams, 1998; Cherniak and Watson, 2001, 2003; Geisler et al., 2003). In the calculation, the temperature of 900 °C is reached after only 6000a, below which no more considerable Pb loss with accompanied juvenescence is possible. The study of Ashwal et al. (1999) can be used as a reference for the conditions necessary to permit volume diffusion of Pb in zircon triggered by high temperatures. These authors investigated the Ankafotia body of southwest Madagascar and calculated cooling rates of 1-2 °CMa^{-1} or less, yielding a concordant time span of more than 80 Ma. Therefore, it is reasonable to argue that the rapid cooling of the Fei di Doccio pipe with cooling rates well above 50 °Cka^{-1} prevents any Pb diffusion related to the formation and subsequent cooling history. At the regional scale of the Ivrea-Verbano Zone, cooling rates of the granulitized Kinzigite Formation intruded by the Fei di Doccio pipe were calculated at ~8 °CMa^{-1} (Henk et al., 1997). These data are also by far too high to permit significant age shifts by volume diffusion of Pb in zircon and to be responsible for the observed juvenescence. Another characteristic of the Fei di Doccio zircons that does not support temperature related Pb loss is provided by their trace element pattern and distribution. In fact, in case of Pb diffusion the margins of the zircons should display excess radiogenic Pb and be commonly enriched in U (Mezger and Krogstad, 1997), which is not the case for zircon from the Fei di Doccio pipe. In addition, the textural observation of Zircon B and Zircon-Set C exclude Pb loss caused by diffusion during slow cooling. If temperature-induced reactions had occurred, each of the zircon grains, regardless of size and shape, would be rejuvenated equally, which is not the case (Tab. 1). In conclusion, it is reasonable to argue that the rapid cooling of the Fei di Doccio pipe itself as well as the comparably fast regional cooling following the underplating event (Henk et al., 1997) prevents any Pb diffusion and age juvenescence following any anomalous thermal history.

2.5.2. Juvenescence triggered by metamictization

Metamictization of zircons resulting in enhanced Pb loss by diffusion may occur when they are cooled below their annealing temperature of 600-650°C (Mezger and Krogstad, 1997). Cherniak et al. (1991) and Cherniak and Watson (2001) experimentally investigated the influence of metamictization on the diffusion rate. The activation energies of Pb diffusion were found to be about 4 times lower for metamict zircons (~142 $kJmol^{-1}$; Cherniak et al. (1991)) compared to pristine zircons (550 $kJmol^{-1}$; Cherniak and Watson (2001)). However, the zircons would have to be heated up again after the metamictization, because the diffusivity at 600 °C is far too low for considerable Pb loss (around 10-22 m^2s^{-1}; Cherniak et al. (1991)), but this does not seem to be realistic. In fact, following Sm-Nd results from plagioclase, clinopyroxene and amphibole in rocks from the Sessera Valley (Mayer et al., 2000), it is possible to exclude a thermal overprint exceeding 650°C in the Ivrea-Verbano Zone after 267±21Ma. Since the samples of this study were taken from the presumably deepest part of the Mafic Complex, the interpretation of Mayer et al. (2000) is also valid for the overlying Kinzigite Formation that hosts the Fei di Doccio pipe. Therefore, it is possible to exclude juvenescence triggered by metamictization processes that may have affected the zircons resulting in high Pb diffusion rates.

2.5.3. Fluid related juvenescence

Fiorentini and Beresford (2008)put forward the hypothesis that the formation of the alkaline Ultramafic Pipes and associated Ni-Cu-PGE mineralization in the Ivrea-Verbano Zone was genetically associated with widespread metasomatism that affected the lithospheric mantle in the Late Carboniferous (Garuti et al., 1995). Their hypothesis is mainly based upon geochemical and minero-chemical ground, with the common alkaline and incompatible element enriched signature and the ubiquitous presence of hydromagmatic phases intimately associated with the sulfide mineralization. Vavra et al. (1999) studied the influences of fluids on the isotopic composition of zircons from the IVZ and observed a general surface depletion in Th and U and particularly a stronger decrease in thorium. Vavra et al. (1999) called this phenomenon “surface-controlled alteration (SCA)”. Peressini et al. (2007) described a similar phenomenon from amphibole-gabbro-hosted zircons from the IVZ. They referred to the thick CL bright rim on zircons as “white pest”. Similarly, Zeck and Whitehouse (2002) documented the presence of zircons with “CL bright domains” from the Betic-Rif tectonic belt. All these observations ("SCA", "white pest" and CL bright domains) were interpreted as recrystallized areas influenced by interstitial fluids. Furthermore, Pidgeon et al. (1998) documented nebulously zoned zircons from the Darling Range batholith (South Australia) and proposed an open system recrystallization process, which overprints the trace element concentration and leads to a fine-scaled solution and re-deposition reaction caused by an interaction of the zircons with external fluids resulting in Pb and minor U loss. Rubatto et al. (2008) described an analogous process, a dissolution-reprecipitation reaction, for zircons of the Lanzo Massif (Italy) in contact with alkaline metamorphic fluids. Of particular interest is the regularity of the age distribution in the large Zircon A (Fig. 13), where young ages were obtained next to cracks as well as in the rim of the grain. Conversely, the smaller grains of Zircon-Set C are characterized by differing juvenescence grades: the age range of the smaller

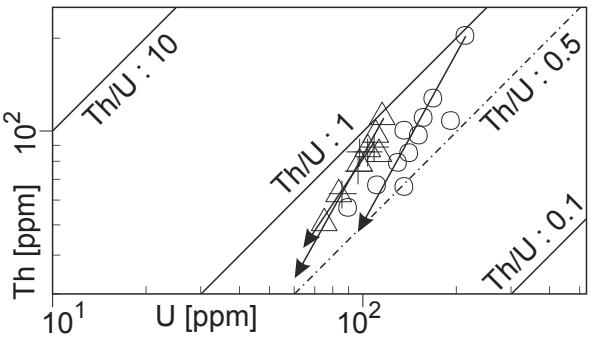

Figure 16: Thorium and U concentrations in zircons. Circles: Zircon A; triangles: Zircon B, crosses: Zircon-Set C. The arrows indicate U-Th depletion trends.

zircons (260-271 Ma) is comparable to the range observed in the larger Zircon A (251-277 Ma). These observations and data argue in favor of the occurrence of fluid activity. It is hypothesize that large zircon grains such as Zircon A were affected by a migrating fluid, which strongly interacted with and altered the zircon grains around the rims and along the cracks within the minerals whereas it largely did not affect the core and the areas of the zircon grains devoid of cracks. The smaller grains such as those of Zircon-Set C display an age range of 260-271 Ma. Due to their size of 20 - 50µm, they do not show an internal isotopic zonation that is resolvable with SHRIMP analysis. However, similarly to the bigger grains their age variability may still be due to variable interaction with fluids, depending on their relative textural setting within the rock. In samples from this study, zircon grains are generally spatially associated and locally intimately intergrown with hydromagmatic phases. From a mineral chemistry point of view, zircons display a strong variation in Th and U contents both within the same crystal and among different grains (c.f. Table 1 and Figure 16). At relatively high Th+U contents, Th/U ratios are close to 1 (Fig. 16). However, at lower Th+U concentrations a significantly stronger decrease in Th over U becomes obvious, leading to Th/U ratios of about 0.5 (Fig. 16). The lowering of the Th/U ratio is interpreted as indicative of disturbance from fluids. This chemical behavior coincides with experimental results by Geisler et al. (2003), which show that extensive radiogenic Pb loss occurs in contact with fluids simultaneously with a dominant Th and lesser U loss.

2.5.4. Age of the Fei di Doccio pipe in the context of the evolution of the Ivrea-Verbano Zone

On the basis of the reasoning outlined above, the age data derived from spots displaying relatively low Th/U ratios are interpreted as rejuvenated ages due to disturbance from fluids. By contrast, age data derived from spots displaying relatively high Th/U ratios are interpreted as true crystallization magmatic ages. The age of 277±6 Ma from analysis spot 3 on Zircon B (Tab. 1) is from an area with a Th/U ratio of 1. Therefore, this age value is interpreted as the true crystallization age of the Fei di Doccio pipe. However, this study provides clear evidence that the pipe underwent significant fluid metasomatism after emplacement and cooling, as suggested by the observed age rejuvenescence of magmatic zircons. Garuti et al. (2001) proposed an intrusion age for two of the Ultramafic Pipes

of the Ivrea-Verbano Zone (i.e. Bec d'Ovaga and Fei di Doccio) at around 288 Ma. Pin and Sills (1986) and Peressini et al. (2007) suggested that the main underplating event in the Ivrea-Verbano Zone also occurred at around 288 Ma. On the basis of these data, earlier workers have put forward the hypothesis that the emplacement of the Ultramafic Pipes is synchronous with the large scale underplating event. However, the zircons for the study of Garuti et al. (2001) were concentrated through a conventional heavy liquid method, whereby all textural information was lost. Therefore, the zircons that have been analyzed may have actually been xenocrystic zircons derived from the Main Gabbro during the emplacement of the pipes. Conversely, the new precise age data in this study were generated from zircons that were precisely cut out of their original positions from polished thin sections, whereby preserving textural information. Therefore, based on the geotectonic concept of Henk et al. (1997), it is suggested that the emplacement of the Ultramafic Pipes was not synchronous to the underplating event, but slightly younger. An emplacement age for the Fei di Doccio pipe at 277±6 Ma seems reasonable in the geodynamic context of the Ivrea-Verbano Zone. This interpretation is in accordance with the field data, which indicate that the pipes consistently have sharp intrusive contacts with the Main Gabbro (i.e. rocks formed during the underplating event) and the overlying granulitized Kinzigite Formation. It is also important to emphasize that all available ages regarding the granulitization event of the Kinzigite Formation are significantly older than the age of the underplating event and emplacement of the pipes. In fact, the youngest available age of the granulite facies metamorphic event is at ~293 Ma (Koeppel, 1974; Henk et al., 1997; Vavra and Schaltegger, 1999). Results from this study suggest that the intrusive event of the pipes was followed by an intensive fluid activity. Argon data from Biino and Meisel (1996) on biotites from the Valmaggia pipe indicate ages from 177 to 181 Ma. Biino and Meisel (1996) also reported Rb-Sr isochron from biotite from 190 to 210 Ma. Data from Vavra et al. (1999) also indicated the occurrence of strong fluid activity. They reported ages of around 210 Ma from monazites and zircons from the metapelites of the Kinzigite Formation. These young ages were interpreted to be caused by a long lived fluid system within the Kinzigite Formation, thus indicating that the Fei di Doccio pipe and its host were affected by at least one fluid event following the emplacement of the pipe. The emplacement age of the pipe presented in this study supports the idea of Garuti et al. (2001), who put forward the hypothesis that the intrusion of alkaline ultramafic magmas into the deep crust of the Ivrea-Verbano Zone is genetically associated with widespread mantle metasomatism in the lithospheric mantle of the Ivrea-Verbano Zone during the late Carboniferous at 293 ± 13 Ma (Voshage et al., 1987). On the basis of geochemical and isotopic data, Fiorentini and Beresford (2008) suggested that the volatiles implicated in the formation of hydromagmatic phases in the pipes originated from mantle-derived juvenile water. In their model, regional metasomatism introduced elevated contents of alkalis, Cu, PGEs and S into the depleted mantle of the Ivrea-Verbano Zone. Increased water activity caused the harzburgite to undergo partial melting, thus producing pockets of volatile-rich sulfide-bearing ultramafic magma that evolved to form independent intrusions that host Ni–Cu–PGE mineralization.

2.5.5. Detailed discussion of literature age data

Overall 35 literature age values were taken into consideration and grouped according to the geological formations: the Finero and Balmuccia peridodites, the metasedimentary Kinzigite Formation and the magmatic Mafic Complex (Fig. 17). In addition data from the tectonic contact between the IVZ and the adjacent Strona-Ceneri Zone, the Cossato-Mergozzo-Brissago Line (CMB Line) was compiled and documented (Fig. 11). Within this shear zone, syn-mylonitic intrusion (dikes) were dated. Age information concerning the pipes is sparse. Overall seven age values are published, obtained via different techniques (Biino and Meisel (1996) and Garuti et al. (2001)).

As a consequence, each geological formation provides specific information for the interpretation of the genetic development of the IVZ. Age values gained on Mafic Complex rocks can be correlated with the main magmatic event within the IVZ which is related to the underplating of the lithospheric mantle (Henk et al., 1997). The Kinzingite Formation, structurally located above the Mafic Complex, represents the granulite facies metamorphic lower crust (Quick et al., 1995) wherein the peak metamorphic conditions are recorded. Accordingly the two geological units, the Mafic Complex and the Kinzigite Formation, are genetically closely related and the age data can be considered representative for one single magmatic event, namely the underplating of the lithospheric mantle. The emplacement and crystallization of the pipes can be described as a direct consequence of the main magmatic underplating event in the IVZ, which provided an energetic input, extensional tectonics and fluid flow (Garuti et al., 2001).

The dikes of the adjacent Cossato-Mergozzo-Brissago Line (CMB Line) (Mulch et al., 2002) are isochronous with the underplating event and, thus, have to be interpreted as cogenetic. For a conclusive interpretation of the available aga data from the IVZ, Figures 18 and 19 illustrate the frequency of all recorded age values. The onset of the magmatic event dates back to about 290 Ma where the highest frequency of age values is reached within the Mafic Complex (Fig. 18 and 19). This event is isochronous with the first recorded metamorphic peak conditions within the Kinzigite Formation. Within the Mafic Complex, the magmatic processes diminish relatively fast at around 260 Ma, whereas the metamorphic evolution of the Kinzigite Formation approximately lasts until around 240 Ma. The age values recorded for the pipes exhibit a direct correlation with other magmatic phenomena within the IVZ: i) the isochronous Balmuccia peridodite (Voshage et al., 1988; Gebauer et al., 1992), ii) mantle metasomatism in the Finero peridotite (Voshage et al., 1987), and iii) the emplacement of syn-mylonitic intrusions along the Cossato-Mergozzo-Brissago Line (Mulch et al., 2002). The spatial proximity between the CMB intrusions and the IVZ-pipes support the hypothesis of a syngenetic development within a high temperature post regional-magmatic extensional regime where a strong magmatic-fluid impact triggered the ascent of juvenile melts through local conduits. The onset of these conditions can be determined at around 275 Ma, correlating with the oldest zircon ages analyzed in this study. The fluid processes may be described as relatively short-lived, ending around 270 to 265 Ma.

2.5.5.1. Meta peridodites Within the Finero peridodite two groups of age values were recorded. The data of Boriani and Villa (1997) obtained by ^{39}Ar-^{40}Ar stepwise heating of amphibole (282±8 Ma), and the values obtained by Voshage et al. (1987) (293±13 Ma) via

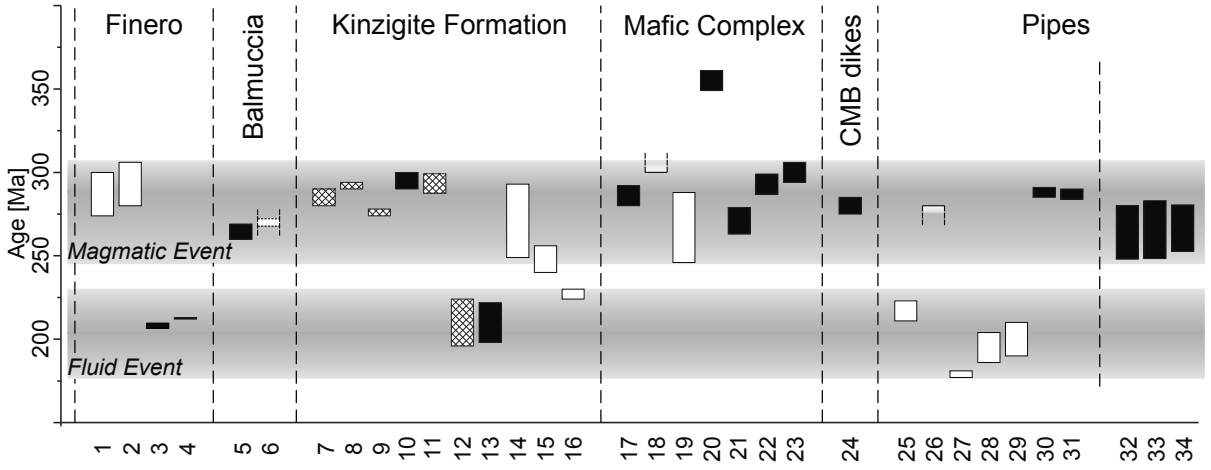

Figure 17: Compilation of published age data, grouped according to the geological units, together with data of this study (32-34). (1) Boriani and Villa (1997), Sample IZ4, Finero, ^{39}Ar-^{40}Ar stepwise heating of amphibole, 282±8 Ma. (2) Voshage et al. (1987), Rb-Sr whole rock isochron, Finero, 293±13 Ma. (3) Grieco et al. (2001), zircon dissolution, Finero, 207.9 +1.7/-1.3 Ma. (4) Oppizzi and Schaltegger (1999), zircon, Finero, 212.5 ±0.5 Ma. (5) Gebauer et al. (1992), magmatic zircons, SHRIMP, Balmuccia peridotite 265 +4/-5 Ma. (6) Voshage et al. (1988) Balmuccia peridotite, Sm-Nd isotope dilution - thermal ionization mass spectrometry, around 270 Ma. (7) Teufel and Schärer (1989) U-Pb ages, monazite single-grain, granulite- and amphibolite- facies metasedimentary rocks, Strona Valley, 280 to 290 Ma. (8) Henk et al. (1997), monazite, Val Strona Profile, near the Periadriatic Lineament (PL), oldest age 292±2 Ma. (9) Henk et al. (1997), U-Pb in monazite, Val Strona Profile, at the base of the IVZ, 276±2 Ma. (10) Koeppel (1974), U-Pb zircons and monazite, paragneiss (Kinzigite Formation) 295±5 Ma. (11) Vavra and Schaltegger (1999), U-Pb in single monazites, granulite facies metapelites (Kinzigite Formation), upper intercept age of 293.4±5.8 Ma. (12) Vavra and Schaltegger (1999), U-Pb in single monazites, granulite facies metapelites (Kinzigite Formation), lower intercept age 210±14 Ma. (13) Vavra and Schaltegger (1999) U-Pb in zircons, granulite facies metapelites (Kinzigite Formation), rejuvenated at 210±12 Ma. Ma. (14)(15)(16) Voshage et al. (1987), Sm/Nd mineral isochrons, Val Sesia and Val Strona 271±22 Ma; 248±8 Ma and 227±3 Ma. (17) Pin and Sills (1986), conventional U/Pb multigrain analysis on zircons, Upper Mafic Complex, diorite, 285+7/-5 Ma. (18) Graeser and Hunziker (1968), whole rock Rb-Sr, gabbro intrusion Mafic Complex, minimum age 300 Ma. (19) Mayer et al. (2000), Sm-Nd analyses of plagioclase, clinopyroxene and amphibole, Mafic Complex, 267±21 Ma. (20) Vavra et al. (1996), zircons, ion microprobe U-Th-Pb analyses, meta-igneous granulite (sample: ISO4), 355±6 Ma. (21) Vavra et al. (1996), zircons, ion microprobe U-Th-Pb analyses, meta-igneous granulite, partially recrystallized domains, 271±8 Ma. (22) Vavra et al. (1999), U-Pb ages of magmatic zircons, Mafic Formation, metagabbro, 293±6 Ma. (23) Vavra et al. (1999), U-Pb ages of magmatic zircons, Mafic Formation, metaperidotite, 300±6 Ma. (24) Mulch et al. (2002), zircon, TIMS U-Pb data, dikes in the CMB mylonite on the border to the IVZ, 275-285 Ma. (25) Biino and Meisel (1996), Valmaggia pipe, whole rock and mineral separate, Re-Os isochron 217±6 Ma. (26) Biino and Meisel (1996), Valmaggia pipe, Ar-Ar, Hornblende crystals with Ar overpressure, maximum age 280 Ma. (27) Biino and Meisel (1996), Valmaggia pipe, Ar-Ar, biotites, from 177 to 181 Ma. (28) Biino and Meisel (1996), Valmaggia pipe, Rb-Sr isochron, whole rock and mineral separates, 195±9 Ma. (29) Biino and Meisel (1996), Valmaggia pipe, Rb-Sr isochron, biotite, from 190 to 210 Ma. (30) Garuti et al. (2001), zircon evaporation, U-Pb, Bec d'Ovaga, 288±3 Ma. (31) Garuti et al. (2001), zircon evaporation, U-Pb, Fei di Doccio, 287±3 Ma. (32) This study, Zircon A, 248-280 Ma. (33) This study, Zircon B, 248.3-283 Ma. (34) This study, Zircon-Set C, 252.7-280.6 Ma.

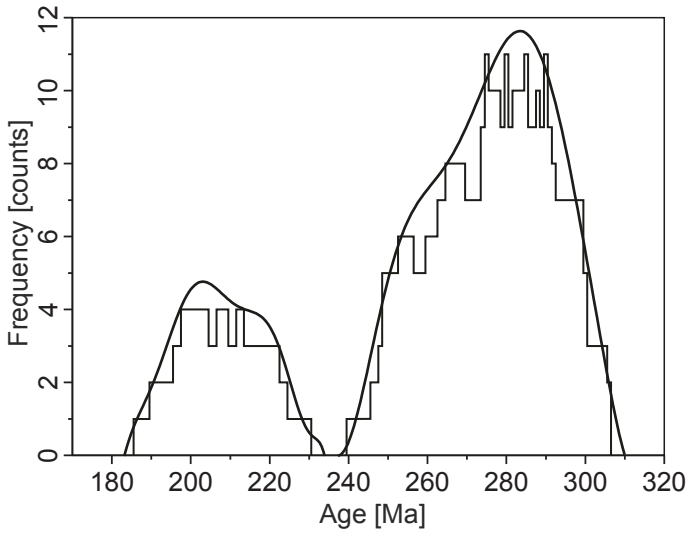

Figure 18: Frequency of age data cited in Figure 17.

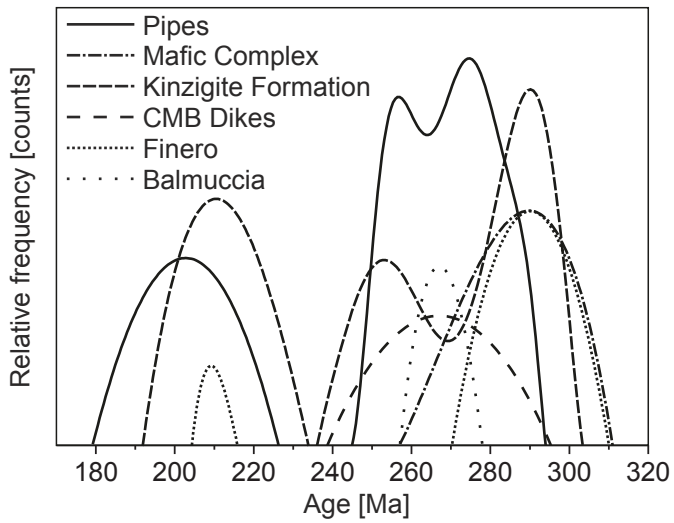

Figure 19: Frequency of age data cited in Figure 17 grouped according to the geological units.

a Rb-Sr whole rock isochrons, can be related to the main magmatic event. The second group of age values were postulated by Grieco et al. (2001) (207.9 +1.7/-1.3 Ma) and Oppizzi and Schaltegger (1999) (212.5 ±0.5 Ma). Both authors concluded that these values were caused by a strong metasomatic impact within the Finero peridodite. Compared to the Finero peridodite values, significantly younger data (265+4/-5 Ma) was ascertained by Gebauer et al. (1992) via U-Pb dating (SHRIMP) of magmatic zircons for the Balmuccia peridotite. Ultramafic and mafic dikes in the Balmuccia peridotite were dated by Sm-Nd isotope dilution - thermal ionization mass spectrometry (Voshage et al., 1988) and yielded values around 270 Ma. These results lead to the interpretation that the Finero peridodite was closer related to the main magmatic event than the Balmuccia peridodite which was apparently not influenced by a subsequent fluid impact (Mazzucchelli et al., 2009).

2.5.5.2. Kinzigite Formation Koeppel (1974) interpreted the age value of 295±5 Ma, gained from zircons and monazites hosted by paragneiss (Kinzigite Formation), as the minimum age of granulite facies metamorphism. This assumption was reinforced by Vavra and Schaltegger (1999). They analyzed U-Pb in single monazites of the granulite facies metapelites (Kinzigite Formation) and reached an upper intercept age of 293.4±5.8 Ma. Henk et al. (1997) analyzed monazites within a profile parallel to the Val Strona. Near the Insubric Lineament the oldest ages of (292±2 Ma) were obtained. Closer to the the base of the IVZ, the age values are getting younger reaching 276±2 Ma. This characteristic younging was explained by a propagation of the cooling front subsequent to the underplating event (Henk et al., 1997). Consequently, it can be concluded that the peak metamorphic conditions were reached between these two age values when the base of the IVZ was heated above the zircon blocking temperature before 276±2 Ma. This assumption is verified by U-Pb ages of 280 to 290 Ma derived from monazite single-grains in granulite- and amphibolite- facies metasedimentary rocks of the Strona Valley (Teufel and Schärer, 1989).

Within the Kinzigite Formation a second group of age values were documented. The lower intercept age analyzed by Vavra and Schaltegger (1999) in monazites from the granulite facies metapelites, was found to be 210±14 Ma. This lower intercept was interpreted, together with rejuvenated zircons yielding 210±12 Ma, as a fluid induced Pb-loss event causing external corrosion structures in monazites as well as in zircons. The subsequent cooling history of the Kinzigite Formation was dated by Voshage et al. (1987) with the aid of Sm/Nd mineral isochrons (garnet, plagioclase, orthopyroxene and whole rock) from the Val Sesia and Val Strona valleys and revealed 271±22 Ma; 248±8 Ma and 227±3 Ma. The highest age value again corresponds to the assumed peak metamorphic conditions, whereas the lower ages agree well with the subsequent cooling.

2.5.5.3. Mafic Complex The majority of data published on the Mafic Complex was collected from magmatic zircons. Peressini et al. (2007) investigated, amongst other samples, zircons from the Upper Mafic Complex and described relatively simple igneous zoning. The age data of these zircons were related to the main intrusive phase around 288 Ma. They interpreted data from other authors to be influenced by an irregular cooling front, locally perturbed, and the single data as discrete events during the slow cooling history. On the basis of this investigation and the blocking temperatures described for

diffusive Pb loss in zircon and monazite (around 1100 and 1000 °C, respectively), this assumption should not be used for the interpretation of age values provided by these two minerals. Vavra et al. (1996) investigated magmatic zircons from the border between the Main Gabbro and the Kinzigite Formation and obtained 355±6 Ma on magmatic cores and 271±8 Ma within partially recrystallized domains. The age value of 355 Ma is comparably too high, if compared with the data of other authors and may be caused by inherited cores. The value of 271±8 Ma is in the lower range of the magmatic event. Again relatively old age values were ascertained by Vavra et al. (1999) for magmatic zircons from the metagabbro (293±6 Ma) and a metaperidotite (300±6 Ma). These ages were genetically attributed to the magmatic underplating event. A similar minimum age (300 Ma via whole rock Rb-Sr analyses) for the gabbro intrusion in the Mafic Complex was postulated by Graeser and Hunziker (1968). Pin and Sills (1986) obtained an age of 285+7/-5 Ma, based on conventional U/Pb multigrain analyses on zircons from the Upper Mafic Complex, whereas the Upper Mafic Complex is in direct contact with the Kinzigite Formation. Mayer et al. (2000) revealed an age value of 267+/-21 Ma from Sm-Nd analyses of plagioclase, clinopyroxene and amphibole from the Mafic Complex. This age was interpreted as either a minimum age of formation of the metamorphic texture or as a cooling age after the youngest thermal overprint, due to the lower blocking temperature for the Nd isotope equilibrium. The data of this study clearly favours the second suggestion.

2.5.5.4. CMB On a regional scale, age data from the IVZ surrounding geological units have to be incorporated. U-Pb zircon data from syn-mylonitic mafic and felsic dikes occurring within the adjacent Cossato-Mergozzo-Brissago (CMB) Line, the border between the IVZ and the Strona-Ceneri Zone (SCZ), was ascertained by Mulch et al. (2002). They described the CMB mylonite belt as an Early Permian shear zone related to the final stages of magmatic underplating in the Mafic Complex and dated the dikes at 275-285 Ma (zircon, TIMS U-Pb data). This assumed late stage of underplating is in accordance with the oldest measured ages in the Fei di Doccio pipe. Mulch et al. (2002) related the origin of the dikes to the subhorizontal part of the transcurrent shear zone allowing the ascent of melts. Therefore, based on the proximity of the Fei die Doccio pipe and the CMB Line and the age match, similar processes could have been active during the genesis of the Fei di Doccio pipe.

2.5.5.5. Ultramafic Pipes The only age data from the Ultramafic Pipes available so far, was published by Biino and Meisel (1996) and Garuti et al. (2001). Biino and Meisel (1996) investigated rocks from the Valmaggia pipe using several techniques. Ar-Ar measurement on hornblende crystals with Ar overpressure revealed a maximum age of 280 Ma which is in accordance with the maximum ages of this study. All the other postulated data by Biino and Meisel (1996), whole rock and mineral separate Re-Os isochrons (217±6 Ma), Ar-Ar on biotites (177 to 181 Ma), Rb-Sr isochron in whole rock and mineral separates (195±9 Ma and Rb-Sr isochron in biotite (190 to 210 Ma) can be interpreted as dating a fluid event, also recorded in the same range in the Kinzigite Formation as well as in the Finero peridodite. Garuti et al. (2001) described a similar appearance of zircons from Bec d'Ovaga and Fei di Doccio as identified in this study. The lack of inherited cores or oscillatory zoning was reported characteristic for zircons precipitated from a melt. The

U-Pb zircon evaporation ages (Bec d'Ovaga 288±3 Ma and Fei di Doccio 287±3 Ma) are about 10 Ma older than the values of this study. Probably this difference appears, because the evaporation technique is not sensitive to internal isotopic anomalies, which are clearly documented within the samples from Fei di Doccio of this study.

2.6. Conclusion

This study addresses the widely debated and poorly understood chronological relationship between a series of alkaline Ultramafic Pipes hosting base metal sulfide mineralization and the Late Carboniferous underplating event that affected the Ivrea-Verbano Zone of Northern Italy. The new in-situ SHRIMP ages derive from zircons from the Fei di Doccio pipe that intruded the Kinzigite Formation, a crustal sequence of high-grade ortho- and parametamorphic rocks. A total of 23 analyses have been performed on two larger zircons (up to 170µm) and five smaller grains (around 30µm). In spite of textural homogeneity, the U-Pb isotopic results as well as the Th and U contents show significant variation in analysis spots from both, within the same crystal and among different grains, leading to an age range between 251 and 277 Ma. The age of 277±6 Ma derived from spots displaying Th/U ratios of ~1 is interpreted as the true crystallization age of the pipe. Conversely, the age data derived from spots displaying relatively low Th/U ratios are interpreted as rejuvenated ages due to disturbance of the isotope equilibrium by fluids. As the new crystallization age of the pipe is ca. 10 Ma younger than previous estimates, it can be suggested that the emplacement of the pipe was not synchronous with the regional underplating event at ca. 288 Ma, but slightly younger. This interpretation is in accordance with the field data, which indicate that all the known pipes in the Ivrea-Verbano Zone consistently have sharp intrusive contacts with the Main Gabbro and the overlying granulitized Kinzigite Formation. These age data also confirm earlier hypotheses, suggesting that the intrusion of alkaline ultramafic magmas into the deep crust of the Ivrea-Verbano Zone is genetically associated with widespread mantle metasomatism in the lithospheric mantle during the late Carboniferous.

3. Raman spectroscopic analyses of the (F vs. Cl+OH) anion composition in apatite

3.1. Abstract of this section

This study deals with an accurate determination of the anion compositions (F vs. Cl+OH) of apatites via Raman spectroscopic analyses for the first time. This newly invented methodology takes advantage of the full range of analytical capacity of Raman spectroscopy, such as almost no sample preparation, in combination with the high accuracy in the analyses of F, Cl and OH. The samples investigated were collected from Ni-Cu-PGE sulfide deposits hosted in pipe-like ultramafic bodies of the Ivrea-Verbano Zone, NW Italy. The chemical composition of the apatites were measured by electron microprobe, followed by the Raman analyses, in order to correlate the variance of the gained spectra with the differing compositions. This study provides a simple and useful tool for a quantitative determination of the anion composition (F vs. Cl+OH) of in-situ apatite samples in the range between the end members, fluorapatite, chlorapatite and hydroxylapatite. The anion composition is predicted using an empirical equation which takes the whole Raman data set, and not only single peaks, of each apatite in account. This leads to a very high accuracy of the method. With the aid of a multivariate regression method, all data sets were combined to calculate the empirical formula. Compared to other methods, such as electron microprobe analyses, sample preparation can almost be neglected. Even small crystals can be investigated and a fast procedure to analyse large amounts of samples can be established. This study demonstrates clearly that Raman spectroscopy can be used for a relatively simple and fast semi-quantitative to quantitative analysis of F vs. Cl+OH in apatite. This innovative technique is considered immanently important for further investigations because it opens a wide range for a non destructive and easy-to-use analysis of apatites and also other minerals and materials where a chemical change is influencing the Raman-active vibration modes. The area of application goes beyond pure mineralogy and petrology, can be of immanent importance in mineral processing and reaches into the fields of biological studies (dental and bone investigation), paleontology (fossilised teeth) and medicine (cancer research). The general applicability also for other minerals and materials proves the great perspective of this invented methodology in the future.

3.2. Introduction

The structure of apatite, the most abundant phosphate mineral on Earth, is strongly influenced by the presence of F, Cl and OH in its crystal lattice. Due to its structure and chemistry, it is tolerant to substitution, vacancies and solid solutions. In particular, the different size and structural position of these three monovalent anions result in a shifting of the cell parameters. According to the concentrations of F, Cl and OH the following three apatite end-members can be distinguished: fluorapatite, chlorapatite and hydroxylapatite. For the investigation of ore genesis processes, the analysis of apatite is of great importance because they are intimately intergrown with the Ni, Cu, Fe, and PGE minerals occurring in the base metal sulfide deposits of the Ivrea-Verbano Zone. The anion compositions of apatites provide an excellent indicator for the fluids involved in the ore forming process. The software package R version 2.12.2 (2011-02-25) (R Development Core Team, 2011) with the according libraries of Ligges and Maechler (2003); Filzmoser and Steiger (2011); Fox (2011) was used for statistics in Figures and Tables.

3.2.1. Analytical difficulties

Electron microprobe quantitative analysis (EMPA) is one of the most commonly used techniques to discriminate the three apatite end-members. However, the analysis of light elements ($Z < 9$) such as O and F is challenging and often fraught with errors. Hydrogen cannot be detected, thus the hydroxyl contents may exclusively be calculated stoichiometrically. Reliable analyses of F can only be obtained by the use of modern electron microprobe systems and the single mineral grains have to have a diameter of at least 10 µm, in order to obtain reasonable quantitative analytical results. Additionally, most of the apatites are very small in size (around 5 µm) and sometimes fractured, which prevents precise microprobe analysis. As a consequence, Raman spectroscopy was applied in this study, in order to gain a sufficient amount of analyses for each sample investigated and to obtain quantitative results from very small and fractured apatite grains.

3.2.2. Apatite structure

The structure of apatite with the general chemical formula of $Ca_5(PO_4)_3(F,Cl,OH)$ is discussed in Bhatnagar (1969); Chang et al. (1996); Deer et al. (1992); Mackie et al. (1972); O'Shea et al. (1974); Sudarsanan et al. (1972). The fluorine, chlorine and hydroxyl ions are surrounded by three Ca ions at one level and a hexagonal network with the spacegroup of $C6_3/m$ is formed by the linkage of Ca - O columns with PO_4 groups (Fig. 20a). Due to the differing sizes of the monovalent anion complexes, which are arranged along the axes 6_3 (Fig. 20b), the cell parameters are shifted. The fluorine ion is centered between the three calcium atoms and the cell parameters are reported by Sudarsanan et al. (1972) for synthetic and mineral fluorapatite. The chlorine and the hydroxyl ions are displaced from the center (Fig. 20b). This displacement comes along with minor perturbations in the position of the calcium ions and the phosphate groups. For synthetic stoichiometric chlorapatite a monoclinic space group ($P2_1/b$) is described by Mackie et al. (1972). This monoclinic structure is generated by the ordering of chlorine atoms along the pseudo-hexagonal axis with a displacement of about 0.38 $\AA$, which tilts and offsets the associated

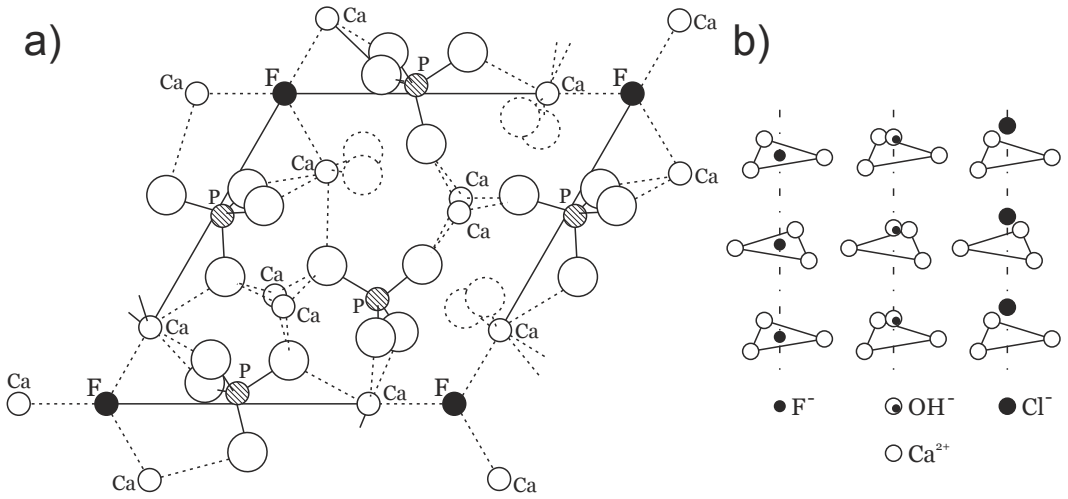

Figure 20: a) Fluorapatite structure (after Deer et al. (1992) and references therein) b) Schematic position of fluorine, chlorine and hydroxyl ions in apatite (after Siddall and Hurford (1998) and references therein).

phosphate tetrahedron. Additionally, Mackie et al. (1972), describe Cl vacancies which promote the occurrence of a hexagonal phase. For hydroxylapatite, Bhatnagar (1969) describes that the hydroxyl dipole - calcium ion repulsion pushes the oxygen atom out from the plane of the calcium triangles. An additional, minor position change of the phosphate groups is produced by the ordering of the chlorine and hydroxyl, forming a glide plane, when the composition is getting stoichiometric. (Chang et al. (1996)). All these influencing factors cause the differences in the cell parameters (Tab. 3), as reported by Chang et al. (1996).

3.2.3. Raman-active vibration modes of apatite

Apatites provide several Raman-active vibration modes. The lattice modes occur at low wavenumbers from 40 to 320 cm^{-1}. The four phosphate modes, produced by the vibration of the PO_4^{3-} group, range between 420 and 1100 cm^{-1} (Fig. 21) In hydroxylapatites additionally three OH vibrations, related to translation, libration and stretching of OH, occur at 337 cm^{-1}, 655 cm^{-1} and 3573 cm^{-1} (Bhatnagar (1969)). The phosphate vibration modes can be used for compositional studies. The free PO_4^{3-} groups provide four Raman-active vibration modes (Fig. 21): ν_1 (980 cm^{-1}), ν_2 (363 cm^{-1}), ν_3 (1082 cm^{-1}) and ν_4 (514 cm^{-1}). Due to crystalline field effects, line splitting (Fig. 21) occurs for each mode beside the ν_1 mode of the fluorapatites (O'Shea et al. (1974)). In chlor- and hydroxylapatite also the ν_1 modes are affected by line splitting. The impact of the chemical composition on the crystal lattice also influences the Raman-active vibration modes. Due to the different sizes and positions of F, Cl and OH in the cell structure, the frequencies of the single vibration modes are affected and the peak shapes are modified. Awonusi et al. (2007) and Antonakos et al. (2007) investigated the 960 cm^{-1} phosphate peak in correlation with the mass percent of substituting CO_3^{2-} either at the phosphate site or at the hydroxyl site and found linear correlations for the full width at half maximum (FWHM) and a peak shift towards intermediate numbers.

3.3. Sample material

The samples investigated in this study derive from five pipe-like ultramafic bodies at the localities Valmaggia, Bec d'Ovaga, Castello di Gavala, Fei di Doccio and Piancone la Frera. The geological details are delineated in the General Geology chapter. These Ultramafic Pipes, hosting the Ni–Cu–PGE sulphide deposits, (Garuti et al., 2001) are characterised by the accessory occurrence of hydrmagmatic mineral phases such as apatite, phlogopite and amphibole (Ferrario et al., 1982; Garuti and Rinaldi, 1986b; Garuti et al., 1990). In particular the apatites are intimately intergrown with the Ni, Cu, Fe, and PGE minerals occurring in the base metal sulfide deposits of the Ultramafic Pipes. Several polished sections were prepared from the collected samples for the microscopic investigation, the microprobe and the Raman analyses.

3.4. Analytical Methods

3.4.1. Electron-microprobe analyses

Electron-microprobe analyses in WDS mode were conducted using a Jeol JXA 8200 Superprobe at the "Eugen F. Stumpfl Laboratory" at the Department of Applied Geosciences and Geophysics, Chair or Resource Mineralogy, University of Leoben (Austria), operating with 20 kV accelerating voltage and 50 nA beam current. Back scattered electron (BSE) images were also obtained by the use of this instrument. The analyses of Ca, P, Cl and F were carried out using the Kα lines, and were calibrated on natural apatite, atacamite and fluorite. The counting times for peak and backgrounds were 20 and 10 seconds, respectively. The following diffracting crystals were used: PETH for phosphorous, PETJ for calcium and chlorine, and LDE1 for fluorine. The contents of hydroxyl were stoichiometrically calculated, because it cannot be detected by EMPA. The anion compositions of the apatites investigated are reported in Table 2

3.4.2. Raman spectroscopic analyses

Raman spectroscopic investigations were undertaken by using a LABRAM (ISA Jobin Yvon) instrument with a frequency-doubled 120mW polarized 532.2nm Nd-YAG laser. To ensure the reproducibility of the Raman measurement a frequency calibration was carried out with an absolute frequency standard (neon lamp) according to the the frequency shift data published by McCreery (2000). The neon emission was measured before and after the apatite measurement set. The relative frequency shift in proportion to the used 532.02 nm laser was separately calculated for each Raman-active vibration mode. The nearest neon emission lines below and above the frequency of each investigated vibration mode were applied to interpolate the proportional offset. Each investigated apatite grain was measured three times on different positions within it's sectional area. One analysis was set in direct proximity to the microprobe measurement spot and the other two analyses were randomly distributed on the apatite´s sectional area, to achieve a adequate statistical overview and to estimate the uncertainties arising from the varying fluorescence values. The software package PeakFit v.4.12 (SeaSolve (2003)) was used for the deconvolution of the raw data. Fluorescence was eliminated by a baseline-fit with subsequent subtraction. For peak separation and the analyses of the peak parameters a deconvolution method using

a Gauss-Lorentzian amplitude alignment was chosen. The resulting peak parameter data were normalized according to the offset, ascertained by the neon frequency calibration.

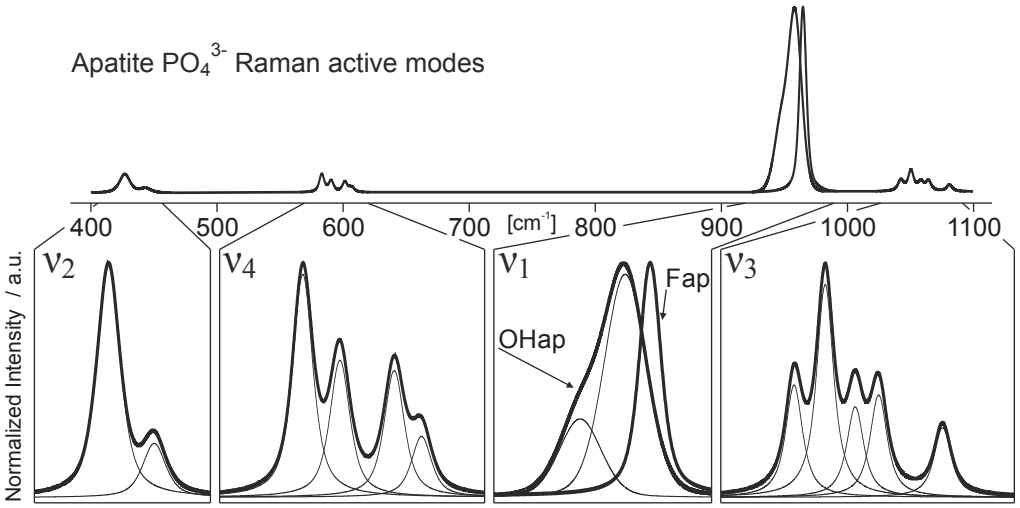

Figure 21: Representative Raman spectrum after fluorescence baseline-correction. The windows are showing the Raman-active phosphate vibration modes (ν_1-ν_4). Thick lines: cumulative curves; narrow lines: track the measurement points (not shown). OHap: Hydroxylapatite; Fap: Fluorapatite.

3.5. Results

3.5.1. Apatite electron microprobe composition

Microprobe analyses (EMPA) of the apatites revealed distinctive differences in the fluorine and chlorine contents in the samples from Bec d'Ovaga (BO6), Valmaggia (VM1) and Castello di Gavala (GV1262B) (Tab. 2). This set of samples can be divided into two groups: 1) F-OH apatites from Bec d'Ovaga (BO6) and 2) F-Cl-OH apatites from the other localities. Because of the compositional spread, these samples were chosen for the Raman investigations. The electron microprobe compositions of the analyzed apatites, in terms of F, Cl and OH, are plotted in the ternary diagram (Fig. 22) to show the predominant compositional spread between F and OH. The apatites of Castello di Gavala and some apatites from Bec d'Ovaga are slightly enriched in Cl. Chemical compositions with approximate end-member composition (fluorapatite, chlorapatite or hydroxylapatite) have not been found. A possible substitution of the phosphate group by carbonate could not be verified by EMPA. The results for the anion composition, as the relative number per formula unit, calculated on the basis of 26 anions (O, OH, F and Cl), are shown in Tab. 2

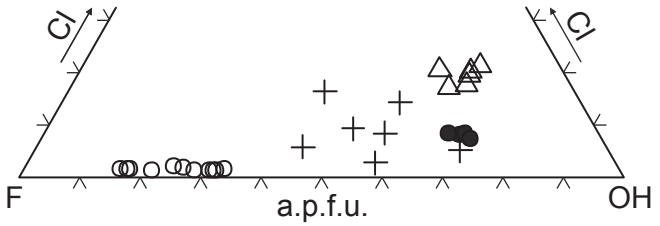

Figure 22: Apatite anion compositions of this study. F-OH apatites from: Bec d´Ovaga (Sample BO6: open circles; Sample BO1: filled circles); F-Cl-OH apatites from: Valmaggia (Sample VM1: crosses) and Castello di Gavala (Sample GV1232B: triangles).

Table 2: Anion composition of the apatites obtained by EMPA with corresponding peak position and FWHM values, calculated by the RAMAN data deconvolution method.

	particle coefficient[a]			peak position cm^{-1}					peak width $cm^{-1(c)}$					
Sample	F	Cl	OH[b]	ν_1	ν_4	ν_4	ν_2	ν_2	ν_1	ν_4	ν_4	ν_4	ν_4	ν_2
BO6-ap1	0.81	0.01	0.17	965.95	592.88	582.54	451.01	432.18	5.12	5.57	5.57	5.57	5.57	20.71
BO6-ap2	0.72	0.02	0.26	966.01	593.09	582.63	448.77	432.41	5.19	4.98	5.64	6.00	5.54	19.27
BO6-ap3	0.68	0.01	0.31	965.99	593.12	582.72	448.58	431.97	5.17	5.53	5.67	5.29	5.37	17.67
BO6-ap4	0.70	0.01	0.28	966.22	592.95	582.82	448.69	432.27	5.13	5.67	5.16	5.40	5.39	18.42
BO6-ap5	0.67	0.01	0.32	966.09	593.11	582.67	448.41	432.09	5.16	5.74	5.55	5.61	5.52	21.52
BO6-ap6	0.81	0.02	0.17	966.07	592.75	582.69	446.71	432.55	4.94	4.61	6.22	6.08	5.97	23.97
BO6-ap7	0.65	0.02	0.33	966.07	593.06	583.05	446.19	432.19	5.22	4.89	6.36	6.13	6.38	26.44
BO6-ap8	0.74	0.02	0.25	966.20	593.11	582.72	448.06	432.24	5.31	5.36	5.99	6.02	5.96	20.04
BO6-ap9	0.83	0.01	0.16	966.08	593.14	582.45	448.43	432.32	4.87	5.74	5.46	5.43	5.36	18.93
BO6-ap10	0.77	0.01	0.21	966.25	593.15	583.20	450.95	432.54	4.91	4.01	5.45	6.00	5.96	22.22
BO6-ap11	0.67	0.01	0.32	966.16	592.93	582.51	448.75	432.02	4.78	5.49	4.85	5.53	4.99	17.03
VM1-ap2	0.30	0.14	0.56	963.99	592.40	581.85	446.50	431.52	7.68	7.65	7.04	7.37	7.54	27.35
VM1-ap3	0.35	0.08	0.56	964.07	592.66	581.42	448.12	430.79	8.01	6.40	6.40	6.40	6.40	21.33
VM1-ap4	0.50	0.06	0.44	964.73	592.84	581.70	446.57	431.65	6.63	8.03	6.27	6.80	6.53	24.71
VM1-ap5	0.40	0.09	0.51	964.35	592.55	581.64	447.68	431.43	7.07	7.23	6.43	6.76	6.54	21.16
VM1-ap8	0.40	0.03	0.58	964.27	592.38	582.70	449.76	431.70	7.49	7.00	7.01	7.04	7.09	29.22
GV1262B-ap1	0.20	0.17	0.62	962.75	592.13	580.74	445.33	430.26	10.08	7.14	7.89	7.47	7.10	29.89
GV1262B-ap2	0.17	0.18	0.65	962.88	592.58	580.47	444.03	430.84	9.89	10.00	7.32	7.73	7.84	28.73
GV1262B-ap3	0.20	0.20	0.59	962.94	592.09	580.76	445.28	430.93	9.64	6.16	7.90	8.21	8.77	30.04
GV1262B-ap4	0.13	0.21	0.66	962.65	592.60	580.26	445.35	430.55	10.45	10.96	7.95	8.49	6.67	27.33
GV1262B-ap5	0.15	0.20	0.65	962.69	592.20	580.40	446.71	430.65	10.69	9.38	7.10	8.55	6.46	23.55
GV1262B-ap6	0.16	0.20	0.65	962.78	592.52	580.36	446.25	430.25	10.23	10.97	7.07	8.14	6.88	26.92

[a]Number of ions calculated on the basis of 26 anions (O,OH,F,CI). [b]The atomic proportions of OH are stoichiometrically calculated. [c]The FWHM data belong to the peaks occurring at the vibration modes in the sequence of, ν_1 (∼962cm^{-1}), ν_4 (∼618cm^{-1}), ν_4 (∼609cm^{-1}), ν_4 (∼593cm^{-1}), ν_4 (∼582cm^{-1}) and ν_2 (∼448cm^{-1}).

3.5.2. Results of the Raman analyses

The Raman analyses were characterized by a high reproducibility and were not influenced by a drift of the equipment. The three individual measurements of each apatite grain showed only small differences in the properties of the Raman-active phosphate modes. The fluorescence varied strongly within the test series and even for different areas on one individual grain. The expected peak shift with varying anion compositions can be recognized for the whole spectrum. The resolving power of the deconvolution method is diminishing with increasing overlapping of the single peaks (Fig. 21), demonstrated by a drop in the coefficients of determination (R^2) of the Gauss-Lorentzian alignment. In particular the uncertainties for the FWHM data increases strongly. This situation leads to a decline in accuracy from the best results gained for the ν_1 mode, over ν_2 and ν_4 to the worst mode ν_3. Notably the ν_3 mode is characterized by a strong overlapping of the single peaks which results in highly variable deconvolution results. Independently, whether the apatite grain belongs to the F-OH, or the F-Cl-OH group, linear shifts for the peak positions and a linear behavior of FWHM's in correlation with the stoichiometric composition is preserved. The precisions of the linear correlation gradients of the peak shifts (Fig. 23) and shapes (Fig. 24), indicated by the coefficients of determination (R^2), are varying between the vibration modes and even within a set of single peaks belonging to one distinct mode. In contrast to other authors (i.e. Pasteris and Ding (2009)), only linear trends were observed and non-linearity could not be detected. The vibration modes < 320 cm^{-1}, produced by lattice vibrations involving all atoms of the crystal simultaneously, do not show a clear difference between the endmembers, as discussed by O'Shea et al. (1974). Due to the non-orientated samples and the high fluorescence, the OH modes could not be taken into consideration for quantitative investigations. There is no evidence for additional peaks induced by other substitutes in any of the spectra.

Table 3: Cell parameter of the major end-member compositions of apatite according to a hexagonal unit cell; given by Chang et al. (1996).

	a $\mathring{A}$	c $\mathring{A}$
Fluorapatite	9.39	6.88
Chlorapatite	9.60	6.78
Hydroxylapatite	9.42	6.87
Carbonate-apatite	9.36-9.32	6.89

3.6. Discussion

3.6.1. Influence of carbonate vibration mode

The absence of a peak at 1070 cm^{-1} (ν_1 carbonate mode) and the evidence that there is no visible influence of carbonate on the ν_3 phosphate mode, as described for carbonate bearing apatites by Awonusi et al. (2007), it can be presumed that the apatites of the Ivrea-Verbano Zone host, if at all, only low amounts of carbonate. Therefore, a negligible influence of carbonate is suggested.

3.6.2. Which Raman data is suitable for empirical calculations?

In principle each Raman-active phosphate vibration mode provides a measure for the stoichiometric anion composition of apatites. The overlap of a series of minor Raman vibration modes near the ν_3 mode (Fig. 21) do not show a conclusive estimation of the peak position in the deconvolution procedure. These deconvolution difficulties are also shown, to a lower extent, by the ν_4 and ν_2 modes, but the overlaps are not so strong compared to the ν_3 mode. Therefore, sufficient correlations with the chemical composition (Fig. 23 and 24) can be detected, which enables the application for the empirical calculations. This assumption is reinforced by studies of other authors using different phosphate modes. In comparison to the Raman spectroscopy, Siddall and Hurford (1998) used infrared spectroscopy to determine the P–O antisymmetric stretching vibration of

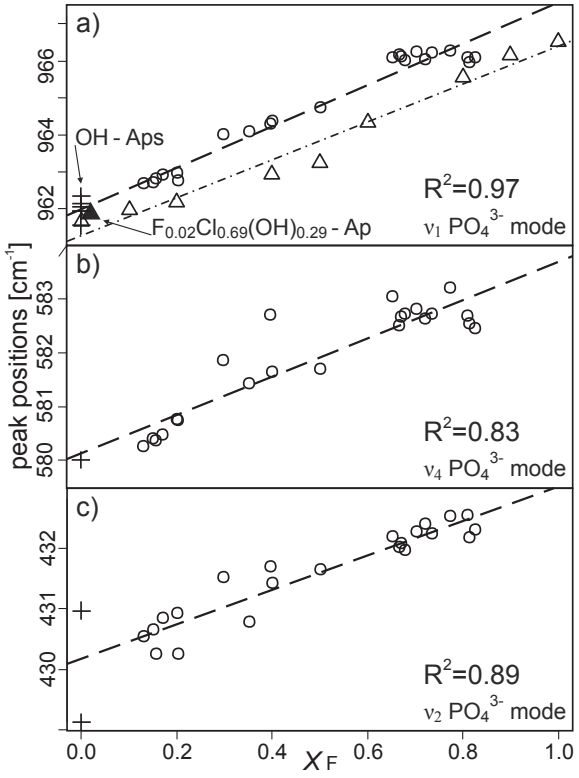

Figure 23: Peak positions compared to the apatite´s anion composition X_F (X_F=F/(F+Cl+OH)) (EMPA). Data: this study (circles); F-Cl apatites (open triangles) by O'Donnell et al. (2009); F-Cl-OH apatite (filled triangle) No. R060192 by RRUFF (2011); diverse OH apatites (crosses) by De Mul et al. (1986); Pasteris et al. (2004); Pasteris and Ding (2009); Tsuda and Arends (1993); Yu et al. (2007).

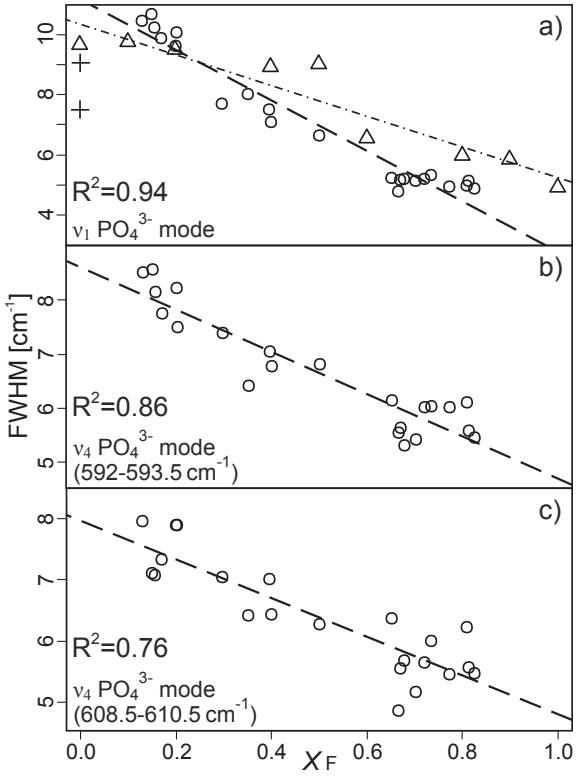

Figure 24: Full width at half maximum (FWHM) compared to the apatite´s anion composition X_F (X_F=F/(F+Cl+OH)). Data: this study (circles); F-Cl apatites (open triangles) by O'Donnell et al. (2009); OH apatites (crosses) by Pasteris et al. (2004); Pasteris and Ding (2009).

the phosphate modes in the region between 1100 cm^{-1} and 1050 cm^{-1} and found good correlations with the fluorine and chlorine contents. Zattin et al. (2007) used the Raman shift of two phosphate modes (~448 cm^{-1} and ~1048 cm^{-1}), measured parallel to the c-axis, and described acceptable correlations with the chlorine contents. Pasteris and Ding (2009) investigated nanocrystalline, biological apatite and observed a nonlinear shift of the 960 cm^{-1} between the end-members hydroxylapatite and fluorapatite. On the contrary, in this study only linear trends for the correlation of the peak position with the anion stoichiometry are observed. The quality of the single correlations, which are demonstrated by the coefficients of determination (R^2), are varying quite significantly. Therefore, only some of them are suitable for an empirical calculation. Focusing on the R^2 values, a clear preference for the ν_1 phosphate mode is derivable. This is also reinforced by the addition of data gained by other authors (e.g. O'Donnell et al. (2009)) shown in Figure 23. The data of O'Donnell et al. (2009) shows clearly the same trend with the same gradient, but a slight offset to lower wavenumbers which is considered to be caused by differences in the calibration of the measurement equipment. Also the FWHM's of the peaks were correlated with the anion stoichiometry, for comparison. In general, the coefficients of determination (R^2) are lower than those for the peak positions, because the peak spreading is fraught with higher uncertainties during the deconvolution method where the widths of the single peaks are modified to gain the highest correlation of the sum-curve with the measured values. Nevertheless, negative trends to lower peak widths with rising fluorine contents can be observed for each peak of the Raman spectrum. Similar to the peak positions, only some of the FWHM data sets are suitable. Three of them with the highest coefficients of determination (R^2) are shown in Figure 24 and also here the ν_1 mode shares the highest R^2 values. The peak splitting of the ν_1 mode occurring in OH apatites has little effect because the absolute intensities of the two peaks are varying significantly, whereupon the deconvolution results for the main peak are only slightly influenced.

3.6.3. Empirical calculation

For simplicity, only the peak position and the FWHM data of the ν_1 phosphate vibration mode were used to establish an empirical formula, to estimate the significance of the gained results and to verify the general use of the method, in a first step. To improve the fitting results of the empirical formula and to dispel concerns about the measurement accuracy of the Raman equipment, several data sets for peak positions and FWHM's were applied in a second step, whereby very high coefficients of determination (R^2) were reached.

3.6.3.1. Using the ν_1 phosphate vibration mode The data of De Mul et al. (1986); O'Donnell et al. (2009); Pasteris et al. (2004); Pasteris and Ding (2009); RRUFF (2011); Tsuda and Arends (1993); Yu et al. (2007) was included in this study for correlation (Fig. 23 and 24), because the sample set investigated does not contain apatites with an pure endmember composition (i.e. pure F, Cl or OH apatites). The peaks of pure OH-apatites, pure Cl-apatites as well as apatites with intermediate Cl-OH compositions (e.g. $Cl_{0.69}OH_{0.29}F_{0.02}$), but with very low F contents, share more or less the same ν_1 peak position and FWHM. Consequently, a differentiation between chlorine- and hydroxylapatite

is not possible, because there is no difference between the influence of the two elements (Cl and OH) on the Raman-active phosphate modes. However, the presence of OH-vibrations (3500-3600 cm^{-1}) can be used to distinguish hydroxylapatite. Nevertheless, the excellent correlation of the substitution between fluorapatites on the one hand and chlorine-hydroxyl apatites on the other hand is preserved. This is expressed in the peak shift versus X_F (X_F=F/(F+Cl+OH)) diagram (Fig. 23a). This relationship is confirmed by the similar crystallographic cell parameters of chlorine- and hydroxylapatites, shown in Table 3, causing the same environmental conditions for the phosphate molecules and their vibrational modes. The nonlinearity in band position, as ascertained by Pasteris and Ding (2009), may be caused by a spurious correlation evoked by spectra worsening. They used biological materials (i.e. horse's and shark's teeth) where a decrease of the fluorine content was accompanied by a decline of the spectra quality due to biological parameters (i.e. base to the top of the tooth). Nonlinearity can be excluded for the samples investigated. When the FWHM's of the ν_1 peaks are correlated to the stoichiometric composition X_F, stronger scattering occurs compared to the peak position plot (Fig. 24). This scattering is emphasized by comparing the gained data with data from the literature. In contrast to analyses gained in this study, the F-Cl apatites of O'Donnell et al. (2009) show another gradient and the linearity of the trend is not well assured. The values for OH apatites, recorded by Pasteris et al. (2004), do not fit the data gained in this study, although Pasteris et al. (2004) pointed out that their investigated hydroxylapatites were influenced by a lack of OH widening the ν_1 P-O phosphate peak. Therefore, the FWHM of the pure OH apatites should be at least as high as the Cl-OH apatites of this study and not lower as they appear. In general, the comparison of FWHM data is more difficult, because varying Raman equipment setups and uncertainties in the deconvolution treatment cause modifications of the peak width. The apatites of this study comprise a clear linear trend with a high coefficient of determination (R^2) and, therefore, it can be taken in consideration for empirical calculations. Based on the differences between the data of this study and the values of the other authors, arising from discrepancies in calibration, only the data of this study was used for the empirical calculation. This is acceptable, as it is already proven that only linear trends occur and the data of this study features a sufficient compositional spread.

Significance tests The significance of the observed correlations as well as the confidence interval of the single data pairs XF, peak position and FWHM have to be determined. For this purpose the Pearson´s correlation method was used and a bivariate normal distribution was assumed. This assumption is valid for the empirical calculation because only two measured values, (i.e. Raman and EMPA results for the anion composition of the individual apatites) are compared independently from the absolute values of their actual compositions. This hypothesis is confirmed, as long as the residuals of the analyses are normally distributed over the whole compositional range. This can be proved by repeated measurements (three times for each mineral). In contrast to this, when properties themselves are compared (e.g. fluorine versus chlorine contents), the bivariate normal distribution should be rejected, because this is very unlikely for features of accessory minerals in nature. The resulting Pearson´s correlation factors are ranging between 0.97 to 0.99 and each of the correlations are highly significant (Tab. 4).

Table 4: Pearson´s correlation, Spearman rank correlation coefficients and Coefficients of Determination (R^2) for peak position (PP), full width at half maximum (FWHM) and stoichiometric composition X_F (X_F=F/(F+Cl+OH)) (EMPA) of the ν_1 phosphate mode main peak.

Pair	Pearson	Spearman	R^2
X_F-PP	0.98 ***	0.85 ***	0.97
X_F-FWHM	-0.97 ***	-0.91 ***	0.94
PP-FWHM	-0.99 ***	-0.90 ***	0.96

The stars are indicating the high significance of the single test routines.

To verify this result also the non-parametric (distribution-free) Spearman rank correlation method was used which also produced high correlation values (0.85 to 0.91) and high significances reinforcing the applicability of the data gained. Table 4 shows the calculated values. Comparing the factors it becomes obvious that only the Spearman rank correlation method produces lower values for the peak position versus X_F in comparison to the FWHM. This is caused by the compositional scatter around X_F=0.75 and the rank sensitivity of the method. In order to avoid the definition of the more appropriate factor for the chemical characterisation, both factors, the peak position as well as the FWHM, have to be taken in consideration for further calculations. The Pearson´s correlation with the tolerance ellipse is shown in Figure 25. The tolerance ellipse representing the 97.5% quartile of the Chi-square distribution follows the high significance of the Chi-square test. The significance area, which is enclosed by the tolerance ellipse, covers approximately peak positions between 961 and 969 cm^{-1} and FWHM values between 1 and 13 cm^{-1}. These limiting values lie beyond the physically possible values of the end members. This confirms the applicability of the empirical formula over the entire range of calculation. This diagram (Fig. 25) is also representative for the single, high significant correlations between the two data sets and the apatite´s anion composition X_F (X_F=F/(F+Cl+OH)). The high correlation coefficients as well as the high significances confirm the legitimacy of the multivariate regression calculation.

Multivariate regression In order to take both factors into consideration (i.e. the peak position as well as the FWHM), a multivariate regression method was applied for the calculation. This method enables the use of several independent variables, such as peak position and FWHM data of different peaks. In this case, the peak position and the FWHM of the ν_1 phosphate modes are the independent (explanatory) variables and the stoichiometric composition X_F (X_F=F/(F+Cl+OH)) is the dependent (to be predicted) variable. The resulting regression plane, visible as reticulate area in Figure 26, was calculated to illustrate the relationship. The positions of the single points show the deviation between the actually measured value for X_F (EMPA) and the calculated values on the regression plane (residuals). The empirical formula was calculated using the peak posi-

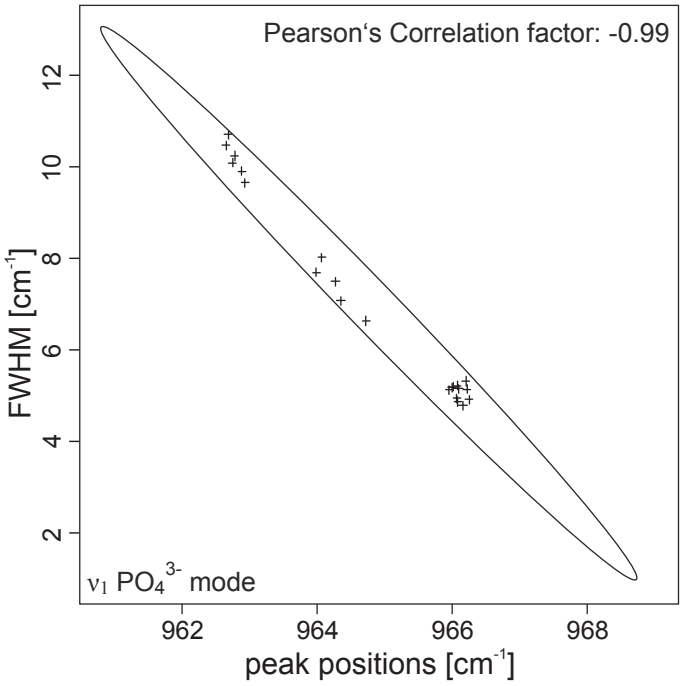

Figure 25: Pearson's bivariate correlation between the peak position and FWHM of the ν_1 phosphate mode. The tolerance ellipse represents the 97.5% quartile of the Chi-square distribution.

tion (PP) and the full width at half maximum (FWHM) of the ν_1 phosphate mode as the predictors, in terms of $y = \beta_1 + x_1\beta_2 + x_2\beta_3 + ... + x_n\beta_n$, resulting in (1)

$$X_F = 0.16354 * PP - 0.005464 * FWHM - 157.24401 \quad (1)$$

With this formula the stoichiometric composition (F vs. Cl+OH) of the apatite can be calculated, using the peak position and the FWHM of one single peak of the Raman spectrum, i.e. the main peak of the ν_1 phosphate mode. For verification, the calculated, fitted values are compared to the microprobe measurements of the stoichiometric composition (X_F). The result shows a high quality of the fit as well as high correlation factors and significances. The Pearson, the Spearman as well as the Adjusted R^2 correlation coefficients are 0.98, 0.86 and 0.96, respectively. In particular the Spearman factor is higher than for the single correlation of the peak position (Tab. 4). This confirms the use of a multivariate regression for the calculation. Another advantage of applying two predictors is the lower sensitivity to single outliers. In addition, the FWHM is generally not so sensitive to calibration errors, because it is independent from the peak´s position.

Verification of the multivariate regression During the significance tests a bivariate normal distribution was assumed because only measured values for the same property were compared. This assumption can be checked utilizing normality tests for the residual values of the multivariate regression calculation. This was accomplished using the methods quantile-quantile Plot (QQ Plot) and a density plot with fitted normal distribution graph,

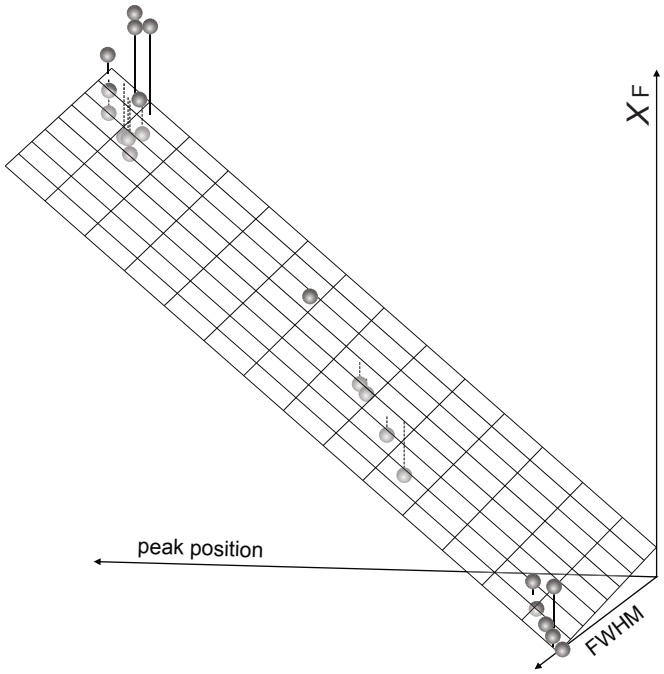

Figure 26: Multivariate regression between the peak position (PP) and the full width at half maximum (FWHM) as the independent variables and the apatite´s anion composition X_F (X_F=F/(F+Cl+OH)) as the dependent variable.

illustrated in Figure 27. Both tests illustrate the high confidence level of the multivariate regression, the high similarity to a bivariate normal distribution of the residuals and the quality of the obtained empirical formula.

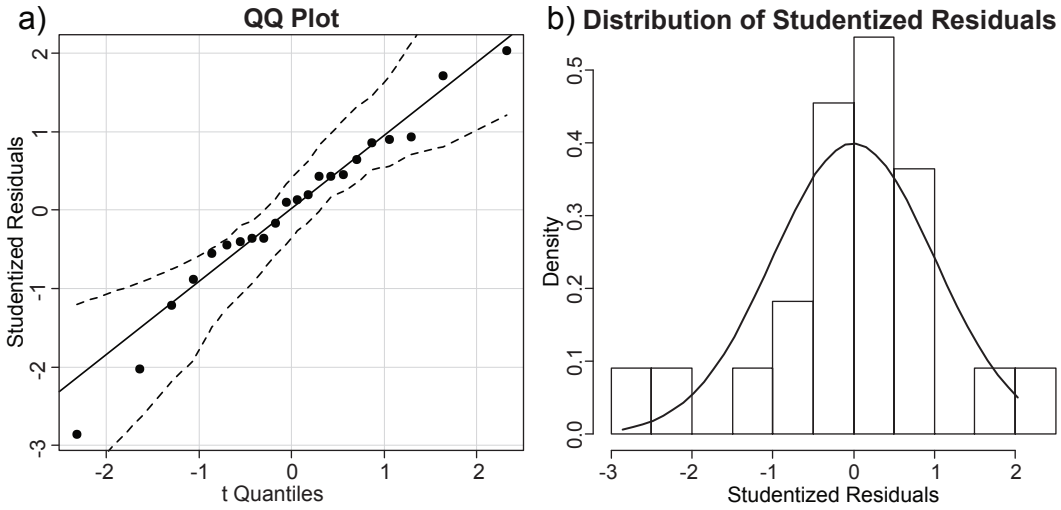

Figure 27: a) Quantile-Quantile Plot for the Studentized residuals of the multivariate regression calculation. Dashed lines represent the 95% envelope. b) Density plot for the Studentized residuals with fitted distribution graph.

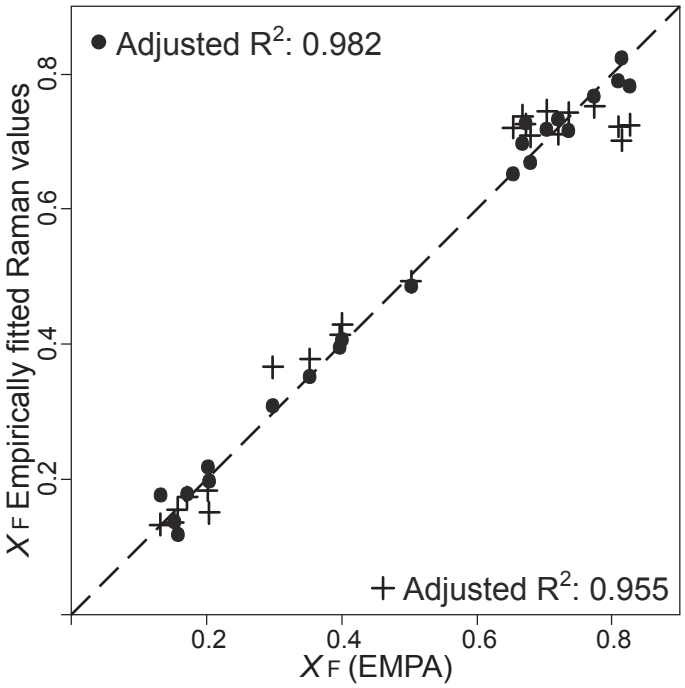

Figure 28: Anion composition (X_F=F/(F+Cl+OH)) EMPA data in correlation with the empirically calculated values. Crosses: Fitted values ascertained using formula 1. Circles: Strongly improved R^2 ascertained using the predictors of Table 5.

3.6.3.2. Using five peak positions and six data sets of FWHM The quality of the fitted data, expressed by the correlation between the compositions gained by Raman and microprobe analyses, can be further improved by the addition of data for the multivariate regression calculation. Five Raman data sets for peak positions and six data sets for FWHM were taken as the maximum number of independent variables. With this extensive record, Adjusted R^2 correlation coefficients up to 0.982 were reached between EMPA and Raman regression fitted anion values (Fig. 28). This illustrates the high precision of the multivariate regression method. The enhanced empirical formula can be expressed by the predictors shown in Table 5.

3.6.4. General use of the method

Raman spectroscopy, in combination with the obtained empirical formula to calculate the chemical composition, is an eminently suitable method for compositional analyses of apatites. The empirical formula, shown in equation (1), describes the samples of this study well. However, looking at the data of O'Donnell et al. (2009) in Figure 23, the discussed offset of their values has a great influence on the calculation. Insufficient calibration may cause strongly varying results. Therefore, the whole procedural method has to be used for each new measurement project. The procedure can be described as: 1) Calibration of the Raman equipment with neon or argon lines. Actually, an absolute calibration of the

Table 5: Predictors of the enhanced empirical formula. The values noted next to the predictors describe the intermediate peak position of the used data.

Predictors cm^{-1}	Estimate
(Intercept)	-133.17323
PP-964	0.20824
PP-593	-0.04233
PP-582	-0.21313
PP-447	0.03114
PP-432	0.15746
FWHM-964	0.00799
FWHM-618	-0.00978
FWHM-609	0.06614
FWHM-593	-0.07723
FWHM-582	-0.04104
FWHM-448	0.01462

wavenumbers is not necessary, as long as the equipment runs stable over the measurement period. This simplification is permitted because the multivariate regression deals with absolute numbers. 2a) Either measurement of apatite standards with end-member compositions to construct a two-point multivariate linear regression model using all phosphate modes of the single endmembers. This is possible because their linear behavior is proved by this study several times. 2b) Or chemical analyses of at least 20 apatites using alternative methods, i.e. EMPA. The required population is depending on the compositional spread between the approximate endmember compositions; minor spread calls for more samples. 3) Raman spectroscopic analyses adjacent to the microprobe measurement spots and randomly distributed over the apatite's surface. At least three analyses for each grain are necessary to preclude outliers. 4) Deconvolution of the phosphate vibration modes to evaluate the peak positions as well as the FWHM's. 5) Review of data using significance tests and prediction of the confidence interval of the whole data set 6) Calculation of the multivariate regression and establishment of the empirical formula. 7) Verification of the fitted values in comparison with the alternatively measured data.

3.7. Conclusion

The relationship between the three endmembers fluorapatite, chlorapatite and hydroxylapatite and the influence of F versus Cl plus OH in solid solution is verified by Raman spectroscopy. There is an excellent correlation, provided by the Raman measurement, between fluorapatites on the one hand and chlorine-hydroxyl apatites on the other hand. A direct differentiation between chlorine- and hydroxylapatites is not possible via this method, but they can be distinguished on the presence of OH vibration modes in the Raman spectra. Accurate predictors of the chemical composition are provided by the phosphate vibration modes of the apatites. Only by using the peak position and the full width at

half maximum of the ν_1 phosphate mode, a fast method using a simple empirical formula for approximate prediction of the anion composition can be established. In general, each Raman-active vibration mode provides a predictor for the anion stoichiometry as long as the correlation with the chemical composition is sufficient. Each of the observed correlations, whether positive or negative, clearly show linear trends. If further data is collected, the accuracy of the invented method can be strongly improved. In this study a very high correlation between EMPA and Raman regression fitted data was achieved, using five Raman data sets for peak positions and six data sets for FWHM. This large data volume enables a high accuracy in the prediction of the chemical composition. The results of the calculations accomplished, are legitimized by high significances of the assumed linear relationship as well as by the high correlation coefficients of the multivariate regression. The bivariate normal distribution, necessary for the use of a multivariate linear regression calculation, could be established beyond any doubt. The same procedure is also feasible for other minerals and materials where a chemical change is influencing the Raman-active vibration modes. Due to the high susceptibility to errors caused by calibration and measurement biases, the empirical formula has to be calculated new for each new measurement project. In general there is no need for a linear correlation, when using multivariate regression methods, as long as a mathematically interpretable relation between the chemical composition and the Raman behavior exists. The advantages of this method are: i) the easy and fast applicability compared to other methods, i.e. EMPA, because there is no need for a special treatment of the samples. ii) Even very small minerals (down to 2 µm in diameter) can be measured. iii) This facilitates a great area of application in research going beyond the area of mineralogy and petrology, such as biological studies (e.g. dental and bone investigation: De Mul et al. (1986); Nishino et al. (1981); Rehman et al. (1995); Tsuda and Arends (1993)), paleontology (e.g. fossilised teeth: McKeegan et al. (2007); Pasteris and Ding (2009)) and medicine (e.g. cancer research: Haka et al. (2002)).

4. Evaluation of fluids related with the formation of the Ultramafic Pipes within the Ivrea-Verbano Zone; Based on REE and anion composition (F, Cl, OH) of apatites

4.1. Abstract of this section

On the basis of a joint interpretation of the halogen composition (F, Cl, OH) together with the trace element contents (REE, U, Th, Y), the geochemical processes which occurred in the lower crust - upper mantle region in the system liquids - fluids - mineral (apatite) during the genesis of the Ultramafic Pipes were identified by this study. It becomes evident that at least the fluids, if not the liquids (i.e. different magmas), in the frame of the magmatic systems, forming the pipes, have to consist of multiple distinct phases which were presumably formed by demixing processes. This can be assumed, because apatites with the apparent anion and trace element composition are not common for magmatic systems that are affected by common mantle-metasomatic fluids. There is strong evidence, that magmatic fluids have exsolved into different phases (liquids and vapors) before one (or several) of them, rich in OH and poor in Cl and CO_2, interacted with the IVZ pipes. In general it becomes evident that the fluids as well as the melts are exclusively mantle derived within the Mafic Complex and an influence by the overlying metasediments of the Kinzigite Formation can be neglected.

Based on both, the anion composition, a well as the trace element contents of the hosted apatites, the Bec d' Ovage pipe can be clearly distinguished from the other localities. It is assumed that this pipe was at least influenced by fluids and therefore preserved the magmatic signatures best. Very similar genetical conditions can be assumed for the Valmaggia and the Fei di Doccio pipes where the magmatic conditions were moderately influenced by an interaction with OH rich and Cl poor fluids. For the Castello di Gavala pipe it is supposed that the apatites experienced the comparatively strongest fluid impact, which is demonstrated by elevated Cl and REE compositions. The conditions present during the formation of the Piancone la Frera pipe are interpreted as approximately similar to those prevailing during the ascent of the Valmaggia as well as the Fei di Doccio pipes.

These findings are of special importance when interpreting the Fe-Ni-Cu-PGE ore formation within the investigated Ultramafic Pipes.

4.2. Introduction

In the central part of the Ivrea-Verbano Zone (IVZ) pipe like ultramafic bodies with an alkaline signature occur at the localities: Bec d' Ovaga, Castello di Gavala, Valmaggia, Fei di Doccio and Piancone la Frera. The geological details are delineated in the General Geology chapter. Each pipe hosts base metal sulfide mineralizations (Fe-Ni-Cu-Platinum

group mineral (PGM) ores) which were economically mined in the past century. These mineralizations occur together with hydromagmatic mineral phases, like amphiboles, pholgopite and of course apatites. These hydromagmatic phases partly occur with pronounced modal abundances among the rock forming minerals which suggests a strong influence of coexisting fluids during the genesis of the different pipes. Therefore a mineralogical study of these minerals will give a proxy information on the composition of these fluids, a tool for genetic interpretations as well as a possibility for a specification and diversification of the different localities. The mineralogical investigations were focused on apatites and their geochemical substitution mechanisms on two different crystallographic positions. One of them is the apatites anion position where a substitution of F, Cl and OH may occur. The compositional analyses aimed on these substitution mechanisms, provide an integrated information on the hydro-magmatic system as well as an indirect measure of the salinity of coexisting fluids. The second structural position where detectable substitutions may occur is Ca position. The possible and investigated substitutes are rare earth elements (REE), U, Th and Y. Due to the high fractionation coefficient of these elements the single apatite compositions as well as the intermediate apatite compositions of the individual localities provide extensive information for the prevailing environmental conditions during the formation of the pipes. Furthermore a differentiation between the single pipes becomes possible. For example, it can be clarified whether, an interaction between the intruding ultramafic melts and the country rock, which could have influenced the geochemical signatures, took place, or not. The joint interpretation of the halogen composition (F, Cl, OH) together with the trace element contents (REE, U, Th, Y) is therefore a powerful tool which allows an identification and clarification of geochemical processes which occurred in the lower crust - upper mantle region in the system liquids - fluids - mineral (apatite) during the genesis of the IVZ pipes. Furthermore the results can be taken for further interpretation of the fluids related with the formation of the Fe-Ni-Cu-PGM sulfide mineralizations.

4.3. Material and Methods

4.3.1. Samples

Around ten samples of each ultramafic pipe at Bec d' Ovaga, Castello di Gavala, Piancone la Frera, Valmaggia and Fei di Doccio were selected and polished sections prepared for microscopic and microanalytical studies.

Based on microscopic investigations, two to three samples from each locality with a sufficient amount of apatites were selected. From the polished sections chosen, 30 to 42 single apatite grains were analyzed from each locality, except from Piancone la Frera, where 9 analyses could be obtained due to a limited number of apatites.

4.3.2. Electron microprobe measurement

The electron microprobe analyses were conducted at the "Eugen F. Stumpfl Laboratory" at the Department of Applied Geosciences and Geophysics, University of Leoben (Austria) using a Jeol JXA 8200 Superprobe. The accelerating voltage was set to 20.0 kV and the probe current was adjusted to $5*10^{-8}$A. With the aid of wavelength-dispersive X-ray

spectroscopy (WDX) the following elements were analyzed: Mg, Al, Ca, Si, P, F, Y, Dy, La, Th, Sm, Ce, Fe, Tb, Pr, Cl, Gd, Nd, Eu, Ho, Tm, Er, Yb, Lu, U and Ti.

4.3.3. RAMAN measurement

The Raman analyses was accomplished to verify the occurrence of CO_3^{2-} within the apatites. The analyses were conducted at the Department of Applied Geosciences and Geophysics, University of Leoben (Austria) using a LABRAM (ISA Jobin Yvon) instrument with a frequency-doubled 120mW polarised 532.2nm Nd-YAG laser. To exactly evaluate the spectral record the raw data was treated using the software package PeakFit v.4.12 (SeaSolve (2003)). With the aid of this software the occurring fluorescence was eliminated and the baselines were corrected by subtraction.

4.4. Results

4.4.1. Halogen concentrations

Overall 154 single apatite grains of the five pipes of Bec d' Ovaga (n = 39), Castello di Gavala (n = 30), Valmaggia (n = 34), Fei di Doccio (n = 42), Piancone la Frera (n = 9), were analyzed (Appendix C). In general, all the analyzed apatites are dominated by OH and the halogen contents are comparably low, as illustrated in in the F-Cl-OH-triangular diagram (Fig. 29). The analyses of this stidy are compared with those from various igneous complexes and a partly overlap with apaptites from the Great Dyke and Ora Banda (data from Boudreau (1993)) becomes obvious, wheras apatites from the Stillwater and Bushveld complex and those from the Muni Muni complex are compositionally different (Fig. 29). Apatites of the Bec d' Ovaga pipe are an exception. They are defined by nearly pure fluorine-endmember compositions and almost lack Cl concentrations. The Castello di Gavala apatites display a counterpart to the Bec d' Ovaga samples, as they host the Cl richest and the F poorest apatites. The Piancone la Frera as well as the Castello di Gavala pipe host the OH richest apatite assemblages. Between the mentioned counterparts, the pipes of Valmaggia and Fei di Doccio are characterised by intermediate apatite compositions (Fig. 29). The Valmaggia apatites are comparably Cl rich and OH poor, whereas the apatites of the Fei di Doccio pipe show the second lowest Cl values.

The narrow distribution of the Fei di Doccio apatites is remarkable, particularly when regarding the relatively high sample number (n = 42). Thus, the narrow compositional range can be considered highly significant. In contrast, the narrow distribution filed of the Piancone la Frera apatites may be interpreted to be mainly caused by the low amount of analyses (n=8).

With the aid of bivariate box plots, the distribution of the analyzed halogen compositions were examined to determine reliable intermediate values for the comparison of the different localities. The results of these evaluations are shown in Figure 30 whereas the center values describing the intermediate compositions are noted in the text. The distribution of the analyzed halogen compositions of the apatites of Bec d' Ovaga, Castello di Gavala and Fei di Doccio can be described as normal-distributed concerning both, the F as well as the Cl contents. The distribution of the Valmaggia apatites shows some skewness which is caused by the higher density of high F and low Cl apatites in respect to low

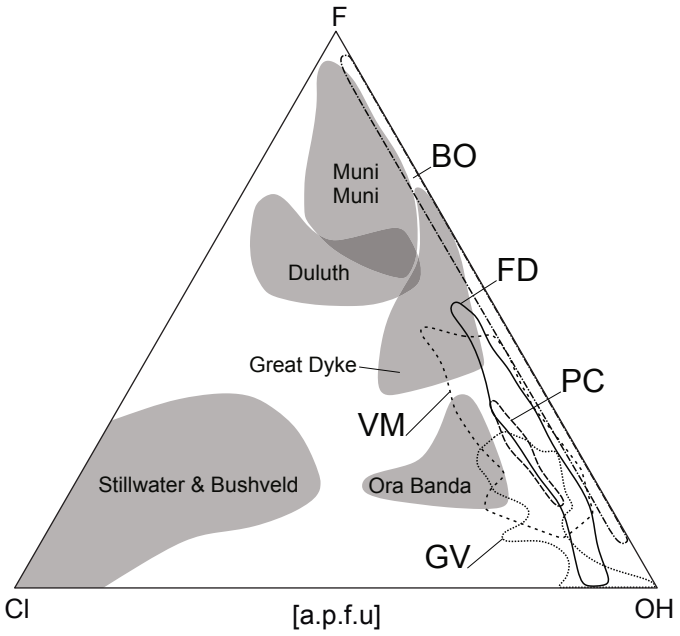

Figure 29: Halogen composition of the analyzed apatite grains. Localities: Bec d' Ovaga (BO); Castello di Gavala (GV); Fei di Doccio (FD); Valmaggia (VM); Piancone la Frera (PC). Apaptite compositions of various other igneous intrusions, taken from Boudreau (1993) are shown in shaded areas for comparison

F and high Cl apatites. Apart from the relatively low sample number, also the halogen compositions of the Piancone la Frera apatites show an approximate normal distribution. In general the number of outliers is low, with a maximum number of two found in the distribution of the Valmaggia apatites.

Consequently, the pipes can be classified on the basis of their halogen contents of the apatites: The median values of the Bec d' Ovaga apatites (Cl: 0.0098 a.p.f.u F: 0.6098 a.p.f.u) indicate the Cl poorest and the F richest assemblages among the five localities. Additionally the corresponding OH compositions (0.3803 a.p.f.u) are the lowest determined. The Fei di Doccio (Cl: 0.0587 a.p.f.u, F: 0.2955 a.p.f.u, OH: 0.6457 a.p.f.u) as well as the Valmaggia apatites (Cl: 0.0618 a.p.f.u, F: 0.3300 a.p.f.u, OH: 0.6082 a.p.f.u) exhibit quite similar mean compositions, whereas the distribution of the Valmaggia apatites is influenced by the discussed skewness. The Castello di Gavala pipe hosts the OH (0.7353 a.p.f.u) as well as the Cl (0.1025 a.p.f.u) richest apatites whereas the F contents are remarkably low (0.1622 a.p.f.u). The composition of the Piancone la Frera apatites plot in the intermediate field (Cl: 0.0875 a.p.f.u, F: 0.2601 a.p.f.u, OH: 0.6524 a.p.f.u) which are resembling the Fei di Doccio as well as the Valmaggia apatites, whereas the low sample number (n=9) has to be taken in consideration.

4.4.2. REE concentrations

The single REE analyses are varying at several orders of magnitude (see Apendix C). These strong variations exist both, between the samples of the single deposits, and between the single apatite grains of the individual samples. To smooth these variations and to

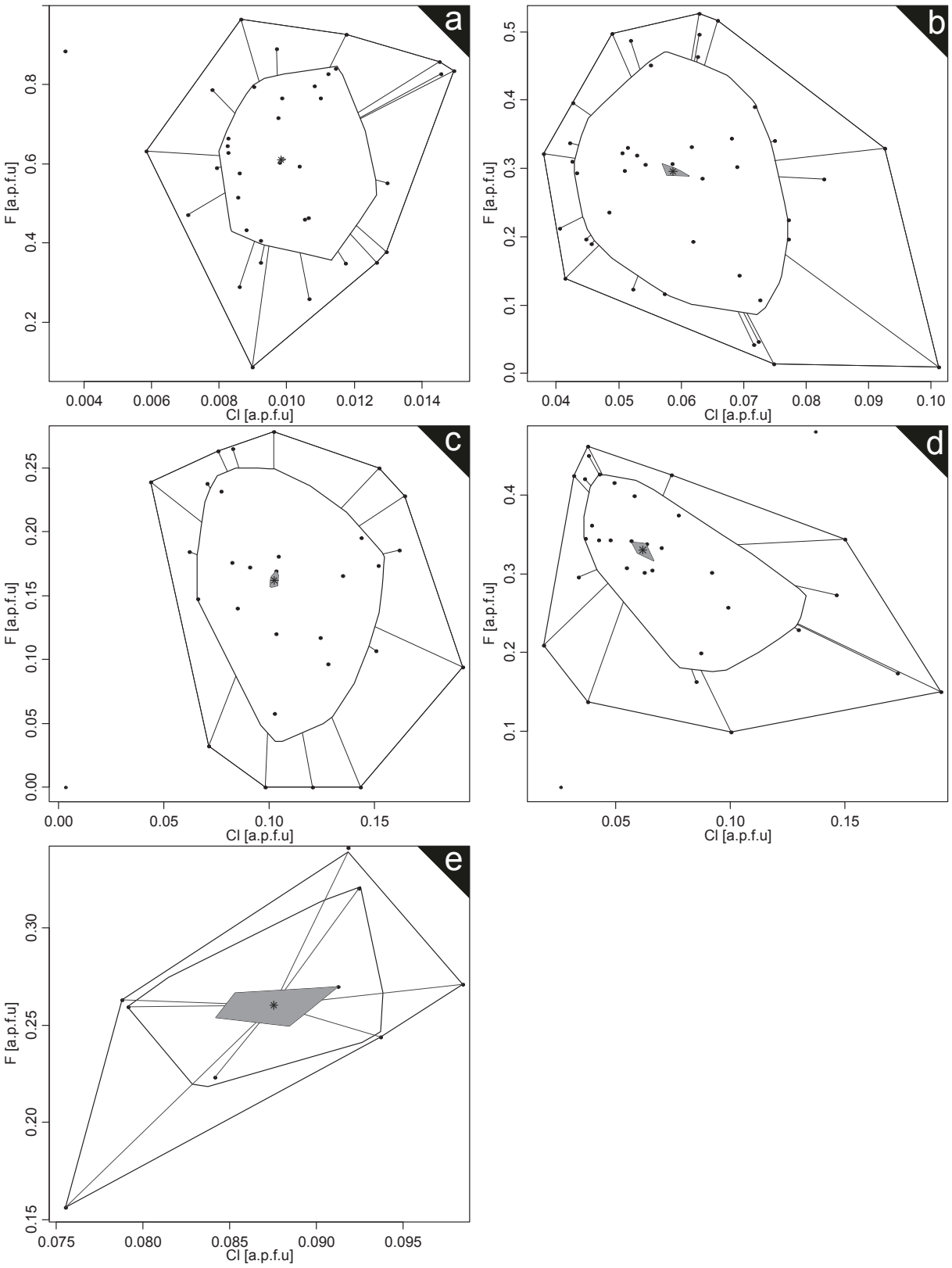

Figure 30: Bivariate Boxplots of the F and Cl values of the different localities. Localities: a) Bec d' Ovaga; b) Fei di Doccio; c) Castello di Gavala; d) Valmaggia; e) Piancone la Frera.

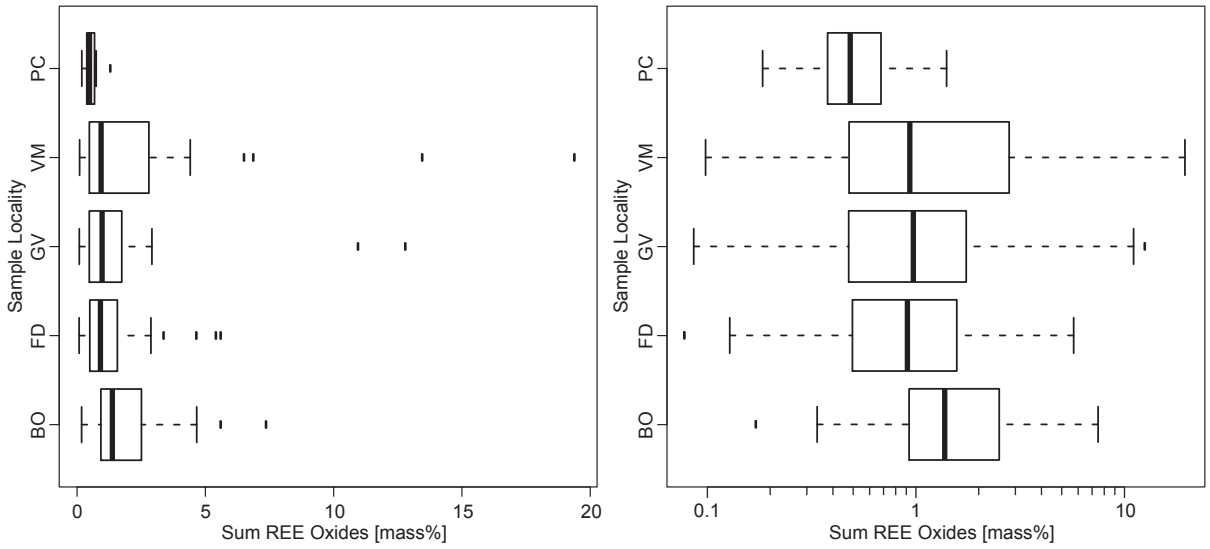

Figure 31: Box Plots of the sum of the apatite REE Oxide mass proportions (Σ REE). a) linear scale of mass% b) logarithmic scale of mass%. Localities: Bec d' Ovaga (BO); Castello di Gavala (GV); Fei di Doccio (FD); Valmaggia (VM); Piancone la Frera (PC).

evaluate the general distribution of REE in the analyzed apatite assemblages, in a first step, the sums of REE as oxides (La_2O_3-Lu_2O_3; Σ REE) were calculated and compared. To estimate the shape and style of the distributions the Σ REE contents were examined using box-plots (Fig. 31a). Already at the first glance, the strongly differing absolute sum values of the single analyses as well as the pronounced skewness of the distribution becomes obvious. Therefore normal distributions must not be assumed for any of the examined sample populations. Because of this appearance, it is statistically incorrect to use standard arithmetic mean or median values to describe the intermediate Σ REE contents of a sample set, in the case of this study, the different localities. However, this is carried out by many authors with insufficient statistical knowledge. To find an appropriate value the following procedure was chosen: In a first step the data was log-transformed whereupon almost log-normal distributed Σ REE values were obtained, as illustrated in Figure 31b. The Box plots (Fig. 31b) show that the log-normal median values are almost centered within the inter-quartile ranges. The applicability of this method is reinforced by the evidence, that similar log-normal distributions are illustrated by each sample set deriving from the different pipes, regardless of the sample number or the absolute median values. Additionally the lower and upper Whiskers follow a log-normal trend and the number of outliers is generally below one. To verify the assumed normal-distributions, a statistical test method was applied. The graphic Normal-QQ-plots, illustrated in Figure 32, confirm that log-normal distributed concentrations of the Σ REE oxides can be assumed, when the amount of samples is sufficient. The reliability of this method is graphically shown by the inclusion of each data point by the 95% confidence interval envelopes (Fig. 32). Additionally the normal distributions are statistically proved by passed Shapiro-Wilk normality tests.

The Σ REE budget of the different pipes is varying relatively strong. The highest contents are measured in the apatites of the Bec d' Ovaga pipe. The log-normal median

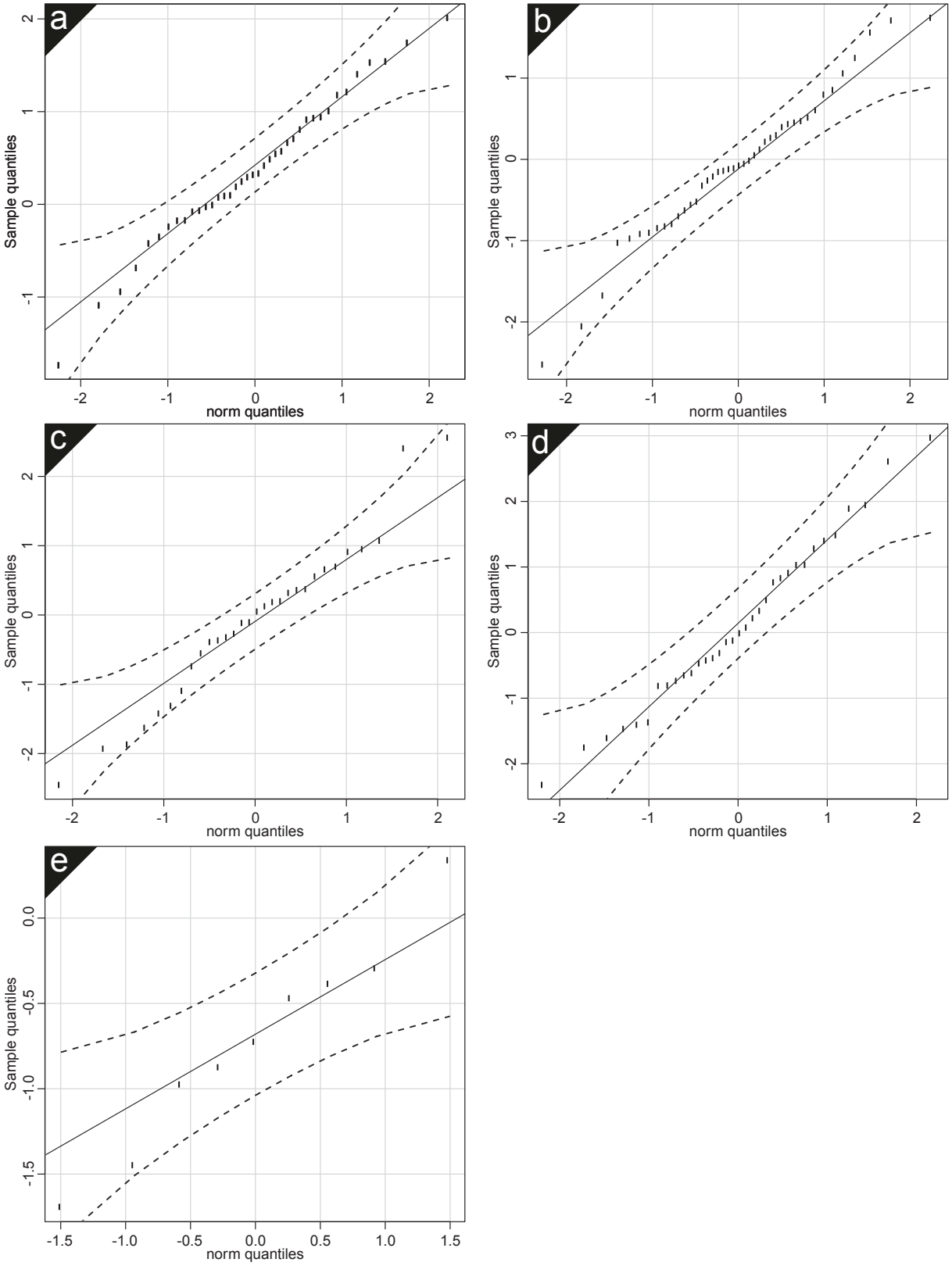

Figure 32: Normal QQ-plots of the sum of the apatite REE Oxide mass proportions. Localities: a) Bec d' Ovaga; b) Fei di Doccio; c) Castello di Gavala; d) Valmaggia; e) Piancone la Frera.

composition is 1.37 mass%, the standard deviation is relatively small and low concentration outliers are few. The second highest intermediate concentrations were ascertained in the Castello di Gavala pipe (median 0.97 mass%), whereas the interquartile range is relatively wide. The Valmaggia apatites show an elevated upper quartile concentration which indicates a relatively high amount of strongly enriched apatites. However the median of the general distribution lies in the intermediate field of the different pipes (median 0.93 mass%). Apart from the Piancone la Frera pipe with a low sample number (n = 9), the pipe of Fei di Doccio hosts apatites with the lowest Σ REE amounts measured within the sample set analysed (median 0.91 mass%). The log-normal distribution of the Fei di Doccio Σ REE contents is relatively narrow. Due to the low sample number of the Piancone la Frera pipe, the distribution of the Σ REE should be interpreted with care.

The log-transformation method is of particular importance, when the individual REE-element concentrations of the different localities are compared. The Sm concentration of the apatites of the Bec d' Ovaga pipe as well as the Ce contents of the Fei di Doccio apatites are representative for these characteristics and illustrated in Figure 33. The single REE contents exhibit logarithmic distributions throughout the whole data set. This behavior is clearly evident for the Sm concentrations of the Bec d' Ovaga apatites (Fig. 33 a) and the log-transformation yields clearly normal-distributed values (Fig. 33 b). Therefore, also the fitted normal-distribution, using a maximum-likelihood fitting of univariate distributions method, follows exactly the assumed distribution (Fig. 33 c). Not in each case the normal distribution of the log-transformed values are that distinct, as exemplary illustrated for the Ce contents of the Fei di Doccio apatites (Fig. 33 e). In this case the fitting method is of great importance because a statistically correct mean value can be estimated, as demonstrated in Figure 33 f. To avoid a subjective influence always the mean values with the according log-normal standard deviations of the statistically fitted normal distributions were taken for further investigations.

The single log-normal arithmetic mean values, resulting from the maximum-likelihood fitting procedures, are summarised in Table 6. These values were recalculated (Tab. 7) to facilitate the construction of chondrite-normalized REE-patterns (Fig. 34), in order to evaluate the general geochemical behavior of the different pipes. The chondrite values of McDonough and Sun (1995) were used for normalization. The average chondrite normalized enrichment factors of the individual REE are ranging between 10^3 and 10^4. The elements La, Ce, Pr and Nd, a part of the LREE, show the lowest enrichment factors, however, Sm exhibits the strongest accumulation within each individual pipe sample set. In general, the trends between the LREE and the HREE (La-Lu) are more or less flat without any pronounced gradient (Fig. 34). Strong anomalies of single elements are absent. The patterns of the single REE exhibit no distinctive differences between the five pipes and the trends follow the slight enrichment and depletion trends of almost each single REE. Additionally, the geochemical behavior of Y and the radioactive elements U and Th are illustrated in Figure 34. Compared to the REE contents, the Y concentrations of each locality are only slightly enriched without any exception and the differences between the pipes are relatively small. The chondrite normalized enrichment factors are ranging between 44 and 92. In contrast, the U and especially the Th contents are strongly enriched. The Th concentrations are reaching factors between $1.4\,10^4$ and $4.7\,10^4$ and U values between $8.7\,10^3$ and $1.6\,10^4$ which shows that Th is varying stronger.

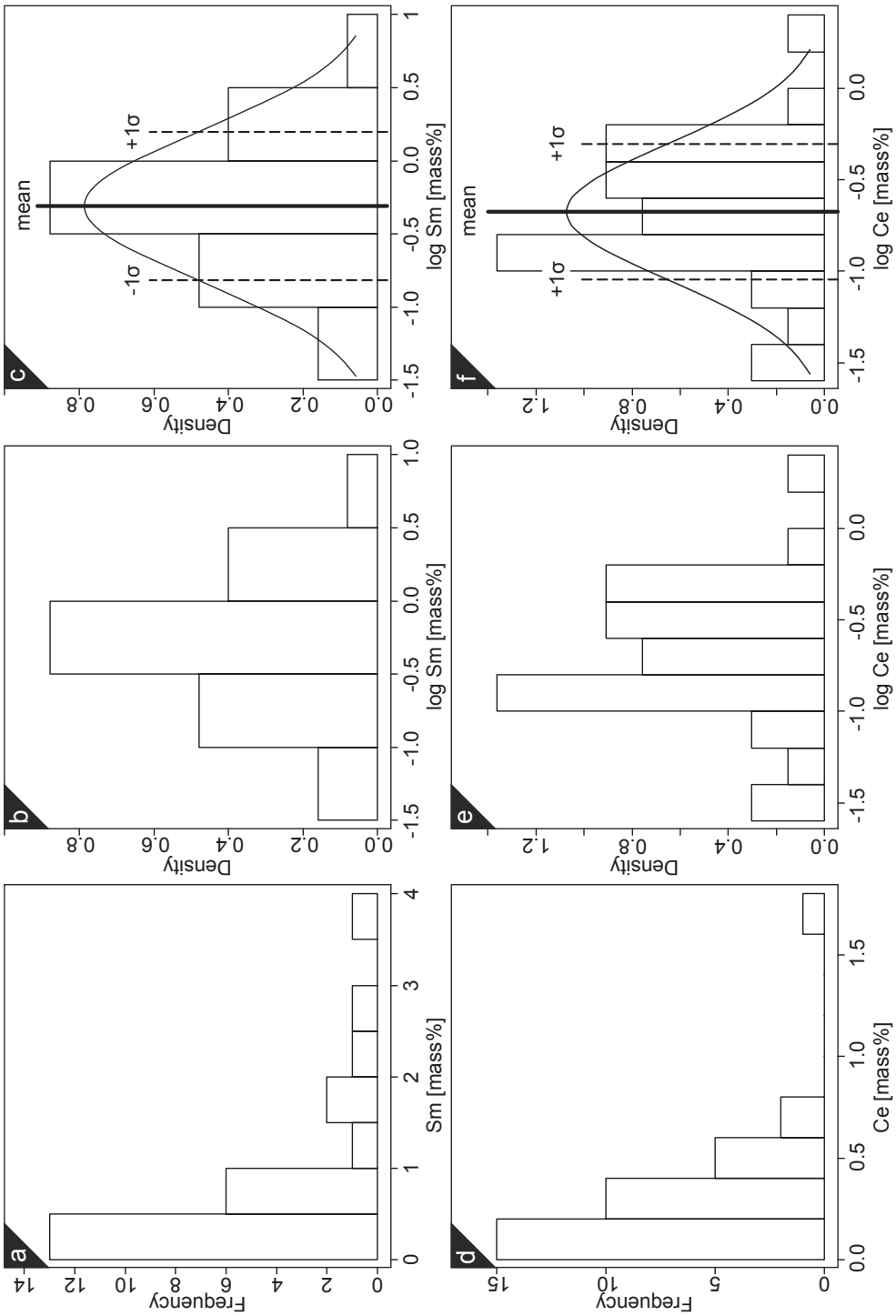

Figure 33: Log-transformation and distribution fitting method shown on the example Sm concentration of the apatites of the Bec d' Ovaga pipe. a) Standard density plot of the Sm concentration in mass%. b) Density plot with logarithmic Sm concentration. c) Density plot with fitted log-normal density line. The vertical lines depict the mean value with the according standard deviation. d), e) and f) similar plots for the Ce contents of the Fei di Doccio apatites.

Table 6: Log-normal mean composition with the according standard deviations of the fitted distributions for the values REE, Y, Th and U (in mass %). The apatites are grouped according to the localities.

	Bec d Ovaga n = 39		Fei di Doccio n = 42		C. di Gavala n = 30		Valmaggia n = 34		Piancone la F. n = 9	
	log m.%	log σ	log m.%	log σ	log m.%	log σ	log m.%	log σ	log m.%	log σ
La	-1.65	0.08	-1.42	0.11	-1.15	0.08	-1.40	0.06	-1.42	0.13
Ce	-0.80	0.12	-0.67	0.06	-0.88	0.09	-0.70	0.12	-1.50	0.12
Pr	-1.13	0.13	-1.28	0.12	-1.17	0.18	-0.97	0.17	-1.78	0.18
Nd	-0.87	0.15	-0.84	0.15	-0.84	0.15	-0.87	0.18	-1.18	0.23
Sm	-0.31	0.10	-0.65	0.12	-0.72	0.20	-0.48	0.13	-0.60	0.11
Eu	-1.22	0.14	-1.55	0.13	-1.21	0.17	-1.40	0.19	-1.82	0.03
Gd	-1.28	0.11	-1.34	0.12	-1.40	0.22	-1.20	0.17	-1.07	0.14
Tb	-1.29	0.15	-1.26	0.16	-1.49	0.16	-1.25	0.15	-1.82	0.22
Dy	-2.28	2.28	-1.25	0.21	-	-	-0.79	0.38	-	-
Ho	-1.63	0.11	-1.51	0.09	-1.49	0.14	-1.31	0.10	-1.39	0.09
Er	-1.90	0.20	-1.88	0.13	-1.88	0.19	-1.48	0.20	-2.08	0.21
Tm	-1.60	0.10	-1.53	0.07	-1.60	0.10	-1.39	0.07	-1.30	0.16
Yb	-1.34	0.18	-1.64	0.21	-0.86	0.47	-1.65	0.20	-	-
Lu	-1.49	0.28	-1.53	0.14	-1.69	0.29	-1.62	0.28	-	-
Y	-2.04	0.10	-1.99	0.08	-2.16	0.09	-1.84	0.07	-2.12	0.20
Th	-0.87	0.14	-1.38	0.11	-1.24	0.19	-1.28	0.21	-0.98	0.25
U	-2.07	0.08	-1.93	0.07	-2.18	0.06	-2.06	0.14	-2.19	0.18

The single mean values illustrated in Table 7 reveal some differences between the pipes. The high Σ REE concentrations of the Bec d' Ovaga apatites are mainly made up by high Sm contents. Additionally the HREE values of these minerals are comparably low with the exception of moderate Yb and Lu contents. Also relatively high Sm concentrations are found in the apatites of Valmaggia accompanied by high Ce and Pr contents. These apatites additionally exhibit the highest HREE contents compared to the other localities. The highest Ce concentrations are hosted by apatites of Fei di Doccio, whereas the remaining REE concentrations are in intermediate ranges, as also illustrated by the moderate Σ REE contents. The apatites of the Castello di Gavala pipe are characterized by high La, Eu and especially Yb contents, although the remaining HREE concentrations are comparatively low. The concentrations of the two high field strength elements (HFSE) of U and Th show a behavior different from the relationships between the REE concentrations. The U concentrations exhibit only slight variations between 64 and 118 ppm (log-normal mean values). The highest U mean concentration was analyzed in the Fei di Doccio apatites, whereas the absolute difference to the apatite U contents of the remaining deposits is low. Two groups of localities can be distinguished, on the basis of the the Th contents. The first group (Bec d' Ovaga pipe and Piancone la Frera pipe) is characterized by high Th contents of 1357 ppm and 1047 ppm, respectively. The second group (Valmaggia, Castello di Gavala and Piancone la Frera) exhibits lower and almost similar concentrations of around 500 ppm. The Y concentrations exhibit only slight variations with intermediate values between 69 and 144 ppm, whereupon no significant differentiation between the localities can be made.

Table 7: Mean composition of the fitted distributions recalculated from maximum-likelihood fitting of univariate distributions method. REE, Y, Th and U (in mass %).

	Bec d Ovaga n = 39 ppm	Fei di Doccio n = 42 ppm	C. di Gavala n = 30 ppm	Valmaggia n = 34 ppm	Piancone la F. n = 9 ppm
La	225	382	711	402	379
Ce	1587	2114	1311	2007	314
Pr	746	526	670	1063	166
Nd	1359	1456	1457	1340	667
Sm	4882	2220	1922	3336	2491
Eu	598	279	616	394	151
Gd	520	457	399	632	852
Tb	511	551	326	563	151
Dy	52	566	-	1639	-
Ho	236	309	320	487	404
Er	125	131	132	333	83
Tm	249	292	253	404	506
Yb	456	228	1370	226	-
Lu	323	297	204	239	-
Y	91	101	69	144	76
Th	1357	417	573	526	1047
U	84	118	66	87	64

4.5. Discussion

A number of petrological and genetic interpretations are provided by the halogen (F, Cl and OH) and REE compositions of the analyzed apatites. Furthermore, parameters, such as liquid - solid - fluid interactions, that may have played a significant role in the formation of the apatites, can be evaluated. Therefore, a detailed comparison of the IVZ pipe apatite composition of this study with mineralogical and geochemical data from the literature is accomplished in this following discussion. First of all, it should be stressed that the quality of the data, collected in this study, is confirmed by the normal distribution of the halogen analyses of each pipe sample set, together with the low amount of outliers. These two factors approve the analytical procedure, the sufficiency of the sample numbers, as well as the applicability of the accomplished analyses for geochemical investigations.

Geochemical information of the individual IVZ pipes was collected by Garuti et al. (2001) who proposed either an supra-subduction setting or an subcontinental mantle-plume system as the prevailing environment during the intrusion of the pipes. Garuti et al. (2001) preferred the latter, and assumed primitive subcontinental mantle metasomatic fluids that played the major role. The composition of these fluids was estimated to be rich in H_2O and CO_2, with significant P, S, F and Cl contents. This assumption is contradicted by the low Cl content and absence of CO_2 found in the apatites of this study.

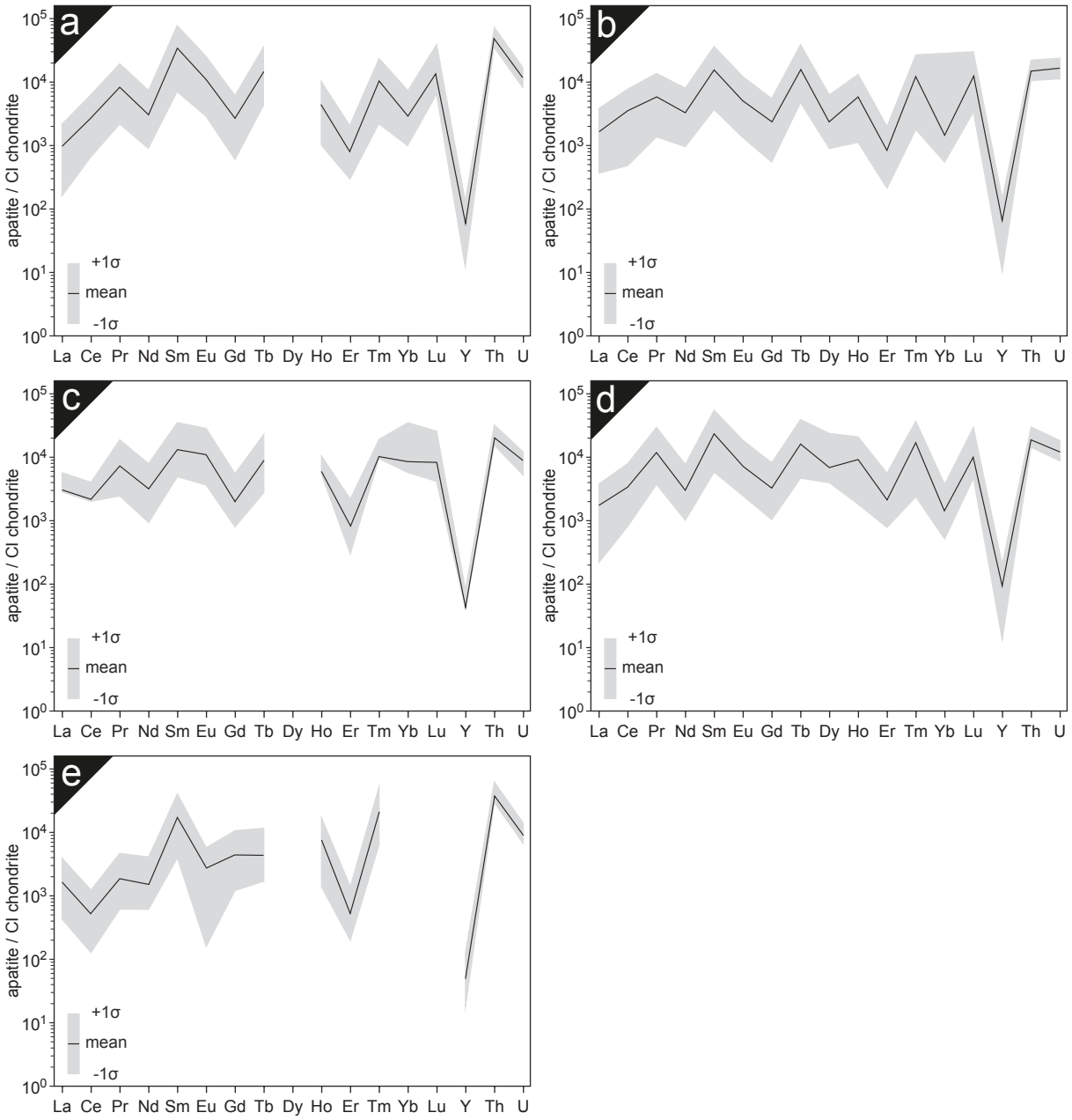

Figure 34: Chondrite normalized REE patterns with mean values produced by the maximum-likelihood fitting method shown in Table 7. Localities: a) Bec d' Ovaga; b) Fei di Doccio; c) Castello di Gavala; d) Valmaggia; e) Piancone la Frera.

To compare single data-sets and to discriminate different geochemical settings, influenced by a variety of interacting processes, the following discussion was divided according to different phenomena which are presumabely dominating the present compositions of the apatites.

4.5.1. General implications based on the halogen contents of apatites

The general geochemical behavior of phosphate bearing minerals was experimentally investigated by Watson (1980). On the basis of the ascertained high solubility of apatite in basic magmas it was concluded that residual apatite in the mantle is either not present, or occurs only in very low amounts in a H_2O bearing upper mantle residue. This was continuatively tested by Green and Watson (1982) for different magma compositions. They demonstrated that apatite saturation is strongly dependent on the SiO_2 concentrations in silicate melts. O'Reilly and Griffin (2000) investigated the general behavior of apatite in the Phanerozoic lithospheric mantle and concluded, that magmatic apatites are relatively F-rich, whereas metasomatically formed apatites are richer in Cl, in accordance with the results of Patiño Douce et al. (2011). Furthermore a low bulk Cl content of the mantle (around 3 ppm) is ascertained by several studies (Allègre et al., 2001; Burgess et al., 2002; John et al., 2010). Additionally, Marks et al. (2012) stressed the commonly low CO_3^{2-} content of magmatic apatites. Mathez and Webster (2005) studied the partitioning behavior of Cl and F between apatite, mafic silicate melt, and aqueous fluid, concluding that the D_{Cl} apatite/melt is 0.8 for a silicate melt containing less than 3.8 wt.% Cl. This means that Cl partitions preferentially into the melt, whereas F becomes relatively enriched in apatite, e.g. the D_F apatite/melt is 3.4 (Mathez and Webster, 2005). Similarely Boudreau et al. (1993) described apatite associations rich in the F endmember in cumulates derived from compositionally evolved magmas of the Munni Munni Complex (Western Australia). The general evolution of the magmatic system will result in a decrease of the Cl/F and OH/F ratios in the course of degassing of the magma and fractional crystallization (Boudreau et al., 1986), because of the higher ratios in the vapor compared to those in the melt and the lowest ratios found in the apatites. Therefore Boudreau and Kruger (1990) concluded, that Cl rich apatite compositions are mainly found, when a previously formed, magmatic apatite is re-enriched by a high Cl bearing fluid. However, sufficient halogen rich fluids can only be formed during magmatic evolution when a reasonably large magma chamber is present, i.e. a magma chamber volume of > 1000 km^3 (Boyce and Hervig, 2008) is required in order obtain a "thick" cumulate pile. These halogen rich fluids will migrate through the magma chamber, interact with allready crystallised magmatic apatite and might re-enrich the latter in chlorine. Brenan (1993) investigated the kinetics of fluorine, chlorine and hydroxyl exchange in fluorapatite and found out that the halogen chemistry of apatite is rapidly changing with coexisting fluids. The partitioning factor between fluid and silicate melt ($D_{Cl\ fluid/melt}$) is supposedly always positive between 4 and 14 (Alletti et al., 2009), independend on bulk concentrations, temperature and pressure. Consequently the the general occurrence of Cl rich apatites requires the interaction with Cl-rich hydrothermal fluids, also because extremely high Cl/F ratios are unknown in silicate melts (Boudreau et al., 1986). Boudreau and Hoatson (2004) reported a general positive correlation of the Cl/F ratios with the bulk rock Mg/(Mg + Fe) ratios from apatites of the Halls Creek orogen (East Kimberley, Western Australia). However,

variable Cl/F ratios in apatite were explained by the a combined processes of crystallization, degassing, and fractionation, producing interstitial silicate liquid and a volatile-rich fluid phase, the latter particularly changing the apatite composition.

The apatites of the Ultramafic Pipes studied are generally characterised by relatively high F and comparatively low Cl contents, variable in OH (Fig. 29) and lack of CO_3^{2-} (see chapter 3). According to the compositional characteristics of apatites occuring in magmatic systems, as summarised above, the apatites of the Ultramafic Pipes show general magmatic signatures, but indicate variable fluid overprint too. Furthermore, it can be concluded that the apatites derived from melts characterized by low Cl/(F+OH) ratios and that the fluids, involved in the formation of the pipes, were of low salinity. It is suggested that a limited interaction with internaly derived mantle fluids was responsible for compositional characteristics of the pipe apatites. The differences in the halogen compositions of the apatites can be explained as follows: The lowest fluid alteration is represented by the apatites of the Bec d' Ovaga pipe, as shown by almost F endmember composition and the lowest Cl contents. On the opposite the apatites of Castello di Gavala show the strongest fluid alteration indicated by comparatively high Cl contents. Intermediate fluid alteration can be suggested for the apatites of Valmaggia and Fei di Doccio. A totat reset of the magmatic signatures of the apatites did not take place, because the Ultramafic Pipes of the IVZ represent small intrusive bodies, beeing far away of a volume of 1000 km^3 as stressed by (Boyce and Hervig, 2008). Therefore, insufficient fluid was generated during their magmatic evolution (e.g. fractionation, crystallisation, degassing, etc.) in order to allow a stronger alteration of the magmatic apatites.

The apatites of the IVZ pipes, furthermore, are anomalously rich in OH (Fig. 29). A cryptic explanation of such apatite composition is given by Boyce and Hervig (2009) who assumed a mixing of a mafic melt and an evolved component within a magma chamber to form OH enriched apatites. However, because of the size and the shape of the IVZ pipes this explanation can be neglected, because there is no evidence for a single large magma chamber giving supply to the melts of the pipes. Therefore the OH rich nature of the IVZ pipe apatites can be ascribed to the mantle origin of the melts and the fluids as also described by Pearson and Taylor (1996) and Stoppa and Yu (1995) for different ultramafic systems.

A connection between the halogen compositions of the apatites and the trace element contents was established by Meurer et al. (2004). They investigated samples of the Kläppsjö Gabbro layered intrusion consisting of horizons of ultramafic cumulates as well as evolved gabbroic cumulates. Within these lithologies Pt- and Au-enriched samples are coexisting with Cl rich apatites which are occurring in the ultramafic cumulates, whereas the evolved portions mainly host Cl poor assemblages. This behavior was ascribed to the injection of a magma enriched in PGE, Au, and Cl, which had previously ponded on the floor of the intrusion, and accumulated sulfide. On the one hand this explanation is insufficient because the provenance of the enriching elements remains unexplained by Meurer et al. (2004), but on the other hand, this data shows a relationship between Cl and trace element compositions, in this case the PGE contents, within ultramafic suites.

4.5.2. General implications based on the REE and trace element contents of apatites

The substitution mechanisms of REE at the Ca structural positions in fluorapatite were studied in detail by Fleet and Pan (1995, 1997b). The two Ca positions in the crystal lattice are variably occupied depending on the ionic radii of the REE. Fleet et al. (2000) investigated the REE partitioning between chlorapatite, fluorapatite and hydroxylapatite. They found strongly varying partitioning coefficients between apatite and melt. The highest partitioning coefficients are reached for Nd within each endmember (i.e. chlorapatite, fluorapatite and hydroxylapatite), whereas the estimated D values are 0.128 for chlorapatite, around 7 (Fleet and Pan, 1997a) for fluorapatite and 3 for hydroxylapatite. These results show that especially F apatites are preferential candidates for REE substitution, followed by OH-apatites. In contrast, Cl-apatites will not be enriched in REE by mineral melt interactions. This is clearly shown in Figure 35, where the high F assemblages of Bec d' Ovaga follow in particular this REE preference. The Σ REE contents are positively correlated with the F+OH contents within each individual pipe sample-set.

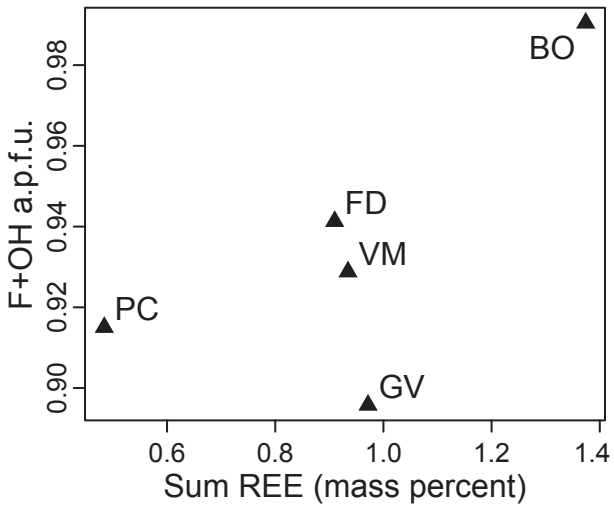

Figure 35: Comparison of F+OH [a.p.f.u.] and the Σ REE [mass %] contents (calculated according to log mean values) in apatites of the localities: BO - Bec d' Ovaga; FD - Fei di Doccio; GV - Castello di Gavala; VM - Valmaggia; PC - Piancone la Frera.

Therefore it can be assumed that the apatite trace element compositions were preferentially influenced by their magmatic formation, however, the single compositions have to be interpreted in context with a supposed interaction with coexisting fluids during the formation.

The interactions of crystallizing apatites with coexisting melts, fluids and vapor phases yielding different REE distributions and contents were investigated by several authors, e.g. (Boudreau et al., 1986, 1993; Chazot et al., 1996; Mathez and Webster, 2005; Prowatke and Klemme, 2006; Chevychelov et al., 2008). Belousova et al. (2002) in accordance with O'Reilly and Griffin (2000) reported REE patterns of magmatic apatites within cumulate mantle peridotite showing a steep decline of the chondrite normalized enrichment factors

from LREE to HREE. (Roeder et al., 1987) as well as (Sha and Chappell, 1999) found more or less flat REE paterns in acidic rocks such as granites or pegmatites. Furthermore O'Reilly and Griffin (2000) showed that magmatic apatites are stronger enriched in LREE than in Th and U, whereas metasomatically formed apatites are enriched in Th and U.

The IVZ-pipe apatites are characterised by zick-zack shaped REE distribution patterns (Fig. 34) with neither a positive, nor negative trend between LREE and HREE. Furthermore IVZ-pipe apatites are marked by high U and especially high Th contents with median compositions up to 120 ppm and 1350 ppm, respectively. This characteristic contradicts to a simple magmatic signature of the IVZ pipe apatites. Also, there is no systematic correlation between the strongly varying $(Ce/Yb)_{cn}$ values and the Σ REE content, clearly indicating the irregular REE composition of the rocks forming the Ultramafic Pipes, as illustrated in Figure 36. The relatively high Th (417-1356 ppm) as well as the U (64-118 ppm) concentration of the pipe apatites are in some agreement with those in lherzolite xenoliths (Th: 42-630 ppm, U: 15-280 ppm), but also with those of fluid dominated rocks (e.g. carbonatites as shown in Figure 36). The absence of a negative Eu anomaly with accompanying Eu/Eu* values near to 1 is in accordance with the low fractionation factors which can be assumed for ultramafic mantle rocks which have not undergone strong fractionation. Also the Y concentrations (intermediate values around 100 ppm in each pipe) are comparable to those in mantle-derived lherzolites (Fig. 36).

Prowatke and Klemme (2006) conducted experiments on trace and REE element partitioning between apatite and silicate melts at 1.0 GPa and 1250 °C. These conditions can be assumed for the lower crust - upper mantle transition in the IVZ during the underplating event, as proposed by Henk et al. (1997), Schaltegger and Brack (2007) and Schreiber et al. (2010).

The experiments of Prowatke and Klemme (2006) showed convex REE partitioning patterns with moderate factors for La, the highest apatite affinity (highest $D_{ap/melt}$) for Sm and the lowest ratios for Lu. The partition coefficients for U, Th, and Pb were close to unity. Such REE patterns show similarity to the LREE distribution patterns of the IVZ pipes (Fig. 34). However, the HREE distribution deviates and needs alternative explaination. One explanation is given by Exley and Smith (1982) who suggested prolonged fractionation of deep seated magmas to form apatite REE patterns similar to those of the IVZ pipes. This is unlikely, because the IVZ pipes are not considered deep seated, but direved from the crust-mantle transition, and there is no evidence for significant fractionation. To other possible explainations were given by Wilson et al. (1996) and Ripley et al. (1998). Wilson et al. (1996) investigated xenoliths hosted by alkalic basalt flows and cones from Dish Hill, California, USA. They found the REE patterns of anhydrous xenoliths being slightly LREE depleted to flat. Metasomatism caused a stronger enrichment in LREE compared to the HREE, shown by a ratio LREE/HREE > 1. This clearly contradicts with the REE of the IVZ apatites. Therefore, if a fluid contributed to the REE patterns of the IVZ apatites, then it was not of metasomatic origin. Ripley et al. (1998) studied apatites within dike-like ultramafic intrusions in the Duluth Complex (Minnesota, USA). The REE and Cl signatures of the apatites of these dikes are compatible with those of the IVZ pipes. Ripley et al. (1998) interpreted the signatures as a product of liquid immiscibility prozesses. Consequently the prozess of liquid immiscibility might have been also responsible for the REE characteristics of the IVZ apatites.

Several phenomena have interacted to form the extraordinary trace element and halogen compositions found in the IVZ apatites. These phenomena comprise melt-mineral-fluid reactions, chemical demixing as well as physical liquid - vapor separation processes.

4.5.3. Composition of fluids involved in the formation of the IVZ apatites

There is a strong mantle metasomatic event recorded within the IVZ, which particularly influenced the Finero peridotite. The associated phenomena were investigated by several authors Zanetti et al. (1999); Grieco et al. (2001, 2004); Zaccarini et al. (2004); Raffone et al. (2009); Selverstone and Sharp (2011). Selverstone and Sharp (2011) supposed metasomatism in a fore-arc wedge with fluids provided by subducted components. For such fluids a halogen rich composition can be assumed, which should have the capacity to form Cl rich mineral assemblages. Grieco et al. (2004) divided between an early, high-temperature metasomatism and a later K-metasomatism, whereas the dating of Grieco et al. (2001) exludes the second event to be related with the fluid event of the pipes. The processes and effects of mantle metasomatism were recently investigated by several authors (e.g. Tomlinson et al. (2009); Newton and Manning (2010); Köhler et al. (2009); Frezzotti et al. (2010)). Tomlinson et al. (2009) showed that metasomatic agents (fluids) were strongly enriched in LREE. Newton and Manning (2010) emphasized the importance of chloride-rich brines for rock alteration and mass transfer in the deep crust and the upper mantle. They stated that the solubility of fluorapatite rises monotonically with increasing NaCl and followed that complexing formed anhydrous ionic solutes and/or ion pairs. Because of these high solubilities it can be assumed that apatites may not preserve, their initial magmatic compositions in contact with such fluids. The origin of metasomatic fluids in the deep-crust and upper mantle region were investigated by Yardley and Graham (2002), who related the salinity of metamorphic fluids to the values present in the initial sedimentary sequence. Nijland et al. (1993) stated that Cl preferentially partitions into the fluid or vapor phase during high grade metamorphic processes. Based on phlogopite and amphibole compositions from the Horoman peridotite complex Arai and Takahashi (1989) concluded that magmatic volatiles were successively released from evolving magmas. This assumption was proved by Banks et al. (2000), who concluded a magmatic origin of fluids affecting granites based on Cl isotopic studies. Spinel lherzolite xenolith suites from Quaternary lavas at Injibara described by Frezzotti et al. (2010) contain chlorine-rich H_2O - CO_2 fluid inclusions. The metasomatic fluid composition was estimated at X_{CO_2} = 0.64, X_{H_2O} = 0.33 and X_{Cl} = 0.018, (salinity = 14-10 NaCl eq. mass.%, Cl = 4-5 mol.%); these are comparably high Cl contents. According to Mathez and Webster (2005) such fluids would coexist with apatites with a X_{Cl} ratio of at least 0.2. These values are only reached by some comparably strongly Cl-enriched apatites of the Castello di Gavala pipe, wherefore a general equilibrium of apatites with fluid compositions stated by Frezzotti et al. (2010) for lherzolites can be neglected. Zanetti et al. (1999) stressed that such fluids should be rich in CO_2, and minerals assemblages crystallising should be carbonate-rich.

In summary, it has to be emphasized that metasomatic fluids deriving from the mantle are very unlikely to have played a significant role for the formation and alteration of the Ultramafic Pipes of the IVZ. The general Cl-poor and F-rich composition and the lack of CO_3^{2-} (See chapter 3) in the apatites of the pipes are consideres as strong arguments

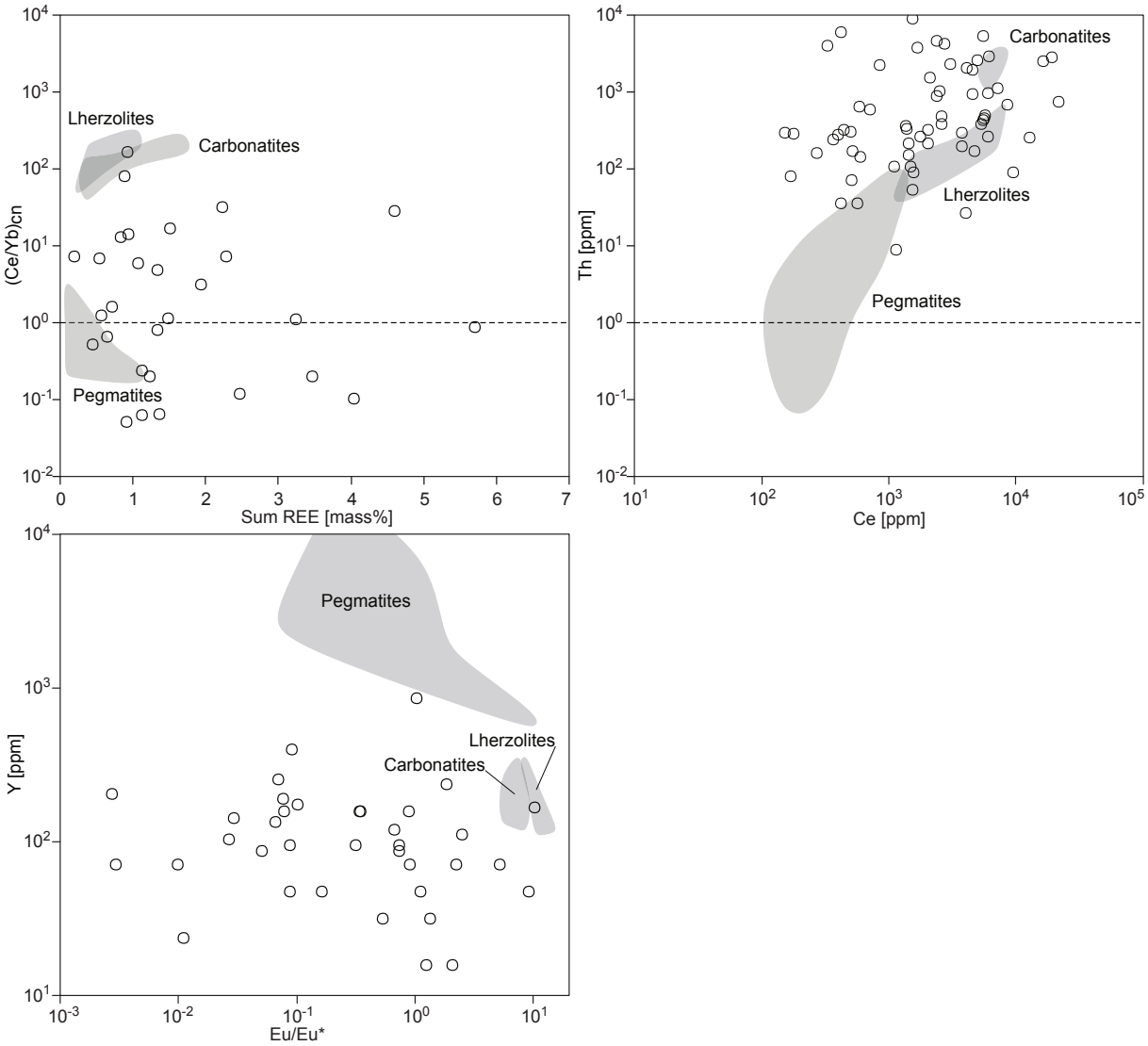

Figure 36: (Ce/Yb)cn vs. Σ REE diagram Eu/Eu* vs. Y ppm diagram. The compositional fields are of pegmatites, lherzolites and carbonatites (grey shading) are approximated to the data collected by Belousova et al. (2002).

against metasomatic fluids.

The fluids involved in the formation of the Valmaggia pipe were investigated by Fiorentini and Beresford (2008). They concluded, based on in situ H, Li, B analyses of hydromagmatic phases, that the fluids were not derived from a dehydrated, subducted slab but had a juvenile mantle origin. The REE paterns of amphiboles from the Valmaggis pipes, recorded by Fiorentini and Beresford (2008), show a more or less flat chondrite normalized trend between LREE and HREE, similar to the REE patterns of the apatites analysed in this study. Furthermore, these minerals experienced the strongest enrichment in Nd, whereas the La_{cn}/Nd_{cn} ratio is below one. This supports the assumed irregular REE composition of the fluids involved in the formation of the pipes.

As a consequence, it is suggested in this study, that the fluids involved in the formation of the Ultramafic Pipes of the IVZ are most likely magmatic fluids which evolved during the magmatic evolution of the pipes. Due to the anomalous REE and trace element compositions of the apatites it is assumed that the fluids experienced some evolutionary steps likes demixing or degassing processes as discussed in the following paragraph.

4.5.3.1. Effect of fluid demixing Phase stability investigations in the fluid systems H_2O - NaCl (Anderko and Pitzer, 1993; Driesner and Heinrich, 2007) as well as in the system H_2O - NaCl - CO_2 (Duan et al., 1995) showed pronounced immiscibility between the single phases up to conditions which can be presumed for the emplacement of the IVZ pipes. Carroll (2005) observed a negative pressure dependence of Cl solubility in aqueous fluids which could re-enrich the coexisting melt, whilst decompression during the ascent. Similar results were obtained by Lowenstern (1994) investigating chlorine, fluid immiscibility, and degassing in peralkaline magmas. Villemant and Boudon (1999) studied the H_2O and halogen (F, Cl, Br) behavior during shallow magma degassing processes and concluded that F is highly incompatible and remains unaffected by any degassing processes. Shinohara (1994) described a vapor-liquid immiscibility of fluids exsolving from a crystallizing silicate melt. The behavior of CO_2 in hydrothermal system was studies by Lowenstern (2001) who stated a decrease of the CO_2/H_2O ratio during progressive crystallization-induced degassing.

Based on fluid inclusion investigations in quartz-cassiterite veins Heinrich et al. (1992) concluded an unmixing of a magmatic vapor and a hypersaline brine, which yielded differences in heavy metals transportation due to chloride complexing. Again Heinrich et al. (1999) concluded a fluid phase separation ("boiling") in high-temperature magmatic-hydrothermal deep pluton systems.

These investigations clearly indicate that fluid and vapour de-mixing processes would have played an important role in the formation of the Ultramafic Pipes as shown by the irregular REE, trace element and halogen composition of the apatites.

4.5.4. Significance of the IVZ apatite compositions

This chapter represents an approach to explain the origin of the Ultramafic Pipes of the IVZ and their associated fluids, based on the halogen and REE composition of the apatites. On the basis of the intermediate halogen as well as the REE compositions of the apatites, along with some significant single element contents, the origin of the five

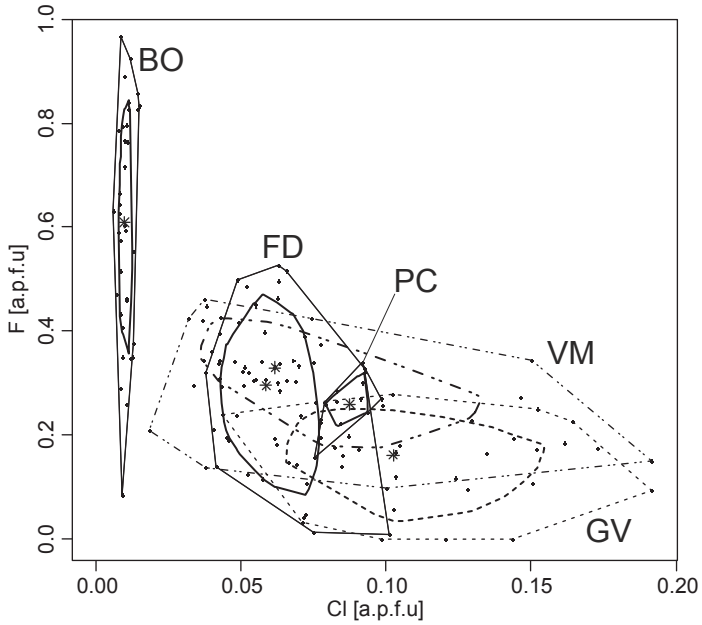

Figure 37: Bivariate Boxplots of the F and Cl values of the different localities. Plotted on the same scale for comparison. Localities: Bec d' Ovaga (BO); Castello di Gavala (GV); Fei di Doccio (FD); Valmaggia (VM); Piancone la Frera (PC).

pipes were discriminated. the compositional characteristics of apatites of this study, i.e. general low halogen contents, particularly low Cl-contents, but variable Cl-enrichment, are significantly distinct from those of various igneous complexs world-wide (Boudreau (1993); Fig. 29).

The Bec d' Ovaga pipe is dominated by F-rich apatites whereas the Cl values are extremely low (Fig. 37). Therefore, the apatites of this pipe can be described as almost pure F-OH solid solutions, whereas the F-content is the dominating factor. The high Σ REE concentrations of the Bec d' Ovaga apatites, which are mainly made up by high Sm contents together with comparably low HREE valuesmost likely mirror pure magmatic REE patterns. From these two perspectives the Bec d' Ovaga pipe can be described as the pipe which preserved the juvenile magmatic character best. Moreover, it can be assumed, that the apatites of the Bec d' Ovaga pipe were least affected by fluids causing Cl, OH and HREE enrichment. The high mean Th contents (1357 ppm) additionally distinguish the Bec d' Ovaga pipe from the further pipes.

The Valmaggia and the Fei di Doccio apatite analyses feature a quite similar halogen as well as REE composition. The intermediate values of both, the Σ REE contents (Fig. 31) and the F vs. Cl contents (Fig. 37), as well as their corresponding distribution ranges are largely overlapping. Due to the resembling compositions of these two pipes, it can be concluded that the genesis of the apatites took place in a generally comparable environment. However, a differentiation is possible on the basis of the single REE composition and the individual halogen distributions. The Valmaggia pipe apatite assemblages host the highest HREE contents and additionally relatively high Sm, Ce and Pr concentrations, if compared to the other pipes. This characteristic is accompanied by partly Cl enriched individual apatites, causing the skewness of the distribution (Fig. 37). These

two findings are in accordance with the REE - Cl relationship which was described for fluid affected systems. Therefore, it can be assumed, that the genetic environment of both pipes were generally equal, but the Valmaggia pipe was stronger influenced by fluids causing the selective enrichment features of the apatites. This assumption is reinforced by analog Th contents of around 500 ppm, similar to the Castello di Gavala pipe apatites, although the halogen compositions are differing strongly. The particular low F-contents together with relatively high mean Cl compositions (Fig. 37) as well as OH dominated assemblages (Fig. 29), indicate that the Castello di Gavala pipe is the most fluid affected pipe within the IVZ. These interacting fluids are expected to cause an overprint of the magmatic halogen signatures. The elevated Cl-contents, accompanied by increased S REE contents (i.e. compared to the Valmaggia and Fei di Doccio pipes) are the main arguments for this interpretation. Further evidence is provided by the shape of the REE pattern, characterised by comparably high LREE contents (high La, Eu and especially Yb) and low HREE concentrations. Therefore, it can be concluded that the Castello di Gavala pipe experienced the strongest influence by coexisting fluids during their genesis.

I spite of the low sample number of the Piancone la Frera pipe, several significant characteristics can be noticed. The compositional characteristics of the apatites show similarities to those of the Fei di Doccio, Valmaggia and Castello di Gavala pipes. The halogen contents plot in an intermediate range (Fig. 37), whereas slightly elevated Cl contents and similar OH and F intermediate composition (Fig. 29) are shown. A different signature is shown by the Σ REE contents (Fig. 31), because the intermediate REE contents are markedly low. Most likely these low intermediate REE contents are simply caused by a non sufficient number of samples to exactly evaluate the geochemical characteristics of the REE in this pipe. As mentioned before, the REE behave as trace elements and possess a logarithmic distribution, which is dominated by a high density of low content individuals. Therefore, it can be assumed, that only minerals with low REE concentrations were sampled in the case of the Piancone la Frera pipe. Consequently, the REE values are not directly comparable to the other pipes.

4.6. Conclusion

The interpretations of the halogen compositions suggest a generally juvenile character of the melts forming the Ultramafic Pipes of Bec d' Ovaga, Castello di Gavala, Piancone la Frera, Valmaggia and Fei di Doccio. The generally F-rich nature of the analyzed apatites is diagnostic for magmatic apatites. The consistently low Cl-contents are presumably induced by alteration via a variable mixture of coexisting fluids. These mainly mantle derived fluids are additionally expected to be responsible for the partial enrichment in OH. The absence of CO_3^{2-} in the apatites reinforces the assumed magmatic origin of both, the melts and the fluids. As the halogen chemistry is rapidly changed with coexisting fluids, it can be concluded that the slight differences between the single pipes are mainly caused by differences in the local crystallization, degassing, and fractionation processes which are dependent on the evolvement of the ascending melts.

On the basis of the REE compositions of the apatites, it can be assumed that their trace element contents were preferentially affected by their magmatic formation. This becomes particularly evident when the REE and the halogen compositions are compared.

However, the appearing irregularities in the trace element patterns (REE, U, Th, Y, again indicate that the apatites were additionally influenced by coexisting fluids during their formation.

It is clearly evident that the fluids affecting the Ultramafic Pipes are not related to the metasomatic fluids of the Finero Complex as described in literature. In contrast to the Finero fluids, a juvenile mantle origin without any influence by the metasediments of the adjacent Kinzigite Formation can be assumed. This assumption becomes clearly evident by the apatites of Fei di Doccio pipe, directly intruding the Kinzigite Formation. They are very similar to those of the Valmaggia pipe. Thereupon it is concluded that the fluids were exclusively, provided by a magmatic source. Additionally, complex de-mixing processes of fluids and vapors have to be taken in consideration to form the described varying trace element compositions.

A differentiation between the single localities is possible, although the apatites are in general magmatically controlled. Each pipe was influenced by interacting fluids, but to a varying extent. The Bec d' Ovage pipe preserved the magmatic signature best, indiating a comparabely low fluid impact. The Valmaggia and the Fei di Doccio apatites share more or less the same environmental conditions during there formation, and were intermediately affected by coexisting fluids. The strongest chlorine enrichment, with accompanying REE accumulation, is shown by the Castello di Gavala pipe, assuming the strongest fluid impact. The conditions of the Piancone la Frera pipe can be interpreted to be similar to those of the Valmaggia and the Fei di Doccio pipes, in spite of low sample number. .

5. Overall conclusion

The single conclusions and interpretations of the four parts of this thesis (i.e. subsections 1.7, 2.7, 3.7 and 4.7) fit very well together. This facilitates a comprehensive evaluation of the origin of each single deposit, the environmental conditions during their evolvement, as well as a prediction of the relationship between the ore parageneses of each individual ultramafic pipe. This final chapter provides a short comprehensive conclusion of the most significant results of the four main topics of this study.

An exclusive mantle origin of the magmas can be assumed for the Sella Bassa deposit, which is hosted by the Main Gabbro, the deepest part of the IVZ. This deposit experienced, most likely, no contamination by crustal material. A similar mantle derived origin of the ores can be assumed for the deposits hosted by the genetically overlying formations of the Cyclic Units. These deposits, the Gula, Guaifola and Isola deposits, show the comparatively strongest influence and contamination by the intercalated units of the Kinzigite Formation metasediments. It is reasonable to argue that each of the five Ultramafic Pipes of the IVZ possess the same mantle related magma origin, however, the source is interpreted to be different from those of the Main Gabbro and the Cyclic Units. Within the group of pipes intruding the Main Gabbro, the pipes of Bec d' Ovaga, Fei die Doccio, Castello di Gavala and Piancone la Frera, no influence by the metasediments of the Kinzigite Formation is supposed. In contrast, the single pipe, which directly intrudes the Kinzigite Formation, the Fei di Doccio pipe, a contamination by metasedimentary sulfur becomes evident.

In the course of the detailed apatite investigation, Raman spectroscopy was applied as a new analytical tool. With the aid of statistical data analysis the quality of the gained Raman data was strongly improved. The advantages of this method, i.e. the high precision and the possibility to analyze small grains, strongly improved the validity of the assumptions and interpretations, based on apatite compositions. The general interpretations lead to the conclusion, that a multi phase system of fluids, vapors and melts interacted during the geneses of the single pipes.

Apatite trace element analysis revealed that the pipe of Bec d' Ovaga was least altered by these fluids and retained the magmatic signatures best. Intermediate influences on the trace element compositions were recorded for the deposits of Valmaggia, Fei die Doccio and Piancone la Frera. The strongest fluid related changes in the anion composition of the apatites as well as the trace element patterns is supposed for the pipe of Castello di Gavala.

These fluids were almost certainly not related to the metasomatic fluids that influenced the Finero Complex in the northern part of the IVZ. This assumption is based on the trace element patterns as well as on the in-situ age information gained on zircons of the Fei di Doccio pipe. The maximum age of emplacement of the Fei di Doccio pipe was ascertained at 277±6 Ma, whereas the fluid event of Finero is postulated at around 210 Ma in the literature. The detailed in-situ zircon investigations verified the strong fluid impact assumed for the Ultramafic Pipes. The combination of all investigations confirmed for the first time that the Piancone la Frera pipe actually belongs to the group of Ultramafic Pipes. The deposits hosted by the La Balma - Monte Capio ultramafic sill, the Campello Monti, Alpe Laghetto and Penninetto deposits, clearly indicate a discrete magma origin without

a direct relationship to the remaining nine investigated deposits. The sulfur isotopic signatures indicate a distinct evolution of the melts which comprised mass independent fractionation. An influence by the adjacent Kinzigite Formation is only evident within the deposit of Penninetto, where the ore minerals incorporated metasedimetary sulfur.

References

Alard, O., Lorand, J.P., Reisberg, L., Bodinier, J.L., Dautria, J.M., O'Reilly, S.Y., 2011. Volatile-rich Metasomatism in Montferrier Xenoliths (Southern France): Implications for the Abundances of Chalcophile and Highly Siderophile Elements in the Subcontinental Mantle. Journal of Petrology 52, 2009–2045. URL: http://petrology.oxfordjournals.org/content/52/10/2009.abstract, doi:10.1093/petrology/egr038.

Alletti, M., Baker, D.R., Scaillet, B., Aiuppa, A., Moretti, R., Ottolini, L., 2009. Chlorine partitioning between a basaltic melt and H2O-CO2 fluids at Mount Etna. Chemical Geology 263, 37 – 50. URL: http://www.sciencedirect.com/science/article/pii/S0009254109001685, doi:10.1016/j.chemgeo.2009.04.003. <ce:title>Halogens in Volcanic Systems and Their Environmental Impacts</ce:title>.

Allègre, C., Manhès, G., Lewin, E., 2001. Chemical composition of the Earth and the volatility control on planetary genetics. Earth and Planetary Science Letters 185, 49 – 69. URL: http://www.sciencedirect.com/science/article/pii/S0012821X00003599, doi:10.1016/S0012-821X(00)00359-9.

Anderko, A., Pitzer, K., 1993. Equation-of-state representation of phase equilibria and volumetric properties of the system NaCl-H2O above 573 K. Geochimica et Cosmochimica Acta 57, 1657–1680. URL: http://www.sciencedirect.com/science/article/pii/0016703793901056, doi:10.1016/0016-7037(93)90105-6.

Antonakos, A., Liarokapis, E., Leventouri, T., 2007. Micro-Raman and FTIR studies of synthetic and natural apatites. Biomaterials 28, 3043 – 3054. doi:DOI: 10.1016/j.biomaterials.2007.02.028.

Arai, S., Takahashi, N., 1989. Formation and compositional variation of phlogopites in the Horoman peridotite complex, Hokkaido, northern Japan: implications for origin and fractionation of metasomatic fluids in the upper mantle. Contributions to Mineralogy and Petrology 101, 165–175. URL: http://dx.doi.org/10.1007/BF00375303. 10.1007/BF00375303.

Arndt, N.T., Lesher, C.M., Czamanske, G.K., 2005. Mantle-derived magmas and magmatic Ni-Cu-(PGE) deposits. Economic Geology 100th Anniversary Volume, 5–23.

Ashwal, L.D., Tucker, R.D., Zinner, E.K., 1999. Slow cooling of deep crustal granulites and Pb-loss in zircon. Geochimica et Cosmochimica Acta 63, 2839 – 2851. URL: http://www.sciencedirect.com/science/article/pii/S0016703799001660, doi:10.1016/S0016-7037(99)00166-0.

Awonusi, A., Morris, M., Tecklenburg, M., 2007. Carbonate Assignment and Calibration in the Raman Spectrum of Apatite. Calcified Tissue International 81, 46–52. URL: http://dx.doi.org/10.1007/s00223-007-9034-0. 10.1007/s00223-007-9034-0.

Baker, A.J., 1988. Stable isotope evidence for limited fluid infiltration of deep crustal rocks from the Ivrea Zone, Italy. Geology (Boulder) 16, 492–495.

Baker, A.J., 1990. Stable Isotopic Evidence for Fluid-Rock Interactions in the Ivrea Zone, Italy. Journal of Petrology 31, 243–260. URL: http://petrology.oxfordjournals.org/content/31/1/243.abstract, doi:10.1093/petrology/31.1.243.

Banks, D.A., Green, R., Cliff, R.A., Yardley, B.W.D., 2000. Chlorine isotopes in fluid inclusions: determination of the origins of salinity in magmatic fluids. Geochimica et Cosmochimica Acta 64, 1785 – 1789. URL: http://www.sciencedirect.com/science/article/pii/S001670379900407X, doi:10.1016/S0016-7037(99)00407-X.

Bea, F., Montero, P.G., 1997. Rare earth elements, yttrium, thorium, and uranium in crustal melting; the behavior of accessories during metamorphism and anatexis of metapelites; the Kinzigite Formation (Ivrea-Verbano, northern Italy). LPI Contribution 921, 21.

Belousova, E.A., Griffin, W.L., O'Reilly, S.Y., Fisher, N.I., 2002. Apatite as an indicator mineral for mineral exploration: trace-element compositions and their relationship to host rock type. Journal of Geochemical Exploration 76, 45 – 69. URL: http://www.sciencedirect.com/science/article/pii/S0375674202002042, doi:DOI: 10.1016/S0375-6742(02)00204-2.

Bhatnagar, V.M., 1969. Refinement of the synthetic hydroxyapatite cell parameters. Contributions to Mineralogy and Petrology 22, 375–378. URL: http://dx.doi.org/10.1007/BF00400132. 10.1007/BF00400132.

Biino, G.G., Meisel, T., 1996. Ar–Ar, Re–Os, Rb–Sr, Sm–Nd and U–Pb isotopic, trace element and petrologic study of alkaline mineralized ultramafic pipes in the Ivrea Verbano Zone, Italy. Schweizerische Mineralogische und Petrographische Mitteilungen 76, 98–99.

Boriani, A.C., Villa, I.M., 1997. Geochronology of regional metamorphism in the Ivrea-Verbano zone and Serie dei Laghi, Italian Alps. Schweizerische Mineralogische und Petrographische Mitteilungen 77, 381–401.

Boudreau, A.E., 1993. Chlorine as an exploration guide for the platinum-group elements in layered intrusions. Journal of Geochemical Exploration 48, 21 – 37. URL: http://www.sciencedirect.com/science/article/pii/0375674293900806, doi:10.1016/0375-6742(93)90080-6.

Boudreau, A.E., Hoatson, D.M., 2004. Halogen variations in the paleoproterozoic layered mafic-ultramafic intrusions of East Kimberley, Western Australia: implications for platinum group element mineralization. Economic Geology 99, 1015–1026. URL: http://economicgeology.org/cgi/content/abstract/99/5/1015, doi:10.2113/gsecongeo.99.5.1015.

Boudreau, A.E., Kruger, F.J., 1990. Variation in the composition of apatite through the Merensky cyclic unit in the western Bushveld Complex. Economic Geology 85, 737–745. URL: http://economicgeology.org/cgi/content/abstract/85/4/737, doi:10.2113/gsecongeo.85.4.737.

Boudreau, A.E., Love, C., Hoatson, D.M., 1993. Variation in the composition of apatite in the Munni Munni Complex and associated intrusions of the West Pilbara Block, Western Australia. Geochimica et Cosmochimica Acta 57, 4467 – 4477. URL: http://www.sciencedirect.com/science/article/pii/001670379390496J, doi:DOI: 10.1016/0016-7037(93)90496-J.

Boudreau, A.E., Mathez, E.A., McCallum, I.S., 1986. Halogen Geochemistry of the Stillwater and Bushveld Complexes: Evidence for Transport of the Platinum-Group Elements by Cl-Rich Fluids. Journal of Petrology 27, 967–986. URL: http://petrology.oxfordjournals.org/content/27/4/967.abstract, doi:10.1093/petrology/27.4.967.

Boyce, J., Hervig, R., 2009. Apatite as a monitor of late-stage magmatic processes at Volcnn Irazu, Costa Rica. Contributions to Mineralogy and Petrology 157, 135–145. URL: http://dx.doi.org/10.1007/s00410-008-0325-x. 10.1007/s00410-008-0325-x.

Boyce, J.W., Hervig, R.L., 2008. Magmatic degassing histories from apatite volatile stratigraphy. Geology 36, 63–66. URL: http://geology.gsapubs.org/content/36/1/63.abstract, doi:10.1130/G24184A.1.

Brenan, J., 1993. Kinetics of fluorine, chlorine and hydroxyl exchange in fluorapatite. Chemical Geology 110, 195 – 210. URL: http://www.sciencedirect.com/science/article/pii/000925419390254G, doi:10.1016/0009-2541(93)90254-G. <ce:title>Geochemistry of Accessory Minerals </ce:title>.

Burgess, R., Layzelle, E., Turner, G., Harris, J.W., 2002. Constraints on the age and halogen composition of mantle fluids in Siberian coated diamonds. Earth and Planetary Science Letters 197, 193 – 203. URL: http://www.sciencedirect.com/science/article/pii/S0012821X02004806, doi:10.1016/S0012-821X(02)00480-6.

Canty, A., Ripley, B., 2010. boot: Bootstrap R (S-Plus) Functions. R package version 1.2-43. ETH Zurich - Seminar for Statistics. URL: http://stat.ethz.ch/R-manual/R-patched/library/boot/html/envelope.html.

Carroll, M.R., 2005. Chlorine solubility in evolved alkaline magmas. Annals of Geophysics 48, 619–631.

Chang, L.L.Y., Howie, R.A., Zussman, J., 1996. Non-silicates: Sulphates, carbonates, phosphates, halides. Rock-forming minerals 5B, Longman Group, London, UK.

Chazot, G., Menzies, M.A., Harte, B., 1996. Determination of partition coefficients between apatite, clinopyroxene, amphibole, and melt in natural spinel lherzolites from Yemen: Implications for wet melting of the lithospheric mantle. Geochimica et Cosmochimica Acta 60, 423 – 437. URL: http://www.sciencedirect.com/science/article/pii/0016703795004122, doi:10.1016/0016-7037(95)00412-2.

Cherniak, D.J., Lanford, W.A., Ryerson, F.J., 1991. Lead diffusion in apatite and zircon using ion implantation and Rutherford Backscattering techniques. Geochimica et Cosmochimica Acta 55, 1663 – 1673. URL: http://www.sciencedirect.com/science/article/pii/001670379190137T, doi:10.1016/0016-7037(91)90137-T.

Cherniak, D.J., Watson, E.B., 2001. Pb diffusion in zircon. Chemical Geology 172, 5 – 24. URL: http://www.sciencedirect.com/science/article/pii/S0009254100002333, doi:10.1016/S0009-2541(00)00233-3. <ce:title>What are we dating? Understanding the Crystallogernesis of U-Pb</ce:title>.

Cherniak, D.J., Watson, E.B., 2003. Diffusion in Zircon. Reviews in Mineralogy and Geochemistry 53, 113–143. URL: http://rimg.geoscienceworld.org/content/53/1/113.short, doi:10.2113/0530113.

Chevychelov, V., Bocharnikov, R., Holtz, F., 2008. Experimental study of chlorine and fluorine partitioning between fluid and subalkaline basaltic melt. Doklady Earth Sciences 422, 1089–1092. URL: http://dx.doi.org/10.1134/S1028334X08070192. 10.1134/S1028334X08070192.

Cumming, G.L., Koeppel, V., Ferrario, A., 1987. A lead isotope study of the northeastern Ivrea Zone and the adjoining Ceneri Zone (N-Italy); evidence for a contaminated subcontinental mantle. Contributions to Mineralogy and Petrology 97, 19–30.

De Mul, F., Hottenhuis, M., Bouter, P., Greve, J., Arends, J., Ten Bosch, J., 1986. Micro-Raman Line Broadening in Synthetic Carbonated Hydroxyapatite. Journal of Dental Research 65, 437–440. URL: http://jdr.sagepub.com/content/65/3/437.abstract, doi:10.1177/00220345860650031301.

Deer, W.A., Howie, R.A., Zussman, J., 1992. An Introduction to the Rock-Forming Minerals. 2 ed., Longman Scientific Technical, Harlow, United Kingdom (GBR).

Diehl, T., Husen, S., Kissling, E., Deichmann, N., 2009. High-resolution 3-D P-wave model of the Alpine crust. Geophysical Journal International 179, 1133–1147.

Driesner, T., Heinrich, C.A., 2007. The system H2O-NaCl. Part I: Correlation formulae for phase relations in temperature-pressure-composition space from 0 to 1000;°C, 0 to 5000;bar, and 0 to 1 XNaCl. Geochimica et Cosmochimica Acta 71, 4880–4901. URL: http://www.sciencedirect.com/science/article/pii/S0016703707002943, doi:10.1016/j.gca.2006.01.033.

Duan, Z., Moller, N., Weare, J.H., 1995. Equation of state for the NaCl H2O CO2 system: prediction of phase equilibria and volumetric properties. Geochimica et Cosmochimica Acta 59, 2869–2882. URL: http://www.sciencedirect.com/science/article/pii/0016703795001824, doi:10.1016/0016-7037(95)00182-4.

Exley, R.A., Smith, J.V., 1982. The role of apatite in mantle enrichment processes and in the petrogenesis of some alkali basalt suites. Geochimica et Cosmochimica Acta 46, 1375 – 1384. URL: http://www.sciencedirect.com/science/article/pii/0016703782902733, doi:10.1016/0016-7037(82)90273-3.

Farquhar, J., Wing, B.A., 2003. Multiple sulfur isotopes and the evolution of the atmosphere. Earth and Planetary Science Letters 213, 1 – 13. URL: http://www.sciencedirect.com/science/article/pii/S0012821X03002966, doi:10.1016/S0012-821X(03)00296-6.

Farquhar, J., Wu, N., Canfield, D.E., Oduro, H., 2010. Connections between Sulfur Cycle Evolution, Sulfur Isotopes, Sediments, and Base Metal Sulfide Deposits. Economic Geology 105, 509–533. URL: http://economicgeology.org/cgi/content/abstract/105/3/509, doi:10.2113/gsecongeo.105.3.509.

Ferrario, A., Garuti, G., Rossi, A., Sighinolfi, G.P., 1983. Petrographic and metallogenic outlines of the "La Balma – M. Capio" ultramafic-mafic body (Ivrea-Verbano Basic Complex, NW Italian Alps). volume Mineral Deposits of the Alps and of the Alpine Epoch in Europe; Proceedings/IV. ISMIDA. Special publication of the Society for Geology Applied to Mineral Deposits.

Ferrario, A., Garuti, G., Sighinolfi, G.P., 1982. Platinum and palladium in the Ivrea-Verbano basic complex, Western Alps, Italy. Economic Geology and the Bulletin of the Society of Economic Geologists 77, 1548–1555.

Filzmoser, P., Steiger, B., 2011. StatDA: Statistical Analysis for Environmental Data. URL: http://CRAN.R-project.org/package=StatDA. r package version 1.5.

Fiorentini, M.L., Bekker, A., Rouxel, O., Wing, B.A., Maier, W., Rumble, D., 2012. Multiple Sulfur and Iron Isotope Composition of Magmatic Ni-Cu-(PGE) Sulfide Mineralization from Eastern Botswana. Economic Geology 107, 105–116. URL: http://economicgeology.org/content/107/1/105.abstract, doi:10.2113/econgeo.107.1.105.

Fiorentini, M.L., Beresford, S.W., 2008. Role of volatiles and metasomatized subcontinental lithospheric mantle in the genesis of magmatic Ni-Cu-PGE mineralization; insights from in situ H, Li, B analyses of hydromagmatic phases from the Valmaggia ultramafic pipe, Ivrea-Verbano Zone (NW Italy). Terra Nova 20, 333–340.

Fiorentini, M.L., Grieco, G., Ferrario, A., Tunesi, A., 2002. Petrological and metallogenic outlines of the Valmaggia ultramafic pipe (Ivrea Zone), NW Alps, Italy. Periodico di Mineralogia 71, 219–239.

Fleet, M.E., Liu, X., Pan, Y., 2000. Rare-earth elements in chlorapatite [Ca10(PO4)6Cl2]: Uptake, site preference, and degradation of monoclinic structure. American Mineralogist 85, 1437–1446. URL: http://ammin.geoscienceworld.org/content/85/10/1437.abstract, arXiv:http://ammin.geoscienceworld.org/content/85/10/1437.full.pdf+html.

Fleet, M.E., Pan, Y., 1995. Site preference of rare earth elements in fluorapatite. American Mineralogist 80, 329–335.

Fleet, M.E., Pan, Y., 1997a. Rare earth elements in apatite: Uptake from H2O-bearing phosphate-fluoride melts and the role of volatile components. Geochimica et Cosmochimica Acta 61, 4745 – 4760. URL: http://www.sciencedirect.com/science/article/pii/S0016703797002925, doi:10.1016/S0016-7037(97)00292-5.

Fleet, M.E., Pan, Y., 1997b. Site preference of rare earth elements in fluorapatite; binary (LREE+HREE)-substituted crystals. American Mineralogist 82, 870–877.

Fox, J., 2011. Rcmdr: R Commander. with contributions from Liviu Andronic and Michael Ash and Theophilius Boye and Stefano Calza and Andy Chang and Philippe Grosjean and Richard Heiberger and G. Jay Kerns and Renaud Lancelot and Matthieu Lesnoff and Uwe Ligges and Samir Messad and Martin Maechler and Robert Muenchen and Duncan Murdoch and Erich Neuwirth and Dan Putler and Brian Ripley and Miroslav Ristic and and Peter Wolf. URL: http://CRAN.R-project.org/package=Rcmdr. r package version 1.6-3.

Frezzotti, M.L., Ferrando, S., Peccerillo, A., Petrelli, M., Tecce, F., Perucchi, A., 2010. Chlorine-rich metasomatic H2O-CO2 fluids in amphibole-bearing peridotites from Injibara (Lake Tana region, Ethiopian plateau): Nature and evolution of volatiles in the mantle of a region of continental flood basalts. Geochimica et Cosmochimica Acta 74, 3023 – 3039. URL: http://www.sciencedirect.com/science/article/pii/S0016703710000670, doi:10.1016/j.gca.2010.02.007.

Garuti, G., 1993. Guidebook for the Post-Symposium Field Excursion 2 - Guide to the post-symposium field trip to the Balmuccia peridotite and Ni-sulfide deposits of the Ivrea-Verbano basic complex (Western Alps, Italy). International symposium on mineralization related to mafic ultramafic rocks.

Garuti, G., Bea, F., Zaccarini, F., Montero, P., 2001. Age, geochemistry and petrogenesis of the ultramafic pipes in the Ivrea Zone, NW Italy. Journal of Petrology 42, 433–457.

Garuti, G., Fiandri, P., Rossi, A., 1986. Sulfide composition and phase relations in the Fe-Ni-Cu ore deposits of the Ivrea-Verbano basic complex (Western Alps, Italy). Mineralium Deposita 21, 22–34.

Garuti, G., Gazzotti, M., Torres-Ruiz, J., 1995. Iridium, rhodium, and platinum sulfides in chromitites from the ultramafic massifs of Finero, Italy, and Ojen, Spain. The Canadian Mineralogist 33, 509–520.

Garuti, G., Gorgoni, C., Sighinolfi, G.P., 1984. Sulfide mineralogy and chalcophile and siderophile element abundances in the Ivrea-Verbano mantle peridotites (Western Italian Alps). Earth and Planetary Science Letters 70, 69–87.

Garuti, G., Naldrett, A.J., Ferrario, A., 1990. Platinum-group elements in magmatic sulfides from the Ivrea Zone; their control by sulfide assimilation and silicate fractionation. Economic Geology and the Bulletin of the Society of Economic Geologists 85, 328–336.

Garuti, G., Rinaldi, R., 1986a. Mineralogy of melonite-group and other tellurides from the Ivrea-Verbano basic complex, western Italian Alps. Economic Geology and the Bulletin of the Society of Economic Geologists 81, 1213–1217.

Garuti, G., Rinaldi, R., 1986b. Platinum group and related minerals from the Ivrea-Verbano sulfide deposits. Rendiconti della Societa Italiana di Mineralogia e Petrologia 41, 229–244.

Garuti, G., Rivalenti, C., Rossi, A., Siena, F., Sinigoi, S., 1980. The Ivrea-Verbano mafic ultramafic complex of the Italian western Alps: discussion of some some petrological problems and a summary. Rendiconti Società Italiana di Mineralogia e Petrologia 36, 717–749.

Gebauer, D., Schmid, R., vonQuadt, A., Ulmer, P., 1992. Oligocene, Permian and Panafrican zircon ages from rocks of the Balmuccia peridotite and the Lower Layered Group in the Ivrea Zone. Schweizerische Mineralogische und Petrographische Mitteilungen 72, 113–122.

Geisler, T., Pidgeon, R.T., Kurtz, R., van Bronswijk, W., Schleicher, H., 2003. Experimental hydrothermal alteration of partially metamict zircon. American Mineralogist 88, 1496–1513. URL: `http://ammin.geoscienceworld.org/content/88/10/1496.abstract`, `arXiv:http://ammin.geoscienceworld.org/content/88/10/1496.full.pdf+html`.

Giuliani, A., Kamenetsky, V.S., Kendrick, M.A., Phillips, D., Goemann, K., 2012. Nickel-rich metasomatism of the lithospheric mantle by pre-kimberlitic alkali-S-Cl-rich C-O-H fluids. Contributions to Mineralogy and Petrology 0, 1–17. URL: `http://dx.doi.org/10.1007/s00410-012-0801-1`, doi:10.1007/s00410-012-0801-1.

Graeser, S., Hunziker, J.C., 1968. Rb-Sr- und Pb-Isotopen-Bestimmungen an Gesteinen und Mineralien der Ivrea-Zone. Schweizerische mineralogische und petrographische Mitteilungen 48, 189–204.

Green, T.H., Watson, E.B., 1982. Crystallization of apatite in natural magmas under high pressure, hydrous conditions, with particular reference to 'Orogenic' rock series. Contributions to Mineralogy and Petrology 79, 96–105. URL: `http://dx.doi.org/10.1007/BF00376966`. 10.1007/BF00376966.

Grieco, G., Ferrario, A., Mathez, E.A., 2004. The effect of metasomatism on the Cr-PGE mineralization in the Finero Complex, Ivrea Zone, southern Alps. Ore Geology Reviews 24, 299–314.

Grieco, G., Ferrario, A., vonQuadt, A., Koeppel, V., Mathez, E.A., 2001. The zircon-bearing chromitites of the phlogopite peridotite of Finero (Ivrea Zone, Southern Alps); evidence and geochronology of a metasomatized mantle slab. Journal of Petrology 42, 89–101.

Haka, A.S., Shafer-Peltier, K.E., Fitzmaurice, M., Crowe, J., Dasari, R.R., Feld, M.S., 2002. Identifying Microcalcifications in Benign and Malignant Breast Lesions by Probing Differences in Their Chemical Composition Using Raman Spectroscopy. Cancer Research 62, 5375–5380. URL: http://cancerres.aacrjournals.org/content/62/18/5375.abstract, arXiv:http://cancerres.aacrjournals.org/content/62/18/5375.full.pdf+html.

Heilmann, H., Lensch, G., 1977. Sulfur isotope investigation of sulfides and rocks from the Main Basic Series of the Ivrea Zone. Schweizerische Mineralogische und Petrographische Mitteilungen 57, 349–360.

Heinrich, C.A., Günther, D., Audétat, A., Ulrich, T., Frischknecht, R., 1999. Metal fractionation between magmatic brine and vapor, determined by microanalysis of fluid inclusions. Geology 27, 755–758. URL: http://geology.gsapubs.org/content/27/8/755.abstract, doi:10.1130/0091-7613(1999)027<0755:MFBMBA>2.3.CO;2, arXiv:http://geology.gsapubs.org/content/27/8/755.full.pdf+html.

Heinrich, C.A., Ryan, C.G., Mernagh, T.P., Eadington, P.J., 1992. Segregation of ore metals between magmatic brine and vapor; a fluid inclusion study using PIXE microanalysis. Economic Geology 87, 1566–1583. URL: http://economicgeology.org/content/87/6/1566.abstract, doi:10.2113/gsecongeo.87.6.1566.

Henk, A., Franz, L., Teufel, S., Oncken, O., 1997. Magmatic Underplating, Extension, and Crustal Reequilibration: Insights From A Cross-Section Through the Ivrea Zone and Strona-Ceneri Zone, Northern Italy. The Journal of Geology 105, 367–378.

John, T., Layne, G.D., Haase, K.M., Barnes, J.D., 2010. Chlorine isotope evidence for crustal recycling into the Earth's mantle. Earth and Planetary Science Letters 298, 175 – 182. URL: http://www.sciencedirect.com/science/article/pii/S0012821X10004772, doi:10.1016/j.epsl.2010.07.039.

Katsura, T., 1995. Thermal diffusivity of olivine under upper mantle conditions. Geophysical Journal International 122, 63–69. URL: http://dx.doi.org/10.1111/j.1365-246X.1995.tb03536.x, doi:10.1111/j.1365-246X.1995.tb03536.x.

Köhler, J., Schönenberger, J., Upton, B., Markl, G., 2009. Halogen and trace-element chemistry in the Gardar Province, South Greenland: Subduction-related mantle metasomatism and fluid exsolution from alkalic melts. Lithos 113, 731 – 747. URL: http://www.sciencedirect.com/science/article/pii/S0024493709002953, doi:10.1016/j.lithos.2009.07.004.

Koeppel, V., 1974. Isotopic U-Pb Ages of Monazites and Zircons from the Crust-Mantle Transition and Adjacent Units of the Ivrea and Ceneri Zones (Southern Alps, Italy). Contributions to Mineralogy and Petrology 43, 55–70.

Lesher, C.M., Burnham, O.M., Keays, R.R., Barnes, S.J., Hulbert, L., 2001. Trace-element geochemistry and petrogenesis of barren and ore-associated komatiites. The Canadian Mineralogist 39, 673–696. URL: http://www.canmin.org/content/39/2/673.abstract, doi:10.2113/gscanmin.39.2.673.

Ligges, U., Maechler, M., 2003. Scatterplot3d - an R Package for Visualizing Multivariate Data. Journal of Statistical Software 8, 1–20. URL: http://www.jstatsoft.org.

Lowenstern, J., 2001. Carbon dioxide in magmas and implications for hydrothermal systems. Mineralium Deposita 36, 490–502. URL: http://dx.doi.org/10.1007/s001260100185. 10.1007/s001260100185.

Lowenstern, J.B., 1994. Chlorine, fluid immiscibility, and degassingin peralkaline magmas from Pantelleria, Italy. American Mineralogist 79, 335–369.

Mackie, P.E., Elliot, J.C., Young, R.A., 1972. Monoclinic structure of synthetic $Ca_5(PO_4)_3Cl$, chlorapatite. Acta Crystallographica Section B 28, 1840–1848. URL: http://dx.doi.org/10.1107/S0567740872005114, doi:10.1107/S0567740872005114.

Marini, L., Moretti, R., Accornero, M., 2011. Sulfur Isotopes in Magmatic-Hydrothermal Systems, Melts, and Magmas. Reviews in Mineralogy and Geochemistry 73, 423–492. URL: http://rimg.geoscienceworld.org/content/73/1/423.short, doi:10.2138/rmg.2011.73.14.

Marks, M.A.W., Wenzel, T., Whitehouse, M.J., Loose, M., T, Z., Barth, M., Worgard, L., Krasz, V., Eby, G.N., Stosnach, H., Markl, G., 2012. The volatile inventory (F, Cl, Br, S, C) of magmatic apatite: An integrated analytical approach. Chemical Geology 291, 241 – 255. URL: http://www.sciencedirect.com/science/article/pii/S0009254111004384, doi:10.1016/j.chemgeo.2011.10.026.

Mathez, E.A., Webster, J.D., 2005. Partitioning behavior of chlorine and fluorine in the system apatite-silicate melt-fluid. Geochimica et Cosmochimica Acta 69, 1275 – 1286. URL: http://www.sciencedirect.com/science/article/pii/S0016703704006957, doi:DOI: 10.1016/j.gca.2004.08.035.

Mayer, A., Mezger, K., Sinigoi, S., 2000. New Sm-Nd ages for the Ivrea-Verbano Zone, Sesia and Sessera valleys (northern-Italy). Journal of Geodynamics 30, 147–166.

Mazzucchelli, M., Rivalenti, G., Brunelli, D., Zanetti, A., Boari, E., 2009. Formation of highly refractory dunite by focused percolation of pyroxenite-derived melt in the Balmuccia peridotite massif (Italy). Journal of Petrology 50, 1205–1233.

McCreery, R.L., 2000. Raman spectroscopy for chemical analysis. Chemical Analysis v. 157. 1 ed., Wiley-Interscience, New York, USA.

McDonough, W.F., Sun, S.s., 1995. The composition of the Earth. Chemical Geology 120, 223 – 253. doi:DOI: 10.1016/0009-2541(94)00140-4. chemical Evolution of the Mantle.

McKeegan, K.D., Kudryavtsev, A.B., Schopf, J.W., 2007. Raman and ion microscopic imagery of graphitic inclusions in apatite from older than 3830 Ma Akilia supracrustal rocks, west Greenland. Geology 35, 591–594. URL: http://geology.gsapubs.org/content/35/7/591.abstract, doi:10.1130/G23465A.1.

Mehnert, K.R., 1975. The Ivrea Zone; a model of the deep crust. Neues Jahrbuch für Mineralogie Abhandlungen 125, 156–199.

Meurer, W.P., Hellstrom, F.A., Claeson, D.T., 2004. The relationship between chlorapatite and PGE-rich cumulates in layered intrusions: the Klappsjo gabbro, North-Central Sweden, as a case study. Canadian Mineralogist 42, 279–289. URL: http://www.canmin.org/cgi/content/abstract/42/2/279, doi:10.2113/gscanmin.42.2.279.

Mezger, K., Krogstad, E.J., 1997. Interpretation of discordant U-Pb zircon ages: An evaluation. Journal of Metamorphic Geology 15, 127–140. URL: http://dx.doi.org/10.1111/j.1525-1314.1997.00008.x, doi:10.1111/j.1525-1314.1997.00008.x.

Mulch, A., Rosenau, M., Doerr, W., Handy, M.R., 2002. The age and structure of dikes along the tectonic contact of the Ivrea-Verbano and Strona-Ceneri zones (southern Alps, northern Italy, Switzerland). Schweizerische Mineralogische und Petrographische Mitteilungen 82, 55–76.

Naldrett, A.J., 2004. Magmatic Sulfide Deposits: Geology, Geochemistry, and Exploration. Springer.

Naldrett, A.J., Craig, J.R., Kullerud, G., 1967. The central portion of the Fe-Ni-S system and its bearing on pentlandite exsolution in iron-nickel sulfide ores. Economic Geology and the Bulletin of the Society of Economic Geologists 62, 826–847.

Newton, R.C., Manning, C.E., 2010. [Role of saline fluids in deep-crustal and upper-mantle metasomatism: insights from experimental studies. Geofluids 10, 58–72. URL: http://dx.doi.org/10.1111/j.1468-8123.2009.00275.x, doi:10.1111/j.1468-8123.2009.00275.x.

Nijland, T.G., Jansen, J.H., Maijer, C., 1993. Halogen geochemistry of fluid during amphibolite-granulite metamorphism as indicated by apatite and hydrous silicates in basic rocks from the Bamble Sector, South Norway. Lithos 30, 167 – 189. URL: http://www.sciencedirect.com/science/article/pii/0024493793900144, doi:10.1016/0024-4937(93)90014-4.

Nishino, M., Yamashita, S., Aoba, T., Okazaki, M., Moriwaki, Y., 1981. The Laser-Raman Spectroscopic Studies on Human Enamel and Precipitated Carbonate-containing Apatites. Journal of Dental Research 60, 751–755. URL: http://jdr.sagepub.com/content/60/3/751.abstract, doi:10.1177/00220345810600031601.

O'Donnell, M.D., , Hill, R.G., Law, R.V., Fong, S., 2009. Raman spectroscopy, 19F and 31P MAS-NMR of a series of fluorochloroapatites. Journal of the European Ceramic Society 29, 377 – 384. doi:DOI: 10.1016/j.jeurceramsoc.2008.06.011.

Oppizzi, P., Schaltegger, U., 1999. Zircon bearing plagioclasites from the Finero complex (Ivrea Zone): dating a late Triassic mantle. Schweizerische Mineralogische und Petrographische Mitteilungen 79, 330–331.

O'Reilly, S.Y., Griffin, W.L., 2000. Apatite in the mantle: implications for metasomatic processes and high heat production in Phanerozoic mantle. Lithos 53, 217 – 232. URL: http://www.sciencedirect.com/science/article/pii/S0024493700000268, doi:10.1016/S0024-4937(00)00026-8.

O'Shea, D.C., Bartlett, M.L., Young, R.A., 1974. Compositional analysis of apatites with Laser-Raman spectroscopy: (OH,F,Cl) apatites. Archives of Oral Biology 19, 995 – 1006. doi:DOI: 10.1016/0003-9969(74)90086-7.

Pasteris, J.D., Ding, D.Y., 2009. Experimental fluoridation of nanocrystalline apatite. American Mineralogist 94, 53–63. URL: http://ammin.geoscienceworld.org/cgi/content/abstract/94/1/53, doi:10.2138/am.2009.2926.

Pasteris, J.D., Wopenka, B., Freeman, J.J., Rogers, K., Valsami-Jones, E., van der Houwen, J.A.M., Silva, M.J., 2004. Lack of OH in nanocrystalline apatite as a function of degree of atomic order: implications for bone and biomaterials. Biomaterials 25, 229 – 238. doi:DOI: 10.1016/S0142-9612(03)00487-3.

Patiño Douce, A.E., Roden, M.F., Chaumba, J., Fleisher, C., Yogodzinski, G., 2011. Compositional variability of terrestrial mantle apatites, thermodynamic modeling of apatite volatile contents, and the halogen and water budgets of planetary mantles. Chemical Geology 288, 14 – 31. URL: http://www.sciencedirect.com/science/article/pii/S0009254111002324, doi:10.1016/j.chemgeo.2011.05.018.

Pearson, J.M., Taylor, W.R., 1996. Mineralogy and geochemistry of fenitized alkaline ultrabasic sills of the Gifford Creek Complex,

Gascoyne Province, Western Australia. The Canadian Mineralogist 34, 201–219. URL: http://www.canmin.org/content/34/2/201.short, arXiv:http://www.canmin.org/content/34/2/201.full.pdf+html.

Peressini, G., Quick, J.E., Sinigoi, S., Hofmann, A.W., Fanning, M., 2007. Duration of a large mafic intrusion and heat transfer in the lower crust; a SHRIMP U-Pb zircon study in the Ivrea-Verbano Zone (Western Alps, Italy). Journal of Petrology 48, 1185–1218.

Phipps Morgan, J., 2001. Thermodynamics of pressure release melting of a veined plum pudding mantle. Geochem. Geophys. Geosyst. 2, 39.

Pidgeon, R.T., Nemchin, A.A., Hitchen, G.J., 1998. Internal structures of zircons from Archaean granites from the Darling Range batholith: implications for zircon stability and the interpretation of zircon U-Pb ages. Contributions to Mineralogy and Petrology 132, 288–299. URL: http://dx.doi.org/10.1007/s004100050422. 10.1007/s004100050422.

Pin, C., Sills, J.D., 1986. Petrogenesis of layered gabbros and ultramafic rocks from Val Sesia, the Ivrea Zone, NW Italy: trace element and isotope geochemistry. Geological Society, London, Special Publications 24, 231–249. URL: http://sp.lyellcollection.org/content/24/1/231.abstract, doi:10.1144/GSL.SP.1986.024.01.21.

Prowatke, S., Klemme, S., 2006. Trace element partitioning between apatite and silicate melts. Geochimica et Cosmochimica Acta 70, 4513 – 4527. URL: http://www.sciencedirect.com/science/article/pii/S0016703706006120, doi:10.1016/j.gca.2006.06.162.

Quick, J.E., Sinigoi, S., 1992. Ivrea-Verbano Zone workshop, 1992. U. S. Geological Survey Circular Report: C 1089, 30pp.

Quick, J.E., Sinigoi, S., Mayer, A., 1995. Emplacement of mantle peridotite in the lower continental crust, Ivrea-Verbano Zone, Northwest Italy. Geology (Boulder) 23, 739–742.

Quick, J.E., Sinigoi, S., Snoke, A.W., Kalakay, T.J., Mayer, A., Peressini, G., 2003. Geologic map of the southern Ivrea-Verbano Zone, northwestern Italy. Geologic Investigations Series - U. S. Geological Survey Report: I-2776, 22pp, 1 sheet.

R Development Core Team, 2011. R: A Language and Environment for Statistical Computing. R Foundation for Statistical Computing. Vienna, Austria. URL: http://www.R-project.org/. ISBN 3-900051-07-0.

Raffone, N., LeFevre, B., Ottolini, L., Vannucci, R., Zanetti, A., 2009. Light-Lithophile Element Metasomatism of Finero Peridotite (W ALPS): A Secondary-Ion Mass Spectrometry Study. Microchimica Acta 155, 251–255.

Rehman, I., Smith, R., Hench, L.L., Bonfield, W., 1995. Structural evaluation of human and sheep, bone and comparison with synthetic hydroxyapatie by FT-Raman spectroscopy. Journal of Biomedical Materials Research 29, 1287–1294.

Ripley, E.M., Severson, M.J., Hauck, S.A., 1998. Evidence for sulfide and Fe-Ti-P-rich liquid immiscibility in the Duluth Complex, Minnesota. Economic Geology 93, 1052–1062. URL: http://economicgeology.org/cgi/content/abstract/93/7/1052, doi:10.2113/gsecongeo.93.7.1052.

Rivalenti, G., Garuti, G., Rossi, A., Siena, F., Sinigoi, S., 1981. Existence of different peridotite types and of a layered igneous complex in the Ivrea Zone of the Western Alps. Journal of Petrology 22, 127–153.

Robinson, C.J., Bickle, M.J., Minshull, T.A., White, R.S., Nichols, A.R.L., 2001. Low degree melting under the Southwest Indian Ridge: the roles of mantle temperature, conductive cooling and wet melting. Earth and Planetary Science Letters 188, 383 – 398. URL: http://www.sciencedirect.com/science/article/pii/S0012821X01003296, doi:10.1016/S0012-821X(01)00329-6.

Roeder, P.L., MacArthur, D., Ma, X.P., Palmer, G.R., Mariano, A.N., 1987. Cathodoluminescence and microprobe study of rare-earth elements in apatite. American Mineralogist 72, 801–811. URL: http://ammin.geoscienceworld.org/content/72/7-8/801.short.

RRUFF, 2011. Integrated database of Raman spectra, X-ray diffraction and chemistry data for minerals. URL: http://rruff.info/.

Rubatto, D., Müntener, O., Barnhoorn, A., Gregory, C., 2008. Dissolution-reprecipitation of zircon at low-temperature, high-pressure conditions (Lanzo Massif, Italy). American Mineralogist 93, 1519–1529. URL: http://ammin.geoscienceworld.org/content/93/10/1519.abstract, doi:10.2138/am.2008.2874.

Rutter, E., Brodie, K., James, T., Burlini, L., 2007. Large-scale folding in the upper part of the Ivrea-Verbano Zone, NW Italy. Journal of Structural Geology 29, 1–17.

Schaltegger, U., Brack, P., 2007. Crustal-scale magmatic systems during intracontinental strike-slip tectonics; U, Pb and Hf isotopic constraints from Permian magmatic rocks of the southern Alps. Geologische Rundschau = International Journal of Earth Sciences (1999) 96, 1131–1151.

Schmid, S.M., Fügenschuh, B., Kissling, E., Schuster, R., 2004. Tectonic map and overall architecture of the Alpine orogen. Eclogae Geologicae Helvetiae 97, 93–117. URL: http://www.springerlink.com/content/5u98222y3w94w3kf/, doi:10.1007/s00015-004-1113-x.

Schnetger, B., 1994. Partial melting during the evolution of the amphibolite - to granulite-facies gneisses of the Ivrea Zone, northern Italy. Chemical Geology 113, 71 – 101. URL: http://www.sciencedirect.com/science/article/pii/000925419490006X, doi:10.1016/0009-2541(94)90006-X.

Schreiber, D., Lardeaux, J.M., Martelet, G., Courrioux, G., Guillen, A., 2010. 3-D modelling of Alpine Mohos in southwestern Alps. Geophysical Journal International 180, 961–975.

SeaSolve, 2003. PeakFit v4 Users Guide. peak separation and analysis software ed. SeaSolve Software Inc.

Selverstone, J., Sharp, Z.D., 2011. Chlorine isotope evidence for multicomponent mantle metasomatism in the Ivrea Zone. Earth and Planetary Science Letters 310, 429 – 440. URL: http://www.sciencedirect.com/science/article/pii/S0012821X11004985, doi:10.1016/j.epsl.2011.08.034.

Sha, L.K., Chappell, B.W., 1999. Apatite chemical composition, determined by electron microprobe and laser-ablation inductively coupled plasma mass spectrometry, as a probe into granite petrogenesis. Geochimica et Cosmochimica Acta 63, 3861 – 3881. URL: http://www.sciencedirect.com/science/article/pii/S0016703799002100, doi:10.1016/S0016-7037(99)00210-0.

Shinohara, H., 1994. Exsolution of immiscible vapor and liquid phases from a crystallizing silicate melt: Implications for chlorine and metal transport. Geochimica et Cosmochimica Acta 58, 5215–5221. URL: http://www.sciencedirect.com/science/article/pii/0016703794903069, doi:10.1016/0016-7037(94)90306-9.

Siddall, R., Hurford, A.J., 1998. Semi-quantitative determination of apatite anion composition for fission-track analysis using infra-red microspectroscopy. Chemical Geology 150, 181 – 190. doi:DOI: 10.1016/S0009-2541(98)00057-6.

Sinigoi, S., Quick, J.E., Clemens-Knott, D., Mayer, A., Demarchi, G., Mazzucchelli, M., Negrini, L., Rivalenti, G., 1994. Chemical evolution of a large mafic intrusion in the lower crust, Ivrea-Verbano Zone, northern Italy. Journal of Geophysical Research: Solid Earth 99, 21575–21590. URL: http://dx.doi.org/10.1029/94JB00114, doi:10.1029/94JB00114.

Stern, R.A., 2001. A new isotopic and trace-element standard for the ion microprobe: preliminary thermal ionization mass spectrometry (TIMS) U-Pb and electron-microprobe data. Geological Survey of Canada, Radiogenic Age and Isotopic Studies Current Research 2001-F1, Report 14, 11.

Stoppa, F., Yu, L., 1995. Chemical composition and petrogenetic implications of apatites from some ultra-alkaline Italian rocks. European Journal of Mineralogy 7, 391–402. URL: http://eurjmin.geoscienceworld.org/content/7/2/391.short, arXiv:http://eurjmin.geoscienceworld.org/content/7/2/391.full.pdf+html.

Stüwe, K., 2007. Energetics: Heat and Temperature, in: Geodynamics of the Lithosphere. Springer Berlin Heidelberg, pp. 51–137.

Sudarsanan, K., Mackie, P.E., Young, R.A., 1972. Comparison of synthetic and mineral fluorapatite, Ca5 (PO4)3F, in crystallographic detail. Materials Research Bulletin 7, 1331 – 1337. doi:DOI: 10.1016/0025-5408(72)90113-4.

Teufel, U., Schärer, U., 1989. Unravelling the age of high-grade metamorphism of the Ivrea Zone: A monazite single-grain and small fraction study. Terra Abstracts 1, 350.

Thornber, C.R., Quick, J.E., Mayer, A., Sinigoi, S., 1993. Geologic constraints on metallogeny of magmatically underplated lower crust in the Ivrea-Verbano Zone, northern Italy. Open-File Report - U. S. Geological Survey Report: OF 93-0504, 22pp.

Tomlinson, E.L., Müller, W., EIMF, 2009. A snapshot of mantle metasomatism: Trace element analysis of coexisting fluid (LA-ICP-MS) and silicate (SIMS) inclusions in fibrous diamonds. Earth and Planetary Science Letters 279, 362 – 372. URL: http://www.sciencedirect.com/science/article/pii/S0012821X09000260, doi:10.1016/j.epsl.2009.01.010.

Tsuda, H., Arends, J., 1993. Raman Spectra of Human Dental Calculus. Journal of Dental Research 72, 1609–1613. URL: http://jdr.sagepub.com/content/72/12/1609.abstract, doi:10.1177/00220345930720121401.

Vavra, G., Gebauer, D., Schmid, R., Compston, W., 1996. Multiple zircon growth and recrystallization during polyphase Late Carboniferous to Triassic metamorphism in granulites of the Ivrea Zone (Southern Alps): an ion microprobe (SHRIMP) study. Contributions to Mineralogy and Petrology 122, 337–358. URL: http://dx.doi.org/10.1007/s004100050132. 10.1007/s004100050132.

Vavra, G., Schaltegger, U., 1999. Post-granulite facies monazite growth and rejuvenation during Permian to Lower Jurassic thermal and fluid events in the Ivrea Zone (southern Alps). Contributions to Mineralogy and Petrology 134, 405–414.

Vavra, G., Schmid, R., Gebauer, D., 1999. Internal morphology, habit and U-Th-Pb microanalysis of amphibolite-to-granulite facies zircons; geochronology of the Ivrea Zone (southern Alps). Contributions to Mineralogy and Petrology 134, 380–404.

Villemant, B., Boudon, G., 1999. H2O and halogen (F, Cl, Br) behaviour during shallow magma degassing processes. Earth and Planetary Science Letters 168, 271–286. URL: http://www.sciencedirect.com/science/article/pii/S0012821X99000588, doi:10.1016/S0012-821X(99)00058-8.

Voshage, H., Hofmann, A.W., Mazzucchelli, M., Rivalenti, G., Sinigoi, S., Raczek, I., Demarchi, G., 1990. Isotopic evidence from the Ivrea Zone for a hybrid lower crust formed by magmatic underplating. Nature 347, 731–736.

Voshage, H., Hunziker, J.C., Hofmann, A.W., Zingg, A., 1987. A Nd and Sr isotopic study of the Ivrea Zone, Southern Alps, N-Italy. Contributions to Mineralogy and Petrology 97, 31–42.

Voshage, H., Sinigoi, S., Mazzucchelli, M., Demarchi, G., Rivalenti, G., Hofmann, A.W., 1988. Isotopic constraints on the origin of ultramafic and mafic dikes in the Balmuccia peridotite (Ivrea Zone). Contributions to Mineralogy and Petrology 100, 261–267.

Watson, E.B., 1980. Apatite and phosphorus in mantle source regions: An experimental study of apatite/melt equilibria at pressures to 25 kbar. Earth and Planetary Science Letters 51, 322 – 335. URL: http://www.sciencedirect.com/science/article/pii/0012821X80902149, doi:10.1016/0012-821X(80)90214-9.

Williams, I.S., 1998. U-Th-Pb Geochronology by Ion Microprobe. volume 7 Applications of microanalytical techniques to understanding mineralizing processes. Society of Economic Geologists.

Wilson, M.R., Kyser, T.K., Fagan, R., 1996. Sulfur isotope systematics and platinum group element behavior in REE-enriched metasomatic fluids: A study of mantle xenoliths from Dish Hill, California, USA. Geochimica et Cosmochimica Acta 60, 1933 – 1942. URL: http://www.sciencedirect.com/science/article/pii/0016703796000695, doi:DOI: 10.1016/0016-7037(96)00069-5.

Wingate, M.T.D., Kirkland, C.L., 2011. Introduction to geochronology information released in 2011. Geological Survey of Western Australia, Department of Mines and Petroleum - Government of Western Australia.

Yardley, B.W.D., Graham, J.T., 2002. The origins of salinity in metamorphic fluids. Geofluids 2, 249–256. URL: http://dx.doi.org/10.1046/j.1468-8123.2002.00042.x, doi:10.1046/j.1468-8123.2002.00042.x.

Yu, H., Zhang, H., Wang, X., Gu, Z., X, L., Deng, F., 2007. Local structure of hydroxy-peroxy apatite: A combined XRD, FT-IR, Raman, SEM, and solid-state NMR study. Journal of Physics and Chemistry of Solids 68, 1863 – 1871. doi:DOI: 10.1016/j.jpcs.2007.05.020.

Zaccarini, F., Stumpfl, E.F., Garuti, G., 2004. Zirconolite and Zr-Th-U minerals in chromitites of the Finero Complex, Western Alps, Italy; evidence for carbonatite-type metasomatism in a subcontinental mantle plume. The Canadian Mineralogist 42, 1825–1845.

Zanetti, A., Mazzucchelli, M., Rivalenti, G., Vannucci, R., 1999. The Finero phlogopite-peridotite massif; an example of subduction-related metasomatism. Contributions to Mineralogy and Petrology 134, 107–122.

Zattin, M., Bersani, D., Carter, A., 2007. Raman microspectroscopy: A non-destructive tool for routine calibration of apatite crystallographic structure for fission-track analyses. Chemical Geology 240, 197 – 204. doi:DOI: 10.1016/j.chemgeo.2007.02.007.

Zeck, H.P., Whitehouse, M.J., 2002. Repeated age resetting in zircons from Hercynian-Alpine polymetamorphic schists (Betic-Rif tectonic belt, S. Spain) - a U-Th-Pb ion microprobe study. Chemical Geology 182, 275–292.

Zindler, A., Hart, S., 1986. Chemical geodynamics. Annual review of earth and planetary sciences 14, 493–571.

Appendix

A. S isotopic study: SIMS and EMP analyses

The following tables comprise the SIMS S-isotope analyses for $\delta^{33}S_{VCDT}$, $\delta^{34}S_{VCDT}$, $\delta^{36}S_{VCDT}$, $\Delta^{33}S$ and $\Delta^{36}S$ in ‰ as well as the EMP results for As, S, Co, Fe, Ni and Cu. The units of the EMP analyses are mass percent; kg/100kg. The dataset is devided for the minerals pyrrhotite and pendlandite.

A.1. Pyrrhotite

Pyrrhotite SIMS S-isotope values of $\delta^{33}S_{VCDT}$, $\delta^{34}S_{VCDT}$, $\delta^{36}S_{VCDT}$, $\Delta^{33}S$ and $\Delta^{36}S$ in ‰ and EMP (As, S, Co, Fe, Ni, Cu) analyses (EMP units: mass percent; kg/100kg)

	BM 1312 1	BM 1312 3	BM 1312 4	BM 1312 5	BM 1312 6	BM 1312 7	BO 1 13	BO 1 16	CM 1274 2	CM 1274 5	CM 1274 10	CM 1274 14	CM 1274 16	FD 1 2	FD 1 5
$\delta^{33}S$	-0.934	-0.954	-0.838	-1.145	-1.416	-0.956	0.517	0.563	0.422	0.389	0.487	0.295	0.39	0.845	0.87
$\delta^{33}S\pm1\sigma$	0.066	0.067	0.067	0.067	0.065	0.068	0.026	0.024	0.085	0.086	0.085	0.085	0.086	0.036	0.036
$\delta^{34}S$	-1.894	-1.873	-1.759	-2.337	-2.911	-2.094	0.94	0.999	0.633	0.715	0.728	0.357	0.569	1.491	1.714
$\delta^{34}S\pm1\sigma$	0.082	0.081	0.081	0.083	0.081	0.083	0.036	0.032	0.048	0.049	0.048	0.046	0.046	0.046	0.048
$\delta^{36}S$	-3.672	-3.483	-3.347	-4.545	-5.589	-3.893	2.082	2.207	1.502	1.648	2.18	1.448	1.437	2.861	3.798
$\delta^{36}S\pm1\sigma$	0.229	0.248	0.234	0.245	0.234	0.258	0.151	0.142	0.167	0.165	0.18	0.168	0.163	0.181	0.185
$\delta^{36}S\pm2\sigma$	0.459	0.497	0.468	0.491	0.468	0.516	0.303	0.284	0.334	0.33	0.359	0.337	0.326	0.362	0.369
$\Delta^{33}S$	0.042	0.011	0.068	0.059	0.084	0.123	0.033	0.049	0.096	0.02	0.112	0.112	0.097	0.077	-0.013
$\Delta^{33}S\pm1\sigma$	0.079	0.079	0.079	0.08	0.077	0.08	0.032	0.029	0.088	0.089	0.089	0.088	0.089	0.043	0.044
$\Delta^{33}S\pm2\sigma$	0.157	0.159	0.158	0.16	0.153	0.16	0.064	0.058	0.177	0.178	0.178	0.177	0.178	0.087	0.088
$\Delta^{36}S$	-0.076	0.072	-0.007	-0.109	-0.066	0.081	0.294	0.308	0.298	0.288	0.797	0.77	0.356	0.026	0.539
$\Delta^{36}S\pm1\sigma$	0.229	0.248	0.234	0.245	0.234	0.258	0.151	0.142	0.167	0.165	0.18	0.168	0.163	0.181	0.185
$\Delta^{36}S\pm2\sigma$	0.459	0.497	0.468	0.491	0.468	0.516	0.303	0.284	0.334	0.33	0.359	0.337	0.326	0.362	0.369
As	0.03			0.01	0.01	0.01	0.00	0.00			0.03	0.03	0.04	0.05	0.03
S	52.23	52.21	52.49	49.79	49.82	49.76	52.30	52.48	53.16	53.32	52.96	53.01	52.73	52.09	52.18
Co															
Fe	47.55	47.58	47.28	50.19	50.15	50.21	47.19	46.95	46.41	46.24	46.63	46.65	46.27	47.53	47.58
Ni	0.19	0.22	0.23		0.02		0.51	0.55	0.42	0.44	0.38	0.31	0.96	0.34	0.21
Cu				0.01		0.03		0.02						0.01	

Pyrrhotite SIMS S-isotope values of $\delta^{33}S_{VCDT}$, $\delta^{34}S_{VCDT}$, $\delta^{36}S_{VCDT}$, $\Delta^{33}S$ and $\Delta^{36}S$ in ‰ and EMP (As, S, Co, Fe, Ni, Cu) analyses (EMP units: mass percent; kg/100kg) - extended 1

	FD 1 8	FD 1 11	FD 1 18	G 16 2	G 16 5	GU 4A 1	GU 4A 3	GU 4A 7	GU 4A 11	GU 4A 14	GV 1262A 1	GV 1262A 3	GV 1262A 7	GV 1262A 10
$\delta^{33}S$	0.851	0.915	0.853	0.55	0.508	1.083	1.06	1.07	0.922	1.107	0.527	0.564	0.555	0.539
$\delta^{33}S \pm 1\sigma$	0.042	0.039	0.037	0.068	0.073	0.075	0.075	0.077	0.075	0.075	0.035	0.038	0.038	0.036
$\delta^{34}S$	1.526	1.705	1.625	1.152	0.9	2.09	2.094	2.038	1.816	1.976	0.976	1.057	0.965	1.022
$\delta^{34}S \pm 1\sigma$	0.048	0.048	0.05	0.082	0.092	0.055	0.055	0.057	0.059	0.054	0.043	0.045	0.044	0.05
$\delta^{36}S$	3.184	3.43	3.426	2.408	1.8	3.855	4.02	4.005	3.613	3.617	2.184	2.389	2.161	2.283
$\delta^{36}S \pm 1\sigma$	0.19	0.193	0.214	0.246	0.267	0.211	0.22	0.218	0.205	0.204	0.192	0.17	0.167	0.167
$\delta^{36}S \pm 2\sigma$	0.38	0.387	0.428	0.493	0.533	0.422	0.44	0.436	0.411	0.407	0.385	0.34	0.333	0.334
$\Delta^{33}S$	0.065	0.037	0.016	-0.043	0.045	0.007	-0.018	0.02	-0.013	0.09	0.024	0.02	0.058	0.013
$\Delta^{33}S \pm 1\sigma$	0.049	0.047	0.045	0.08	0.087	0.08	0.08	0.082	0.081	0.08	0.041	0.044	0.044	0.044
$\Delta^{33}S \pm 2\sigma$	0.097	0.093	0.09	0.159	0.173	0.16	0.16	0.165	0.162	0.16	0.083	0.088	0.089	0.088
$\Delta^{36}S$	0.282	0.187	0.336	0.219	0.09	-0.12	0.037	0.128	0.16	-0.141	0.329	0.38	0.326	0.34
$\Delta^{36}S \pm 1\sigma$	0.19	0.193	0.214	0.246	0.267	0.211	0.22	0.218	0.205	0.204	0.192	0.17	0.167	0.167
$\Delta^{36}S \pm 2\sigma$	0.38	0.387	0.428	0.493	0.533	0.422	0.44	0.436	0.411	0.407	0.385	0.34	0.333	0.334
As	0.05	0.03	0.07	0.08	0.01	0.04	0.01		0.03	0.00	0.03		0.07	0.03
S	52.40	51.96	52.37	52.18	52.25	52.33	52.36	52.20	52.31	52.38	52.34	52.33	52.37	52.32
Co														
Fe	47.32	47.85	47.34	47.44	47.51	47.34	47.38	47.46	47.34	47.28	47.16	47.11	46.94	47.13
Ni	0.23	0.16	0.19	0.30	0.23	0.29	0.25	0.33	0.32	0.31	0.47	0.57	0.61	0.50
Cu			0.02	0.00	0.00					0.02			0.01	0.02

Pyrrhotite SIMS S-isotope values of $\delta^{33}S_{VCDT}$, $\delta^{34}S_{VCDT}$, $\delta^{36}S_{VCDT}$, $\Delta^{33}S$ and $\Delta^{36}S$ in ‰ and EMP (As, S, Co, Fe, Ni, Cu) analyses (EMP units: mass percent; kg/100kg) - extended 2

	GV 1262A 15	IS 1 2	IS 1 5	IS 1 10	IS 1 12	IS 1 15	LG 1301 4	LG 1301 7	LG 1301 11	LG 1301 14	LG 1301 16	MO 1220A 1	MO 1220A 4	MO 1220A 7
$\delta^{33}S$	0.347	1.461	1.483	1.491	1.573	1.587	0.063	0.068	0.19	-0.107	0.029	0.382	0.513	0.284
$\delta^{33}S \pm 1\sigma$	0.047	0.025	0.023	0.026	0.024	0.034	0.085	0.086	0.086	0.085	0.085	0.075	0.076	0.076
$\delta^{34}S$	0.648	2.827	2.733	2.715	2.911	2.921	0.088	-0.037	0.155	-0.155	-0.089	0.665	0.914	0.462
$\delta^{34}S \pm 1\sigma$	0.07	0.03	0.032	0.029	0.029	0.031	0.049	0.048	0.05	0.047	0.047	0.056	0.055	0.064
$\delta^{36}S$	1.301	5.021	5.309	5.189	5.038	5.457	0.552	0.147	0.677	-0.04	-0.004	1.562	1.982	1.5
$\delta^{36}S \pm 1\sigma$	0.212	0.158	0.149	0.125	0.139	0.149	0.168	0.16	0.198	0.184	0.186	0.235	0.198	0.206
$\delta^{36}S \pm 2\sigma$	0.424	0.315	0.299	0.251	0.278	0.299	0.337	0.32	0.397	0.367	0.372	0.471	0.397	0.412
$\Delta^{33}S$	0.013	0.007	0.077	0.094	0.074	0.084	0.017	0.087	0.111	-0.027	0.075	0.039	0.042	0.046
$\Delta^{33}S \pm 1\sigma$	0.059	0.029	0.028	0.03	0.028	0.038	0.089	0.09	0.09	0.089	0.088	0.08	0.082	0.083
$\Delta^{33}S \pm 2\sigma$	0.117	0.059	0.056	0.06	0.057	0.076	0.177	0.18	0.179	0.177	0.177	0.16	0.163	0.165
$\Delta^{36}S$	0.069	-0.357	0.109	0.025	-0.501	-0.1	0.384	0.218	0.383	0.255	0.166	0.298	0.244	0.622
$\Delta^{36}S \pm 1\sigma$	0.212	0.158	0.149	0.125	0.139	0.149	0.168	0.16	0.198	0.184	0.186	0.235	0.198	0.206
$\Delta^{36}S \pm 2\sigma$	0.424	0.315	0.299	0.251	0.278	0.299	0.337	0.32	0.397	0.367	0.372	0.471	0.397	0.412
As			0.03	0.02			0.01	0.05	0.04			0.04		0.01
S	52.45	52.40	52.24	52.46	52.34	52.35	52.33	52.24	52.27	52.15	51.88	52.94	53.19	52.86
Co														
Fe	46.90	47.17	47.34	47.10	47.19	47.21	47.38	47.35	47.37	47.55	47.83	46.71	46.49	46.66
Ni	0.63	0.43	0.39	0.41	0.47	0.43	0.29	0.34	0.31	0.30	0.29	0.31	0.31	0.47
Cu	0.01			0.01		0.01		0.03				0.00	0.01	

Pyrrhotite SIMS S-isotope values of $\delta^{33}S_{VCDT}$, $\delta^{34}S_{VCDT}$, $\delta^{36}S_{VCDT}$, $\Delta^{33}S$ and $\Delta^{36}S$ in ‰ and EMP (As, S, Co, Fe, Ni, Cu) analyses (EMP units: mass percent; kg/100kg) - extended 3

	MO 1220A 9	MO 1220A 11	SB 1309 1	SB 1309 5	SB 1309 7	SB 1309 11	SB 1309 13
δ^{33}**S**	0.427	0.434	0.915	0.97	1.008	0.898	1.035
δ^{33}**S**$\pm\mathbf{1}\sigma$	0.075	0.075	0.077	0.076	0.075	0.074	0.075
δ^{34}**S**	0.804	0.775	1.792	1.784	1.98	1.746	2.035
δ^{34}**S**$\pm\mathbf{1}\sigma$	0.054	0.056	0.063	0.056	0.054	0.055	0.057
δ^{36}**S**	1.731	1.816	3.657	3.654	3.578	3.481	3.815
δ^{36}**S**$\pm\mathbf{1}\sigma$	0.199	0.213	0.216	0.204	0.211	0.208	0.193
δ^{36}**S**$\pm\mathbf{2}\sigma$	0.398	0.426	0.433	0.408	0.421	0.415	0.387
Δ^{33}**S**	0.013	0.035	-0.008	0.052	-0.011	-0.001	-0.013
Δ^{33}**S**$\pm\mathbf{1}\sigma$	0.08	0.08	0.083	0.081	0.08	0.079	0.081
Δ^{33}**S**$\pm\mathbf{2}\sigma$	0.16	0.16	0.166	0.163	0.159	0.158	0.162
Δ^{36}**S**	0.203	0.342	0.25	0.262	-0.187	0.16	-0.056
Δ^{36}**S**$\pm\mathbf{1}\sigma$	0.199	0.213	0.216	0.204	0.211	0.208	0.193
Δ^{36}**S**$\pm\mathbf{2}\sigma$	0.398	0.426	0.433	0.408	0.421	0.415	0.387
As	0.02	0.02	0.04	0.03	0.01	0.08	
S	53.00	53.27	52.98	52.92	53.17	53.46	53.13
Co							
Fe	46.46	46.20	46.51	46.76	46.55	46.20	46.61
Ni	0.52	0.50	0.46	0.28	0.27	0.26	0.26
Cu		0.01	0.01		0.00		

A.2. Pendlanite

Pendlandite SIMS S-isotope values of $\delta^{33}S_{VCDT}$, $\delta^{34}S_{VCDT}$, $\delta^{36}S_{VCDT}$, $\Delta^{33}S$ and $\Delta^{36}S$ in ‰ and EMP (As, S, Co, Fe, Ni, Cu) analyses (EMP units: mass percent; kg/100kg)

	BO 1 17	BO 1 19	BO 1 24	BO 1 27	BO 1 29	CM 1274 18	CM 1274 22	CM 1274 24	CM 1274 27	CM 1274 28	FD 1 20	FD 1 22	FD 1 25	FD 1 26	FD 1 29
$\delta^{33}S$	-0.007	0.319	0.089	0.293	0.295	0.040	0.035	-0.001	0.043	0.128	0.593	0.132	0.374	0.457	0.428
$\delta^{33}S\pm1\sigma$	0.069	0.033	0.050	0.051	0.054	0.032	0.032	0.039	0.036	0.031	0.058	0.067	0.058	0.062	0.052
$\delta^{34}S$	-0.056	0.691	0.028	0.461	0.568	-0.122	-0.084	-0.055	0.031	0.101	0.879	0.356	0.779	0.828	0.795
$\delta^{34}S\pm1\sigma$	0.116	0.036	0.076	0.089	0.093	0.046	0.048	0.054	0.048	0.049	0.099	0.129	0.102	0.100	0.100
$\delta^{36}S$	-0.343	0.934	0.503	1.119	1.476	-0.440	-0.133	-0.492	0.122	-0.246	2.219	0.888	1.511	1.813	1.988
$\delta^{36}S\pm1\sigma$	0.266	0.159	0.214	0.236	0.206	0.235	0.215	0.209	0.211	0.193	0.246	0.294	0.238	0.214	0.236
$\delta^{36}S\pm2\sigma$	0.533	0.318	0.427	0.473	0.413	0.470	0.430	0.417	0.422	0.386	0.491	0.588	0.477	0.427	0.472
$\Delta^{33}S$	0.021	-0.037	0.074	0.056	0.003	0.103	0.078	0.028	0.027	0.075	0.141	-0.051	-0.027	0.031	0.018
$\Delta^{33}S\pm1\sigma$	0.092	0.038	0.063	0.069	0.072	0.040	0.041	0.048	0.044	0.040	0.077	0.094	0.078	0.081	0.073
$\Delta^{33}S\pm2\sigma$	0.183	0.076	0.127	0.137	0.145	0.080	0.081	0.097	0.087	0.081	0.154	0.189	0.156	0.161	0.147
$\Delta^{36}S$	-0.237	-0.379	0.449	0.243	0.397	-0.208	0.026	-0.386	0.063	-0.439	0.548	0.212	0.030	0.238	0.477
$\Delta^{36}S\pm1\sigma$	0.266	0.159	0.214	0.236	0.206	0.235	0.215	0.209	0.211	0.193	0.246	0.294	0.238	0.214	0.236
$\Delta^{36}S\pm2\sigma$	0.533	0.318	0.427	0.473	0.413	0.470	0.430	0.417	0.422	0.386	0.491	0.588	0.477	0.427	0.472
As	0.01	0.02		0.06		0.04		0.01	0.00	0.02		0.03	0.01		
S	46.84	47.04	47.34	47.23	47.29	47.25	47.23	47.32	47.15	46.99	47.40	46.95	47.30	47.22	46.86
Co	0.23	0.25	0.18	0.28	0.19						0.05	0.04	0.12	0.12	0.14
Fe	25.38	25.12	24.99	25.05	25.27	25.27	25.22	25.18	25.22	25.30	27.47	27.75	27.38	27.56	27.56
Ni	27.54	27.57	27.47	27.36	27.23	27.40	27.55	27.46	27.60	27.66	25.05	25.23	25.19	25.10	25.43
Cu			0.02	0.02	0.02	0.04		0.03	0.03	0.02	0.03	0.00		0.00	

PendlanditeSIMS S-isotope values of $\delta^{33}S_{VCDT}$, $\delta^{34}S_{VCDT}$, $\delta^{36}S_{VCDT}$, $\Delta^{33}S$ and $\Delta^{36}S$ in ‰ and EMP (As, S, Co, Fe, Ni, Cu) analyses (EMP units: mass percent; kg/100kg) - extended 1

	G 16 18	G 16 19	G 16 20	G 16 20	G 16 21	GU 4A 15	GU 4A 16	GV 1262A 16	GV 1262A 17	GV 1262A 18	GV 1262A 19	GV 1262A 20	IS 1 17	IS 1 18
δ^{33}**S**	1.224	0.865	1.890	3.032	2.546	-1.189	-0.073	0.272	-1.143	-1.456	0.212	0.149	1.370	1.321
δ^{33}**S**$\pm 1\sigma$	0.097	0.098	0.076	0.232	0.104	0.112	0.056	0.059	0.076	0.084	0.058	0.066	0.055	0.048
δ^{34}**S**	2.172	1.748	3.360	5.862	4.872	-2.560	-0.011	0.504	-2.258	-2.783	0.301	0.081	2.710	2.708
δ^{34}**S**$\pm 1\sigma$	0.189	0.129	0.139	0.341	0.203	0.234	0.090	0.099	0.147	0.156	0.103	0.128	0.089	0.087
δ^{36}**S**	4.341	4.238	7.558	11.805	10.604	-5.312	-0.085	0.739	-4.960	-5.272	0.176	0.094	5.229	5.371
δ^{36}**S**$\pm 1\sigma$	0.617	0.465	0.489	0.770	0.540	0.465	0.216	0.196	0.348	0.342	0.220	0.305	0.267	0.243
δ^{36}**S**$\pm 2\sigma$	1.235	0.930	0.979	1.541	1.081	0.931	0.432	0.392	0.696	0.684	0.441	0.610	0.533	0.486
Δ^{33}**S**	0.106	-0.035	0.161	0.017	0.040	0.130	-0.068	0.013	0.020	-0.022	0.057	0.108	-0.025	-0.073
Δ^{33}**S**$\pm 1\sigma$	0.137	0.118	0.104	0.290	0.147	0.165	0.073	0.078	0.107	0.116	0.079	0.093	0.071	0.065
Δ^{33}**S**$\pm 2\sigma$	0.274	0.236	0.208	0.581	0.295	0.330	0.146	0.156	0.214	0.232	0.158	0.187	0.143	0.131
Δ^{36}**S**	0.209	0.914	1.165	0.638	1.328	-0.454	-0.065	-0.218	-0.674	0.008	-0.396	-0.059	0.073	0.220
Δ^{36}**S**$\pm 1\sigma$	0.617	0.465	0.489	0.770	0.540	0.465	0.216	0.196	0.348	0.342	0.220	0.305	0.267	0.243
Δ^{36}**S**$\pm 2\sigma$	1.235	0.930	0.979	1.541	1.081	0.931	0.432	0.392	0.696	0.684	0.441	0.610	0.533	0.486
As			0.03	0.03	0.01		0.03	0.03	0.04					
S	47.28	47.17	47.26	47.26	46.84	47.01	46.91	47.11	47.23	47.02	47.18	47.01	47.26	47.28
Co	1.68	2.24	2.70	2.70	2.82	3.79	5.50	0.19	0.35	0.32	0.22	0.25	3.56	4.35
Fe	25.93	26.36	25.77	25.77	25.81	24.95	24.13	25.90	25.55	25.64	25.74	25.74	24.53	24.12
Ni	25.12	24.24	24.22	24.22	24.52	24.25	23.43	26.77	26.82	26.99	26.85	26.98	24.65	24.25
Cu			0.03	0.03			0.01	0.00	0.02	0.03		0.02		

PendlanditeSIMS S-isotope values of $\delta^{33}S_{VCDT}$, $\delta^{34}S_{VCDT}$, $\delta^{36}S_{VCDT}$, $\Delta^{33}S$ and $\Delta^{36}S$ in ‰ and EMP (As, S, Co, Fe, Ni, Cu) analyses (EMP units: mass percent; kg/100kg) - extended 2

	IS 1 19	IS 1 21	LG 1301 21	LG 1301 22	LG 1301 26	LG 1301 29	LG 1301 32	MO 1220A 13	MO 1220A 16	MO 1220A 18	MO 1220A 19	MO 1220A 20	VM 1329 17
δ^{33}**S**	1.533	0.434	-0.122	-0.188	-0.026	0.232	-0.107	-0.461	0.071	0.056	1.834	-0.603	-1.740
δ^{33}**S**$\pm 1\sigma$	0.057	0.084	0.056	0.052	0.052	0.067	0.051	0.083	0.057	0.060	0.028	0.088	0.096
δ^{34}**S**	2.949	0.784	-0.401	-0.440	-0.297	0.527	-0.364	-1.015	0.034	0.040	3.427	-1.249	-3.454
δ^{34}**S**$\pm 1\sigma$	0.096	0.173	0.097	0.096	0.093	0.144	0.096	0.160	0.105	0.102	0.048	0.166	0.188
δ^{36}**S**	5.639	1.087	-0.708	-0.817	-0.720	1.988	-0.504	-1.961	-0.062	0.237	5.713	-2.624	-6.993
δ^{36}**S**$\pm 1\sigma$	0.223	0.389	0.208	0.242	0.219	0.419	0.197	0.287	0.270	0.217	0.165	0.339	0.385
δ^{36}**S**$\pm 2\sigma$	0.446	0.778	0.417	0.485	0.437	0.838	0.393	0.574	0.541	0.434	0.330	0.678	0.770
Δ^{33}**S**	0.015	0.030	0.084	0.039	0.127	-0.039	0.081	0.062	0.053	0.035	0.070	0.040	0.040
Δ^{33}**S**$\pm 1\sigma$	0.075	0.123	0.075	0.072	0.071	0.100	0.071	0.117	0.079	0.080	0.037	0.123	0.136
Δ^{33}**S**$\pm 2\sigma$	0.151	0.245	0.149	0.143	0.141	0.200	0.142	0.234	0.157	0.159	0.075	0.245	0.273
Δ^{36}**S**	0.028	-0.403	0.053	0.018	-0.155	0.986	0.188	-0.033	-0.127	0.161	-0.809	-0.252	-0.441
Δ^{36}**S**$\pm 1\sigma$	0.223	0.389	0.208	0.242	0.219	0.419	0.197	0.287	0.270	0.217	0.165	0.339	0.385
Δ^{36}**S**$\pm 2\sigma$	0.446	0.778	0.417	0.485	0.437	0.838	0.393	0.574	0.541	0.434	0.330	0.678	0.770
As							0.01			0.05			
S	47.06	47.31	47.10	47.23	47.12	47.34	47.32	47.13	46.99	46.82	47.04	47.31	47.38
Co	4.05	3.88	1.39	1.19	1.25	1.26	1.19						0.57
Fe	24.28	24.20	26.00	26.18	26.25	26.08	26.26	25.04	25.12	25.20	24.99	25.00	30.96
Ni	24.62	24.61	25.51	25.39	25.38	25.28	25.22	27.82	27.85	27.92	27.96	27.67	21.09
Cu				0.00		0.03		0.02	0.03	0.01	0.02	0.02	0.00

PendlanditeSIMS S-isotope values of $\delta^{33}S_{VCDT}$, $\delta^{34}S_{VCDT}$, $\delta^{36}S_{VCDT}$, $\Delta^{33}S$ and $\Delta^{36}S$ in ‰ and EMP (As, S, Co, Fe, Ni, Cu) analyses (EMP units: mass percent; kg/100kg) - extended 3

	VM 1329 20	**VM 1329 21**	**VM 1329 22**
δ^{33}**S**	-0.589	-0.464	-0.692
δ^{33}**S**$\pm$**1**σ	0.053	0.061	0.061
δ^{34}**S**	-1.118	-0.972	-1.299
δ^{34}**S**$\pm$**1**σ	0.098	0.110	0.119
δ^{36}**S**	-2.209	-2.052	-2.532
δ^{36}**S**$\pm$**1**σ	0.255	0.269	0.300
δ^{36}**S**$\pm$**2**σ	0.511	0.537	0.600
Δ^{33}**S**	-0.013	0.036	-0.024
Δ^{33}**S**$\pm$**1**σ	0.073	0.084	0.086
Δ^{33}**S**$\pm$**2**σ	0.147	0.167	0.172
Δ^{36}**S**	-0.086	-0.206	-0.066
Δ^{36}**S**$\pm$**1**σ	0.255	0.269	0.300
Δ^{36}**S**$\pm$**2**σ	0.511	0.537	0.600
As		0.03	
S	47.50	47.47	46.94
Co	0.68	0.64	0.46
Fe	31.16	30.96	31.41
Ni	20.66	20.89	21.19
Cu	0.00	0.01	

B. S isotopic study: Sulfide analyses statistics

Electron microprobe (EMP) analyses of selected sulfide minerals within polished sections of the ore deposits at: BM: Penninetto, BO: Bec d'Ovaga, CM: Campello Monti , FD: Fei di Doccio, G: Guaifola, GU: Gula, GV: Castello di Gavala, IS: Isola, LG: Alpe Laghetto, MO: Piancone la Frera, SB: Sella Bassa, VM: Valmaggia. The data is given in mass percent (kg/100kg).

Statistical description

The plots of the first colums show histograms of the sample density with according density lines (solid lines). The two dashed lines are illustrating the calculated normal distributions wehereas the data bases are the calculated arithmetic means with according standard deviations as well as the results of the fited linear model using a least squares residuals refinement.

The second columns show the empirical cumulative distribution function (grey stepwise line) as well as the calculated probability function (solid black line).

The third columns show quantile-quantile plots (qq plot) with corresponding confidence envelopes of 90% whereas the dashed lines display the upper and lower pointwise confidence envelopes and the solid lines display the envelope which controls the overall error (Canty and Ripley, 2010).

B.1. Fe in pyrrhotite

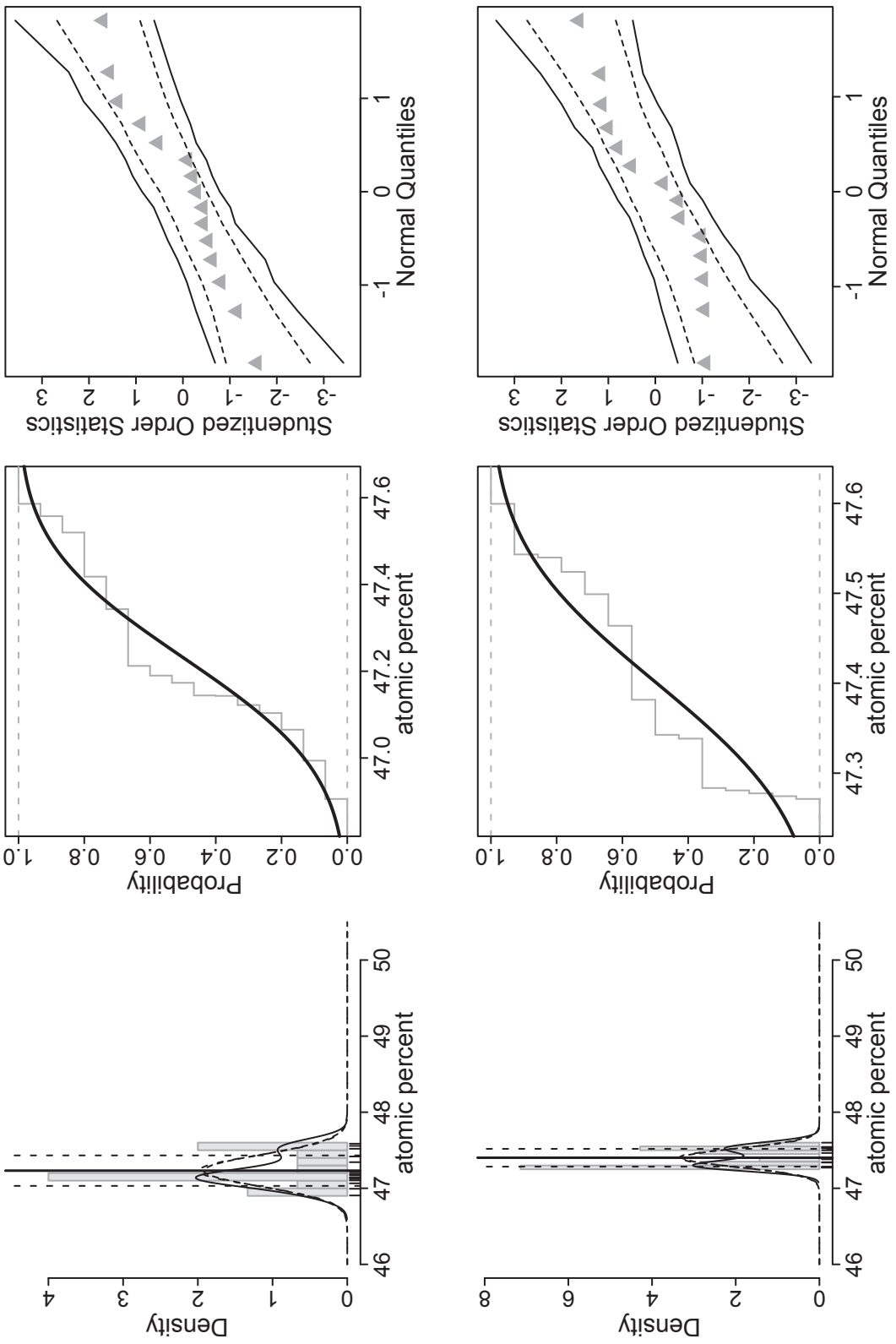

Statistical plots: Fe contents in pyrrhotites of the deposits at Isola (upper row) and Gula (bottom row). For the description of the statistical methods see the information given on top of this appendix (B). The data is given in mass percent (kg/100kg).

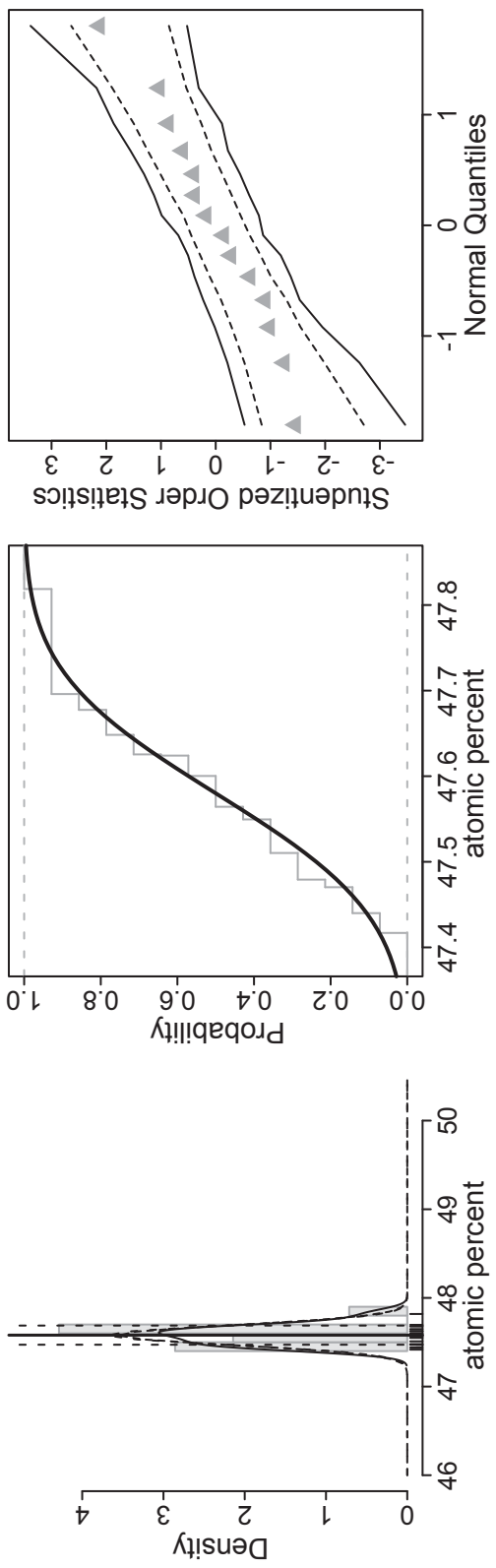

Statistical plots: Fe contents in pyrrhotites of the deposits at Guaifola. For the description of the statistical methods see the information given on top of this appendix (B). The data is given in mass percent (kg/100kg).

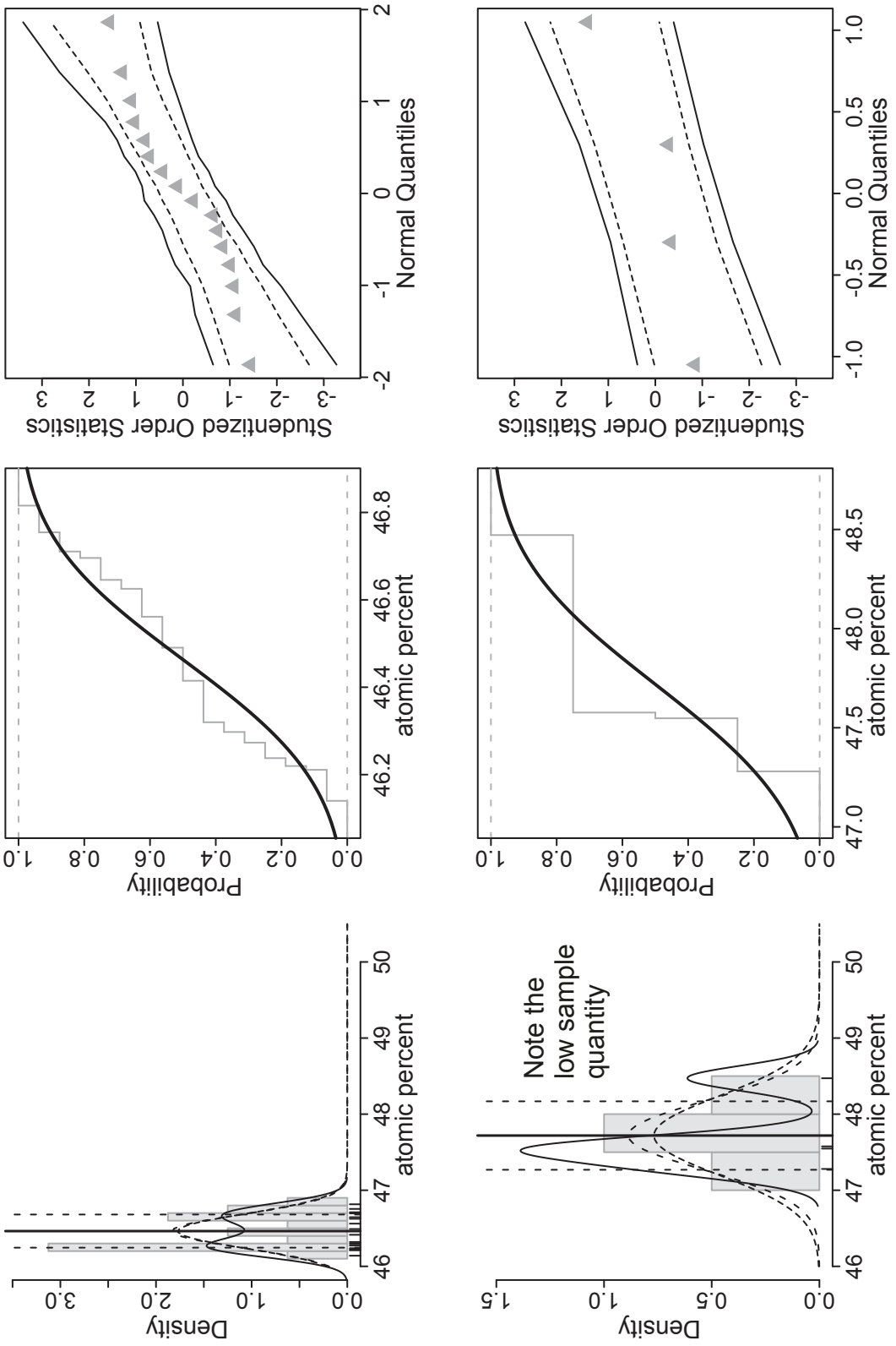

Statistical plots: Fe contents in pyrrhotites of the deposits at Campello Monti (upper row) and Penninetto (bottom row). For the description of the statistical methods see the information given on top of this appendix (B). The data is given in mass percent (kg/100kg).

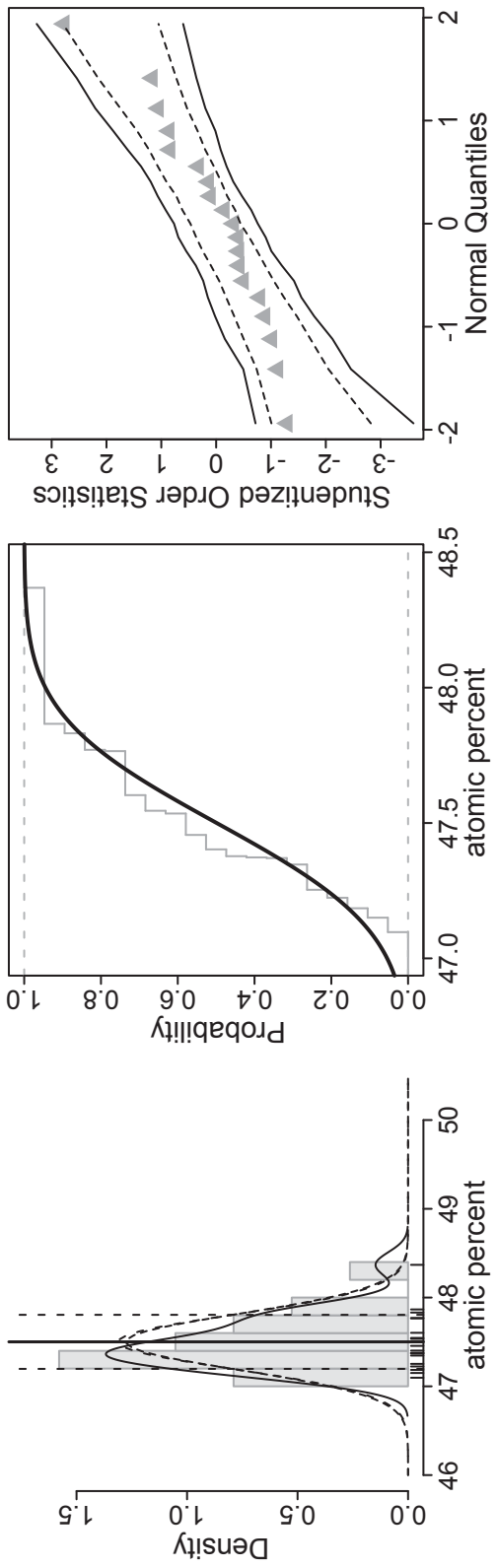

Statistical plots: Fe contents in pyrrhotites of the deposits at Alpe Laghetto. For the description of the statistical methods see the information given on top of this appendix (B). The data is given in mass percent (kg/100kg).

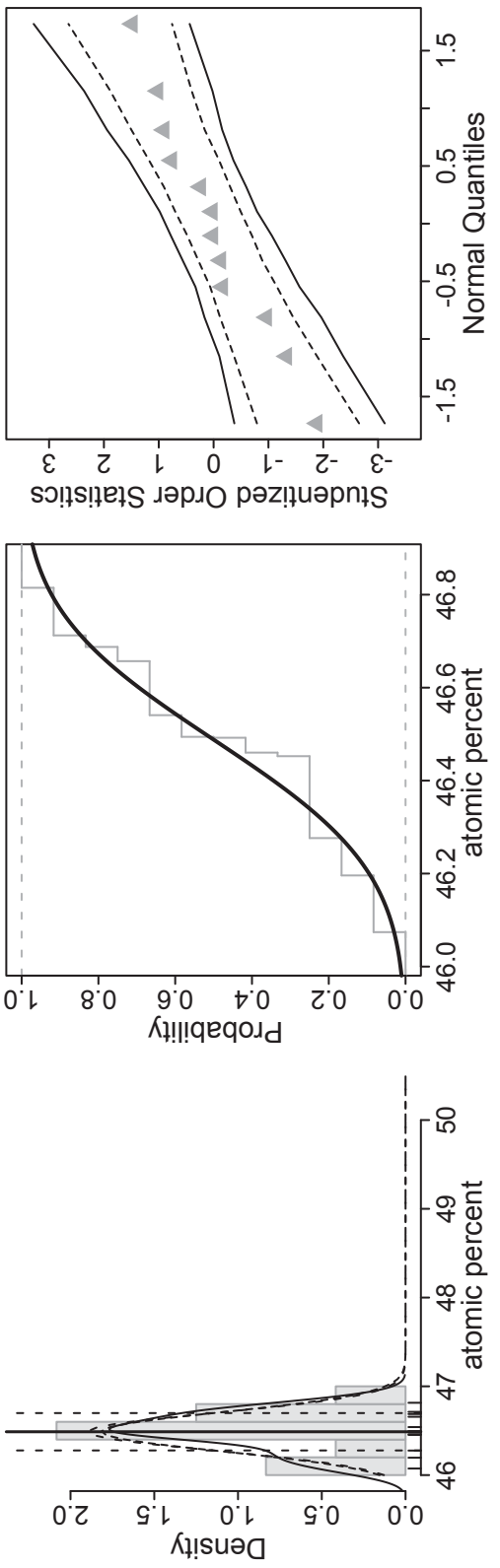

Statistical plots: Fe contents in pyrrhotites of the deposits at Piancone la Frera (upper row) and Fei di Doccio (bottom row). For the description of the statistical methods see the information given on top of this appendix (B). The data is given in mass percent (kg/100kg).

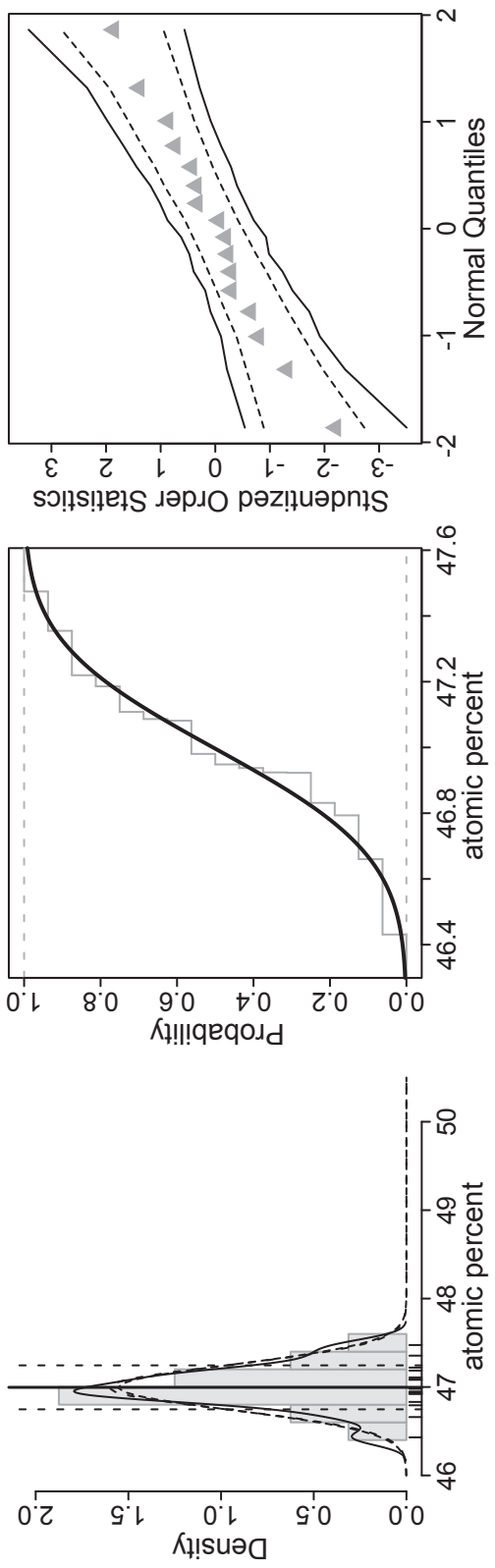

Statistical plots: Fe contents in pyrrhotites of the deposits at Bec d' Ovaga. For the description of the statistical methods see the information given on top of this appendix (B). The data is given in mass percent (kg/100kg).

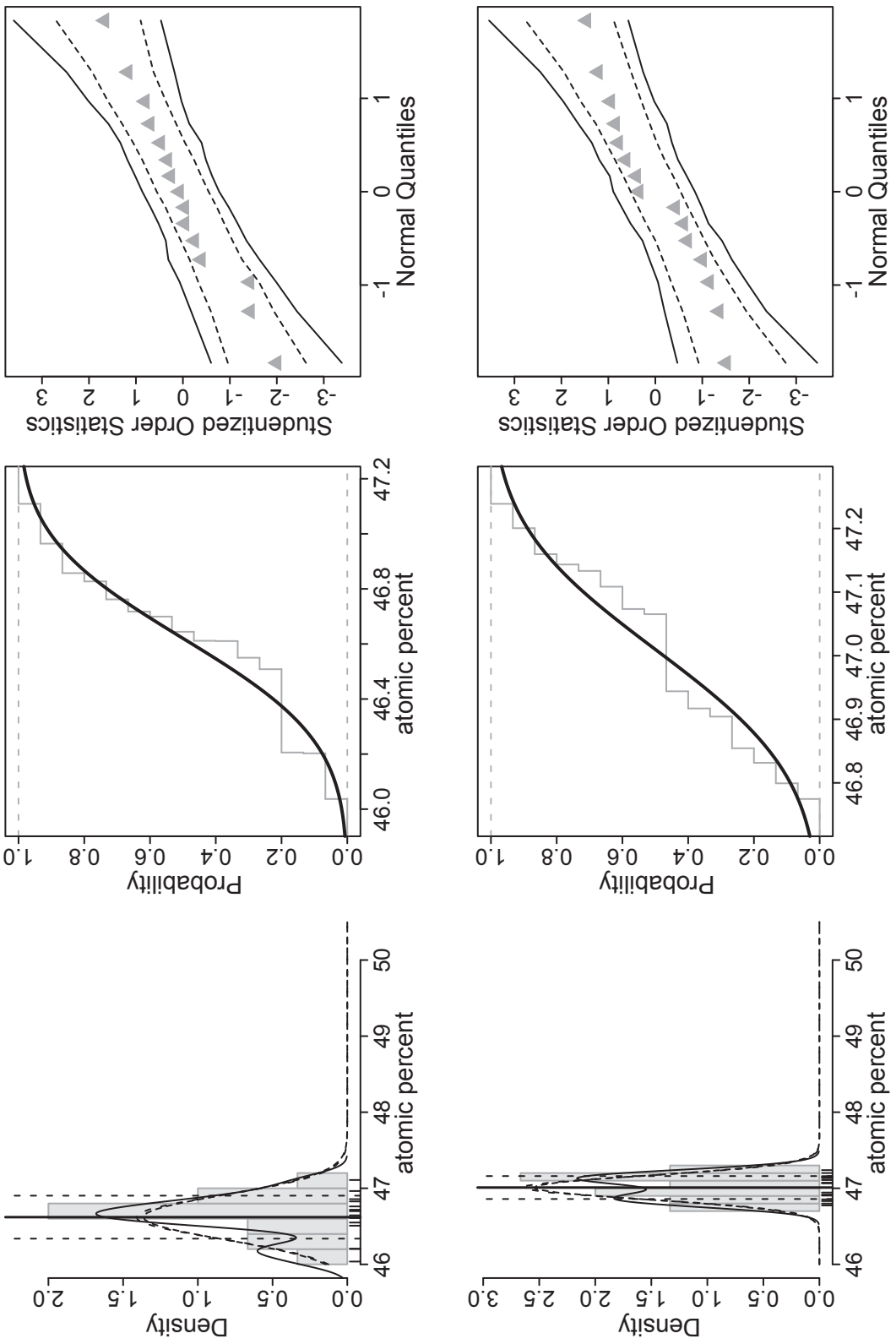

Statistical plots: Fe contents in pyrrhotites of the deposits at Sella Bassa (upper row) and Castello di Gavala (bottom row). For the description of the statistical methods see the information given on top of this appendix (B). The data is given in mass percent (kg/100kg).

B.2. S in pyrrhotite

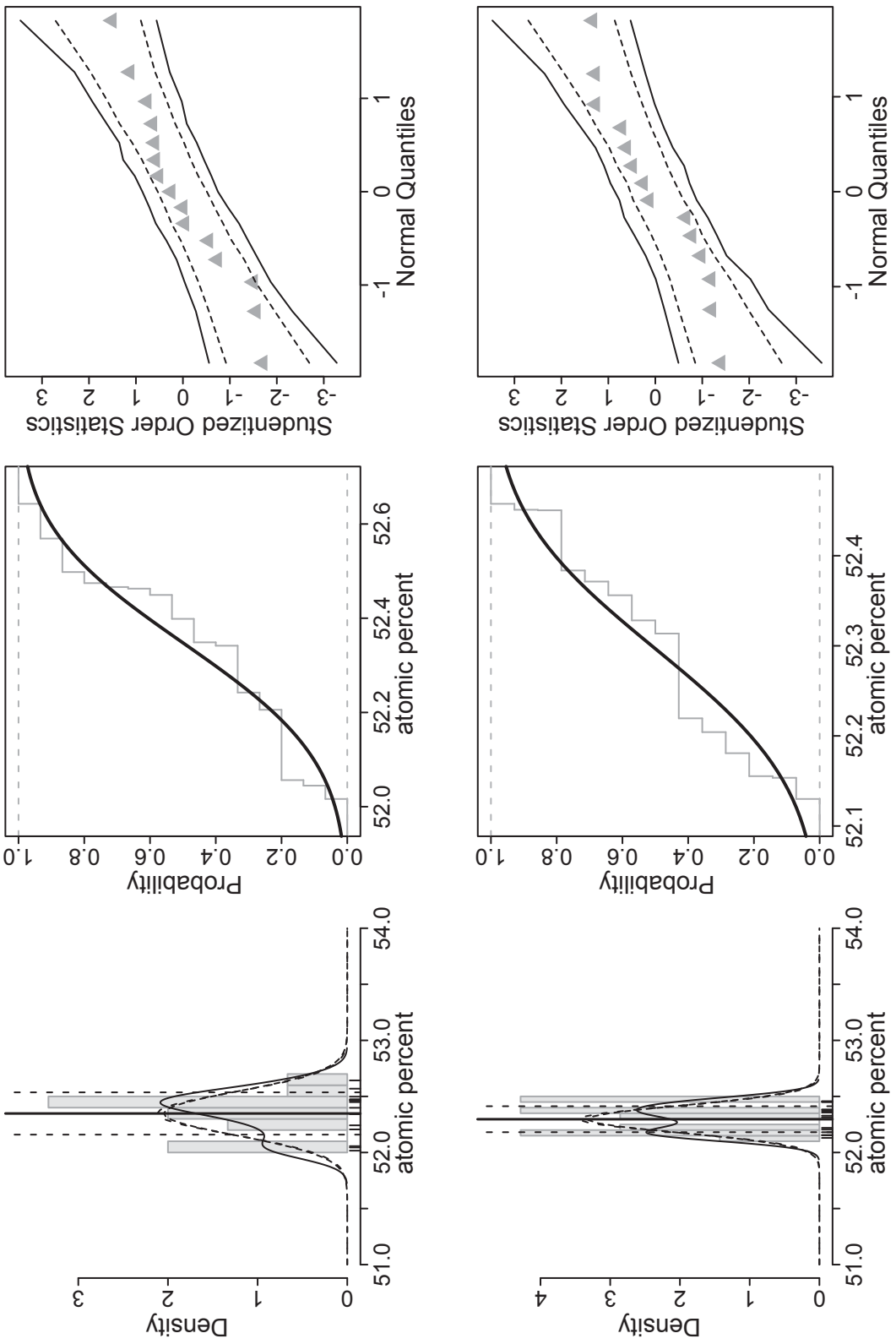

Statistical plots: S contents in pyrrhotites of the deposits at Isola (upper row) and Gula (bottom row). For the description of the statistical methods see the information given on top of this appendix (B). The data is given in mass percent (kg/100kg).

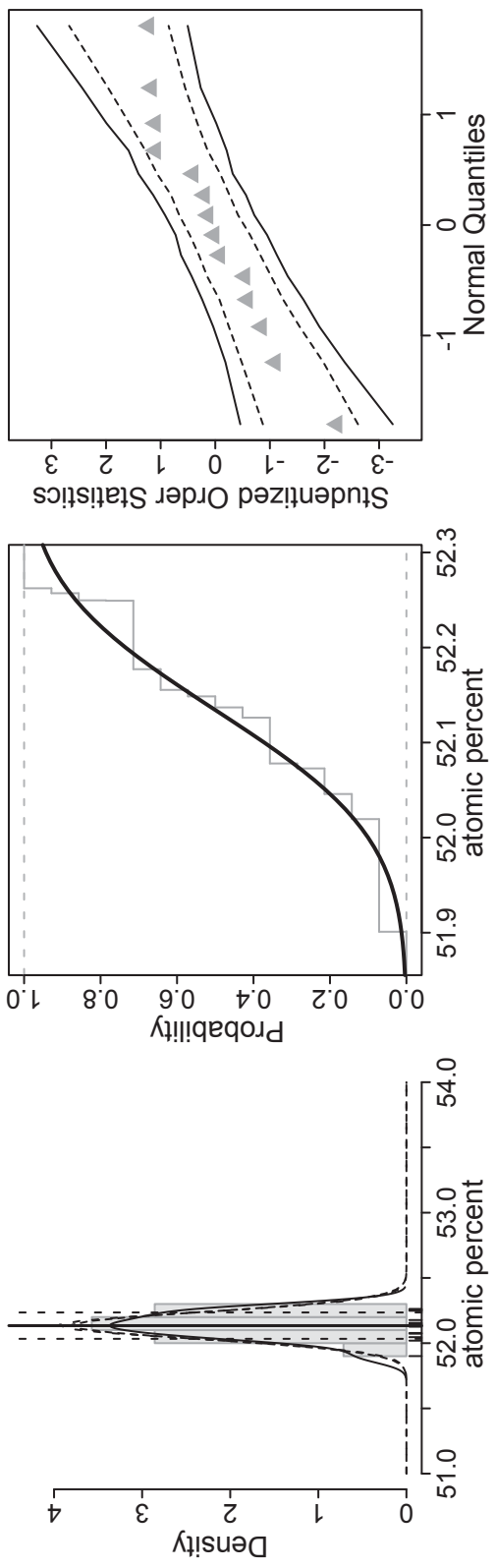

Statistical plots: S contents in pyrrhotites of the deposits at Guaifola. For the description of the statistical methods see the information given on top of this appendix (B). The data is given in mass percent (kg/100kg).

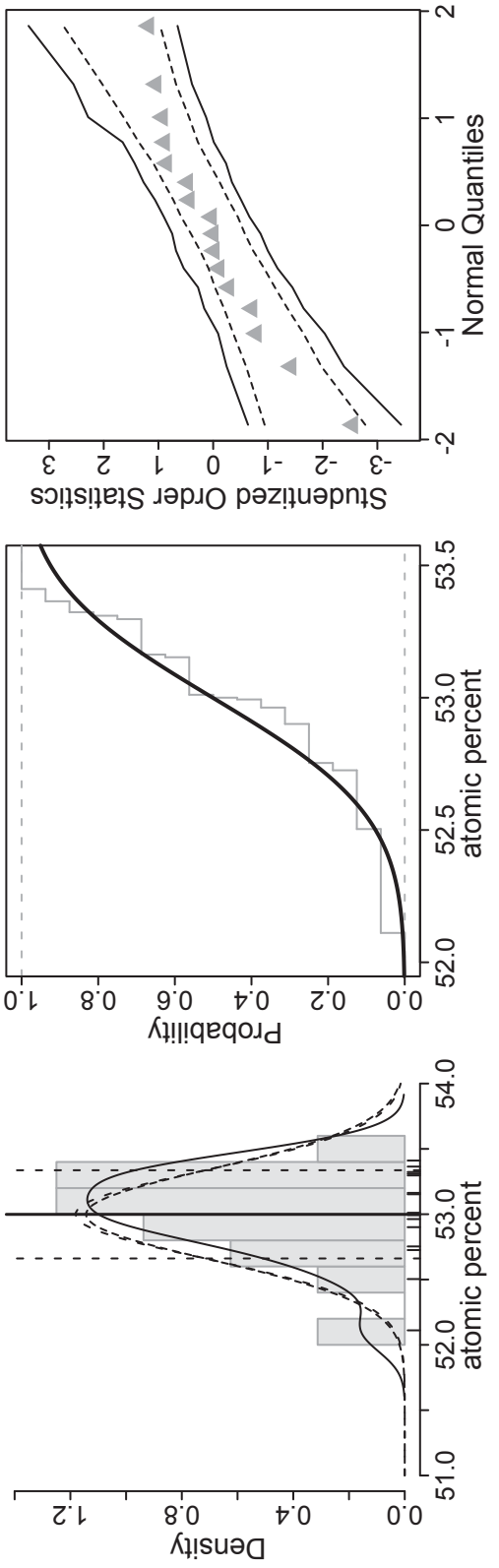

Statistical plots: S contents in pyrrhotites of the deposits at Campello Monti (upper row) and Penninetto (bottom row). For the description of the statistical methods see the information given on top of this appendix (B). The data is given in mass percent (kg/100kg).

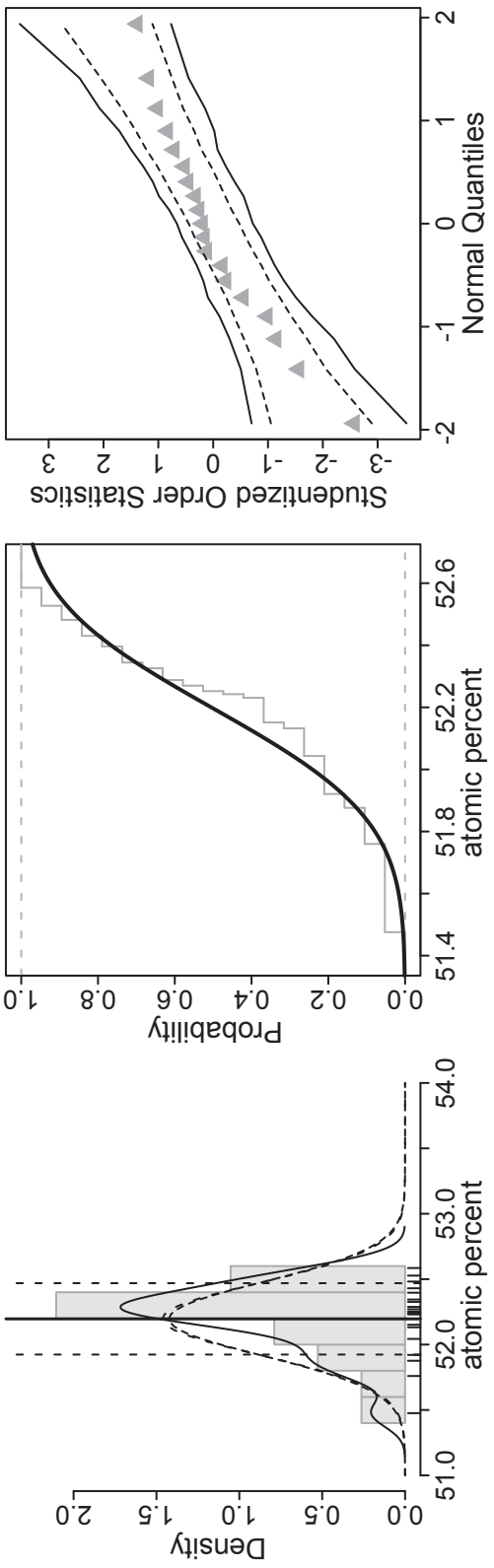

Statistical plots: S contents in pyrrhotites of the deposits at Alpe Laghetto. For the description of the statistical methods see the information given on top of this appendix (B). The data is given in mass percent (kg/100kg).

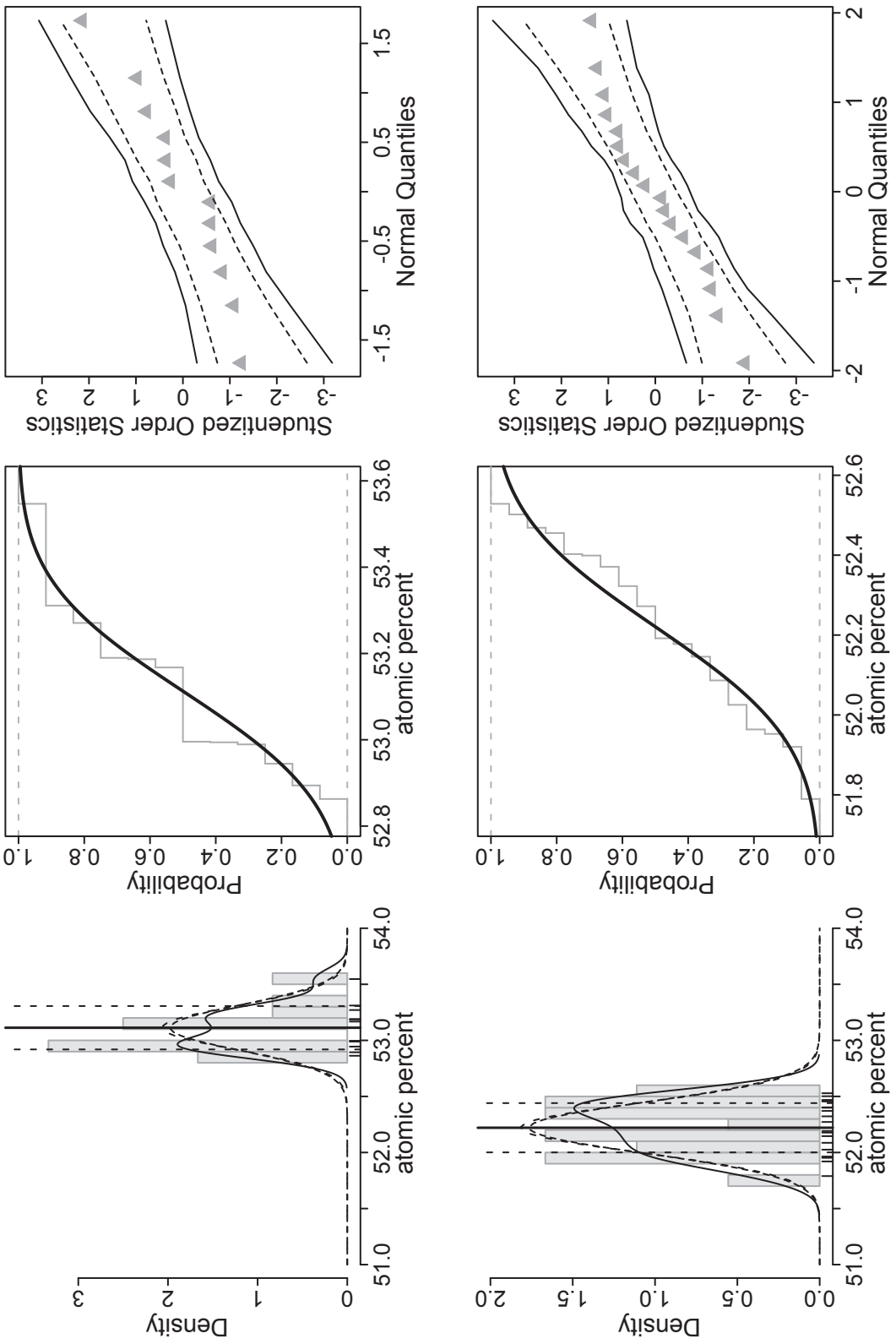

Statistical plots: S contents in pyrrhotites of the deposits at Piancone la Frera (upper row) and Fei di Doccio (bottom row). For the description of the statistical methods see the information given on top of this appendix (B). The data is given in mass percent (kg/100kg).

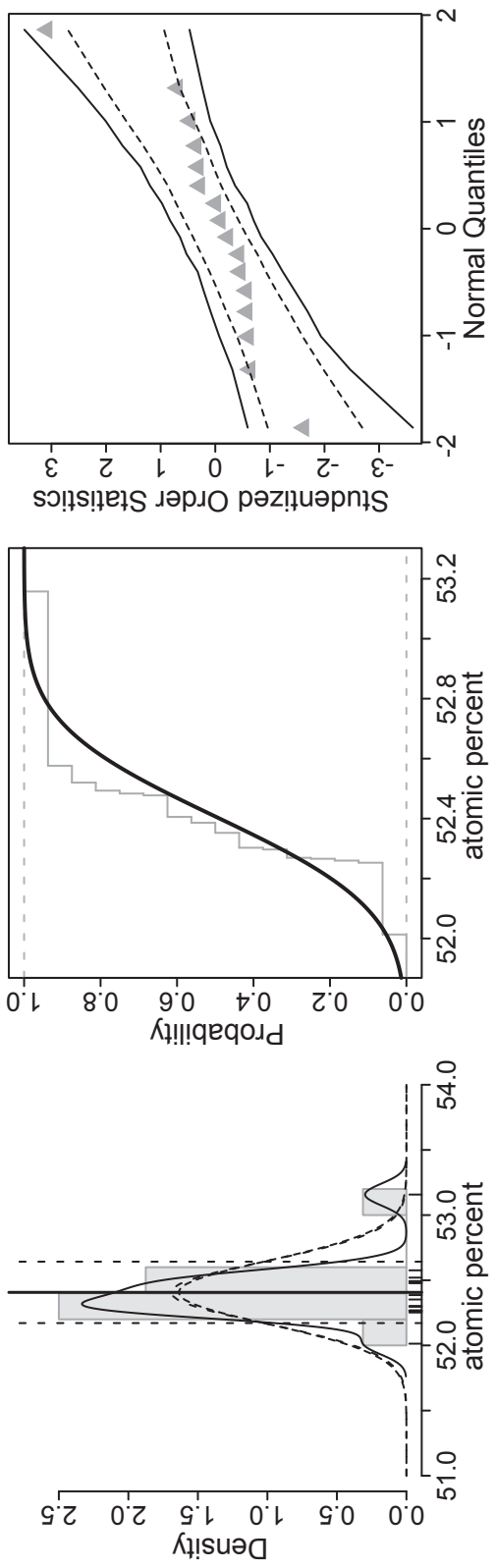

Statistical plots: S contents in pyrrhotites of the deposits at Bec d' Ovaga. For the description of the statistical methods see the information given on top of this appendix (B). The data is given in mass percent (kg/100kg).

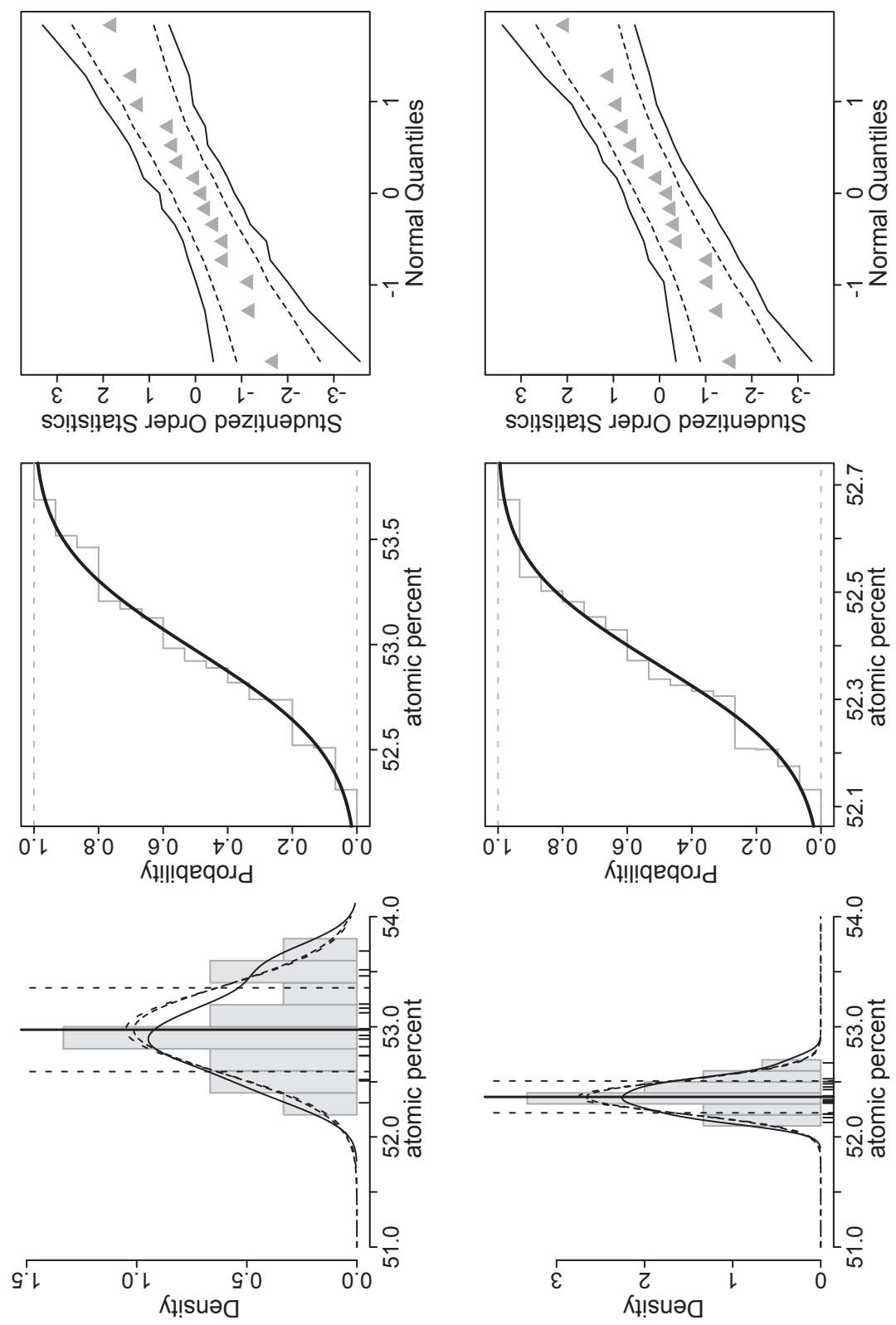

Statistical plots: S contents in pyrrhotites of the deposits at Sella Bassa (upper row) and Castello di Gavala (bottom row). For the description of the statistical methods see the information given on top of this appendix (B). The data is given in mass percent (kg/100kg).

B.3. Ni in pendlandite

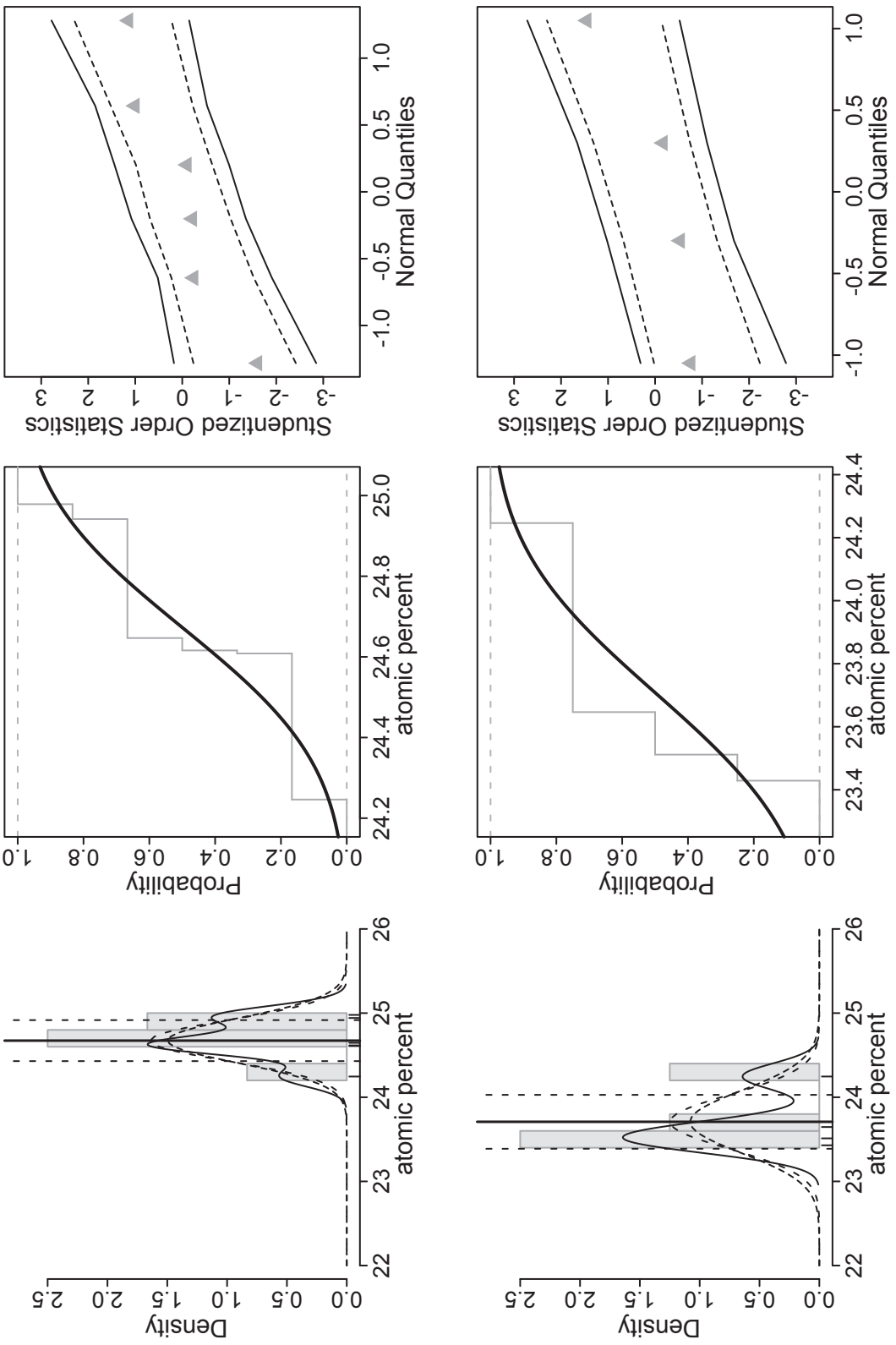

Statistical plots: Ni contents in pendlandites of the deposits at Isola (upper row) and Gula (bottom row). For the description of the statistical methods see the information given on top of this appendix (B). The data is given in mass percent (kg/100kg).

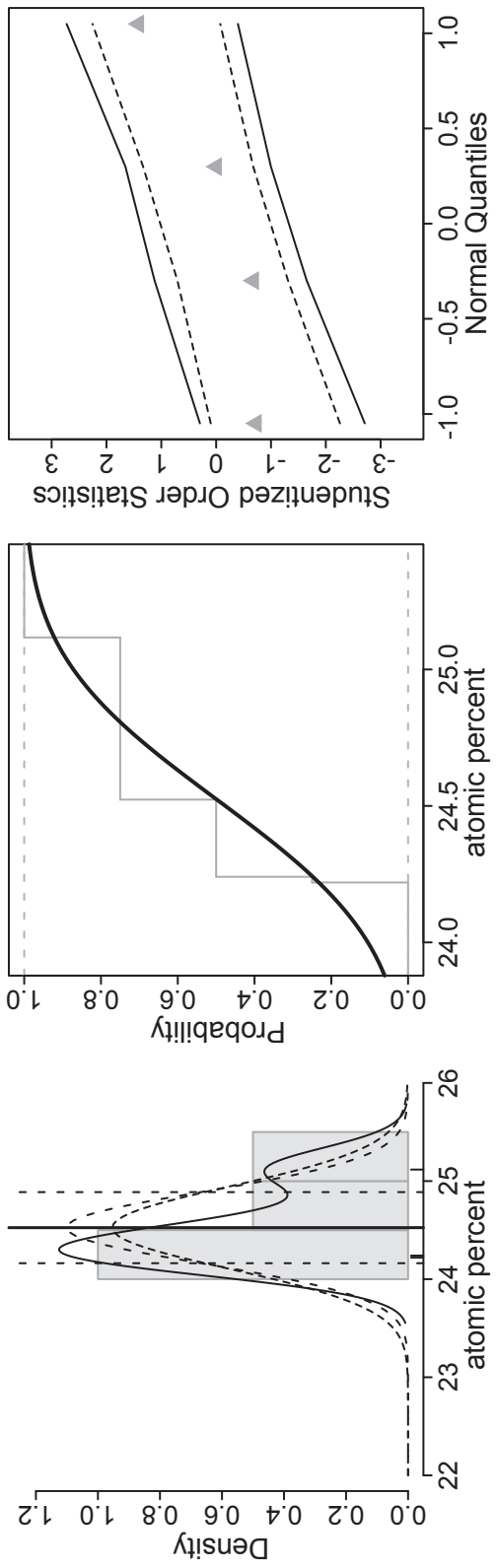

Statistical plots: Ni contents in pendlandites of the deposits at Guaifola. For the description of the statistical methods see the information given on top of this appendix (B). The data is given in mass percent (kg/100kg).

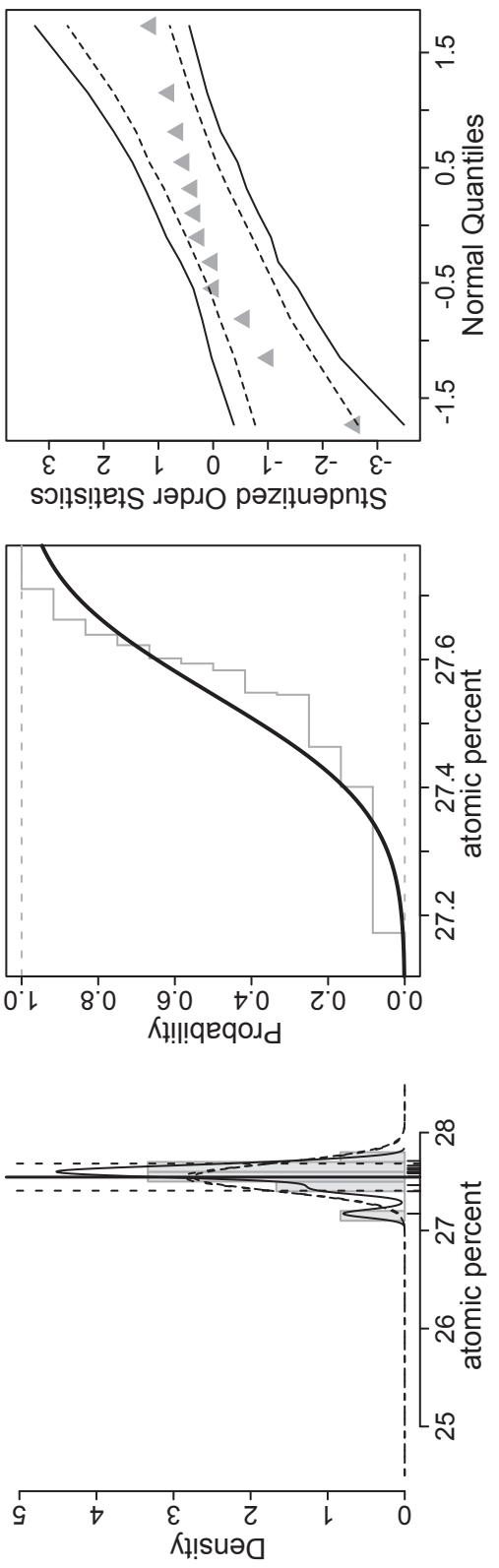

Statistical plots: Ni contents in pendlandites of the deposits at Campello Monti (upper row) and Penninetto (bottom row). For the description of the statistical methods see the information given on top of this appendix (B). The data is given in mass percent (kg/100kg).

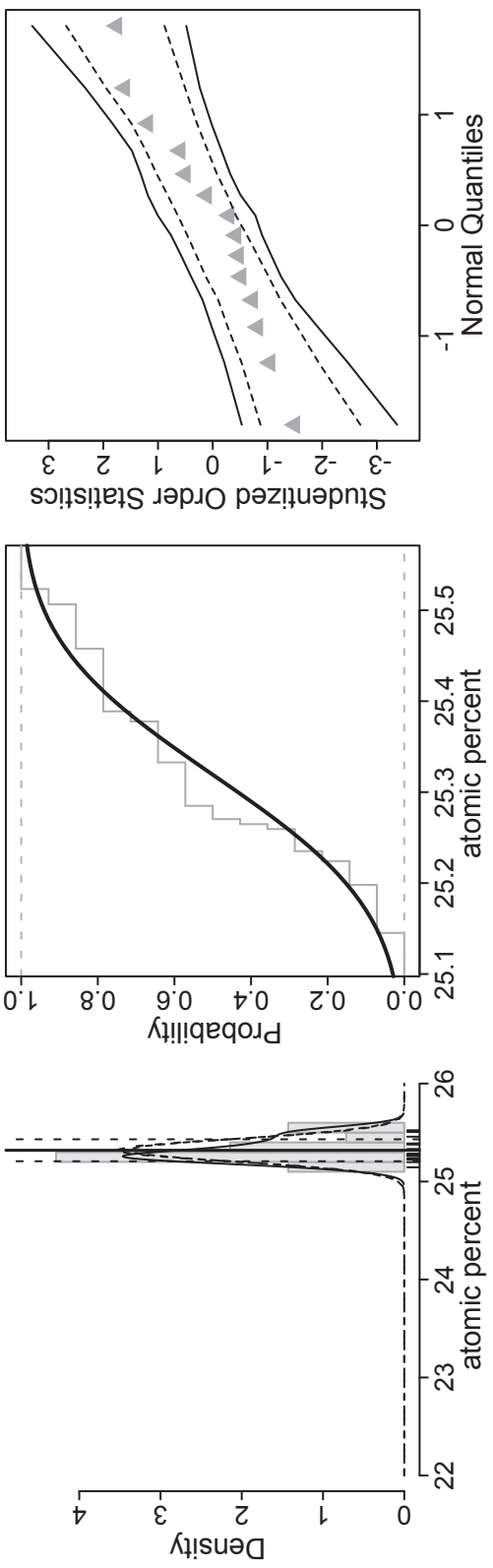

Statistical plots: Ni contents in pendlandites of the deposits at Alpe Laghetto. For the description of the statistical methods see the information given on top of this appendix (B). The data is given in mass percent (kg/100kg).

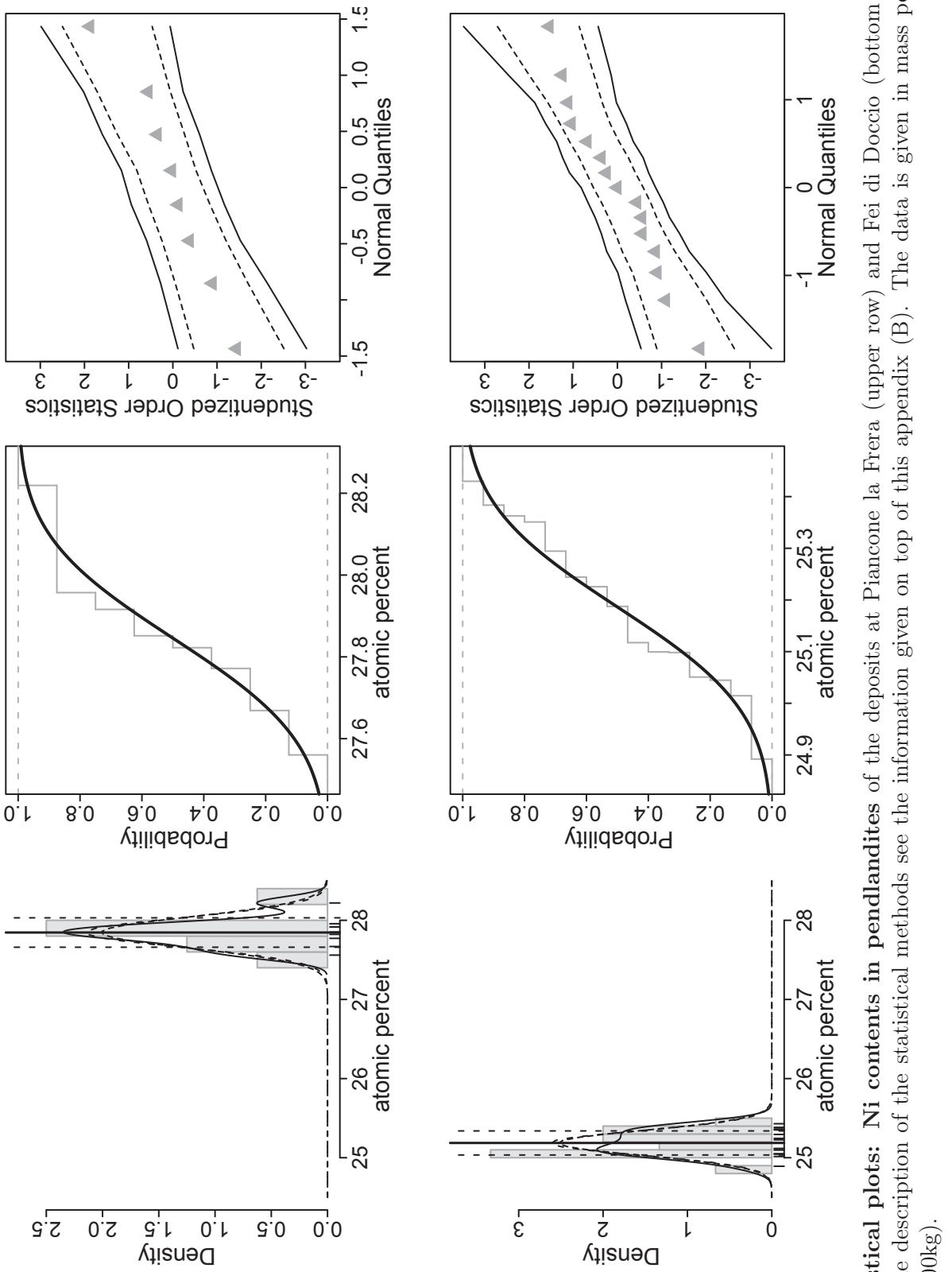

Statistical plots: Ni contents in pendlandites of the deposits at Piancone la Frera (upper row) and Fei di Doccio (bottom row). For the description of the statistical methods see the information given on top of this appendix (B). The data is given in mass percent (kg/100kg).

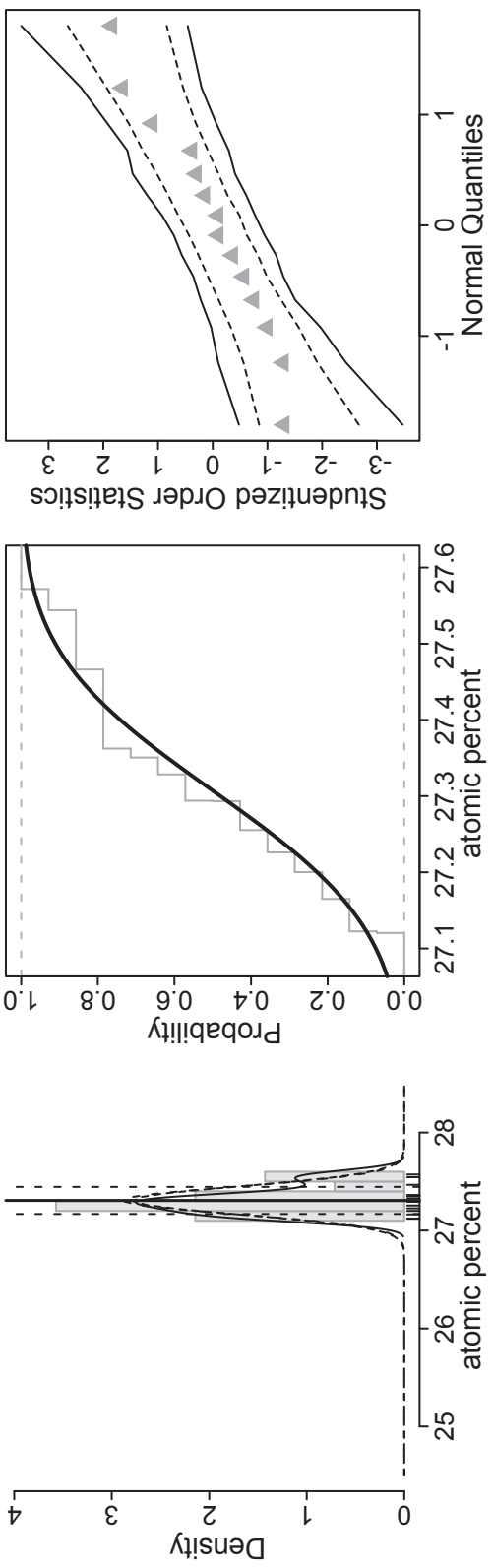

Statistical plots: Ni contents in pendlandites of the deposits at Bec d' Ovaga. For the description of the statistical methods see the information given on top of this appendix (B). The data is given in mass percent (kg/100kg).

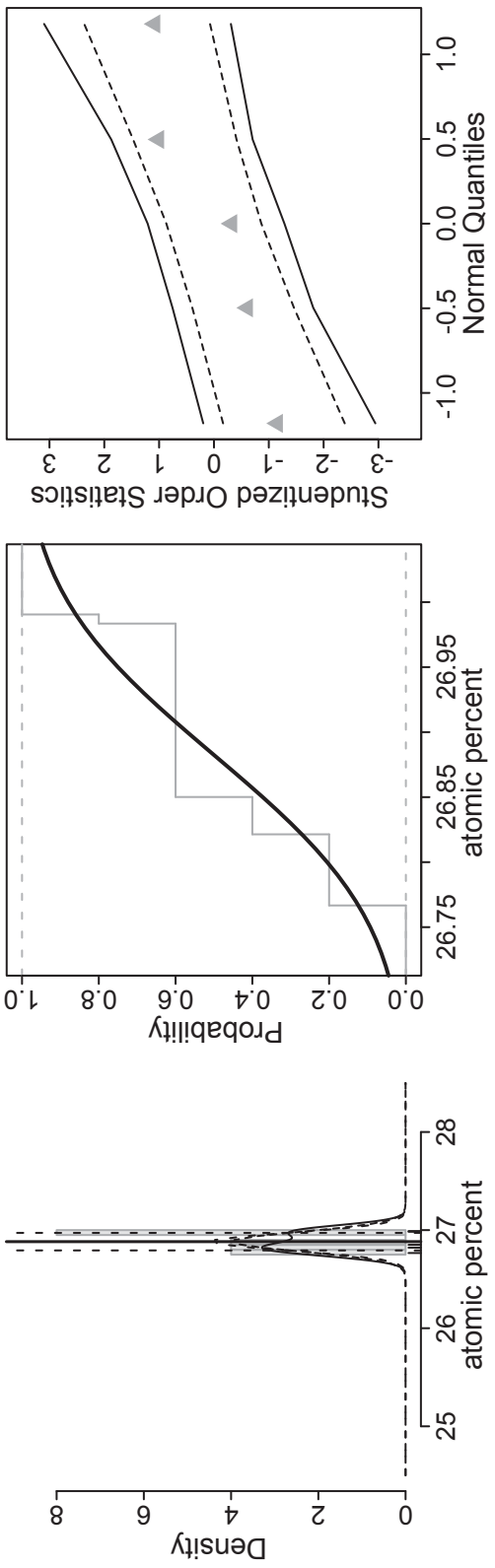

Statistical plots: Ni contents in pendlandites of the deposits at Castello di Gavala. For the description of the statistical methods see the information given on top of this appendix (B). The data is given in mass percent (kg/100kg).

B.4. Fe in pendlandite

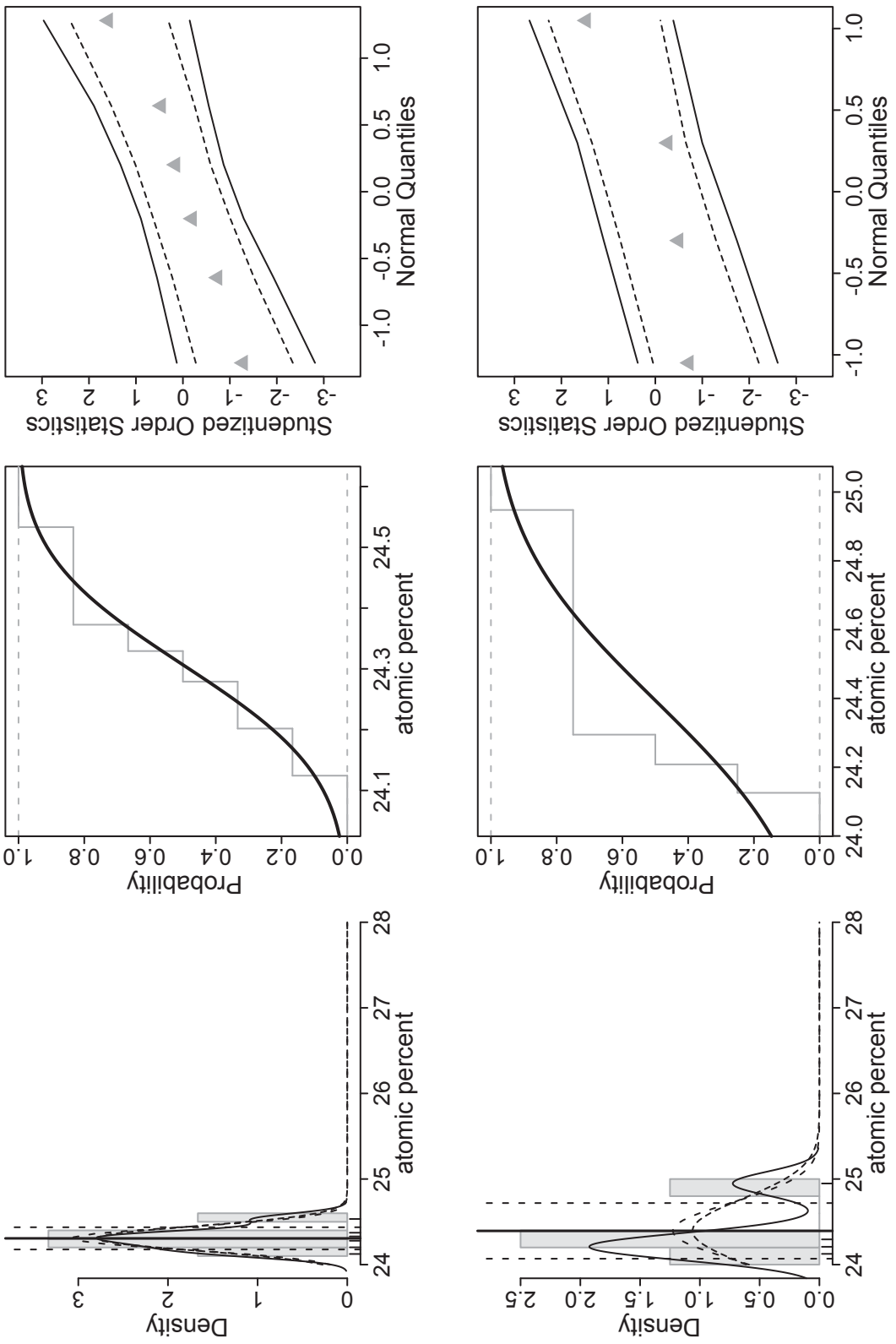

Statistical plots: Fe contents in pendlandites of the deposits at Isola (upper row) and Gula (bottom row). For the description of the statistical methods see the information given on top of this appendix (B). The data is given in mass percent (kg/100kg).

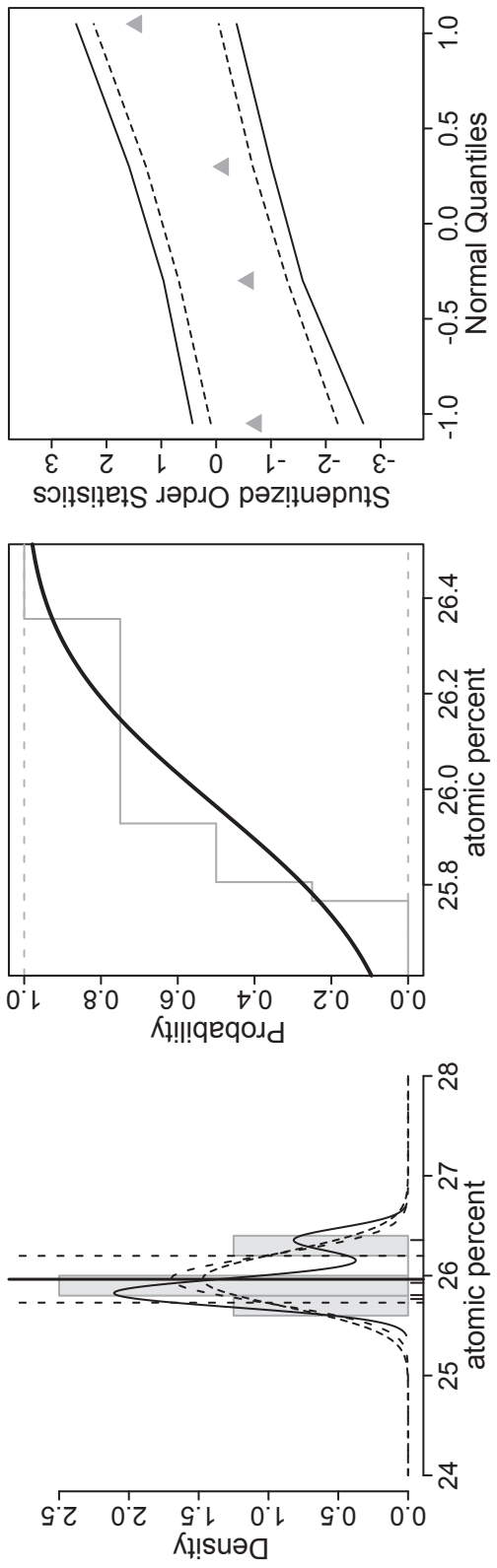

Statistical plots: Fe contents in pendlandites of the deposits at Guaifola. For the description of the statistical methods see the information given on top of this appendix (B). The data is given in mass percent (kg/100kg).

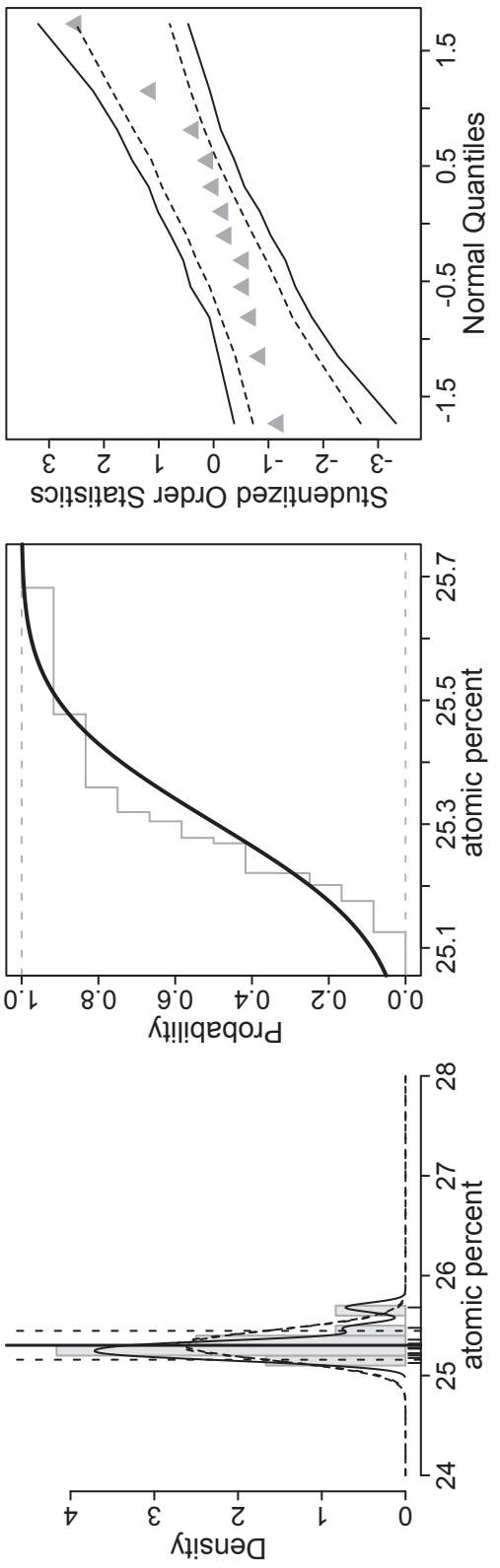

Statistical plots: Fe contents in pendlandites of the deposits at Campello Monti (upper row) and Penninetto (bottom row). For the description of the statistical methods see the information given on top of this appendix (B). The data is given in mass percent (kg/100kg).

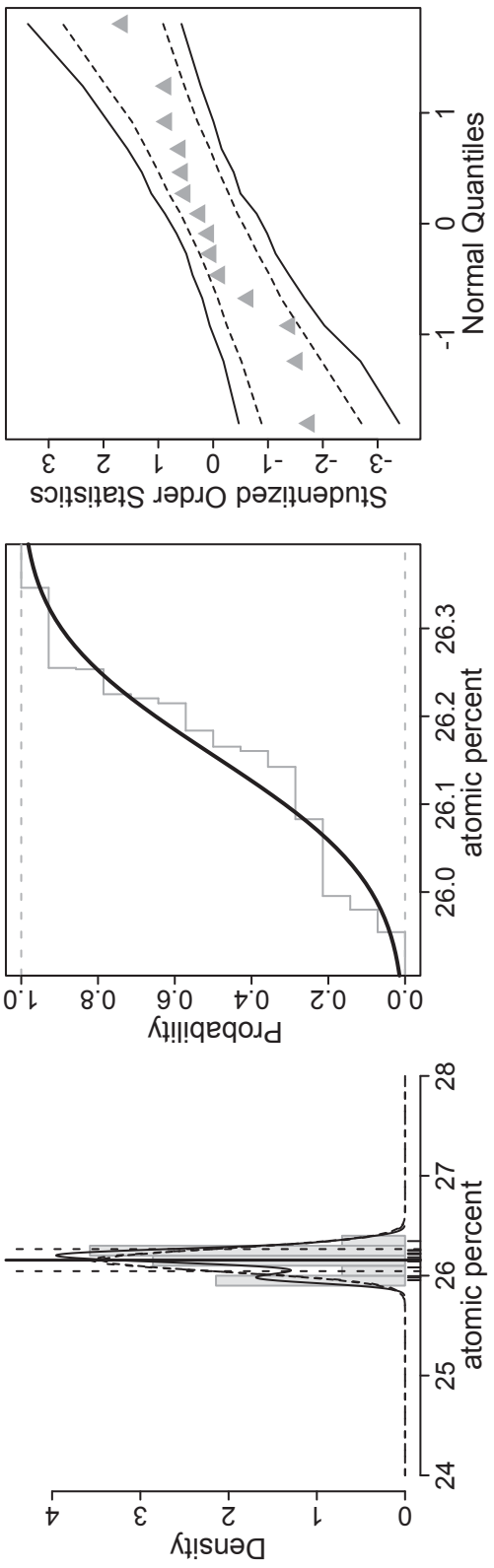

Statistical plots: Fe contents in pendlandites of the deposits at Alpe Laghetto. For the description of the statistical methods see the information given on top of this appendix (B). The data is given in mass percent (kg/100kg).

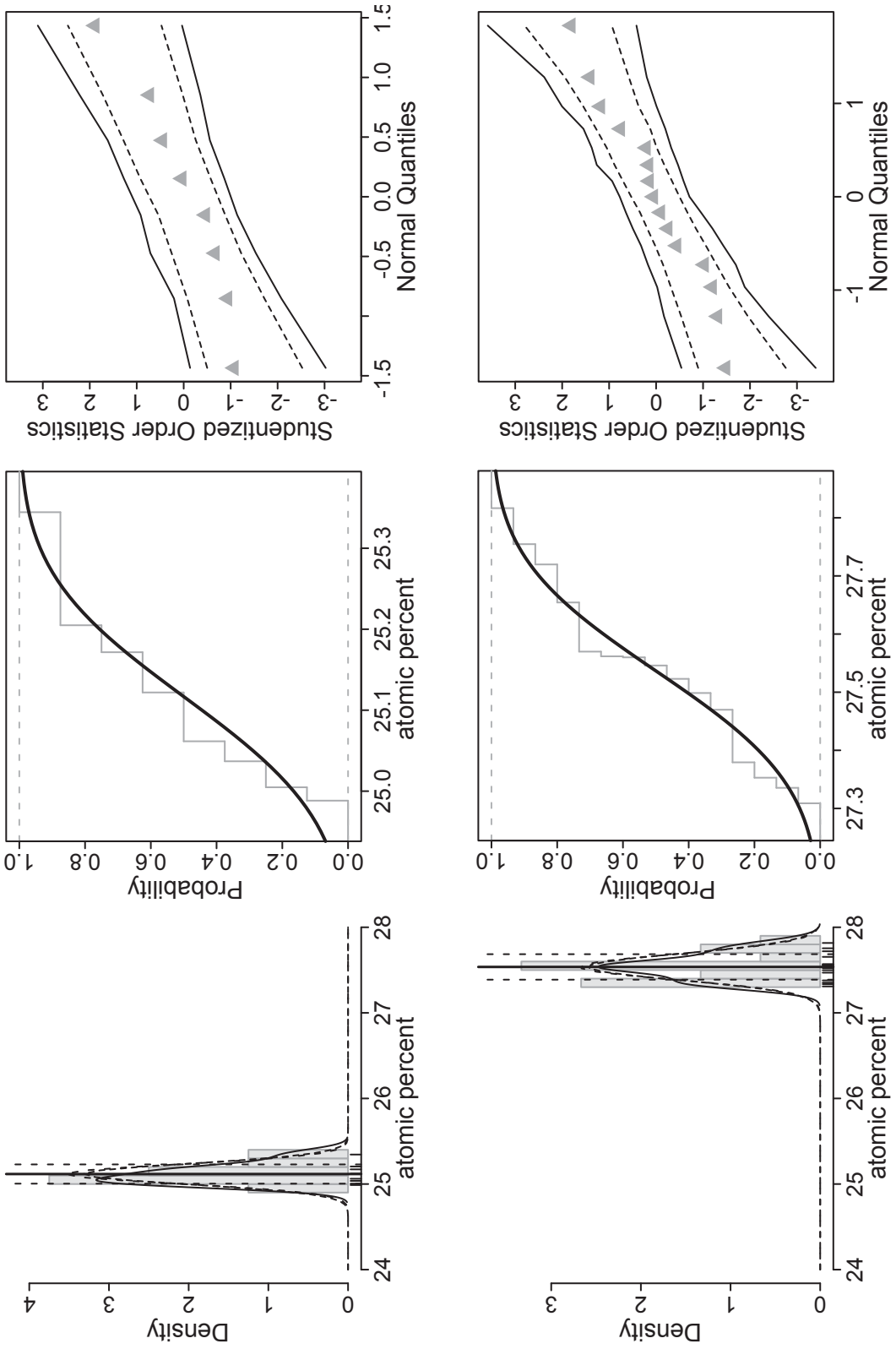

Statistical plots: Fe contents in pendlandites of the deposits at Piancone la Frera (upper row) and Fei di Doccio (bottom row). For the description of the statistical methods see the information given on top of this appendix (B). The data is given in mass percent (kg/100kg).

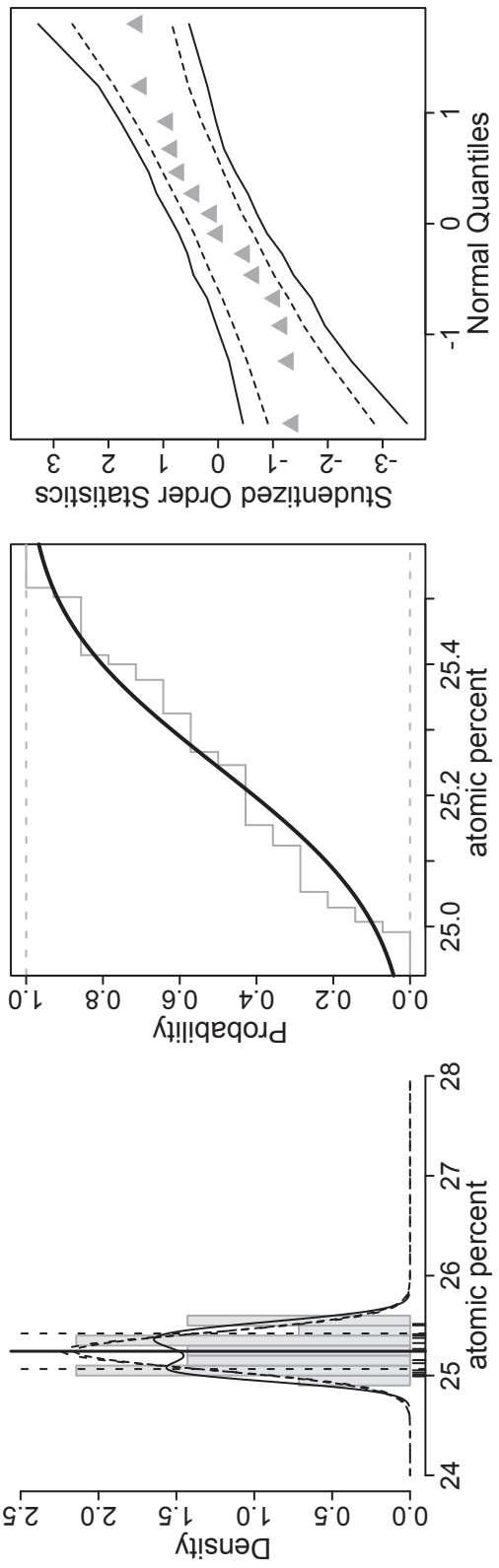

Statistical plots: Fe contents in pendlandites of the deposits at Bec d' Ovaga. For the description of the statistical methods see the information given on top of this appendix (B). The data is given in mass percent (kg/100kg).

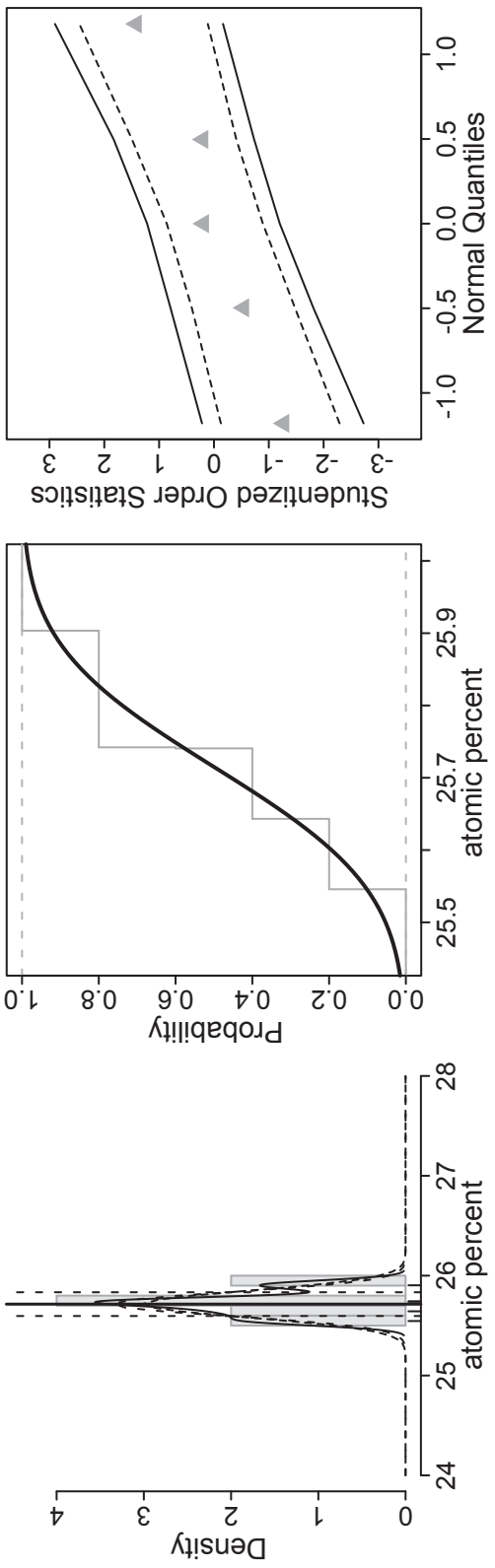

Statistical plots: Fe contents in pendlandites of the deposits at Castello di Gavala. For the description of the statistical methods see the information given on top of this appendix (B). The data is given in mass percent (kg/100kg).

B.5. S in pendlandite

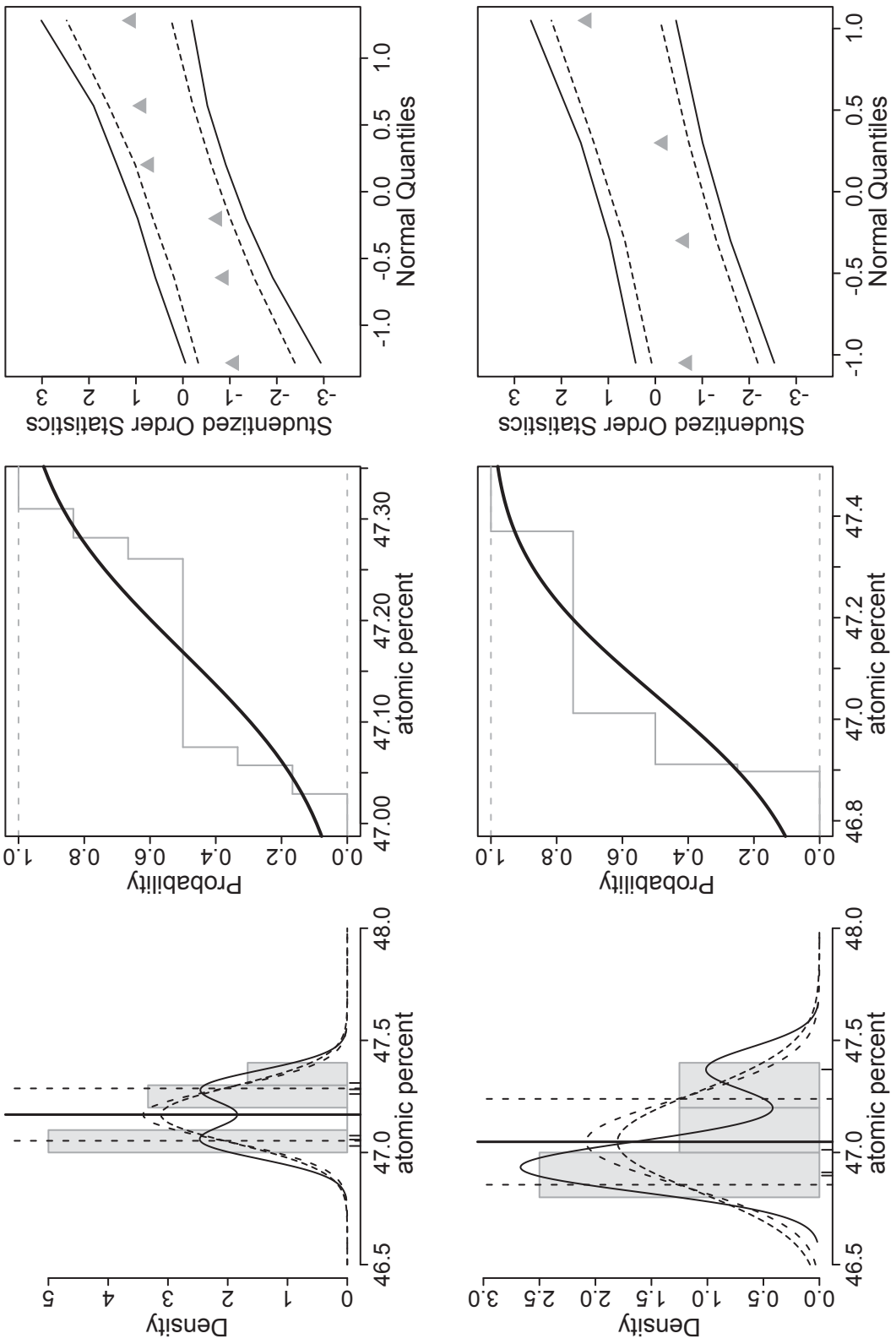

Statistical plots: S contents in pendlandites of the deposits at Isola (upper row) and Gula (bottom row). For the description of the statistical methods see the information given on top of this appendix (B). The data is given in mass percent (kg/100kg).

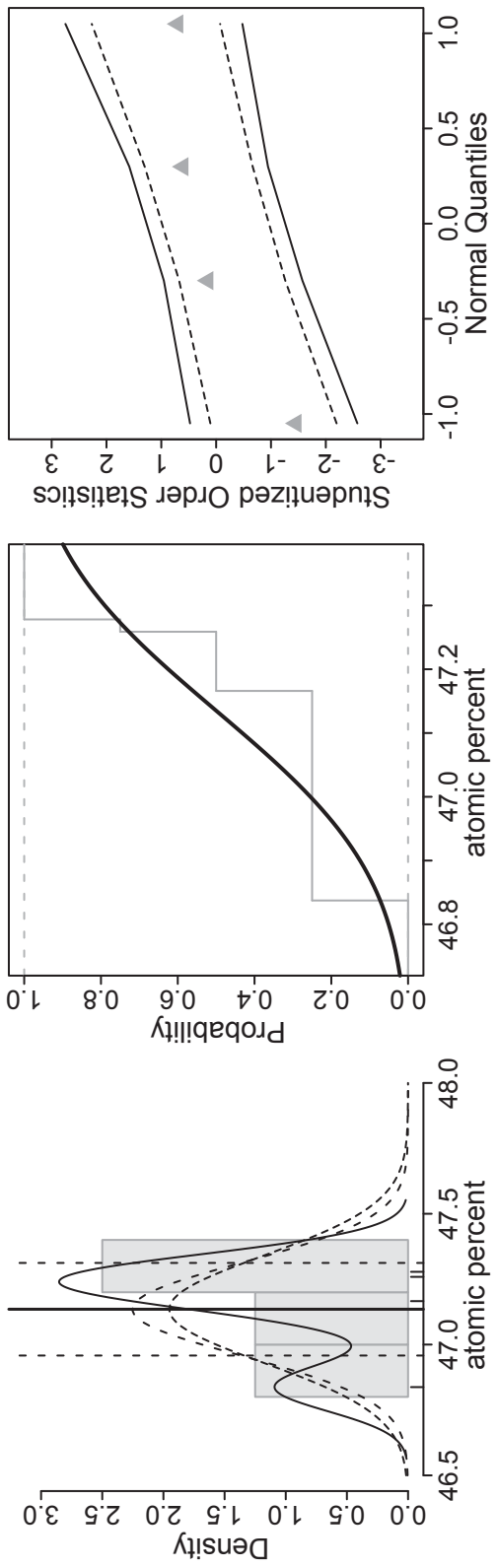

Statistical plots: S contents in pendlandites of the deposits at Guaifola. For the description of the statistical methods see the information given on top of this appendix (B). The data is given in mass percent (kg/100kg).

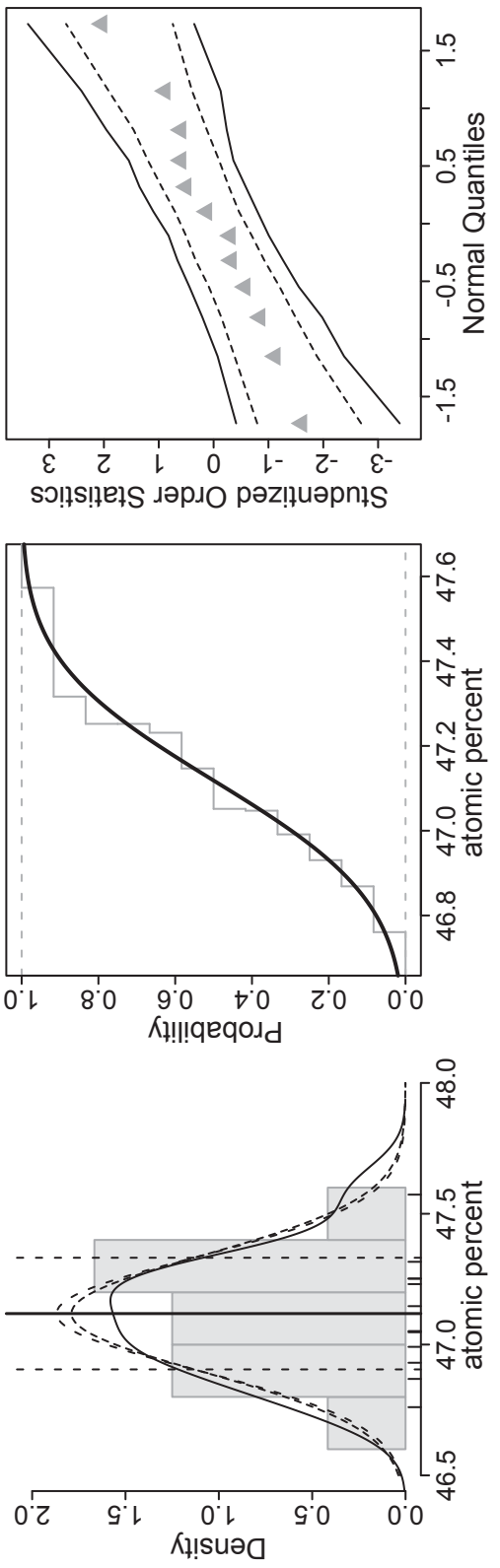

Statistical plots: S contents in pendlandites of the deposits at Campello Monti (upper row) and Penninetto (bottom row). For the description of the statistical methods see the information given on top of this appendix (B). The data is given in mass percent (kg/100kg).

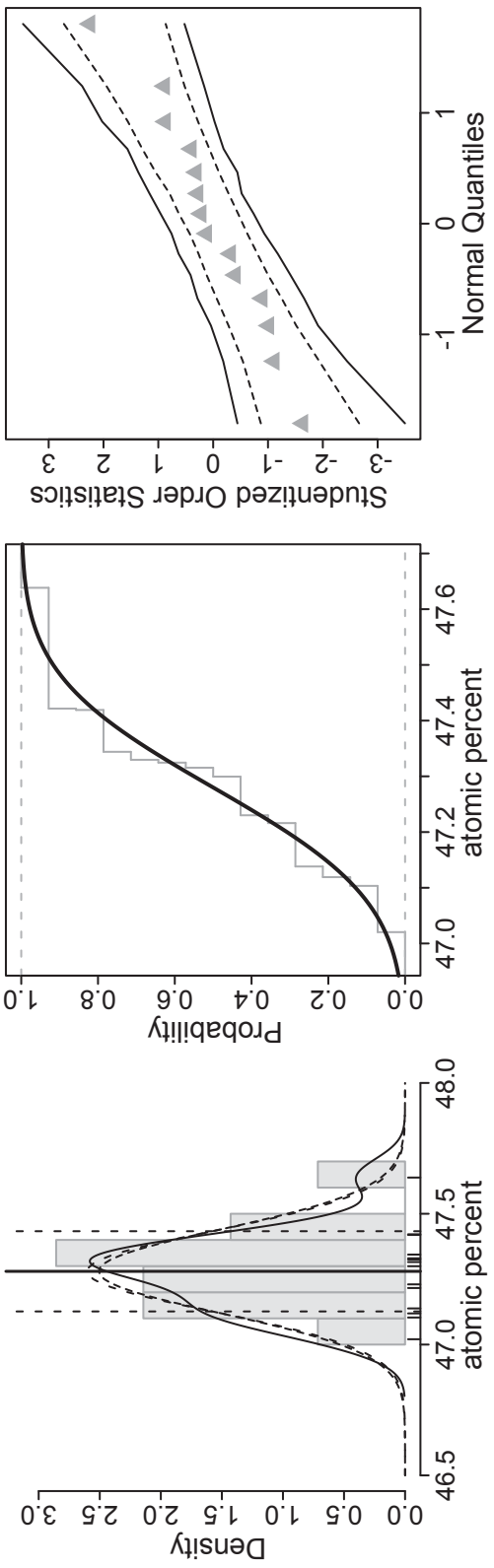

Statistical plots: S contents in pendlandites of the deposits at Alpe Laghetto. For the description of the statistical methods see the information given on top of this appendix (B). The data is given in mass percent (kg/100kg).

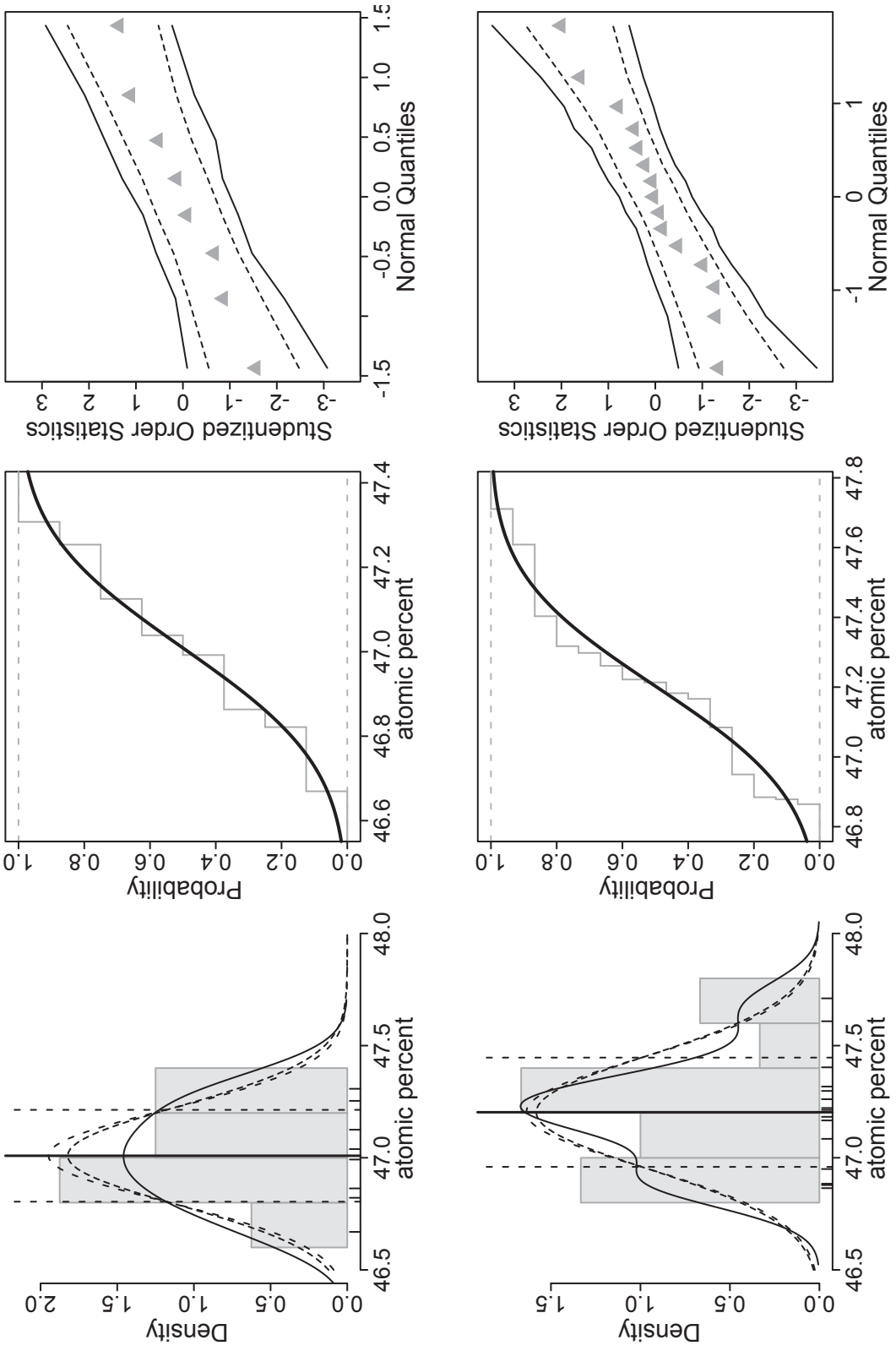

Statistical plots: S contents in pendlandites of the deposits at Piancone la Frera (upper row) and Fei di Doccio (bottom row). For the description of the statistical methods see the information given on top of this appendix (B). The data is given in mass percent (kg/100kg).

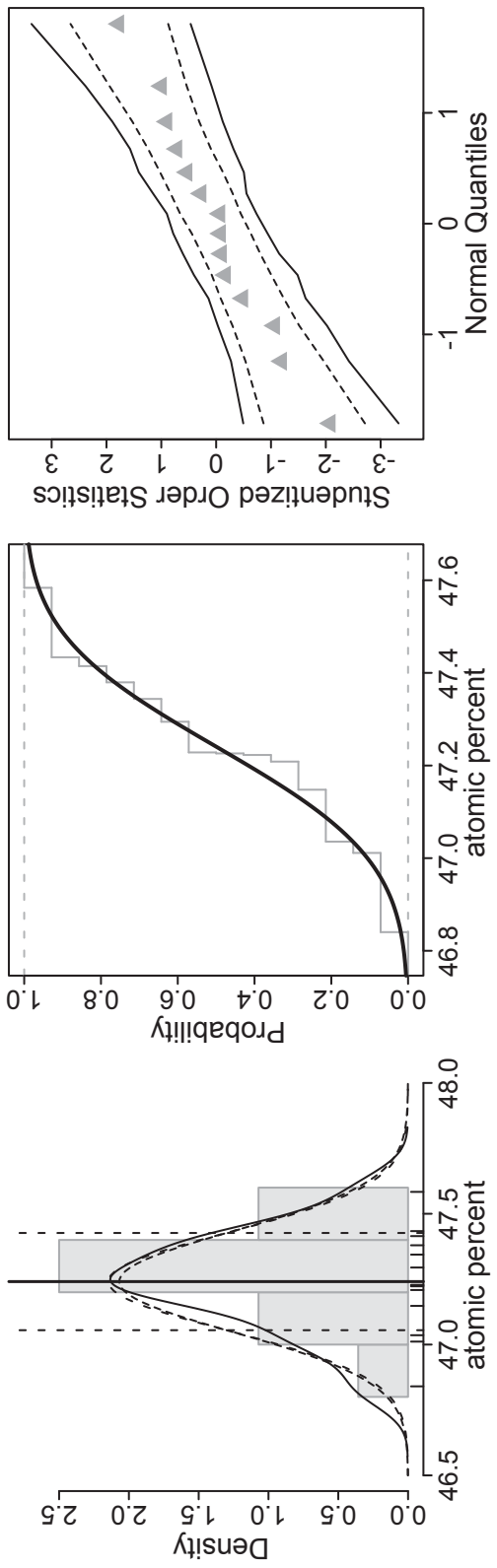

Statistical plots: S contents in pendlandites of the deposits at Bec d' Ovaga. For the description of the statistical methods see the information given on top of this appendix (B). The data is given in mass percent (kg/100kg).

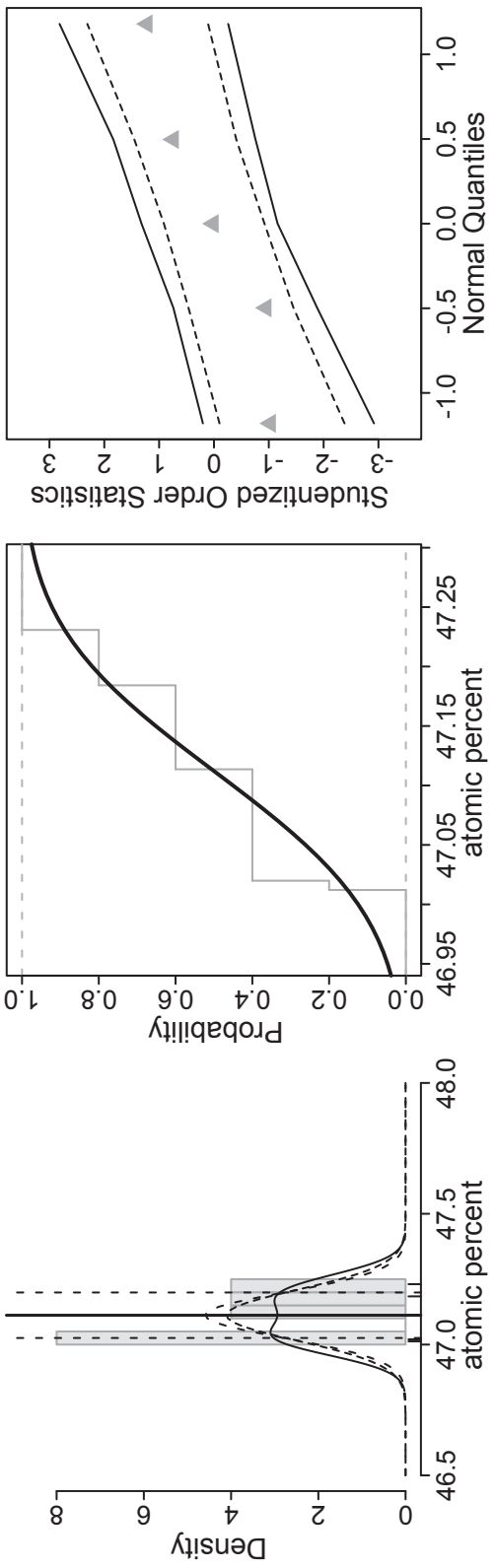

Statistical plots: S contents in pendlandites of the deposits at Castello di Gavala. For the description of the statistical methods see the information given on top of this appendix (B). The data is given in mass percent (kg/100kg).

B.6. Co in pendlandite

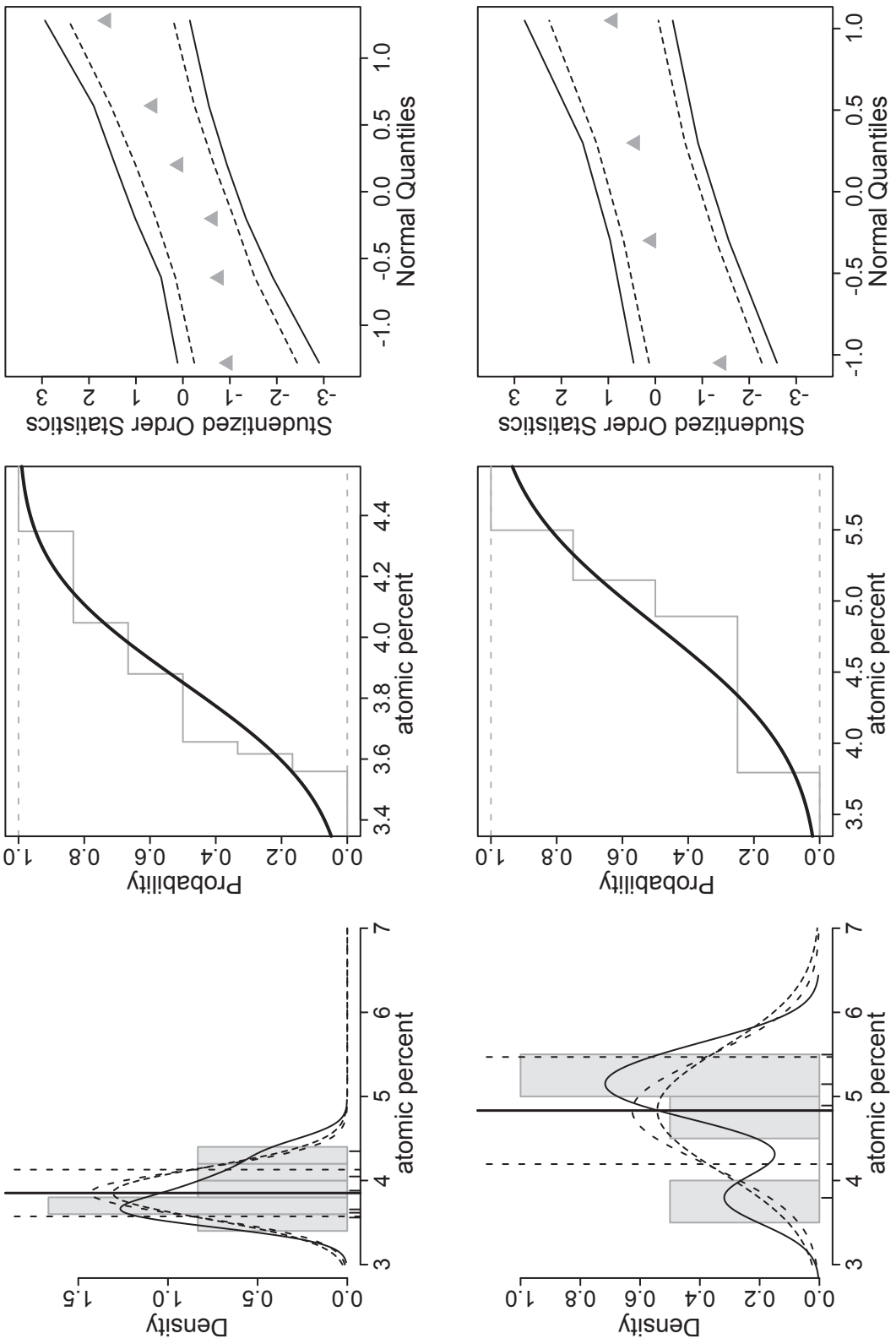

Statistical plots: Co contents in pendlandites of the deposits at Isola (upper row) and Gula (bottom row). For the description of the statistical methods see the information given on top of this appendix (B). The data is given in mass percent (kg/100kg).

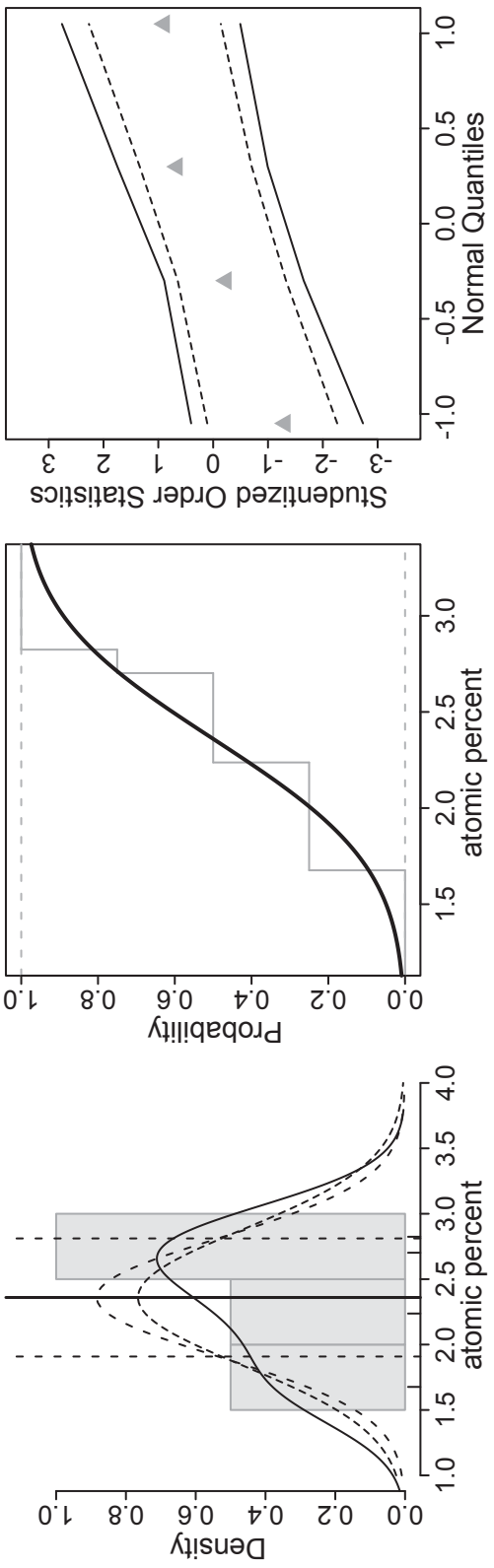

Statistical plots: Co contents in pendlandites of the deposits at Guaifola. For the description of the statistical methods see the information given on top of this appendix (B). The data is given in mass percent (kg/100kg).

Statistical plots: Co contents in pendlandites of the deposits at Campello Monti (upper row) and Penninetto (bottom row). For the description of the statistical methods see the information given on top of this appendix (B). The data is given in mass percent (kg/100kg).

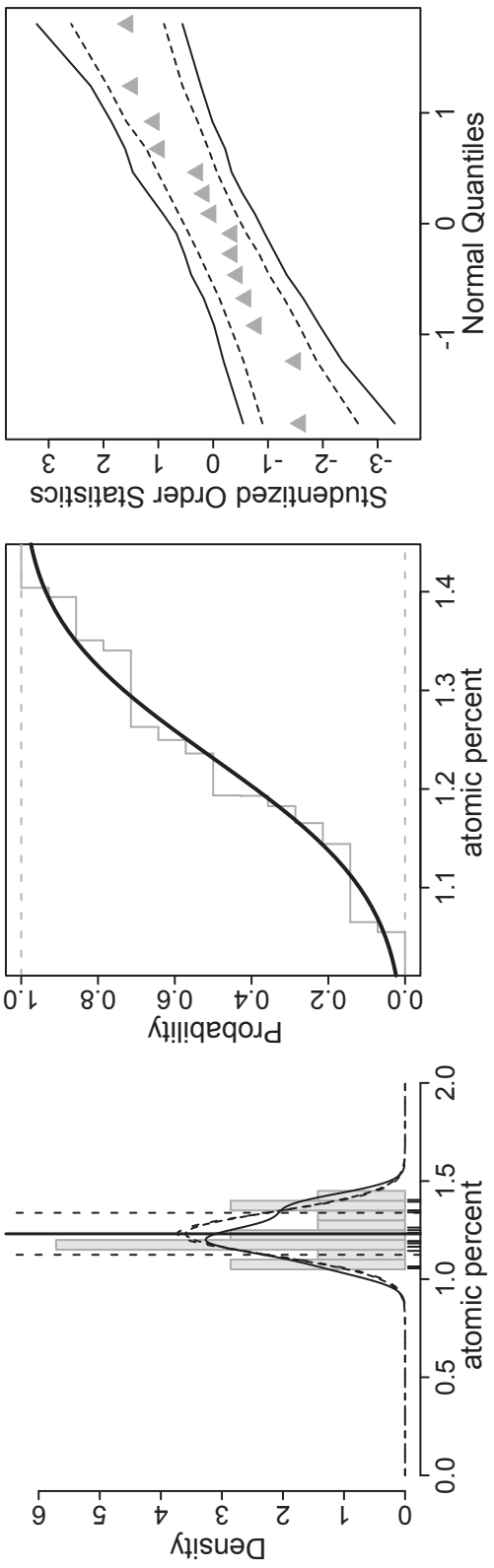

Statistical plots: Co contents in pendlandites of the deposits at Alpe Laghetto. For the description of the statistical methods see the information given on top of this appendix (B). The data is given in mass percent (kg/100kg).

Statistical plots: Co contents in pendlandites of the deposits at Piancone la Frera (upper row) and Fei di Doccio (bottom row). For the description of the statistical methods see the information given on top of this appendix (B). The data is given in mass percent (kg/100kg).

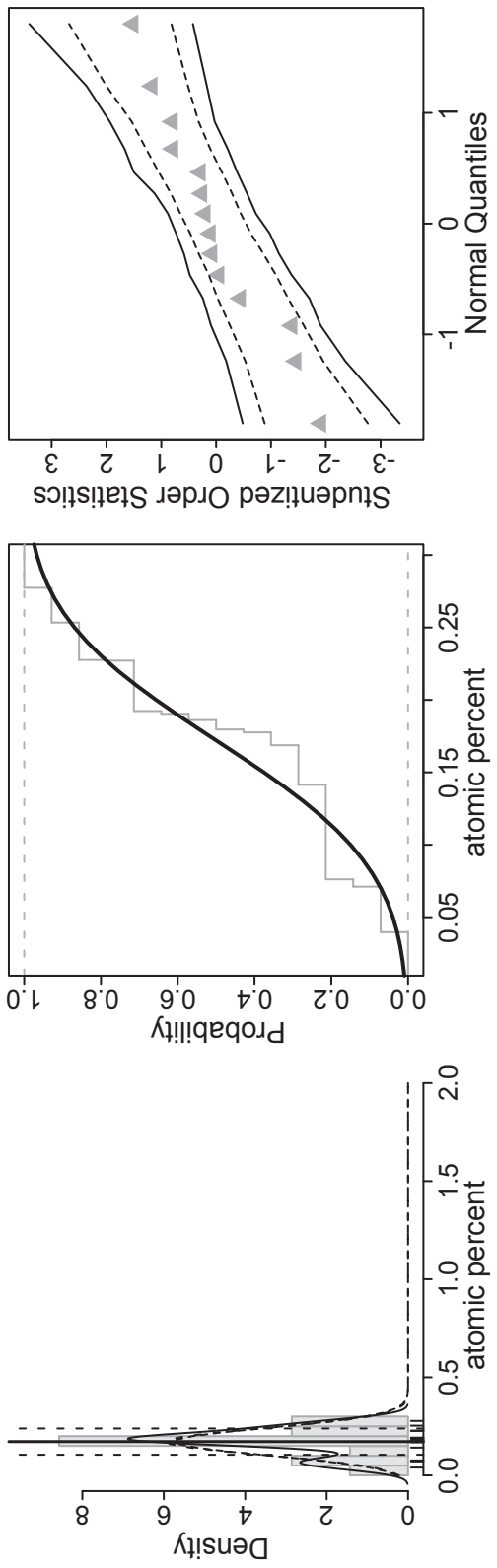

Statistical plots: Co contents in pendlandites of the deposits at Bec d' Ovaga. For the description of the statistical methods see the information given on top of this appendix (B). The data is given in mass percent (kg/100kg).

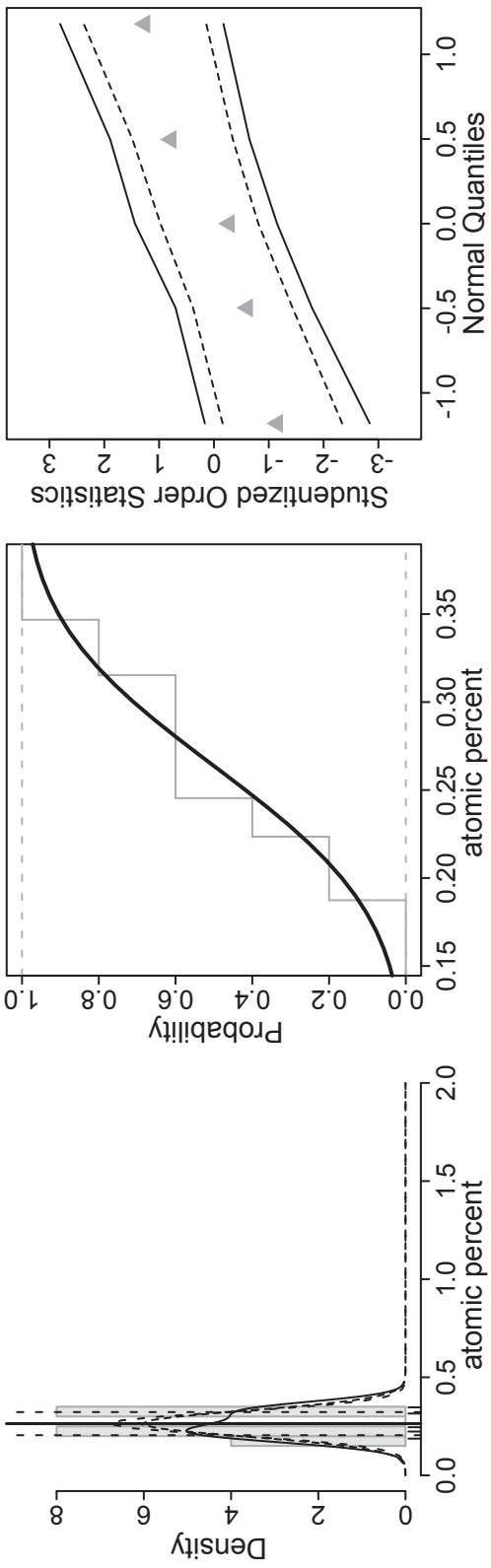

Statistical plots: Co contents in pendlandites of the deposits at Castello di Gavala. For the description of the statistical methods see the information given on top of this appendix (B). The data is given in mass percent (kg/100kg).

C. Apatite analyses

Electron microprobe (EMP) analyses of selected apatite minerals within polished sections of the ultramafic pipe at Bec d' Ovaga (BO 1271A and BO 6), Castello di Gavala(GV 1262A and GV 1279), Piancone la Frera (MO 1220A), Valmaggia (VM 1327 and VM 1) and Fei di Doccio (FD 4 and FD 1). The data is given in mass percent (kg/100kg).

Electron microprobe (EMP) analyses of selected apatites (Unit: mass percent; kg/100kg)

Locality	BO	BO	BO	BO	BO	BO	BO	BO	BO	BO	BO	BO	BO	BO
Sample	1271	1271	1271	1271	1271	1271	1271	1271	1271	1271	1271	1271	1271	1271
Analysis	1	2	3	4	5	6	7	8	9	10	11	12	13	14
MgO	0.04	0.03	0.03	0.04	0.05	0.04	0.04	0.03	0.04	0.09	0.02	0.03	0.04	0.04
Al_2O_3								0.00						
CaO	53.25	53.20	53.10	53.05	51.89	52.21	52.56	52.70	52.33	52.44	53.66	52.63	54.27	53.28
SiO_2	0.05	0.06	0.06	0.11	0.13	0.06	0.06	0.09	0.10	0.19	0.06	0.06	0.04	0.05
P_2O_5	43.83	43.50	43.30	43.53	44.05	43.43	43.37	43.81	43.17	43.01	43.51	42.98	45.41	43.53
F	1.289	1.486	1.710	1.284	1.707	2.414	1.873	2.116	2.760	2.983	2.212	3.031	0.988	1.580
Y_2O_3		0.009		0.020	0.020		0.001		0.030		0.017			
Dy_2O_3														
La_2O_3	0.055					0.061	0.105	0.062	0.056	0.005	0.007	0.019		
ThO_2	0.175	0.022	0.432	0.524	0.076	0.833	0.326	0.260			0.708		0.016	0.109
Sm_2O_3	0.039	0.205	0.392	0.241	0.637	0.547	0.427	1.739			0.910			0.208
Ce_2O_3	0.247	0.447	0.199	0.279	1.008		0.723		0.117	0.118		0.015	0.071	0.710
FeO	0.151	0.140	0.183	0.261	0.237	0.230	0.281	0.295	0.121	0.286	0.173	0.184	0.131	0.130
Tb_2O_3						0.019		0.110	0.524	0.067		0.107	0.024	
Pr_2O_3		0.028			0.549	0.053	0.137	0.402			0.102	0.689	0.039	0.011
Cl	0.087	0.063	0.048	0.063	0.073	0.056	0.058	0.059	0.074	0.098	0.067	0.077	0.076	0.060
Gd_2O_3	0.022	0.020			0.105	0.046	0.012	0.041	0.066	0.392			0.022	
Nd_2O_3	1.335	0.011	0.003	0.738	0.828			0.077	0.084	0.177			0.036	0.258
Eu_2O_3	0.445	0.591		0.108	0.127	0.275		0.036	0.062		0.030	0.071		
Ho_2O_3	0.007	0.524		0.023	0.021	0.048	0.094	0.042	0.063	0.081	0.041		0.017	
Tm_2O_3	0.081	0.080	0.028	0.005	0.066		0.007				0.003	0.032		0.114
Er_2O_3	0.001				0.016									
Yb_2O_3	0.002	0.037				0.052	0.011	0.020					2.022	0.038
Lu_2O_3	0.003		0.081										3.472	
UO_2	0.015			0.013	0.027	0.003		0.008	0.004	0.013	0.009	0.009		
TiO_2	0.003		0.011			0.007	0.013	0.008				0.007	0.001	
Sum	101.12	100.45	99.57	100.29	101.61	100.39	100.09	101.90	99.60	99.95	101.52	99.94	106.68	100.12

Electron microprobe (EMP) analyses of selected apatites (Unit: mass percent; kg/100kg) - extended 1

Locality	BO	BO	BO	BO	BO	BO	BO	BO	BO	BO	BO	BO	BO	BO	BO
Sample	1271	1271	1271	1271	1271	6	6	6	6	6	6	6	6	6	6
Analysis	15	16	18	19	20	1	2	3	5	6	7	8	9	10	11
MgO	0.05	0.05	0.03	0.04	0.03	0.03	0.03	0.01	0.03	0.21	0.00	0.01	0.00	0.02	0.04
Al_2O_3			0.00				0.01			0.26			0.00		0.03
CaO	53.34	52.53	53.58	53.57	53.87	50.30	49.52	51.95	50.68	49.99	51.70	51.97	49.05	49.81	52.06
SiO_2	0.03	0.04	0.04	0.07	0.05	0.16	0.34	0.12	0.15	0.58	0.10	0.10	0.21	0.17	0.50
P_2O_5	43.43	42.21	43.82	43.44	43.35	40.59	40.38	41.20	40.77	40.14	43.01	40.90	40.90	40.92	39.55
F	1.375	1.028	2.030	1.683	1.276	2.724	2.024	2.262	2.735	2.032	3.039	2.903	3.205	3.097	2.624
Y_2O_3			0.004		0.011			0.021			0.009	0.020			0.008
Dy_2O_3													0.006		
La_2O_3		0.011				0.040	0.077	0.034	0.009	0.020			0.035		
ThO_2		0.104	0.018					0.056	0.253		1.324		1.351	0.321	
Sm_2O_3	0.384		0.770		0.258	0.178	0.050	1.056	0.526		4.462		2.264	2.181	
Ce_2O_3	0.349			0.766	0.273		0.011	0.676	0.100	0.055				2.273	
FeO	0.091	0.172	0.148	0.314	0.264	0.215	0.277	0.083	0.155	0.831	0.092	0.084	0.092	0.178	0.118
Tb_2O_3	0.049		0.097					0.092	0.132	0.009	1.511	0.106			
Pr_2O_3										0.005		0.810	0.909	0.059	0.066
Cl	0.088	0.057	0.089	0.072	0.080	0.069	0.066	0.054	0.058	0.051	0.077	0.097	0.076	0.063	0.063
Gd_2O_3	0.009		0.041	0.234	0.014	0.106	0.273	0.013	0.011		0.243		0.107		0.047
Nd_2O_3		0.055	0.080	0.417	0.006	0.045	0.543	0.135			1.208		0.531		0.090
Eu_2O_3	0.024		0.218	0.169	0.007		0.040		0.069		0.007		0.098	0.054	
Ho_2O_3	0.001	0.001	0.040	0.027	0.001		0.094		0.009	0.116	0.038	0.033	0.047	0.017	0.060
Tm_2O_3		0.025	0.031		0.066	0.018	0.057	0.019	0.100		0.002	0.026	0.067		0.004
Er_2O_3	0.014	0.084				0.002	0.062		0.035	0.089				0.005	
Yb_2O_3	0.007									0.219				0.021	0.236
Lu_2O_3				0.012	0.030					0.861	0.002	0.101			
UO_2	0.005		0.011			0.014	0.001			0.039	0.007	0.010	0.015		
TiO_2			0.010	0.017		0.011	0.005	0.011			0.006			0.015	0.019
Sum	99.26	96.36	101.07	100.83	99.58	94.50	93.86	97.79	95.82	95.50	106.84	97.17	98.96	99.22	95.51

Electron microprobe (EMP) analyses of selected apatites (Unit: mass percent; kg/100kg) - extended 2

Locality	BO	BO	BO	BO	BO	BO	BO	BO	BO	BO	FD	FD	FD	FD	FD	FD
Sample	6	6	6	6	6	6	6	6	6	6	4	4	4	4	4	4
Analysis	12	13	14	15	16	17	18	19	20	21	1	2	3	4	5	6
MgO	0.28	0.06	0.01	0.02	0.30	0.20		0.01	0.01	0.04	0.05	0.05	0.03	0.83	0.03	0.09
Al_2O_3	0.42	0.07		0.00	0.21	0.13	0.00	0.00		0.03					0.00	
CaO	49.08	49.17	50.07	48.33	49.05	51.27	50.05	54.52	50.83	52.74	52.83	53.06	53.01	51.51	52.74	53.02
SiO_2	0.88	0.25	0.14	0.15	0.76	0.47	0.11	0.13	0.11	0.21	0.12	0.03	0.04	0.74	0.04	0.06
P_2O_5	40.00	40.00	40.00	40.00	40.00	39.94	40.00	41.37	41.00	41.67	42.98	43.08	43.65	42.53	43.02	44.31
F	3.030	2.438	2.976	3.452	3.497	0.298	2.142	2.810	3.349	2.238	1.192	0.699	0.051	1.102	0.707	0.460
Y_2O_3	0.022	0.015			0.049		0.002		0.016						0.006	0.036
Dy_2O_3																
La_2O_3	0.006	0.018	0.033	0.044	0.009		0.076	0.031	0.026		0.042	0.001	0.033	0.007	0.098	0.001
ThO_2			2.999	0.019	0.008	0.029		0.088	0.328			0.117	0.217	0.604		0.012
Sm_2O_3			3.402	2.508		0.841		0.363	0.830			0.007	0.485	1.329	0.321	
Ce_2O_3	0.029	0.080			0.060	1.503	0.044				0.091	0.294	0.537	0.657		0.174
FeO	0.459	0.277	0.325	0.438	1.917	0.198	0.139	0.265	0.125	0.110	0.632	0.118	0.102	0.309	0.097	0.261
Tb_2O_3	0.010				0.008	0.007				0.137	0.553		0.160	0.048		
Pr_2O_3	0.040	0.039	0.401	0.028		0.046	0.057		0.064					0.100	0.305	
Cl	0.022	0.062	0.094	0.070	0.079	0.058	0.037	0.052	0.056	0.055	0.625	0.417	0.514	0.468	0.519	0.363
Gd_2O_3		0.281				0.026	0.693	0.379	0.040		0.053		0.113	0.062	0.065	
Nd_2O_3		2.792	0.754	0.087			0.041			2.239					0.062	0.125
Eu_2O_3	0.141				0.381	0.002	0.730	0.009				0.022	0.117	0.008	0.017	2.599
Ho_2O_3		0.017		0.039	0.135	0.022		0.002	0.103	0.076	0.070	0.046	0.106			0.259
Tm_2O_3			0.068		0.019	0.041			0.296	0.022		0.016	0.048	0.112		0.056
Er_2O_3							0.010					0.013				
Yb_2O_3		0.019		0.027	0.307				0.411	0.086						0.223
Lu_2O_3	0.110		0.005		0.003		0.070							0.021		0.042
UO_2								0.007		0.037	0.008	0.009		0.011		0.012
TiO_2		0.059		0.009		0.008	0.025	0.005					0.742		0.010	0.004
Sum	94.53	95.64	101.27	95.23	96.79	95.08	94.23	100.04	97.59	99.68	99.24	97.98	99.96	100.45	98.04	102.10

Electron microprobe (EMP) analyses of selected apatites (Unit: mass percent; kg/100kg) - extended 3

Locality	FD	FD	FD	FD	FD	FD	FD	FD	FD	FD	FD	FD	FD	FD	FD	FD
Sample	4	4	4	4	4	4	4	4	4	4	4	4	4	1	1	1
Analysis	7	8	9	10	11	12	13	14	15	16	17	16	20	1	2	3
MgO	0.02	0.04	0.03	0.02	0.03	0.03	0.04	0.06	0.87	0.05	0.06	0.05	0.03	0.09	0.06	0.05
Al_2O_3									0.03							
CaO	53.02	52.70	52.96	53.09	52.65	52.57	52.95	52.81	50.75	52.67	53.15	52.69	53.13	51.84	52.03	48.94
SiO_2	0.04	0.09	0.05	0.05	0.04			0.04	0.81	0.03		0.07	0.05	0.15	0.08	0.08
P_2O_5	43.25	42.74	42.78	42.82	42.05	43.35	43.37	43.43	41.97	43.02	44.57	43.35	43.52	39.62	43.52	41.00
F	0.397	1.022	1.102	1.238	1.208	0.421	1.204	0.524	0.153	0.170	1.069	0.034	0.822	1.691	1.160	1.357
Y_2O_3			0.015			0.026			0.024		0.050	0.011		0.026	0.009	
Dy_2O_3										0.020	0.133					
La_2O_3		0.054	0.027					0.212					0.046	0.012	0.133	0.058
ThO_2	0.036	0.014	0.027	0.006	0.019	0.262			0.030	0.041		0.979		0.024	0.040	
Sm_2O_3	0.503		0.096			0.281	0.644		0.274	0.158	1.962	1.214	0.621		0.596	0.183
Ce_2O_3	0.242		0.043		0.061	0.359		0.328	0.716	0.160			0.617			0.377
FeO	2.746	0.085	0.130	0.191	0.313	0.123	0.114	0.121	0.400	0.123	0.084	0.236	0.120	0.282	0.188	0.117
Tb_2O_3		0.025					0.009	0.019		0.043	0.281	0.116		0.032	1.087	
Pr_2O_3	0.015	0.077	0.082	0.021		0.048	0.085	0.536	0.019	0.007		0.041				0.399
Cl	0.499	0.554	0.393	0.457	0.496	0.388	0.417	0.470	0.478	0.486	0.443	0.688	0.526	0.400	0.358	0.273
Gd_2O_3	0.044	0.261	0.048			0.029		0.308	0.013		0.063	0.013			0.012	
Nd_2O_3					0.046						1.903	0.049		0.013		1.831
Eu_2O_3	0.064		0.049		0.007			0.006	0.011		0.093				0.003	
Ho_2O_3					0.029	0.014	0.048		0.017	0.050	0.025	0.109	0.332			
Tm_2O_3		0.024	0.042	0.031	0.005	0.042	0.056				0.053	0.018	0.055			0.030
Er_2O_3				0.031	0.016			0.001						0.023		
Yb_2O_3	0.260			0.045		0.467	0.014	0.075			0.014	0.010				
Lu_2O_3		0.010	0.042		0.023						0.229					
UO_2	0.007	0.022		0.013	0.014					0.042	0.067		0.005			
TiO_2		0.007	0.007			0.066		0.011		0.011		0.006				
Sum	101.14	97.72	97.93	98.01	97.00	98.48	98.94	98.94	96.56	97.09	104.25	99.68	99.87	94.20	99.28	94.69

Electron microprobe (EMP) analyses of selected apatites (Unit: mass percent; kg/100kg) - extended 4

Locality	FD	FD	FD	FD	FD	FD	FD	FD	FD	FD	FD	FD	FD	FD	FD	FD
Sample	1	1	1	1	1	1	1	1	1	1	1	1	1	1	1	1
Analysis	4	5	6	7	8	9	10	11	12	13	14	15	16	17	18	19
MgO	0.03	0.04	0.03	0.06	2.10	0.05	0.03	0.03	0.04	0.05	0.08	0.02	0.02	0.05	0.01	0.02
Al_2O_3				0.46	0.17	0.00			0.00		0.01					
CaO	51.60	52.09	52.33	48.25	45.88	48.58	49.93	51.49	52.18	52.36	52.01	51.60	44.71	51.51	47.16	50.77
SiO_2	0.06	0.05	0.05	0.47	3.67	0.07	0.07	0.17	0.05	0.07	0.11	0.06	0.10	0.08	0.10	0.07
P_2O_5	41.58	41.67	42.37	42.00	42.00	42.00	42.00	41.43	41.91	41.97	43.32	43.24	42.00	41.28	41.00	40.71
F	1.180	1.036	0.494	1.730	0.697	0.825	0.741	1.088	1.048	0.698	1.180	1.208	1.311	1.067	1.771	1.550
Y_2O_3	0.009				0.012			0.012	0.006			0.006	0.006	0.021	0.020	
Dy_2O_3		0.103														
La_2O_3	0.006			0.041	0.081	0.085	0.130	0.137		0.081	0.174	0.077	0.106	0.072	0.124	0.005
ThO_2	0.018	0.101	0.055	0.017		0.043		0.481		0.006	0.283			0.043		0.022
Sm_2O_3	0.100	0.234	0.085				0.096	0.324			0.860					0.023
Ce_2O_3	0.032	0.281	0.306	0.168	0.178	0.308	0.634	0.326	0.805	0.181	1.922	0.115	0.139	0.635	0.123	
FeO	0.163	0.102	0.122	0.299	1.974	2.091	0.110	0.161	0.138	0.283	0.168	0.158	0.813	0.262	0.237	0.173
Tb_2O_3	0.018		0.071				0.352					0.716	0.001		0.027	0.023
Pr_2O_3	0.092		0.074	0.048		0.065		0.063	0.055	0.059		4.513		0.058	0.023	0.003
Cl	0.275	0.285	0.275	0.317	0.312	0.315	0.265	0.278	0.336	0.296	0.260	0.350	0.449	0.353	0.394	0.353
Gd_2O_3			0.044				0.039		0.021	0.036	0.003		0.013	0.008	0.402	0.416
Nd_2O_3	0.061	0.654	0.137	0.019	0.040	0.257	0.774		0.089		2.447	0.140	0.141			
Eu_2O_3	0.046	0.008		0.048	0.001	0.179		0.051				0.082	0.060	0.042	0.016	0.045
Ho_2O_3	0.003	0.059	0.086	0.013	0.061		0.042	0.032	0.013	0.093	0.088	0.007	0.082	0.054	0.007	
Tm_2O_3		0.066	0.063	0.011	0.044		0.065	0.007		0.083		0.021		0.046	0.048	0.060
Er_2O_3		0.016	0.019	0.029							0.024					0.018
Yb_2O_3						0.001		0.006				0.034	0.029	0.001		
Lu_2O_3		0.122					0.082							0.009		
UO_2	0.017						0.007		0.018	0.018					0.011	
TiO_2			0.003		0.068	0.015		0.007			0.002	0.008		0.012		
Sum	95.28	96.92	96.62	93.98	97.29	94.88	95.37	96.08	96.70	96.29	102.94	102.35	89.98	95.60	91.48	94.26

Electron microprobe (EMP) analyses of selected apatites (Unit: mass percent; kg/100kg) - extended 5

Locality	FD	FD	FD	FD	GV	GV	GV	GV	GV	GV	GV	GV	GV	GV	GV
Sample	1	1	1	1	1262	1262	1262	1262	1262	1262	1262	1262	1262	1262	1262
Analysis	21	22	23	24	1	2	3	4	5	6	8	9	10	11	12
MgO	0.03	0.06	0.02	0.06	0.07	0.12	0.20	0.12	0.14	0.09	0.05	0.10	0.14	1.52	0.11
Al_2O_3				0.02										0.02	
CaO	50.99	50.45	48.72	49.36	51.64	51.43	51.03	47.92	51.15	51.57	47.91	48.47	47.98	46.85	48.08
SiO_2	0.07	0.13	0.11	0.18	0.20	0.06	0.06	0.05	0.24	0.07	0.25	0.08	0.10	2.52	0.08
P_2O_5	40.56	40.31	40.02	39.94	42.52	40.73	39.52	40.00	40.26	41.86	40.00	40.00	40.00	40.00	40.00
F	1.107	1.581	1.736	1.642	0.896	0.596	0.197		0.626	0.341	0.561		0.654	0.491	0.369
Y_2O_3		0.020	0.002					0.004	0.002		0.015				0.008
Dy_2O_3															
La_2O_3	0.124	0.115	0.118	0.102		0.135	0.583	0.206		0.159	0.198		0.138	0.117	0.209
ThO_2	0.037		0.010		5.051		0.009	0.024	0.019		0.030	0.051		0.012	0.024
Sm_2O_3					10.306	0.074	0.183	0.028				0.155			
Ce_2O_3	0.162	0.196	0.185	0.279		0.442	0.020	0.239	0.556	0.153	0.210	0.660	0.141	0.131	0.170
FeO	0.378	0.298	0.213	0.181	0.318	0.200	0.221	0.216	0.310	0.259	2.532	0.206	1.300	0.447	6.534
Tb_2O_3		0.043	0.144		0.100			0.017				0.097			
Pr_2O_3	0.050	0.029						0.071	0.055				0.042		0.044
Cl	0.324	0.399	0.412	0.327	0.306	0.585	0.651	0.750	0.675	0.845	0.851	0.898	0.900	0.555	0.973
Gd_2O_3	0.060	0.235		0.754	0.051			0.003	0.110				0.027	1.319	0.037
Nd_2O_3			0.837		0.537	0.009	0.290	0.115	1.768		0.239	0.024	0.100	1.309	0.114
Eu_2O_3		0.041		0.146	0.012		0.117	0.021	0.070	1.492	0.009			0.026	
Ho_2O_3	0.042		0.002	0.020	0.007			0.061	0.004	0.675	0.034		0.028		
Tm_2O_3	0.004	0.057				0.016	0.025		0.005					0.015	
Er_2O_3					0.028				0.007	0.002		0.230			
Yb_2O_3			0.060								0.034				
Lu_2O_3	0.054	0.007			0.016				0.005			0.208			
UO_2	0.021		0.006		0.006	0.002	0.007	0.008	0.006			0.018		0.004	0.008
TiO_2	0.004						0.034				0.002	0.081			0.016
Sum	94.02	93.97	92.59	93.00	112.06	94.40	93.15	89.86	96.01	97.52	92.92	91.27	91.54	95.33	96.78

Electron microprobe (EMP) analyses of selected apatites (Unit: mass percent; kg/100kg) - extended 6

Locality	GV	GV	GV	GV	GV	GV	GV	GV	GV	GV	GV	GV	GV	GV	GV
Sample	1262	1262	1262	1262	1262	1262	1262	1262	1279	1279	1279	1279	1279	1279	1279
Analysis	13	14	15	16	17	18	19	20	1	2	3	4	5	6	7
MgO	0.13	0.10	0.09	0.06	0.04	0.05	0.05	0.06	0.09	0.08	0.74	0.07	0.07	0.06	0.19
Al_2O_3														0.00	
CaO	48.73	48.85	49.23	50.98	50.72	51.29	47.65	50.61	51.62	51.88	49.76	50.93	48.97	49.53	50.20
SiO_2	0.06	0.06	0.06	0.05	0.07	0.09	0.08	0.10	0.24	0.12	0.12	0.08	0.12	0.13	0.53
P_2O_5	40.00	40.00	40.00	39.76	40.03	40.20	40.00	39.03	40.71	40.89	38.58	41.51	40.21	40.17	39.55
F	0.405		0.114	0.399	0.321	0.636	0.578	0.764	0.867	0.808	0.933	0.516	0.802	0.893	0.580
Y_2O_3	0.006		0.013	0.014	0.012		0.011	0.002			0.012				0.026
Dy_2O_3															
La_2O_3					0.112	0.110	0.023	0.100	0.062	0.064	0.050	0.057		0.062	0.059
ThO_2				0.106		0.031	0.906		0.033	0.235	0.036	0.292	1.026	0.821	0.004
Sm_2O_3	0.078			0.045			0.238			0.417		0.601		0.532	
Ce_2O_3	0.788	0.132		0.537	0.187	0.047		0.175	0.018	0.480	0.052	0.592	0.181		0.067
FeO	0.163	0.158	0.185	0.283	0.185	0.189	0.245	0.256	0.515	0.282	0.947	0.181	0.231	0.184	2.521
Tb_2O_3	0.050		0.667	0.014		0.073		0.024	0.027			0.005			
Pr_2O_3	0.504		5.886	0.643	0.091		0.271	0.012			0.023		0.045	0.028	
Cl	0.648	0.617	0.468	0.789	1.222	1.034	0.944	1.029	0.985	0.503	0.639	0.432	0.444	0.480	0.661
Gd_2O_3			0.004		0.896	0.523	0.058		0.001	0.070		0.057			
Nd_2O_3	0.197	0.599	6.205	0.057			0.282			0.114		0.097		0.033	
Eu_2O_3	0.044	1.216		0.057	0.040	0.055	0.110				0.665	0.018			
Ho_2O_3		0.057	0.078	0.075	0.517	0.044	0.005		0.037		0.100	0.018		0.014	0.012
Tm_2O_3			0.037			0.047	0.063	0.106		0.058					0.016
Er_2O_3			0.024	0.003	0.085							0.005	0.010	0.023	
Yb_2O_3								0.716							
Lu_2O_3	0.081												0.005		
UO_2			0.006	0.009				0.008	0.008	0.006	0.026	0.007	0.002	0.029	0.011
TiO_2	0.018	0.008			0.007			0.013		0.006	0.037	0.003			0.008
Sum	91.90	91.80	103.06	93.87	94.54	94.42	91.51	93.00	95.20	96.01	92.72	95.48	92.10	92.99	94.43

Electron microprobe (EMP) analyses of selected apatites (Unit: mass percent; kg/100kg) - extended 7

Locality	GV	GV	GV	VM	VM	VM	VM	VM	VM	VM	VM	VM	VM	VM	VM
Sample	1279	1279	1279	1327	1327	1327	1327	1327	1327	1327	1327	1327	1327	1327	1327
Analysis	8	9	10	1	2	3	4	5	7	8	9	10	11	12	13
MgO	0.16	0.04	0.14	0.14		0.06			0.06	0.41	0.11	0.24	0.06	0.17	0.08
Al_2O_3	0.01			0.03		0.23				0.61	0.06	0.17		0.05	0.02
CaO	48.12	51.40	50.61	52.56	52.72	46.15	49.82	52.85	49.53	48.34	51.93	51.38	51.80	51.03	51.76
SiO_2	0.37	0.12	0.37	0.18	0.07	0.34	0.14	0.16	0.10	0.96	0.40	0.44	0.08	0.28	0.19
P_2O_5	37.90	40.95	39.11	41.45	41.60	40.00	40.00	44.33	41.00	41.00	41.82	41.85	41.58	41.15	41.04
F	0.603	0.921	0.597	1.211	1.214	1.591	0.588	0.562	1.581	1.466	0.968	1.052	1.497	1.258	1.567
Y_2O_3					0.019	0.019	0.024	0.051				0.025		0.009	
Dy_2O_3								0.009							
La_2O_3	0.017	0.043	0.015	0.071	0.048	0.040	0.081		0.064			0.047	0.054	0.011	0.037
ThO_2	0.004			0.035			0.450		0.375			0.160			
Sm_2O_3				1.076			0.402	1.785	0.041			0.177	0.354		0.304
Ce_2O_3	0.050	0.082	0.051		0.075	0.061				0.041				0.349	0.117
FeO	2.025	0.690	1.675	0.210	0.253	0.768	0.158	0.095	0.379	1.204	0.530	0.099	0.192	0.231	0.241
Tb_2O_3		0.043	0.010	0.009	0.066			0.273			0.158	0.130	0.027		
Pr_2O_3		0.052	0.006	0.018			0.095	4.095							
Cl	0.380	0.536	0.521	0.376	0.989	0.846	1.091	1.343	0.241	0.238	0.968	0.224	0.281	0.258	0.248
Gd_2O_3			0.039		0.049		0.258				0.181		0.126	0.048	0.006
Nd_2O_3	0.129		0.030					0.240			0.092	1.198	0.061		0.016
Eu_2O_3						0.045								0.054	
Ho_2O_3			0.162		0.385	0.027	0.061	0.117		0.057		0.023	0.002		0.040
Tm_2O_3		0.049	0.021	0.044			0.048	0.061	0.076		0.047	0.051		0.063	
Er_2O_3				0.025				0.010							
Yb_2O_3					0.030				0.006			0.003		0.013	
Lu_2O_3							0.043	0.023	0.043			0.012			
UO_2	0.004	0.019			0.001		0.011	0.011		0.011	0.004	0.027		0.015	0.001
TiO_2		0.004	0.003	0.170			0.019					0.006	0.012		
Sum	89.76	94.94	93.37	97.60	97.51	90.18	93.29	106.02	93.50	94.35	97.25	97.31	96.13	94.99	95.66

Electron microprobe (EMP) analyses of selected apatites (Unit: mass percent; kg/100kg) - extended 8

Locality	VM	VM	VM	VM	VM	VM	VM	VM	VM	VM	VM	VM	VM	VM	VM	VM
Sample	1327	1327	1327	1327	1	1	1	1	1	1	1	1	1	1	1	1
Analysis	14	15	16	17	1	2	3	4	5	6	7	8	9	10	11	12
MgO	0.10	0.28	0.08	0.48	0.08	0.11	0.07	0.07	0.09	0.05	1.70	0.08		0.14		0.02
Al_2O_3		0.27		0.34							0.04		0.00			
CaO	49.45	51.42	50.82	50.58	52.68	51.43	47.34	50.95	50.69	52.33	48.35	50.07	48.91	51.36	50.97	47.82
SiO_2	0.09	0.70	0.08	0.73	0.09	0.10	0.10	0.10	0.09	0.07	0.54	0.08	0.11	0.17	0.16	0.18
P_2O_5	41.00	40.94	41.00	41.00	42.29	39.46	41.00	40.63	40.00	43.33	40.00	40.83	41.00	41.89	42.38	42.00
F	1.174	1.415	1.191	1.212	1.492	1.040	0.755	0.560	0.469	1.239	1.063	0.685	0.782	1.184	1.335	1.473
Y_2O_3	0.022		0.018	0.024	0.003	0.008	0.026		0.012		0.018		0.013	0.108	0.020	0.032
Dy_2O_3										0.538						
La_2O_3	0.064	0.023		0.108		0.025		0.029	0.011		0.060		0.039	0.135	0.072	0.109
ThO_2			0.001		0.010				0.049		0.611		0.128	0.003	0.031	0.716
Sm_2O_3	0.441		0.117	0.530	0.809	0.032	10.965		0.099	0.133	1.593			0.857	3.274	1.011
Ce_2O_3		0.117	0.134		1.125	0.044	7.888	0.342	0.652	0.191		0.085	0.846	0.472		
FeO	0.228	2.167	0.178	1.191	0.226	1.176	0.120	0.385	0.337	0.196	0.154	1.067	0.400	0.465	0.169	0.182
Tb_2O_3			0.036	0.043	0.079	0.240	0.152		0.001		0.166				0.081	0.234
Pr_2O_3	0.031			0.018		0.067	0.339	0.010	0.035	0.343		0.069	0.441	0.048		1.268
Cl	0.304	0.386	0.238	0.281	0.331	0.419	0.125	0.548	0.240	0.434	0.354	0.558	0.827	0.463	0.515	0.480
Gd_2O_3	0.043	0.001		0.124	0.084	0.031		0.518		0.285	0.309			0.014	0.082	0.019
Nd_2O_3			0.041			0.153		0.019			0.533			0.249		0.034
Eu_2O_3	0.025				0.005		0.015	0.031	0.037	2.381	0.028		0.050	0.449		0.036
Ho_2O_3	0.046	0.052	0.051		0.034	0.084	0.048	0.057	0.049		0.079	0.043			0.088	0.050
Tm_2O_3	0.032	0.052			0.011		0.068	0.057		0.253	0.031		0.014	0.050		0.044
Er_2O_3							0.008			0.286						
Yb_2O_3			0.067	0.041			0.008	0.015				0.003		0.017		
Lu_2O_3	0.049												0.001			
UO_2			0.001	0.022	0.002				0.007	0.203	0.013		0.009			
TiO_2			0.010	0.003	0.006	0.024				0.146				0.036		
Sum	93.10	97.81	94.05	96.73	99.37	94.44	109.02	94.32	92.87	102.40	95.65	93.57	93.57	98.12	99.18	95.71

Electron microprobe (EMP) analyses of selected apatites (Unit: mass percent; kg/100kg) - extended 9

Locality	VM	VM	VM	VM	VM	VM	MO	MO	MO	MO	MO	MO	MO	MO	MO
Sample	1	1	1	1	1	1	1220	1220	1220	1220	1220	1220	1220	1220	1220
Analysis	13	16	17	18	19	20	1	2	3	4	5	6	7	8	9
MgO	0.11		0.09	0.04	0.08	0.05	0.09	0.06	0.11	0.43	0.11	0.07	0.07	0.04	0.98
Al_2O_3										0.01					0.03
CaO	49.01	49.49	50.33	50.92	50.01	52.10	55.04	53.71	54.03	54.03	52.78	55.50	54.32	55.28	54.03
SiO_2	0.11	0.08	0.05	0.11	0.12	0.08	0.13	0.13	0.12	0.80	0.11	0.12	0.12	0.07	1.32
P_2O_5	42.00	42.00	43.11	40.99	42.00	42.97	45.35	45.47	45.61	45.92	45.90	45.70	46.89	46.08	43.50
F	1.478	0.358	0.105	0.900	1.049	1.095	1.287	0.841	0.920	1.041	0.989	0.992	0.602	1.226	1.014
Y_2O_3	0.013			0.008		0.028		0.005	0.006			0.030			
Dy_2O_3	0.574					0.451									
La_2O_3				0.063	0.045		0.006		0.032	0.060	0.089	0.082	0.116	0.032	0.049
ThO_2	0.033		0.085		0.067		0.448			0.073		0.676	0.034	0.032	
Sm_2O_3	0.297		0.418		0.040	0.235		0.494			0.162	0.301			
Ce_2O_3	0.442	0.242	2.575	0.091	0.084	0.103	0.039	0.063	0.052	0.069	0.056	0.050	0.059	0.021	0.004
FeO	0.185	0.139	0.134	2.385	0.149	0.190	0.187	0.206	0.143	0.277	0.177	0.131	0.317	0.225	0.398
Tb_2O_3			0.076								0.005	0.036	0.029		
Pr_2O_3	0.195	1.748	0.108		0.070			0.008	0.094	0.103	0.005	0.004	0.044	0.021	0.014
Cl	0.208	0.678	0.176	0.645	0.597	0.424	0.650	0.592	0.660	0.705	0.553	0.565	0.543	0.660	0.640
Gd_2O_3		10.268	0.074	0.035	0.042		0.181		0.194	0.069	0.023	0.071	0.226		
Nd_2O_3			3.555	0.065	0.105	2.399	0.047	0.270		0.047	0.273	0.007	0.194		
Eu_2O_3	0.004	0.495	0.014						0.016		0.019				
Ho_2O_3		0.702	0.068				0.063		0.039		0.028	0.058		0.024	0.103
Tm_2O_3			0.088		0.019		0.041	0.567	0.049	0.063	0.085		0.012	0.061	0.028
Er_2O_3		0.033			0.038	0.162		0.001	0.008	0.006		0.016		0.025	0.037
Yb_2O_3	0.968	0.072				0.258									
Lu_2O_3						0.435									
UO_2	0.192	0.005		0.008	0.024	0.024	0.023			0.007	0.019	0.007	0.001	0.007	
TiO_2	0.029			0.004	0.023	0.014	0.045					0.002	0.007		0.010
Sum	95.85	106.31	101.06	96.26	94.56	101.02	103.62	102.42	102.08	103.71	101.38	104.42	103.58	103.81	102.14